# Traces of the Late Bronze Age Santorini and AD 365 tsunami events in the sedimentary record of Crete

–

Reconstruction of the regional tectonic geomorphology and palaeotsunami history

**Dissertation**
zur Erlangung des Grades
Doktor der Naturwissenschaften
im Promotionsfach Geographie

am Fachbereich Chemie, Pharmazie und Geowissenschaften
der Johannes Gutenberg-Universität in Mainz

**Vera Werner**
geb. in Heppenheim

—

Mainz, Mai 2019

**Berichterstatter:**

1. Gutachter:

2. Gutachter:

**Tag der mündlichen Prüfung:**

16. August 2019

*Wenn man die Natur wahrhaft liebt, so findet man es überall schön.*

Vincent van Gogh

# Abstract

The Eastern Mediterranean belongs to one of the most seismically active regions in Europe. On 21 July AD 365, a strong earthquake occurred offshore, close to southwestern Crete and struck the eastern Mediterranean world. An associated tsunami, confirmed by detailed historical reports, destroyed many coastal settlements and infrastructure between the Levante in the east and the Adriatic Sea in the northwest. Already during the 17$^{th}$ cent. BC, the Late Bronze Age, another disastrous tsunami took place, triggered by the eruption of the Santorini volcano. Based on the results of numeric tsunami simulation and field evidence from the surrounding regions in the eastern Mediterranean, both tsunami events are supposed to have affected the island of Crete. Crete Island, due to its unique position in the middle of the Hellenic fore-arc, is prone to tsunami risk origin from the Hellenic subduction zone and the volcanic arc including the still active Colombo-complex near Santorini.

So far, fine-sedimentary archives along the southwestern and northern coast of Crete have been rarely investigated so that evidence of palaeotsunami deposits has been completely missing. In this study, a multi-proxy approach including sedimentological, geochemical, geochronological and microfaunal methods was conducted in three major study sites in order to search for onshore coastal sedimentary archives that functioned as fine-sediment traps and document Crete's palaeotsunami history. The main study aims were (I) to systematically look for adequate near-coast fine-sediment archives on Crete, (II) to search for the imprint of the LBA Santorini and the AD 365 tsunami events and of further extreme wave events using a multi-proxy methodical approach, (III) to investigate and reconstruct the palaeogeographical and palaeoenvironmental evolution of the study sites since the mid-Holocene, (IV) to reconstruct the late-Holocene tectono-geomorphological development of the study sites against the background of the seismotectonically induced uplift of western Crete associated with the AD 365 earthquake.

Fine-sediment geoarchives at the study areas of Sougia, Palaiochora, Pirgos and Geropotamos (southwestern and northern Crete) were found to record up to ten extreme wave events (EWE) some of which seem to be associated with known palaeotsunami events that hit Crete. Deposits of the AD 365 tsunami were encountered in the geoarchives of Sougia, Palaiochora and Pirgos indicating, that this event did not only affect the west and southwest of Crete but also hit wide areas along the northern coast of the island.

At the Geropotamos River site, a narrow and deeply incised river valley, the sediment record contained two tsunamite candidates. These results implicate that tsunami water masses entered the river mouth and propagated at least 1 km upstream triggering mass failures at a presently inactive external bank position of the Geropotamos River. The younger EWE signal appears to have been caused by the AD 365 tsunami event while the older EWE is probably associated with the LBA Santorini eruption. Candidate layers of the LBA Santorini tsunami were also detected near Pirgos. Here, the tsunami layers's age was reconstructed based on linear regression equations calculated from the Pirgos age-depth model to 1675-

1516 cal BC. This age estimate corresponds well with the LBA Santorini eruption. Although numerous historic reports on the impact of the AD 1303 tsunami on Crete's north coast exist, it was not possible to find a reliable AD 1303 tsunamite candidate in fine-sediment geoarchives.

Combining the Pirgos sedimentary archive with the Geropotamos River valley record revealed evidence of ten major EWE that hit Crete's northern coast during the past ~ 7500 years. This leads to a statistical recurrence interval of ca. 750 years for large EWE impact. Moreover, the results of this study illustrate that seismically triggered tsunamis, such as the AD 365 tsunami, extended much farther in their range than assumed and the tsunami hazard along the north coast of Crete has so far been underestimated. Depending on the tsunami wave propagation, the local bathymetry and the local geomorphological setting, tsunami waves may also enter river mouths and extend the tsunami risk inland by causing widespread inundation along the river banks.

In summary, the southwestern and northern coasts of Crete offered a variety of adequate Holocene near-coast geoarchives covering information on the coastal evolution over the last ~ 7500 years. From a tectono-geomorphological point of view, the studied sedimentary records revealed that Holocene vertical crust movements on Crete, triggered by the seismic cycle of the Hellenic subduction zone during different periods, had a strong impact on the coastal evolution. During the long-enduring interseismic phase that started in the 7$^{th}$ mill. BC, the study areas have been predominantly subject to subsidence. The AD 365 earthquake, however, induced an abrupt reversion of the direction of the crust movement, and western Crete was coseismically uplifted by several meters.

# Zusammenfassung

Das östliche Mittelmeer zählt zu den seismisch aktivsten Regionen in Europa. Am 21. Juli 365 n. Chr. wurde der östliche Mittelmeerraum von einem starken Erdbeben, ausgelöst vor der südlichen Küste Kretas, getroffen. Der durch das Beben ausgelöste Tsunami zerstörte, dies ist belegt durch detaillierte historische Überlieferungen, zahlreiche küstennahe Städte und Siedlungen im Bereich zwischen der Levante im Osten und der Adriatischen See im Nordwesten. Bereits während des 17. Jahrhunderts v. Chr., der späten Bronzezeit, löste die Eruption des Santorini Vulkans einen weiteren Tsunami (auch bekannt als Minoischer Tsunami) aus. Abgeleitet von den Ergebnissen nummerischer Tsunamimodellierung und geologischen Feldfunden aus benachbarten Untersuchungsgebieten im östlichen Mittelmeerraum, wird angenommen, dass beide Tsunamiereignisse starken Einfluss auf die Insel Kreta besaßen. Aufgrund der besonderen Lage Kretas in mitten des Hellenischen Bogens, besteht ein Tsunami-Risiko sowohl von Tsunamis, die vom Hellenischen Bogen als auch vom Vulkanischen Bogen generiert werden.

Sedimentarchive entlang der südwestlichen und nördlichen Küste Kretas sind bis jetzt jedoch nur spärlich untersucht worden und Sedimentarchive, die Ablagerungen von Paläotsunamis enthalten, sind gänzlich unbekannt. In dieser Studie wurde mit Hilfe eines multi-proxy Methodenansatzes, bestehend aus sedimentologischen, geochemischen, geochronologischen und mikropaläontologischen Methoden, drei küstennahe Hauptsedimentarchive, die als eine Art Sedimentfalle fungieren, auf Ablagerungen von Paläotsunamis untersucht, um die Paläotsunami-Geschichte von Kreta zu dokumentieren. Die Hauptforschungsziele dieser Studie waren (I) die systematische Suche nach geeigneten küstennahmen Geoarchiven auf Kreta, (II) das Aufspüren mittels eines multi-proxy Methodenansatzes von sedimentären Tsunamisignalen, die durch den Tsunami von 365 n. Chr., den Minoischen Tsunami in der späten Bronzezeit und weiteren extremen Wellenereignissen eingetragen wurden, (III) die Untersuchung und Rekonstruktion der paläogeographischen und der paläoumweltbedingten Entwicklung der Untersuchungsgebiete seit dem Mittleren Holozän, (IV) die Rekonstruktion der tektonisch-geomorphologischen Entwicklung der Untersuchungsgebiete in Verbindung mit der seismisch bedingten Anhebung West-Kretas, ausgelöst durch das Erdbeben von 365 n. Chr.

Die in dieser Studie gefundenen Feinsedimentarchive Sougia, Palaiochora, Pirgos und Geropotamos (Südwestküste und Nordküste) enthalten Signale von bis zu zehn extremen Wellenereignissen (EWE). Von diesen konnten einige Ereignisse eindeutig mit bekannten Paläotsunamis in Verbindung gebracht werden, die die Insel Kreta trafen. Ablagerungen des Tsunamis von 365 n. Chr. konnten in den Geoarchiven von Sougia, Palaiochora und Pirgos nachgewiesen werden. Dies zeigt, dass der Tsunami nicht nur, wie lange angenommen, die Küsten im Süden und Südwesten von Kreta traf, sondern auch weite Gebiete entlang der Nordküste beeinflusste.

Die Sedimentstratigraphie des Untersuchungsgebiets Geropotamos, ein tief eingeschnittenes, steiles Flusstal, umfasste Signale von zwei Tsunami-Kandidaten, deren Wellen sich von der Flussmündung ausgehend bis zu 1 km weit ins Landesinnere ausbreiteten und Hangrutschungen an einem heute inaktiven Prallhang des Geropotamos-Flusses auslösten. Die jüngere Tsunami-Lage scheint von den Tsunami von 365 n. Chr. abgelagert worden zu sein, die ältere Tsunami-Lage könnte mit dem Minoischen Tsunami in Verbindung gebracht werden. Aufgrund von fehlenden Datierungsereignissen, besteht hier jedoch kein eindeutiges Altersmodell. Kandidaten für Ablagerungen des Minoischen Tsunamis wurden im Untersuchungsgebiet von Pirgos nachgewiesen. Basierend auf der linearen Steigung eines Alters-Tiefen-Modells konnte das Alter der tsunamigenen Ablagerungen auf das Zeitfenster von 1675–1516 v. Chr. rekonstruiert werden, was gut mit dem Alter der Minoischen Eruption korreliert. Obwohl zahlreiche historische Überlieferungen die Auswirkungen des Tsunamis von 1303 n. Chr. belegen, konnten im Rahmen dieser Studie keine verlässlichen Hinweise für entsprechende tsunamigene Ablagerungen in den Untersuchungsgebieten gefunden werden.

Werden die Stratigraphien der Untersuchungsgebiete Pirgos und Geropotamos kombiniert, erlangt man Belege für insgesamt zehn extreme Wellenereignisse, die die Nordküste Kretas während der letzten ~ 7500 Jahre getroffen haben müssen. Daraus ergibt sich ein statistisches Widerkehrintervall von ca. 750 Jahren für den Einfluss von größeren EWE. Die Ergebnisse dieser Studie zeigen außerdem, dass sich seismisch induzierte Tsunamis, wie etwa der Tsunami von 365 n. Chr., sehr viel weiter ausbreiten können, als bis jetzt angenommen wurde. Das Tsunamirisiko für die Nordküste Kretas wurde bis her unterschätzt. Abhängig von der Wellenausbreitung des Tsunamis, der lokalen Bathymetrie und den lokalen geomorphologischen Eigenschaften, können sich Tsunamis ebenfalls über exponierte Flussmündungen flussaufwärts ausbreiten und das Risiko von Überschwemmungen entlang der Flussufer weit ins bis in das Landesinnere erhöhen.

Zusammenfassend gesehen, bieten die südwestlichen und nördlichen Küsten Kretas eine Vielfalt an geeigneten Holozänen küstennahen Geoarchiven, die Informationen über die Küstenentwicklung der letzten ~ 7000 Jahre bereithalten. Zudem offenbarten die Sedimentstratigraphien der Untersuchungsgebiete, dass während des Holozäns die vertikale Krustenbewegung auf Kreta durch unterschiedliche seismischen Zyklus-Phasen der Hellenisch Subduktionszone hervorgerufen und stark beeinflusst wurde. Während lang andauernden interseismischen Phasen, die ab dem 7. Jahrtausend v. Chr. begann, waren die Untersuchungsgebiete von Senkungen geprägt. Wohingegen sich dieser Prozess während des starken Erdbebens von 365 n. Chr. umkehrte und der westliche Teil von Kreta um mehrere Meter angehoben wurde.

# Acknowledgement

This PhD thesis was realised in the frame of an interdisciplinary research project directed by the Institute of Geography at the Johannes Gutenberg-Universität Mainz, Germany, and the Ephorate of Antiquities of Rethymnon and Chania, Hellenic Ministry of Culture, Greece. Work permits were kindly approved by the Institute of Geology and Mineral Exploration (IGME), Athens.

Funding was granted by the German Research Foundation (DFG) in the context of the project *'Tracing the spatial and temporal variabilities of tsunamites on Crete Island (Greece) by sedimentological, geophysical and geodetical methods'* (VO 938/12-1 and RE 1361/19-1).

Thank you!

# List of Contents

# List of Figures

# List of Tables

# 1 Introduction

## 1.1 Geodynamic and seismotectonic evolution of Crete

The eastern Mediterranean is characterised by numerous interlocking seismotectonic structures (Fig. 1.1 A) and counts to one of the seismically most active regions in Europe (McKenzie 1972; McClusky et al. 2000; Doutsos & Kokkalas 2001; Hollenstein et al. 2008). The main geotectonic structure is the Hellenic Arc where the African Plate is being subducted underneath the overriding Aegean Microplate with 35–40 mm/yr (McClusky et al. 2000; Reilinger et al. 2006; Hollenstein et al. 2008). In front of the subduction zone lies an accretionary prism, the Mediterranean Ridge, which has been formed by the compressional forces of the northwards moving African Plate (McKenzie 1972; Le Pichon & Angelier 1979; Doutsos & Kokkalas 2001). Induced by the rollback effect of the subducting plate and the movement of the trench towards the south, the Cretan Sea, a back-arc basin with an average water depth of 1000 m, has been formed to the north of Crete (McKenzie 1972; Angelier et al. 1982; Doutsos & Kokkalas 2001; Reilinger et al. 2006; Seidel et al. 2007; Royden & Papanikolaou 2011). In front of the subduction zone, a major trench system including the Ionian, Ptolemy, Pliny and Strabo trenches, reaches water depths of more than 3000 m. The subducted slab dips northward with an angle of 10° to 15° and reaches depths of 35 to 45 kilometres beneath Crete and more than 600 kilometres beneath the central Aegean (e.g., Bohnhoff et al. 2001; van Hinsbergen et al. 2005; Hollenstein et al. 2008). Corresponding with the down-going slab, the Benioff seismic zone reaches a maximum depth of 200 km, and ends beneath the volcanic arc of the Cyclades including the still active Colombo-complex near Santorini and Milos Island (e.g. Hollenstein et al. 2008).

Most earthquakes in the eastern Mediterranean occur on the interface of the Hellenic subduction zone up to a medium depth of 45 km and may reach maximum magnitudes of $M_w$ = 6.5 in average (Hollenstein et al. 2008; Shaw et al. 2008; Shaw & Jackson 2010). Frequent shallow earthquakes are characteristic along the entire Hellenic Arc and are linked to extensional faulting of the overriding Aegean microplate (Taymaz et al. 1990; Papazachos et al. 1997). Strong earthquakes also originate along major faults such as the North Anatolian Fault and the Cefalonia transform fault. However, during history, the Hellenic Arc is known to be capable of generating strong earthquakes such as the AD 365 and 1303 earthquakes with extremely high magnitudes of $M_w$= 8.3 (Stiros 2001; Shaw et al. 2008; Shaw & Jackson 2010) and $M_w$= 8.0, respectively (Papadopoulos et al. 2014).

Crete is located in the central fore-arc of the Hellenic subduction zone. Within the last 13 million years, the subduction and the associated coseismic processes caused a cumulative uplift of Crete of approximately 2–3 km (McKenzie 1978; Meulenkamp et al. 1994; Jolivet et al. 1996). First, the central Iraklion ridge emerged at ~ 4 Ma, then the outer island parts followed ~ 1 Ma later (Shaw & Jackson 2010). Crustal extension of the Aegean microplate started during Miocene with the activity of major detachment faults (Fassoulas et al. 1994; Papanikolaou & Vassilakis 2010), followed by intense active normal faulting that led to the island's fragmentation into fault-bounded blocks creating a prominent horst-and-graben

structure (Peterek & Schwarze 2004; Seidel et al. 2007; Caputo et al. 2010). Crete's topography is characterized by mountain peaks rising up to more than two kilometres above sea level which are located in the footwall of major normal faults forming high escarpments (Peterek & Schwarze 2004). Splay faults located in the accretionary wedge control the growth of Crete's topography by uplifting the overriding Aegean microplate (Shaw & Jackson 2010; Mouslopoulou et al. 2015a).

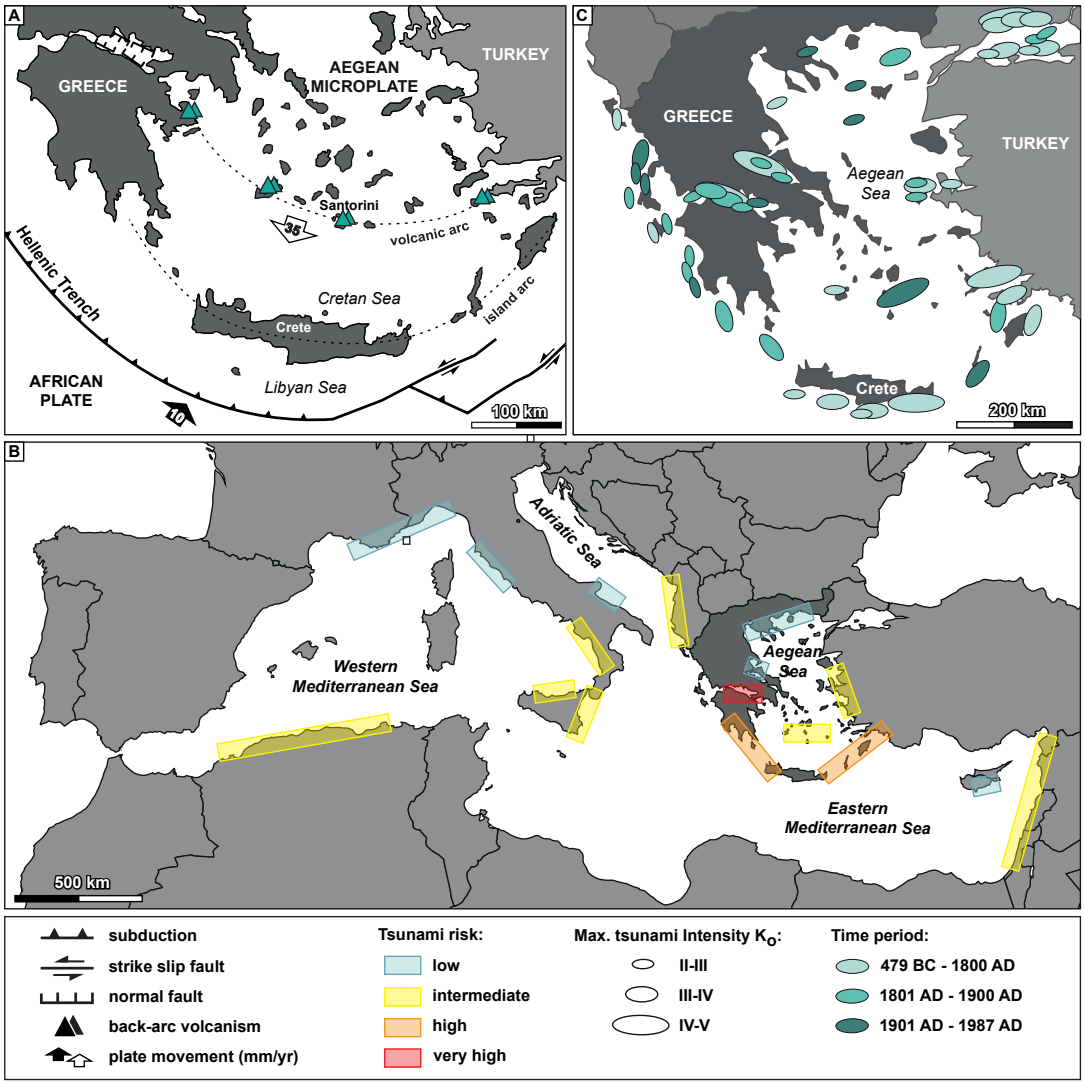


**Fig. 1.1:** Tectonic overview and tsunamigenic zones of the Mediterranean. A: Tectonic background of the eastern Mediterranean with the Hellenic Trench in the south and the volcanic back-arc to the north of Crete (adapted from Doutsos & Kokkalas 2001) B: Tsunamigenic sources in Greece after Papazachos & Dimitriu (1991) based on tsunami catalogues entries. The ellipse size is proportional to the (estimated) maximum tsunami intensity $K_o$. C: Tsunamigenic zones of the Mediterranean Sea defined from documentary sources and their relative tsunami potential classification. The highest tsunami risk is depicted for the Gulf of Corinth and along the Hellenic Arc (modified after Papadopoulos & Papageorgiou 2014).

Crete's geology is characterised by a pile of nappes deriving from different palaeogeographical zones (Franz et al. 2005; Papanikolaou & Vassilakis 2010). These nappes can be subdivided into upper and lower tectonic units that are characterised by high-pressure/low-temperature metamorphism (Seidel et al. 2004). The lower unit comprises (from bottom to top) the Plattenkalk or metamorphic Ionian/Mani unit and the Phyllite-Quartzite unit (in western Crete the Trypalion unit). The upper unit is formed by the Gavrovo-Tripolitsa and the Pindos units (Seidel et al. 2004; Papanikolaou & Vassilakis 2010). Post-Alpine sediments, such as Holocene deposits and Pliocene marls, rest on top of the geotectonic units which were deformed by the Alpine orogenesis.

### 1.1.1 Holocene tectonic crust movements of Crete

A series of superimposed Holocene palaeoshorelines decreasing in age from top to bottom indicate up to eleven stepwise periods of subsidence (each step comprises 20 to 30 cm) of the western Cretan block since at least 2000 BC (Flemming 1978; Pirazzoli et al. 1982). Then, a phase of strong vertical crust uplift followed that uplifted the western part of Crete up to 9 m a.s.l. and tilted the 100 km long lithospheric block in a north-eastward direction (Pirazzoli et al. 1982, 1992). The preserved palaeoshorelines provide valuable information on the seismic behaviour of the Hellenic subduction zone and also on the uplift history of Crete in matters of magnitude and time of large earthquake events (Tiberti et al. 2014; Mouslopoulou et al. 2015a).

By dating these palaeoshorelines, Tiberti et al. (2014) calculated a long-term net uplift rate of 2.5–2.7 mm/yr for the period of 42 ka to present, including both periods of either subsidence or uplift. The last 5 ka show a slightly higher uplift rate (3.0–3.3 mm/yr) than the long-term uplift. The youngest and uppermost palaeo-sea level stand in western Crete is preserved till today as a prominent bio-erosive palaeoshoreline fringing nearly the entire southwestern coast and was described first by Spratt (1865). With regard to their studies in the uplifted ancient harbour of Phalasarna, located at the western coast of Crete, Pirazzoli et al. (1986, 1996) suggested that the strong uplift was correlated with the large AD 365 earthquake, or with a sequence of earthquakes between AD 355 and AD 450 (the so-called Early Byzantine Tectonic Paroxysm, EBTP).

More recent dating analysis of the prominent AD 365 palaeoshoreline by Shaw et al. (2008, 2010) confirmed that the coseismic uplift of up to 9 m is rather assumed to have taken place within one single earthquake event, namely the AD 365 earthquake. They elucidated that the maximum uplift and the absence of corresponding marine bioerosive features, such as *Lithophaga* sp. boreholes, between the youngest palaeo-sea level and the present sea level corroborated their findings. The periods of either up- or downward motions of Crete is supposed to be controlled by coseismic slip on reverse faults in the overriding Aegean Microplate where also the prominent AD 365 earthquake was originated (Shaw et al. 2008; Stiros 2010; Tiberti et al. 2014; Mouslopoulou et al. 2015a).

Western Crete's coseismic uplift, caused by the AD 365 earthquake, was visualised by means of uplift contours by Flemming (1978), Pirazzoli et al. (1982) and Kelletat (1991) (for an overview see Stiros 2010). All three uplift contour diagrams, created on the base of field

observations, show highest uplift rates for the southwestern part of the island. The uplift rates decrease with eastward direction and tend towards nil near the city of Rethymnon (Kelletat 1991; Flemming 1978). In the diagram of Pirazzoli et al. (1982), the nil-contour line is located farther east near the city of Heraklion. In contrast to the western part, the eastern part of Crete was not affected by the coseismic uplift during the AD 365 earthquake. Here, subsidence dominates, leaving submerged palaeoshorelines (Kelletat 1991; Mouslopoulou et al. 2015b). The different uplift patterns of western and eastern Crete were explained by the assumption that the AD 365 uplift was largely aseismic (e.g., Gallen et al. 2014; Strobl et al. 2014). On the opposite, Mouslopoulou et al. (2015a) state that the absence of evidence for uplift events in eastern Crete rather reflects that this area has been seismically quiescent during the Late Holocene.

### 1.1.2 Tsunami risk in the Mediterranean

Tsunamis (Japanese for "harbour wave") are sea waves with large wave length of up to hundreds of kilometres, depending on the trigger mechanisms. Almost all tsunamis are seismically produced by large magnitude submarine earthquakes, but volcanic eruptions and (submarine) landslides are also commonly known as tsunami sources (Flouri et al. 2013; Papadopoulous 2014; Röbke & Vött, 2017). Very few tsunamis are caused by meteoroid impact.

Hence, the tsunami origin in the Mediterranean is dominated by main geotectonic features, such as the Hellenic Arc subduction zone which is known to have generated several strong M > 8 tsunamigenic earthquakes (Tiberti et al. 2014). Strong tsunamigenic earthquakes also occur in other seismically highly active regions in the Mediterranean, such as the Cefalonia transform fault (Greece), the Calabrian Arc (Italy) and the Cyprus Arc (Cyprus) (Tinti & Maramai 1996; Guidoboni & Comastri 2005; Ambraseys 2009). Seismic or landslide tsunami sources can also be located in the Corinthian Gulf (Kortekaas et al. 2011; Hadler et al. 2013; Vött et al. 2018a) and the Marmara Sea (Hébert et al. 2005).

The volcanic back-arc of the Hellenic subduction zone includes two active centres, namely the islands of Milos and Santorini. The latter is known for several strong volcanic eruptions during history as for example the latest eruption in 1950 (Druitt et al. 1999). One of the largest volcanic eruptions in the Mediterranean was the Late Bronze Age (LBA) eruption of Santorini (Thera) which was accompanied by pyroclastic flows entering the sea, flank collapses and finally caldera-forming which resulted in a destructive tele-tsunami (McCoy & Heiken 2000; Bruins et al. 2008; Goodman-Tchernov et al. 2009; Nomikou et al. 2016).

The rich cultural history over thousands of years in the Mediterranean favoured the above-average historical documentation of tsunami events; in particular of catastrophic events with basin-wide impact (e.g., Galanopoulos et al. 1960; Papadopoulos & Chalkis 1984; Guidoboni et al. 1994; Guidoboni & Comastri 1997; Stiros 2001; Ambraseys 2009). However, the absence of historical evidence is not evidence of absence of any further, unmentioned tsunami events (Hadler et al. 2012).

One of the earliest historic records reporting on an earthquake and an associated tsunami that happened in the 5$^{th}$ cent BC during the Peloponnesian War was written by the Athenian

historian *Thucydides* (Thucydides 3.89, translated by Hobbes 1843). Derived from historical records, geological and instrumental data, Papadopoulos & Papageorgious (2014) defined four classes of relative tsunami potential for the Mediterranean coasts (Fig. 1.1 B). Intense studies in western Greece during the last decades have brought to light that the tsunami potential of the Ionian Sea is much higher than previously expected (Röbke et al. 2017; Vött et al. 2018b). It is still assumed to be relatively low to intermediate for the coasts of the Levantine, Aegean and Tyrrhenian Seas.

However, recent studies have provided geological evidence of strong tsunami events also in this area (Hadler et al. 2015, 2019). The tsunami potential of the Gulf of Corinth and along the Hellenic Arc is said to be high to very high but still seems underestimated in science (Hadler et al. 2013; Vött et al. 2018a). For Greece, Papazachos & Dimitriu (1991) analysed the maximum tsunami intensity (II to IV) for events between 479 BC and 1987 AD (Fig. 1.1 C). Similar to Papadopolous & Papageorgious (2014), they identified the highest tsunami intensity for regions exposed to the Hellenic Arc and for regions located in the volcanic back-arc or in the Gulf of Corinth.

In the south of Crete, the eastern Mediterranean basin is characterised by deep waters (of up to 5000 m) and by highly variable bathymetric conditions of the continental slope and shelf regions. Nearly all tsunami sources are located close to the coastline, reducing the tsunami travel time in some cases to less than 20 minutes (Mitsoudis et al. 2012). Considering the main tsunami sources, the characteristics of the eastern Mediterranean basin and the unique location in the middle of for-arc, Crete's coasts are prone to tsunami risk origin from both the volcanic arc in the north and the Hellenic subduction zone in the south.

Today, coastal areas in the Mediterranean and in Greece are still hotspots for human settlement, economy and tourism. Crete's major cities Heraklion, Chania and Rethymnon are located directly on the coast and comprise nearly half of the Cretan population (Hellenic Statistical Authority 2011). To minimize the impact of future tsunami events, it is necessary to assess former tsunami events, e.g., by the investigation of tsunami traces in the field and by numeric simulation.

## 1.2 Sedimentary evidence and historical records of tsunami impact on Crete

In this section, a short overview is given of three of the largest tsunami events and their impact on Crete. For each event, characteristics of the trigger mechanisms and so far discovered sedimentary evidence will be combined with historical records and archaeological findings.

Historical sources have to be considered with caution. Catalogues of historically reported earthquakes and tsunami events have to be considered incomplete (Hadler et al. 2012; Vött et al. 2018b). Reporting persons such as early geographers and historians were often affected by religious, political, military or socio-economic interests and their records must be viewed in the local historical context. An overview of known historical and prehistorical tsunami records in the Mediterranean are listed in earthquake and tsunami catalogues (e.g., Galanopoulos 1960; Papadopoulos & Chalkis 1984; Tinti 1991; Guidoboni et al.

1994; Soloviev et al. 2000; Papadopoulos et al. 2007, 2014; Ambraseys 2009; Hadler et al. 2012).

### 1.2.1 The LBA Santorini eruption and tsunami

The Late Bronze Age (LBA) Santorini eruption (often also called Minoan eruption) was dated by Friedrich et al. (2006) to 1621–1605 cal BC (1σ) and is related to one of the most catastrophic volcanic eruptions in the Mediterranean. Its impact is often compared to huge historical volcanic eruptions such as the well-documented eruption of Krakatau in 1883. Krakatau's eruption lasted several months and reached a volcanic explosivity index (VEI) of 6 during its final stage (Newhall & Self 1982).

In contrast, the VEI of the LBA Santorini eruption was estimated between 6.9 and 7.1 (McCoy & Heiken 2000; Sigurdsson at al. 2006). Similar to the huge impact of the Krakatau tsunami that followed the last eruption stage, Marinatos (1939) supposed a connection between archaeological destruction layers of Minoan age found at numerous sites along Crete's northern coast (e.g., the palaces of Amnissos, Malia and Knossos) and a catastrophic tsunami that was supposed to have been generated by the LBA Santorini eruption. During the explosive main stage of the LBA Santorini eruption, the volcano complex collapsed and formed a huge caldera that is often suggested as the main tsunami trigger mechanism (e.g., Marinatos 1939; McCoy & Heiken 2000). In contrast, Nomikou et al. (2016) assumed that the caldera formation of the LBA Santorini eruption occurred 'syn-eruptively' (Nomikou et al. 2016) and was not open to the sea during the main eruption stage. Instead, they proposed submarine slumping and pyroclastic flows as the main triggers for tsunami formation (Nomikou et al. 2016).

LBA Santorini tsunamites have already been detected at several sites along the coasts of the Aegean Sea and the eastern Mediterranean. At Santorini itself, McCoy & Heiken (2000) found evidence for tsunami-related deposition of reworked volcanic tephra near Pori. Near Didim and Fethye (SW Turkey), Minoura et al. (2000) identified LBA Santorini tephra deposited on top of a layer of allochthonous marine sand. Offshore near ancient Caesarea (Israel), Goodman-Tchernov et al. (2009) found several tsunami layers and the lowermost layer date to the LBA Santorini eruption. On northeastern Crete, Minoura et al. (2000) found a unit of pumice deposited on the floor of a Late Minoan workshop near Gouves (Fig. 1.4), which was overlain by a thin marine sand layer. At Palaikastro (E Crete, Fig. 1.4), Bruins et al. (2008) detected a tsunamite showing typical tsunami signatures, e.g. erosional contact, marine macro- and microfauna and even volcanic Santorini ash intraclasts. Radiocarbon dating and considering the stratigraphic background proved that the tsunamite is related to the LBA Santorini eruption (Bruins et al. 2008).

No written records or graphical representations are known for the LBA Santorini eruption and its associated tsunami, but several historians often associated Greek myth with this event as for example the Theogony (the birth of the gods) by *Hesiod* (Durazzo-Morosini et al. 1936) or the famous legend of the submerged city of Atlantis described by *Platon* (e.g., translated by Hamilton et al. 1961). However, systematically conducted archaeological excavations on Santorini and Crete provided reliable information on the Minoan civilisation,

settlement structures and on seismic destruction layers associated with the eruption (Cioni et al. 2000).

On Santorini, the excavation of the well preserved Minoan settlement of Akrotiri, inhabited since the middle Early Bronze age (Doumas 1980), revealed heavily damaged buildings. The damages were caused by several earthquakes that occurred most likely before and during the eruption (Cioni et al. 2000). The assumption that the LBA Santorini eruption has been preceded by strong earthquake(s) that forced an early evacuation of the island is supported by both the absence of valuables and a thin pumice layer that was deposited during the first eruption stage (Doumas 1980; Cioni et al. 2000). During the second eruption phase, pyroclastic flows completely covered Akrotiri (Cioni et al. 2000).

On Crete, numerous destroyed Minoan palatial centres were predominantly found in the eastern part of the island (Driessen & McDonald 2000). During the excavation of Knossos in the 20th cent. AD, *Sir Arthur Evans* found seismically induced destruction layers and he detected a chronological consistency with archaeological findings in destruction layers found on Santorini (Evans 1928). He hypothesised a relation between both destruction layers which led, together with Marinatos' (1939) tsunami hypothesis, to the mistaken assumption that the LBA eruption caused the abrupt decline of the Minoan culture. Inferred from precise radiocarbon dating of the LBA Santorini eruption (Friedrich et al. 2006) and new archaeological findings, it is, however, most likely that the combination of earthquakes and the volcanic eruption and the tsunami event led to 'an increase in crisis-related situations, culminating in the widespread fire destructions which brought this palatial phase of Minoan civilization to an end and opened the way for mainland Mycenaean domination of the Aegean' (Driessen & McDonald 2000, p.81).

### 1.2.2 The AD 365 earthquake and tsunami

The AD 365 earthquake originated on 21 July AD 365 at a N-E dipping fault, approximately 100 km long and up to 45 km deep, within the overriding Aegean microplate to the southwest of Crete (Shaw et al. 2008; Lorito et al. 2008; Flouri et al. 2013; Mousloupolou et al. 2015a). The earthquake reached a magnitude of Ms = 8.3–8.5 (Papazachos & Papazachou 1997; Shaw et al. 2008; Shaw & Jackson 2010) and historical accounts describe that it generated a tsunami that destroyed coastal settlements and infrastructure from Alexandria in the south to the Peloponnese and the Adriatic Sea in the north (e.g., Thommeret et al. 1981; Kelletat 1991; Guidoboni et al. 1994; Pirazzoli et al. 1996; Stiros 2001; Shaw et al. 2008; Papadopoulos et al. 2014). The recurrence time for such a strong event along the Hellenic subduction zone is assumed to be 800 years regarding the results of seismic studies by Shaw et al. (2008), in case that the same tectonic processes that triggered the AD 365 earthquake are assumed.

Multiple geological traces associated with the AD 365 tsunami impact were found in the Ionian and neighbouring seas underlining the wide-ranging wave propagation of this tsunami. De Martini (2010) and Smedile et al. (2011) documented AD 365 tsunami deposits in the Augusta Bay offshore Sicily and Polonia et al. (2013) attributed the widespread megaturbidite, known in literature as homogenite, to be caused by the AD 365 event. The AD 365

tsunami impact was further documented at the coasts of Aitolo-Akarnania (northwestern Greece) and the Ionian Islands of Lefkada and Corfu (Vött et al. 2006, 2009a, 2009b; May et al. 2012; Finkler et al. 2018a, 2018b, 2019).

On Crete itself, Pirazzoli et al. (1992) and Dominey-Howes et al. (1998) studied the sedimentary record of Phalasarna's ancient harbour (Fig. 1.4). Its archaeological remains are partly well preserved, indicating that the harbour was constructed during the 4th cent. BC and was in use until the 1st cent. BC (Frost & Hadjidaki 1990). Today, the harbour basin and its adjoining infrastructure are located at ca. 6 m above present sea level. Pirazzoli et al. (1992) supposed that the uplift was associated with the coseismic uplift caused by the AD 365 earthquake. Well preserved bio-erosive markers and algal rims from the time before AD 365 fringe the coastline. Within the sedimentary record of the harbour basin, Pirazzoli et al. (1992) identified two tsunamite candidates.

The lower tsunamite candidate was dated by two radiocarbon samples located below and on top of the layer to the 1st cent. BC and the 2nd cent. AD. Pirazzoli et al. (1992) interpreted this layer as being associated with the earthquake and tsunami event of AD 66. For the upper tsunamite candidate, Pirazzoli et al. (1992) do not present any sedimentary, microfaunal or geochronological evidence to prove that this layer is a candidate layer for the AD 365 event. This layer was only associated with the AD 365 earthquake and tsunami event because of its higher stratigraphic position in the sedimentary sequence. Several years later, Dominey-Howes et al. (1998) investigated the same site and also identified two tsunamite candidates. However, similar to Pirazzoli et al. (1992), they did not present any geoscientific evidence of the AD 365 tsunami impact on the ancient harbour of Phalasarna. Boulton & Whitworth (2017) recently reported on tsunami boulders from southern Crete at Laki, Diplomo Petris and Kommos (Fig. 1.4), assuming that their dislocation took place during the AD 365 tsunami event. To conclude, so far, no fine-sedimentary archives are known which record reliable geological traces of the AD 365 tsunami impact on Crete.

Although there is no geological evidence on Crete so far, this event was well documented by historians. One of the most famous reports on the AD 365 earthquake and tsunami was written by the Roman historian and geographer *Ammianus Marcellinus* who lived during the 4th century AD and who described these events in detail:

> *'(…) the solidity of the whole earth was made to shake and shudder, and the sea was driven away, its waves were rolled back, and it disappeared, so that the abyss of the depth was uncovered and many-shaped varieties of sea-creatures were seen stuck in the slime (…) then the roaring sea as if insulted by its repulse rises back in turn, and through the teeming shoals dashed itself violently on islands and extensive tracts of the mainland, and flattened innumerable buildings in towns or wherever they were found (…). For the mass of waters returning when least expected killed many thousands by drowning, and with the tides whipped up to a height as they rushed back, some ships, after the anger of the watery element had grown old, were seen to have sunk, and the bodies of people killed in shipwrecks lay there, faces up or down. Other huge ships, thrust out by the mad blasts, perched on the roofs of houses, as happened at Alexandria, and others were hurled*

> *nearly two miles from the shore, like the Laconian vessel near the town of Methone which I saw when I passed by, yawning apart from long decay.´* (*Ammianus Marcellinus*, Res Gestae 26.10.15-19, after Kelly 2004).

*Athanasios of Alexandria*, a former church leader in Egypt and Libya, who also lived during the 4th century AD, reported on the destruction of more than 100 towns on Crete by a strong earthquake and tsunami during the first year, namely the year AD 365, of the co-reign of the Roman Emperors Valens and Valentinian (Life of Anthansius, PG 25, ccx; Stiros 2001). Moreover, *Socrates Scholasticus*, a Christian church historian who lived in the 5th century AD, reported on a strong earthquake that caused severe coastline changes. In some places, former land areas submerged, in some other places new land emerged from the sea (Historia Ecclesiastica 4, 3, Migne PG 67, 468; Stiros 2001). He also dated this event to the first year of the co-reign of the two Roman Emperors Valens and Valentinian.

### 1.2.3 The AD 1303 earthquake and tsunami

On 8 August AD 1303, a strong earthquake ($M_w$= 8.0) ruptured the eastern section of the Hellenic Arc, approximately 50 to 60 km offshore between Crete and Rhodes, which generated a basin wide tsunami (Papazachos 1996; Papadopoulos et al. 2014; Valle et al. 2014). This earthquake belongs to one of the largest in the eastern Mediterranean and its long-distance impact was reported in over 50 written documents of different languages including Latin, Greek and Arabic (Guidoboni & Comastri 1997).

A compilation of different historic reports by Guidoboni & Comastri (1997) points out that the worst effects occurred at Heraklion (Crete), where two reports by the Duke of Candia (Venetian name for both Crete and Heraklion) documented in detail the heavy damage and even the collapse of e.g., public buildings, the town hall, harbour installations and the city wall. Based on the evaluation of several historic sources, the earthquake was also felt in Egypt, Palestine, Syria and in Greece (for details see Guidoboni & Comastri (1997) and references therein).

The generated tsunami is supposed to have had far-ranging impact on the coast of the eastern Mediterranean and is often compared with the AD 365 tsunami. Numerous historical sources mention the tsunami and its impact was documented e.g., for Heraklion (Crete), Acre (Israel), Alexandria (Egypt), and the Adriatic Sea. At Heraklion, the tsunami swept into the city and destroyed buildings and killed inhabitants (Guidoboni & Comastri 1997).

Despite the fact that the impact of the tsunami is historically well documented, geological field evidence, so far, are rare (Vött & Kelletat 2015). On Rhodes and at the southwestern coast of Turkey at Dalaman, Papadopoulos et al. (2007, 2012) found tsunami sand layers which they attributed to the AD 1303 event. So far, historical reports have not been correlated with geological field evidence and the earthquake's generation mechanisms along with its generated tsunami are still insufficiently explained (Valle et al. 2014).

## 1.3 Numerical simulation of the LBA Santorini and AD 365 and tsunami events

In order to assess the local tsunami risk of defined coastal areas, numerical simulations of tsunami wave propagation are well suited for providing information e.g., on arrival time, maximum wave height and possible inundation areas (Flouri et al. 2013; Röbke et al. 2013, 2016, 2017). The assessment of tsunami risk in the eastern Mediterranean has been characterised by numerous scenarios for tsunamigenic earthquakes in the region (e.g., Tinti et al. 2005; Lorito et al. 2008; Valle et al. 2014). However, uncertainties in the locations and magnitudes of the triggering earthquakes produced a wide range of different scenarios (England et al. 2015). Most tsunami simulations in the eastern Mediterranean were based on initial characteristics from known tsunamigenic earthquakes, such as the AD 365 or AD 1303 earthquakes (Lorito et al. 2008; Shaw et al. 2008; Flouri et al. 2013; Valle et al. 2014; England et al. 2015).

Depending on the initial parameters of the seismic scenarios, such as magnitude, fault length, fault depth or dip (for detail see e.g., Flouri et al. 2013 or Valle et al. 2014), the simulated wave height and wave propagation differs. Inferred from uplift contours of western Crete, Shaw et al. (2008) calculated that the possible AD 365 earthquake's origin is a fault located offshore southwestern Crete (see Section 1.2.2). The simulated tsunami propagation and the calculated sea surface heights at 4, 30, 70 and 90 minutes after the earthquake are depicted in Fig. 1.2 A. Only four minutes after the seismic shock, Crete's southwestern and northwestern coasts are exposed to maximum sea surface heights. After 30 minutes, the tsunami propagates along Crete's northern and eastern coasts and also hits the Aegean Islands and bays of the southern Peloponnese. Underlining the historically reported basin-wide tsunami impact, the simulated waves hit the northern African coast including Alexandria after 70 min at the latest. Because of the uncertainty regarding the exact fault parameters of the AD 365 earthquake, Flouri et al. (2013) calculated four seismic scenarios as initial model conditions for tsunami risk assessment for the city of Heraklion. The calculated wave amplitude (m) of scenario S2, also based on the initial fault parameters of Shaw et al. (2008), is depicted in Fig. 1.2 B. Similar to Shaw et al. (2008), highest wave amplitudes (up to 12 m) were reached along Crete's southwestern and western coasts.

Historical reports, field evidence and uplifted palaeoshorlines suggest that the location and magnitude of the AD 365 earthquake can be narrowed with a high possibility to a fault within the overriding Aegean microplate to the southwest of Crete (Shaw et al. 2008; Shaw & Jackson; Stiros 2010; Mousloupolou et al. 2015a). In contrast, the LBA tsunami simulation has produced several divergent results depending on characterisation of triggering mechanisms and initial model parameters. It had been assumed for a long time that the caldera formation during the LBA Santorini eruption was the main tsunami trigger mechanism (McCoy & Heiken 2000). However, based on new research on caldera-forming, Nomikou et al. (2016) argue that submarine slumping and pyroclastic flows were the main tsunami origin and the generated tsunami wave(s) would have been able to spread towards all directions (see Section 1.2.1). A compilation of selected tsunami simulation scenarios, based on both caldera-forming and pyroclastic flows as the triggering mechanisms of the LBA Santorini tsunami, are depicted in Fig. 1.3.

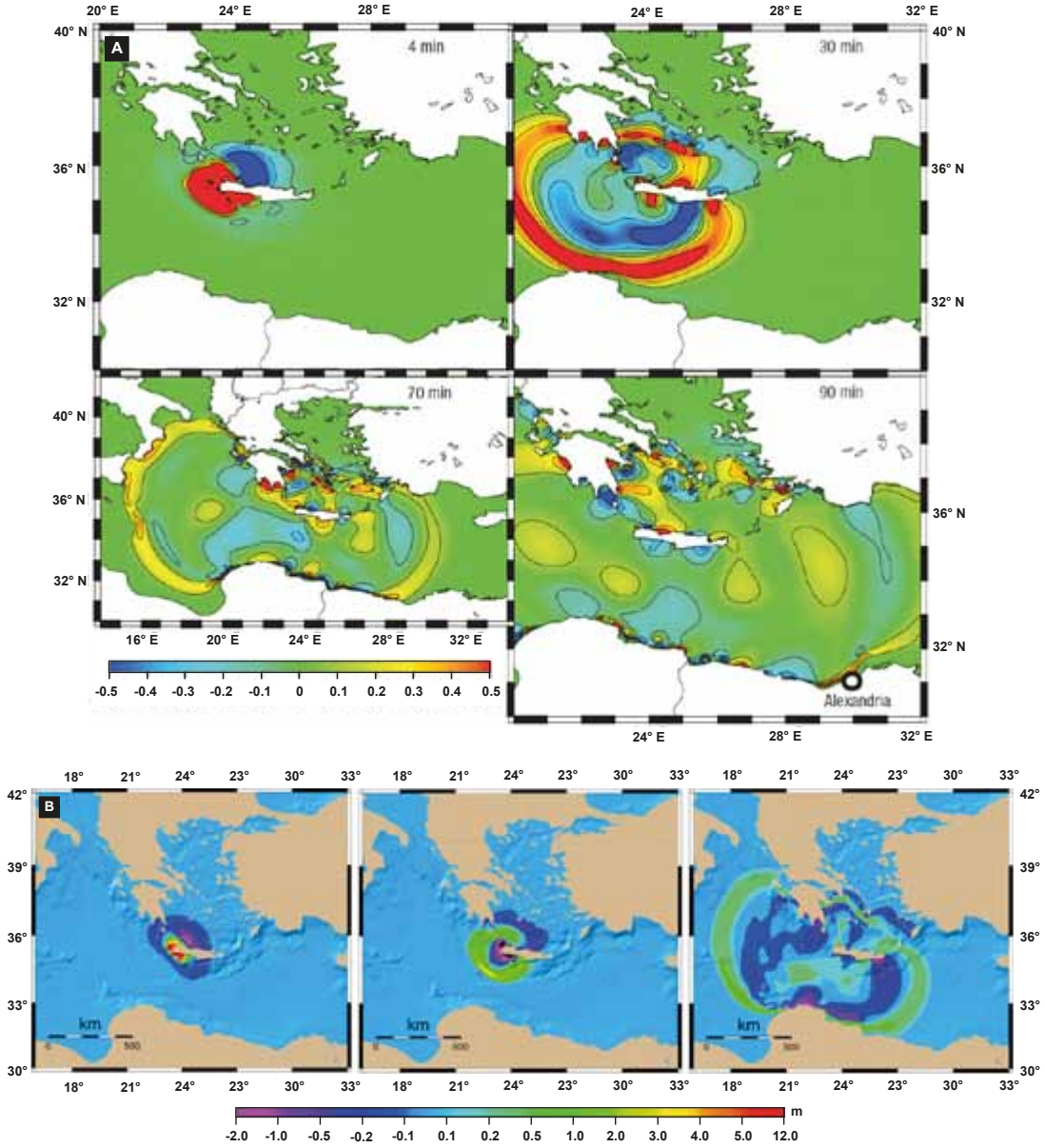


**Fig. 1.2:** Compilation of selected tsunami simulation scenarios based on the initial parameters of the AD 365 earthquake; A: calculated sea surface heights (m) at 4, 30, 70 and 90 min after the AD 365 earthquake (modified after Shaw et al. 2008); B: Calculated wave amplitude at $T_0$+10 min, +12 min and +50 min of scenario S2 (modified after Flouri et al. 2013).

The simulation of Ozel et al. (2011) (Fig. 1.3A) suggests caldera collapse as the trigger mechanism. Maximum impact is given for Santorini's neighbouring islands and Crete's northern coast. Calculated tsunami wave amplitudes based on both caldera collapse (Fig. 1.3 B, top) and pyroclastic flows (Fig. 1.3B, bottom) in a simulation by Periañez & Abril (2014) underline the discrepancy between different trigger mechanisms and initial model parameters. The differences in the direction of the pyroclastic flows into the sea were simulated by Novikova et al. (2011). Depending on the direction, the main inundation area on Crete's

northern coast showed maximum tsunami wave height changes from west to east (Fig. 1.3 C).

In summary, simulation of tsunami events comprises many uncertainties concerning the localization of the triggering fault or volcanic process, any characteristics of the trigger mechanisms and initial model parameter in particular, such as for example the volume of pyroclastic flows, the earthquake magnitude and fault characteristics. Still, tsunami modelling provides useful information, for example on where to search for geologic field evidence, which can vice versa confirm or improve the initial model parameters.

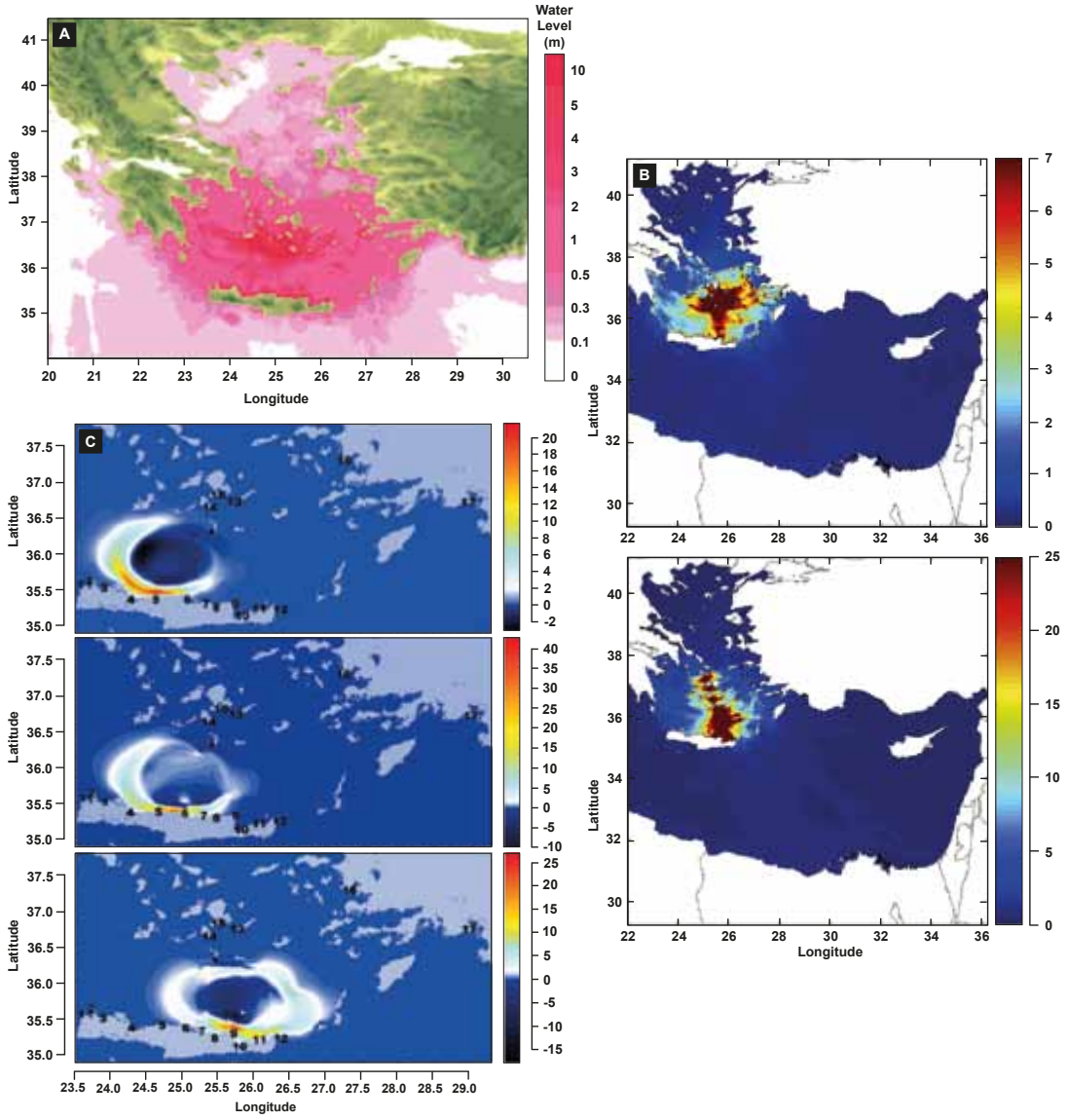


**Fig. 1.3:** Compilation of selected tsunami simulation scenarios based on different initial parameters of the LBA Santorini eruption. A: Distribution of maximum positive water elevation amplitudes 4 hours after the LBA Santorini collapse (modified after Ozel et al. 2011). B: Calculated wave heights (m) for the LBA Santorini tsunami generated by caldera collapse (top) and by pyroclastic flows into the sea (bottom) after 3 hours of simulation (modified after Periañez & Abril 2014). C: Calculated tsunami wave heights (m) generated by pyroclastic flows from the south with three different directions. Numbers represent virtual tide gauges (modified after Novikova et al. 2011).

## 1.4 Tracing palaeotsunami deposits on Crete

### 1.4.1 Study area characteristics

Crete is the largest of the Greek islands and because of its position in the middle of the Hellenic for-arc, Crete's coasts are prone to tsunami risks originating from the Hellenic subduction zone and the volcanic arc including the still active Colombo-complex near Santorini. Three study areas were selected located on Crete's southwestern and on the northern coast (Fig. 1.4). Each study area will be described in detail in the corresponding section.

Caused by the coseismic uplift of western Crete, the coastal erosion was intensified, leading to the destruction of fine-sedimentary archives and potential tsunami signatures that were originally incorporated therein. In addition, the uplift is combined with reduction of accommodation space and uplifted sediments are exposed to weathering processes. Crete's southwestern part, where the uplift reached its maximum, is nowadays dominated by steep rocky coasts. Therefore, near-coast fine-sedimentary archives in southwestern Crete which cover relevant parts of the Holocene are rare.

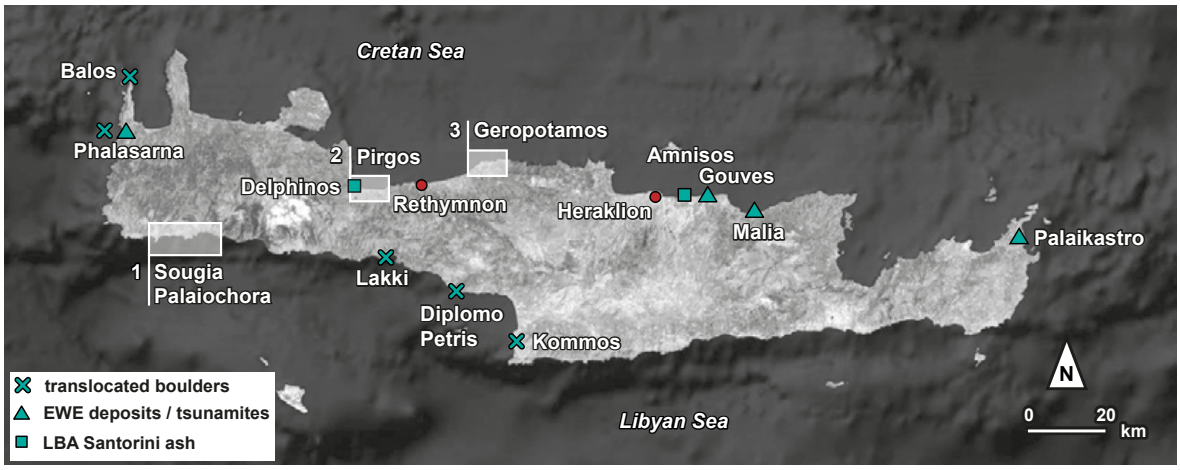


**Fig. 1.4:** Study areas (Section 2: Sougia and Palaiochora; Section 3: Pirgos; Section 4: Geropotamos) of this study and previous tsunami-related findings on Crete (modified after Google Earth 2018).

### 1.4.2 Study aims and research outline

The present study presents the results of geo-scientific investigations in three study areas comprising different types of fine-sediment archives. It intends to extend our knowledge about the palaeotsunami history of southwestern and northern Crete. Studying the palaeotsunami impact on coastal areas provides valuable information on recurrence intervals and local topographical effects that help to better assess the future tsunami hazard of Crete. The main objectives of the study, therefore, are:

(1) to detect adequate near-coast fine-sediment archives along the southwestern and northern coast of Crete with sufficient accommodation space;

(2) to search for and identify LBA Santorini and AD 365 tsunami deposits and further extreme wave event deposits within the sedimentary record of each study area by using a multi-proxy methodical approach;

(3) to investigate and reconstruct the palaeogeographical and palaeoenvironmental evolution of the study areas since the mid-Holocene with focus on the LBA Santorini and AD 365 tsunami impact on coastal evolution of Crete;

(4) to reconstruct the tectono-geomorphological development of the study areas against the background of the seismo-tectonically induced uplift of western Crete associated with the AD 365 earthquake.

The study areas Sougia and Palaiochora (Section 2) are located at Crete's southwestern coast, directly exposed to the AD 365 epicentre, and were selected to investigate the imprint of the AD 365 tsunami. Numeric simulation results of this event suggest that tsunami sediments can be expected in near-coast geo-archives of northwestern Crete as well. Therefore, the Pirgos study site (Section 3) was selected to reconstruct northern Crete's palaeotsunami history, expecting LBA Santorini tsunami imprint here as well. The third study area, the Geropotamos River valley (Section 4) study area, is also located at the northern coast. Here, the focus was set on the interaction of extreme wave events and their flow dynamics with the topography of the incised Geropotamos River valley.

Finally, in a synthesis (Section 5), all study results were compared, discussed and linked to the results of tsunami simulations in order reconstruct the tsunami impact, in particular the LBA Santorini and AD 365 tsunami, on Crete's coastal evolution. Moreover, the study areas were compared and discussed with regard to their mid-Holocene vertical crust movements and palaeogeographical evolution.

# 2 The sedimentary and geomorphological imprint of the AD 365 tsunami on the coasts of southwestern Crete (Greece) — examples from Sougia and Palaiochora

**Abstract.** The southwestern coast of Crete, one of the most seismically active regions in Europe, experienced coseismic crust uplift by 9 m during the $M_s$ = 8.3 mega-earthquake that struck the eastern Mediterranean world on 21 July AD 365. An associated tsunami event caused thousands of fatalities and destroyed many coastal settlements and infrastructure between the Levante in the east and the Adriatic Sea in the northwest. So far, coastal sedimentary archives in southwestern Crete including distinct palaeotsunami fingerprints are rarely investigated. Therefore, a multi-proxy study including sedimentological, geochemical, geochronological and microfaunal methods was conducted in order to detect onshore coastal sedimentary archives that functioned as fine sediment traps and document palaeotsunami imprint. We found adequate archives at the Sougia and Palaiochora coastal plains that were used to reconstruct the palaeogeographical evolution and the palaeoseismological history of SW Crete during the late Holocene. Our studies revealed distinct geomorphological, sedimentological, geochemical and microfaunal traces of high-energy impact from the marine side related to seismic events. At the Sougia coastal plain a sheet of fine sand with a neat microfossil and geochemical fingerprint was found sandwiched between underlying pre-tsunami muds and overlying post-tsunami colluvial silt. In the Palaiochora coastal plain, tsunami overflow of a flat Neogene bedrock platform led to the accumulation of sand-dominated deposits that were subsequently covered by colluvial material from the adjacent hillslopes. Based on radiocarbon and luminescence dating approaches, it is shown that the AD 365 tsunami event is the best-fit candidate for the tsunami-related sediments deposited at both, Sougia and Palaiochora. This study, for the first time, presents multi-proxy evidence of the AD 365 tsunami imprint on fine-sedimentary archives along the western and southwestern coast of Crete.

This section is based on Werner et al. 2018a, published in Quaternary International 473, 66–90.

## 2.1 Introduction

Caused by the subsidence of the African Plate underneath the Aegean Microplate, the eastern Mediterranean is one of the most seismically active regions in Europe (McKenzie 1972; McClusky et al. 2000; Doutsos & Kokkala 2001; Hollenstein et al. 2008). The Hellenic Trench reaching from the Ionian Islands to the west coast of Turkey has produced large earthquakes and tsunamis (Papadopoulos & Chalkis 1984; Guidoboni et al. 1994). On 21 July AD 365, a mega-earthquake ($M_s$ = 8.3–8.5) occurred within the overriding Aegean Mi-

croplate (Papazachos & Papazachou 1997; Shaw et al. 2008; Shaw & Jackson 2010) and struck the Mediterranean world.

Based on historical accounts, e.g. by the historian and geographer *Ammianus Marcellinus* (Kelly 2004), the earthquake is known to have been associated with a tsunami that destroyed many coastal settlements and infrastructure from Alexandria in the south to the Peloponnese and the Adriatic Sea in the north (e.g., Thommeret et al. 1981; Kelletat 1991; Guidoboni et al. 1994; Pirazzoli et al. 1996; Stiros 2001; Shaw et al. 2008; Papadopoulos et al. 2014). Multiple geological traces of the AD 365 tsunami impact were found in the form of teletsunami effects outside of Crete in the Ionian and neighbouring seas. Smedile et al. (2011), for example, documented AD 365 tsunami deposits offshore Sicily in the Augusta Bay and Polonia et al. (2013) attributed the widespread megaturbidite in the Ionian basin, known in literature as homogenite and Augias turbidite, to the AD 365 event.

Further geomorphological, sedimentological and microfaunal evidence by Vött et al. (2006, 2009a, 2009b), May et al. (2012) and Finkler et al. (2018a) document that the AD 365 tsunami also affected northwestern Greece, namely the coasts of Aitolo-Akarnania and the Ionian Islands of Lefkada and Corfu.

However, the geological imprint of the tsunami that occurred on 21 July AD 365 on the coasts of Crete itself is still not well known. By the AD 365 earthquake event, the southwestern Cretan coast, nowadays comprised of steep rocky slopes, experienced coseismic uplift by up to 9 m. This implied intense coastal erosion leading to the destruction of fine-sedimentary archives and potential tsunami signatures incorporated therein. Thus, the probability to find AD 365 tsunami deposits preserved in coastal archives is low because archives covering relevant parts of the Holocene are rare. Besides natural archives, ancient harbours, such as the ancient harbour basin of Phalasarna in western Crete, are known to be well-suited sediment archives that can be used for the reconstruction of coastal changes (e.g., Marriner & Morhange 2007; Goiran et al. 2010; Hadler et al. 2015; Finkler et al. 2018b).

The main objectives of our study were

(1) to detect adequate sediment archives along the southwestern coast of Crete including presumed ancient harbours and

(2) to search for and identify the imprint of the AD 365 tsunami by applying a multiproxy approach. Finally, we sought

(3) to reconstruct palaeogeographical scenarios for coastal changes induced by the AD 365 event. In this paper, we present results from the presumed ancient harbour area of Sougia and the Palaiochora coastal plain (Fig. 2.1).

## 2.2 The AD 365 earthquake and tsunami on Crete

The ancient harbour of Phalasarna is situated at the western coast of Crete (Fig. 2.1 B). It was described by several ancient geographers, such as *Strabo* (Geography, e.g., Roller 2014) and *Scylax* (Periplus of the Inner Sea 47, e.g., Shipley 2012), as closed and protected harbour. It was also mentioned in the Stadiasmus, an ancient periplus that listed and described harbours along the coasts of the Mediterranean Sea (Pirazzoli et al. 1992).

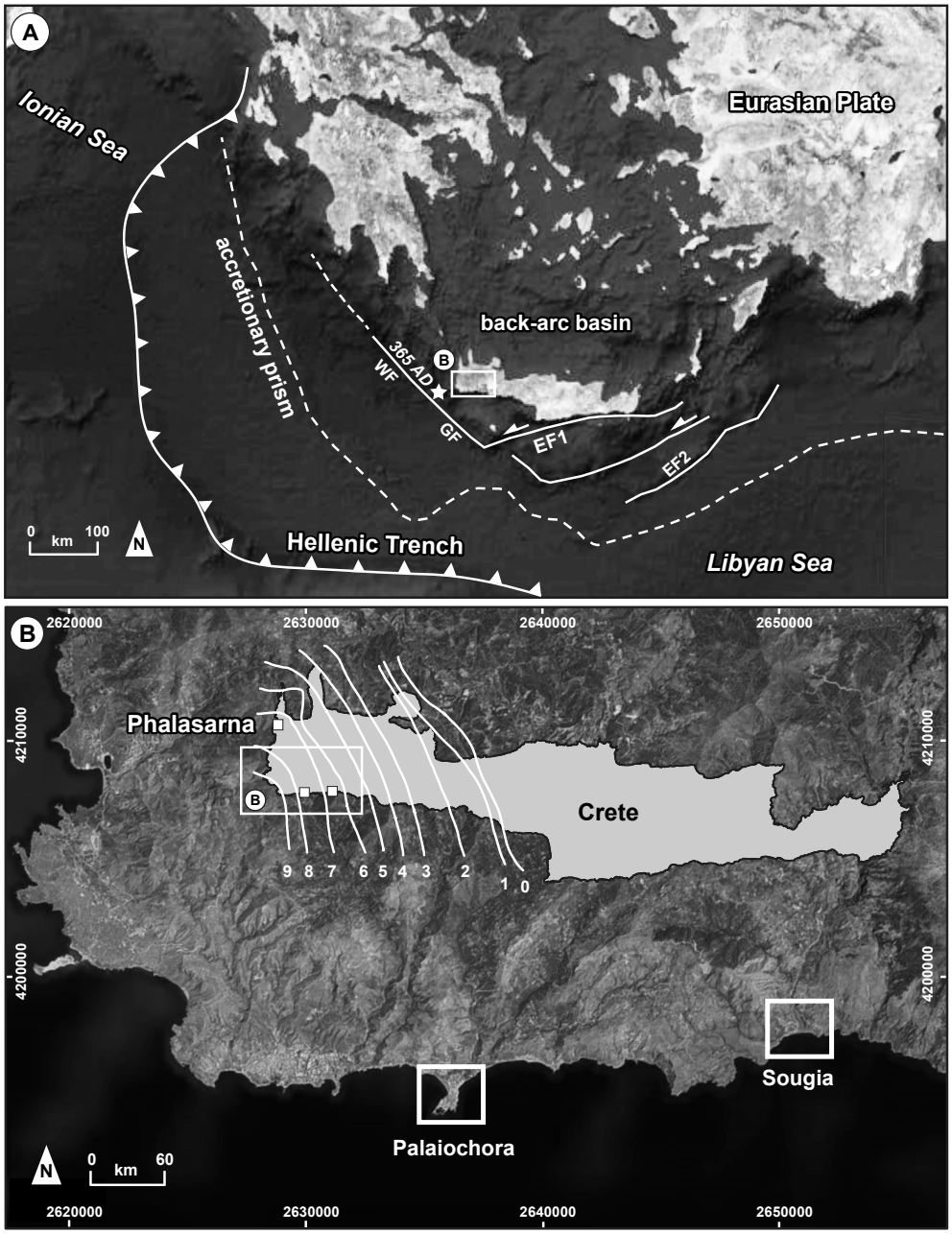


**Fig. 2.1:** Overview of the study area in southwestern Crete. (A) Schematic overview of the Hellenic subduction margin and the main fore arc faults offshore Crete (adapted from Mouslopoulou et al. 2015b). WF – Western Fault GF – Gavdos Fault, EF1 – Eastern Fault 1, EF2 – Eastern Fault 2. Star indicates epicenter of AD 365 earthquake. (B) Southwestern coast of Crete with study sites at Sougia and Palaiochora. Contour lines of inset map mark coseismic uplift associated with AD 365 earthquake in meter (after Kelletat 1991 and Shaw et al. 2008). Maps modified after Google Earth 2015.

Its archaeological remains are partly well preserved, indicating that the harbour was constructed during the 4th cent. BC and was in use until the 1st cent. BC (Frost & Hadjidaki 1990). Archaeological excavations uncovered, amongst others, an ancient quay wall with in situ mooring stones as well as a fortification tower (Hadjidaki 1988). Nowadays, the harbour basin and its adjoining infrastructure are located at 6 to 9 m above present sea level (m a.s.l.) due to the coseismic uplift associated with the AD 365 earthquake. Alongside the uplifted harbour basin of Phalasarna, well-preserved bio-erosive markers and algal rims from the time before AD 365 fringe the coastline. Such prominent features were already described by Spratt (1865). Although the harbour at Phalasarna was already out of use for around four centuries (Hadjidaki 1988), it is believed to have recorded the AD 365 tsunami landfall and thus has experienced strong attention by palaeotsunami researchers.

Pirazzoli et al. (1992) and Dominey-Howes et al. (1998) studied the sedimentary record of the ancient harbour of Phalasarna based on a small archaeological trench, approximately 2 m deep, opened during archaeological investigations in the midst of the former harbour basin. Pirazzoli et al. (1992) identified two tsunamite candidates. These two horizontal layers consist of a mixture of more or less rounded blocks and stones and broken marine shells and are situated at elevations of 5.9 m and 6.6 m a.s.l., measured by Pirazzoli et al. (1992). The authors present sedimentary and few microfaunal findings related with the lower layer that allow identifying this layer as tsunami deposit; foraminifera data document that the harbour was still filled with saltwater when the tsunami hit the area leaving an allochthonous marine signal in the microfauna record (Pirazzoli et al. 1992).

Two radiocarbon dated samples were taken from right below and on top of the tsunamite yielding calibrated ages between the 1st cent. BC and the 2nd cent. AD so that the authors interpret the layer as being associated with a well-known earthquake and tsunami event dated to AD 66. In contrast, Pirazzoli et al. (1992) do not present any sedimentological, microfaunal and geochronological evidence that allows identifying the upper event layer as tsunami deposit. Due to its higher stratigraphical position compared to the presumed AD 66 tsunamite, Pirazzoli et al. (1992) speculate that this layer is related to the AD 365 earthquake and tsunami event.

Dominey-Howes et al. (1998) investigated the same outcrop in the ancient harbour basin. However, inconsistencies concerning topographic levelling resulting in a vertical offset of around 75 cm between the two data sets were revealed by these authors but could not be clarified. Dominey-Howes et al. (1998) also identified two event layers. They undertook detailed microfossil analyses that corroborated the interpretation of Pirazzoli et al. (1992), saying that the lower layer represents a tsunami-related event deposit (Dominey-Howes et al. 1998: Tab. 1).

Based on four radiocarbon ages, this lower event layer was consistently dated to the time between the 1st cent. BC and the 2nd Li AD and interpreted as AD 66 tsunamite. Regarding the upper event layer, no radiocarbon ages were presented. Based on microfossil data, it was concluded that the last episode of marine sedimentation within the harbour was during or just after the AD 66 earthquake and tsunami event. Dominey-Howes et al. (1998: 351) stated that *"Significantly, there is no bio- or lithostratigraphic evidence to infer sedimentary deposition associated with a tsunami reported to have been generated by a large*

*vertical tectonic displacement ca. AD 365"*.

In a summary view, both Pirazzoli et al. (1992) and Dominey-Howes et al. (1998) did not present any geoscientific evidence of an AD 365 tsunami impact on the ancient harbour of Phalasarna. Further studies in search of AD 365 tsunami traces in fine-grained sedimentary archives have not yet been conducted on Crete Island. In contrast, Boulton & Whitworth (2017) recently reported on tsunami boulders from southern Crete east of Frangokastello assuming that their dislocation took place during the AD 365 tsunami event. Geological traces of the AD 365 tsunami event, however, have not yet been reported from fine-sedimentary archives along the coasts of Crete.

There are abundant historical sources that document and describe the AD 365 earthquake and tsunami and its impact to distinct coastal regions. *Ammianus Marcellinus*, for example, a Roman historian and geographer, who lived during the 4th century AD, described in detail both, the earthquake and the tsunami event:

> *"the solidity of the whole earth was made to shake and shudder and the sea was driven away, its waves were rolled back, and it disappeared, so that the abyss of the depth was uncovered and many-shaped varieties of sea-creatures were seen stuck in the slime (…) then the roaring sea as if insulted by its repulse rises back in turn, and through the teeming shoals dashed itself violently on islands and extensive tracts of the mainland (…) Huge ships, thrust out by the mad blasts, perched on the roof of houses, as happened in Alexandria, and others were hurled nearly two miles from the shore (…)" (Ammianus Marcellinus,* Res Gestae, 26.10.15-19, adapted from Kelly 2004*).*

*Athanasios of Alexandria*, a former church leader in Egypt and Libya, who also lived during the 4th century AD, reported on the destruction of more than 100 towns on Crete by a strong earthquake and tsunami during the first year of the co-reign of the Roman Emperors Valens and Valentinian, a time period that comprises the year AD 365 (Life of Anthansius, PG 25, ccx; Stiros 2001). Moreover, *Socrates Scholasticus*, a Christian church historian who lived in the 5th century AD, reported from a strong earthquake that caused severe coastline changes. In some places, former land areas were submerged, in some other places new land emerged from the sea (Historia Ecclesiastica 4, 3, Migne PG 67, 468; Stiros 2001). He dated this event to the first year of the co-reign of the two Roman Emperors Valens and Valentinian, namely to AD 365.

Although historical sources have to be considered with caution because they might be affected by political, military or socio-economic interests of effects, there is no doubt that the AD 365 earthquake and tsunami event did actually exist (e.g., Guidoboni et al. 1994; Ambraseys 2009). Moreover, there is convincing geomorphological and geochronological evidence of strong coseismic effects associated with the AD 365 event. Following the first observations and studies by Thommeret et al. (1981), Pirazzoli et al. (1982) and Kelletat & Zimmermann (1991), Shaw (2012) corroborated that the earthquake of AD 365 was caused by a fault within the overriding Aegean microplate and triggered crust uplift in western Crete in one step by up to 9 m (see also Tiberti et al. 2014).

## 2.3 Physical Setting

### 2.3.1 Geotectonic setting

The Greek island of Crete is located close to the Hellenic Trench System (Fig. 2.1 A) where the African Plate is being subducted underneath the overriding Aegean microplate with 35-40 mm/yr (McClusky et al. 2000; Reilinger et al. 2006; Hollenstein et al. 2008). A major trench system to the immediate south of Crete, more than 3000 m deep, marks this major plate boundary (McKenzie 1972; Le Pichon & Angelier 1979). Within the last 13 million years, subduction and associated coseismic processes caused a cumulative uplift of Crete in several different phases of approximately 2–3 km (McKenzie 1978; Meulenkamp et al. 1994; Jolivet et al. 1996). Recent studies for western Crete have shown that this net uplift results from a sequence of periods dominated by either uplift or subsidence (Tiberti et al. 2014). To the north of Crete, crustal thickness decreases to only 15 km (Bohnhoff et al. 2001), the sea-floor deepens gently down to 2200 m and forms a broad back-arc basin as a reaction to the rollback effect of the Hellenic slab and retreat of the trench towards the south (McKenzie 1972; Doutsos & Kokkalas 2001; Seidel et al. 2007; Royden & Papanikolaou 2011). Crustal extension started during Miocene with the activity of major detachment faults (Fassoulas et al. 1994; Papanikolaou & Vassilakis 2010) followed by intense active normal faulting that led to a fragmentation of the island into fault-bounded blocks creating a prominent horst-graben structure (Peterek & Schwarze 2004; Seidel et al. 2007; Caputo et al. 2010). To the south of Crete, the Mediterranean Ridge, a compressive accretionary prism, is located in front of the subduction zone (McKenzie 1972; Le Pichon & Angelier 1979; Doutsos & Kokkalas 2001). The Benioff zone reaches a maximum depth of 200 km and ends beneath the volcanic arc of the Cyclades including the active Colombo-complex and Milos Island (e.g., Hollenstein et al. 2008).

### 2.3.2 Earthquakes and tsunami events

With regard to the Holocene coastal evolution, Spratt (1865) described well-preserved bioerosive markers and algal rims reflecting uplifted palaeo-sea level stands along the entire coast of western Crete by up to 9 m a.s.l. (Fig. 2.1 B, Pirazzoli et al. 1982, 1996; Stiros 2001). This uppermost palaeo-sea level was found to be the youngest of a series of superimposed levels indicating up to ten stepwise periods of subsidence of the western Cretan block since 2000 BC followed by a phase of strong vertical uplift (Pirazzoli et al. 1992). Pirazzoli et al. (1982) suggested that the strong uplift was correlated with the AD 365 earthquake, a hypothesis which was later confirmed by other researchers, most recently by Shaw (2012). Regarding the maximum uplift and the absence of traces of corresponding marine bioerosion features, such as *Lithophaga* sp. boreholes between the youngest palaeo-sea level and the present sea level, the coseismic uplift is assumed to have taken place within a single earthquake event (Shaw et al. 2008).

In general, the area of the western Hellenic Trench System is characterized by shallow earthquakes linked to the extensional faulting of the overriding plate and by deeper earthquakes triggered by the movement of the subducted plate (Taymaz et al. 1990). Most earthquakes

along the Hellenic Arc occur on the interface of the subduction zone dipping with 15–20° up to a medium depth of 45 km and reach only maximum magnitudes of Mw = 6.5 in average (Hollenstein et al. 2008; Shaw et al. 2008; Shaw & Jackson 2010). Combining the distribution of earthquakes in the eastern Mediterranean and the uplift rates along the west coast of Crete, Shaw et al. (2008), see also Lorito et al. 2008; Flouri et al. (2013), suggested that the best fitting candidate that triggered the AD 365 earthquake is a N-E dipping fault approximately 100 km long and up to 45 km deep that is located within the overriding Aegean microplate. Parameters used for modelling the AD 365 earthquake suggest a magnitude of Mw = 8.3 (Shaw et al. 2008) with a recurrence interval of 5000 years.

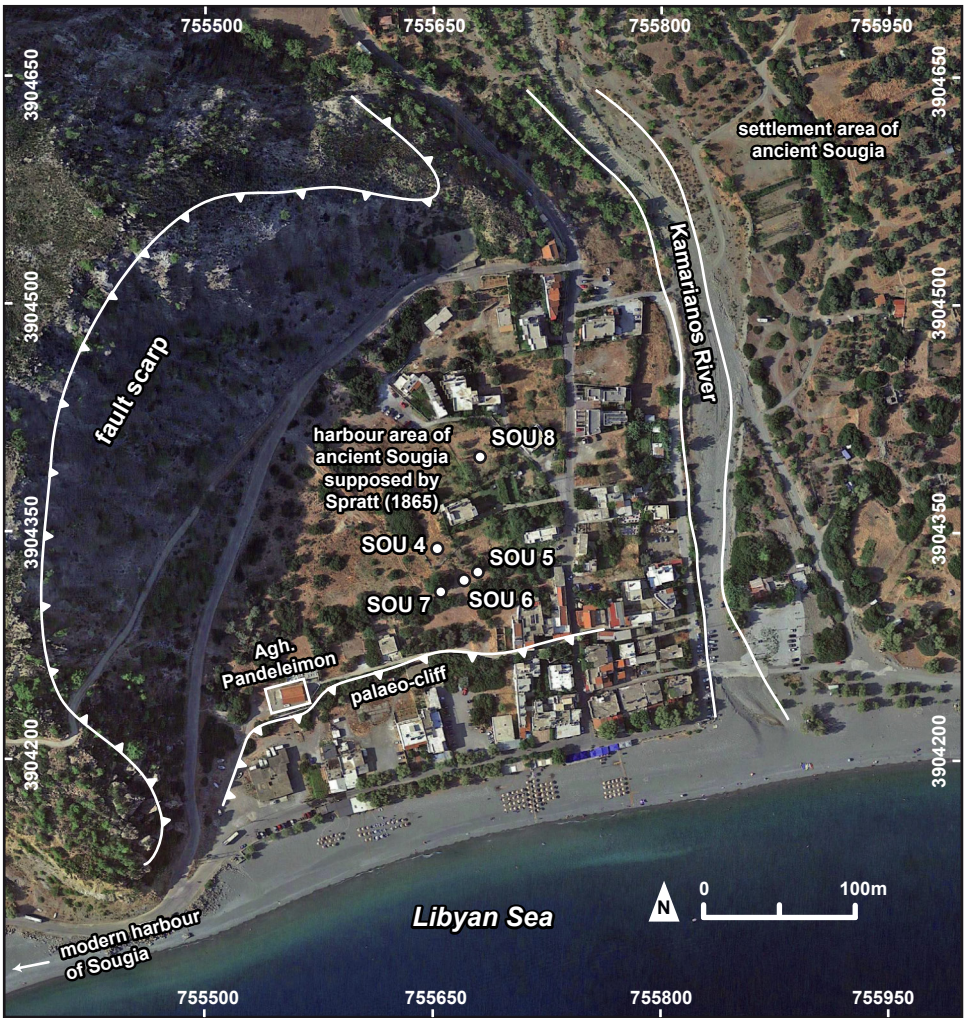


**Fig. 2.2:** Topographical overview of the Sougia coastal plain showing the present course of the Kamarianos River and location of vibracoring sites (SOU 4, SOU 5, SOU 6, SOU 7 and SOU 8). A palaeo-cliff runs from W to E. Map modified after Google Earth 2015.

However, if the same tectonic processes that triggered the AD 365 earthquake would be assumed for the entire Hellenic subduction zone, the repeat time of such events would be once every 800 years (Shaw et al. 2008). Another tsunamigenic earthquake hit the south-

west coast of Crete on AD 66 (Ambraseys 2009). Tsunami deposits of this event were found in the ancient harbour of Phalasarna (Section 2.2, Pirazzoli et al. 1992; Dominey-Howes et al. 1998). Moreover, on 8 August AD 1303, a strong earthquake (Mw = 8.0) ruptured the eastern part of the Hellenic Arc between Crete and Rhodes and the resulting tsunami struck, for example, the capital city of Heraklion (e.g., Papadopoulos et al. 2014). The largest tsunamigenic earthquake in Greece during the last century took place at the Colombo-complex on 9 July 1956 located in the southern Aegean Sea. It reached a magnitude of Mw = 7.5 and was associated with normal faulting (Papadopoulos et al. 2014). Further notable seismically induced tsunami events were observed on 9 March AD 1630, 6 February AD 1866 and 20 September AD 1867 (Papadopoulos 2011). An overview of historical and prehistorical tsunami records in the Mediterranean are listed in earthquake and tsunami catalogues (e.g., Galanopoulos et al. 1960; Papadopoulos & Chalkis 1984; Tinti 1991; Guidoboni et al. 1994; Soloviev et al. 2000; Papadopoulos et al. 2007; Ambraseys 2009; Hadler et al. 2012).

## 2.4 Study area characteristics

### 2.4.1 Sougia

The study area of Sougia is located near the modern village of Sougia at the southwestern coast of Crete (Fig. 2.2). The coastal plain is surrounded by steep rocky slopes and opens to the south in form of a wide indentation. The recent coast at Sougia is characterised by a gravel beach, passing landward into a palaeo-cliff, up to 6 m high. Bioerosive sea level indicators and algal rims that are generally associated with the AD 365 earthquake event (Pirazzoli et al. 1982; Shaw et al. 2008; Mouslopoulou et al. 2015a) are visible on both sides of the embayment, most prominently in the modern harbour of Sougia (Fig. 2.3). Based on studies of Pirazzoli et al. (1982) and Kelletat (1991), the coseismic uplift associated with the AD 365 event for the area of Sougia is between 6 and 7 m. Using DGPS, we measured 6.83 m in the modern harbour of Sougia.

According to *Stephanos Byzantinos* (590.8; e.g., Blackman 1976), Sougia (ancient Syia) was the epeinion (= harbour site) of the city of Elyros which was situated several kilometres distant from the sea. Syia was the main harbour of Elyros, while Lissos was a secondary one (Blackman 1976); or Syia was the most convenient harbour for Elyros (Perlman 2004a). In any case, the harbour-city of Syia served the inland city of Elyros, one of the most important cities in southwestern Crete, during Hellenistic and Roman times. According to the coastal pilot *Stadiasmus* (331-332; e.g., Stefanakis 2010) that dates to the 2$^{nd}$ half of the 3$^{rd}$ century AD, the ancient city Syia had a well-protected and spacious harbour. The city flourished in the Roman and the Early Byzantine period, when three basilicas of considerable dimensions were erected.

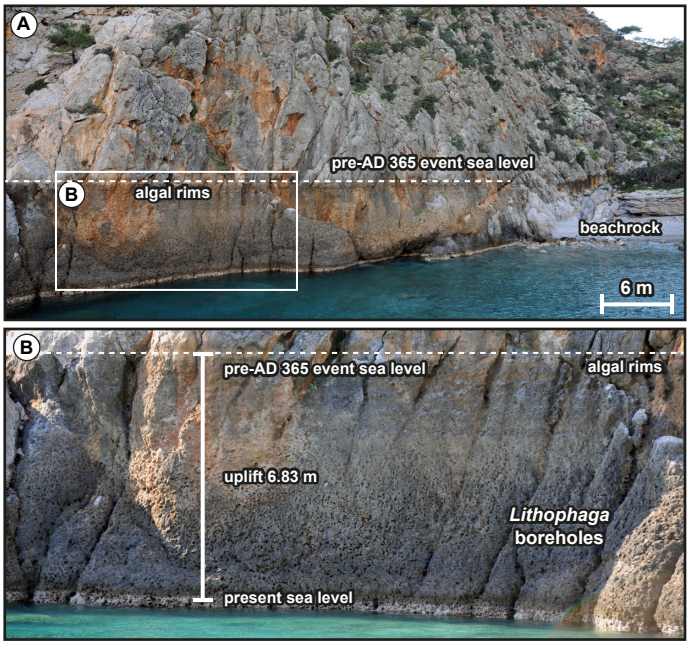


**Fig. 2.3:** Geomorphological evidence of coseismic uplift at the modern harbour of Sougia. (A) Indicators of the AD 365 sea level (algal rims and *Lithophaga* sp. boreholes) associated with layers of beachrock. (B) Detailed view of uplifted indicators of the pre-AD 365 event sea level, namely emerged boreholes of *Lithophaga* sp. and algal rims. Uplift of 6.83 m was measured by DGPS. Photos: A. Vött 2013.

The coastal plain of Sougia is divided into two parts by the Kamarianos torrential river (Fig. 2.2). In the eastern part, extensive archaeological remains of the ancient settlement include, amongst others, buildings of the Roman and Early Byzantine period, fortification walls, residential quarters, public buildings, an extensive complex of thermae and graves. There are also remains of an aqueduct that brought water from a source near Elyros to Syia (Pashley 1837; Markoulaki 1982; Andrianakis 1982; Sanders 1982; Christodoulakos & Markoulaki 2006).

The modern village of Sougia is situated to the west of the river. From here, Pashley (1837) and Spratt (1865) mentioned several wall remains and ceramic fragments. More specifically, Spratt (1865) observed wall remains running parallel to the coast, on top of the palaeo-cliff near the chapel of Agh. Pandeleimon (Pashley 1837; Spratt 1865) that lies 130 m distant from the present shoreline. Spratt (1865) interpreted these remains as harbour installations defining a harbour basin. Until today, however, archaeological field evidence is missing so that Spratt's localization of the ancient harbour basin of the city is conjectural. Still, in this area, archaeological research brought to light remains of an Early Byzantine complex and the impressive mosaic of a 6$^{th}$ century AD basilica. We carried out systematic geomorphological and geoarchaeological research in the supposed harbour area in search of adequate fine-sedimentary archives needed to comprehend the reshaping of the coastal configuration of the area after the AD 365 uplift event that left the harbours of Syia, Lissos and Phalasarna on solid ground (Hadjidaki 1996; Stefanakis 2010).

### 2.4.2 Palaiochora

The second study site, Palaiochora, is located in the immediate proximity to the modern village of Palaiochora, approximately ten kilometres westwards of Sougia (Fig. 2.1 B). A shallow promontory out of Neogene marl, reaching a west-east extension of nearly 350 m, connects the Palaiochora limestone plateau, out of material of the Pindos unit (Seidel et al. 2007), to the mainland of Crete. On both sides of the promontory, a beach has developed consisting of unsorted medium to coarse sands (west) and gravel (east) resulting in a pseudo-tombolo coastline configuration; meanwhile, the shallow marly bedrock of the central promontory is covered by a thin layer of loose Holocene deposits.

To the west and to the east of the Palaiochora peninsula, uplifted generations of reef-type sponges, bioherms, coastal notches, algal rims and bore holes of *Lithophaga* sp. are omnipresent documenting different phases of crust uplift. In the west, in situ beachrock reaches from the present shoreline to more than a hundred metres inland. Scheffers & Scheffers (2007) argue this beachrock must be younger than the coastal uplift in AD 365, since there was no beach existing at that time. To the west of Palaiochora, we measured 7.75 m a.s.l. for the prominent bio-erosive notch associated with the AD 365 uplift using DGPS. This is in good agreement with Pirazzoli et al. (1982), Kelletat (1991) and Mouslopoulou et al. (2015a) who report that the shoreline was uplifted by 7–8 m.

In antiquity, ancient Kalamyde was probably located right to the northeast of the modern town of Palaiochora (Pashley 1837; Branigan 1976; Gondicas 1988). The city probably served as the *epeinion* (= harbour site) of the ancient city of Kantanos (Pashley 1837) and flourished in the Doric and Roman periods, together with the neighbouring cities Syia (modern Sougia), Lissos, Poikilassos and Tarrha (modern Aghia Roumeli) (Perlman 2004b). Except from ceramic evidence, remains of a fort to defend Kantanos were found to the northeast of the Kalamyde site (Branigan 1976).

From a palaeogeographical point of view and considering the AD 365 coastal uplift of 7–8 m for this area, today's promontory at Palaiochora did not exist in antiquity. Before the AD 365 uplift event, the limestone plateau at today's southern end of the peninsula was a small island and the sea covered at least the shallow northern part of the promontory. During late medieval times, around AD 1280, the Venetians founded Castello Selino on the limestone plateau.

## 2.5 Material and methods

### 2.5.1 Field work

We carried out geophysical investigations using Electrical Resistivity Tomography (ERT) in order to examine the bedrock topography and stratigraphical structures in near-coast geological archives. We used a multi-electrode Syscal R1 switch 48 device (type Iris Instruments) with an electrode spacing of 1.5 m and a Wenner-Schlumberger electrode array. Measured data were inverted using the RES2DINV software (Geotomo Software). Stratigraphical data

were obtained by ten vibracores which were also used to calibrate ERT measurements. Vibracores were drilled with a Nordmeyer drill rig (type RS0/2.3) and a Cobra Pro handheld coring device (type Atlas Copco) using open steel augers with diameters of 80 and 60 mm as well as a closed auger system with plastic inliners, 50 mm in diameter.

The coordinates and absolute elevations of ERT electrodes and vibracoring sites were measured using a differential GPS (type Topcon HiPer Pro FC-250) reaching a horizontal and vertical precision of +/– 2 cm. Open vibracores were cleaned, photographically documented and analysed using sedimentological and geomorphological methods according to Ad hoc-AG Boden (2005) and Schrott (2015). Selected samples, representative for different stratigraphical units, were taken for sedimentological analyses under laboratory conditions.

### 2.5.2 Sedimentological and geochemical analyses

Grain size analyses were conducted using the sieve and pipette method after Köhn (Köhn 1929; DIN ISO 11277, 2002). Prior to wet-sieving and pipette analyses standard pre-treatment included dry-sieving in order to determine the amount of coarse particles with diameter > 2 mm followed by peptisation of the fraction < 2 mm in sodium pyrophosphate for 12 hours. We determined percentages of eight grain size classes (clay: < 2 µm, fine silt: 2–6.3 µm, medium silt: 6.3–20 µm, coarse silt: 20–63 µm, finest fine sand: 63–125 µm, fine sand: 125–200 µm, medium sand: 200–630 µm, coarse sand: 630–2000 µm). For each sample, we calculated (mean) relative frequency distribution curves as well as cumulative frequency curves based on a 99-step cosine interpolation function over the grain size classes.

Sediment colour was measured with a spectrophotometer (type Konica Minolta CM-600 d). Colour changes were visualised based on a* and b* values of the chromaticity diagram (CIELAB colour space) reflecting red and green (+a* and –a*) and yellow and blue (+b and –b) colours, respectively. Sediment colour can be used as additional tool to discriminate between sedimentary facies e.g., for differentiating between sediments accumulated under oxic or anoxic conditions or between sediments with different contents of organic material. Element composition and magnetic susceptibility of the sediment were analysed using a Niton XL3t 900 S GOLDD XRF analyser (calibration mode SOIL) and a Bartington MS2K surface sensor, respectively.

### 2.5.3 Microfaunal analyses

We conducted semi-quantitative analyses of the microfossil content of selected sediment samples in order to study faunal assemblages and to differentiate between autochthonous and allochthonous deposits. 15 ml of sediment were sieved in the fractions > 400 µm, 400–200 µm, 200–125 µm and < 125 µm, and analysed using a stereo microscope (type Nikon SMZ 745T). Z-series photos of foraminifera specimens were taken using a light-polarizing microscope (type Nikon Eclipse 50i POL with Digital Sight DS-FI2 digital camera). Foraminifera species were determined after Loeblich & Tappan (1988), Cimerman & Langer (1991), Murray (2006) and Rönnfeld (2008).

### 2.5.4 Geochronostratigraphy

Geochronostratigraphical information was obtained from 15 samples that underwent $^{14}C$ AMS radiocarbon analysis (Tab. 2.1). Conventional radiocarbon ages (Tab. 2.2) were calibrated with calibration software Calib Rev 7.01 and the Marine13 and IntCal13 datasets (Reimer et al. 2013). In addition, four sediment samples from the Palaiochora site (vibracore CHO 3A) were subject to OSL dating. The palaeodose was performed using the coarse-grained quartz (100–200 µm) fraction on an automated Risø-Reader TL/OSL DA 20 (Bøtter-Jensen et al. 2003) equipped with a 90Sr/90Y beta source for artificial irradiation and blue LEDs (470 nm) for optical simulation. The luminescence signal was detected through a Hoya U-340 filter (7.5 mm). Sample pre-treatment followed the procedure as described by Preusser et al. (2009).

**Tab. 2.1:** Radiocarbon dating results of samples from vibracores drilled at Sougia and Palaiochora.

| Sample | Lab. No. (CEZ) | Depth (m b.s) | Depth (m a.s.l) | Sample description | Unit | $\delta^{13}C$ (ppm) | 14C Age (BP) | 1 σ max; min (cal BC/AD) | 2 σ max; min (cal BC/AD) |
|---|---|---|---|---|---|---|---|---|---|
| SOU 5/5 HK2 | 21604 | 1.18 | 6.36 | charcoal | $IV_S$ | –22.3 | 1751±25 | 247;329 AD | 231;379 AD |
| SOU 5/5 HK3 | 21605 | 1.14 | 6.40 | charcoal | $IV_S$ | –27.3 | 1708±27 | 262;385 AD | 253;397 AD |
| SOU 6/10 HK | 21607 | 2.28 | 5.17 | charcoal | $II_S$ | –23.6 | 3843±32 | 2398;2208 BC | 2457;2204 BC |
| SOU 7/13 HK1 | 21608 | 1.17 | 6.20 | charcoal | $II_S$ | –25.1 | 3118±32 | 1430;1310 BC | 1450–1286 BC |
| SOU 7/13 HK2 | 21609 | 1.23 | 6.14 | charcoal | $II_S$ | –26.9 | 3111±31 | 1425;1308 BC | 1439–1286 BC |
| SOU 8/23 HK | 21612 | 6.50 | 0.25 | charcoal | $II_S$ | –20.0 | 6477±37 | 5482;5380 BC | 5509–5364 BC |
| SOU 8/30 PR | 21614 | 7.51 | –0.76 | pl.rem. | $II_S$ | –34.7 | 6412±42 | 5468;5359 BC | 5472–5322 BC |
| SOU 8/31 PR | 21615 | 7.64 | –0.89 | pl. rem. | $II_S$ | 35.9 | 6294±43 | 5312;5226 BC | 5371;5081 BC |
| CHO 1/16 M2 | 21616 | 1.69 | 0.32 | mollusc | $III_P$ | 4.7 | 1994±24 | 361–431 AD | 303–472 AD |
| CHO 1/16 M3 | 21617 | 1.69 | 0.32 | mollusc | $III_P$ | 0.6 | 2173±24 | 142–225 AD | 101–258 AD |
| CHO 1/25 M | 21618 | 2.73 | –0.69 | mollusc | $II_P$ | 4.6 | 1994±25 | 360–431 AD | 299–473 AD |
| CHO 1/26 M | 21619 | 2.85 | –0.81 | mollusc | $II_P$ | 5.4 | 2074±26 | 260–348 AD | 220–398 AD |
| CHO 2/12 M1 | 21620 | 2.43 | –0.58 | mollusc | $II_P$ | 4.8 | 3139±26 | 1009–915 BC | 1071–878 BC |
| CHO 2/13 M | 21621 | 2.66 | –0.81 | mollusc | $II_P$ | 5.6 | 3602±27 | 1592–1506 BC | 1630–1458 BC |
| CHO 4/8 HK | 21622 | 1.80 | 1.86 | charcoal | $II_P$ | –24.0 | 1770±29 | 233;328 AD | 139–344 AD |

Note: Lab. No. (CEZ) – laboratory number, Curt-Engelhorn-Zentrum für Archäometrie, Mannheim, Germany; b.s. – below ground surface; a.s.l. – above sea level; unit – stratigraphical unit; 1σ max; min (cal BC/AD) – calibrated ages, 1σ range; (; – several possible age intervals); 2σ max; min (cal BC/AD) – calibrated ages, 2σ range (; – several possible age intervals), pl. rem. – plant remains. Calibration based on Calib Rev 7.01 with IntCal 13 dataset (Reimer et al. 2013).

The equivalent dose ($D_e$) was determined by applying the single-aliquot regenerative-dose protocol (SAR, Murray & Wintle 2000, 2003). To select a suitable preheat temperature for the SAR protocol, a preheat-plateau test and a dose recovery test were applied for each sample (Wintle & Murray 2006). Mean $D_e$ was calculated with the common or central age model (CAM) after Galbraith et al. (1999), where all $D_e$ values that passed the SAR

acceptance criteria are included in the model. The acceptance criteria comprise the recycling ratio that is supposed to be between 0.9 and 1.1 to guarantee the reproducibility of measured equivalent dose $D_e$ (Preusser et al. 2008). Further, the mean recuperation is recommended not to be higher than 5% (Murray & Wintle 2000; Preusser et al. 2008) which was found valid for the samples from Palaiochora.

The dose rate was estimated from K, Th and U contents, which were determined by high-resolution gamma spectrometry and cosmic radiation. The cosmic dose rate was estimated by the geographical position (altitude, latitude), the sampling depth below surface and the density of overlying sediments (Aitken 1998). The dose rate was calculated using the ADELE software (version v.2015 0.21 beta), considering the water content that includes an error interval of ± 10 %. Both, radiocarbon analyses and OSL dating were carried out at the Curt-Engelhorn-Zentrum für Archäometrie (CEZA), Mannheim, Germany.

**Tab. 2.2.** Luminescence dating results of sediment samples from vibracore CHO 3A drilled on the Palaiochora promontory.

| Sample | Sampling depth (m a.s.l.) | Unit | W (%) | N | Grain size (µm) | Mean recycling ratio (%) | Mean recuperation (%) | $D_e$ (Gy) | U (ppm) | Th (ppm) | K (%) | D (Gy/ka) | Quarz OSL age (ka) |
|---|---|---|---|---|---|---|---|---|---|---|---|---|---|
| CHO 3A OSL 1 | 3.27–3.17 | $V_P$ | 17 | 7 | 100–200 | 1.06±0.15 | 2.83±1.25 | 3.02±0.27 | 3.28±0.12 | 7.34±0.26 | 1.87±0.07 | 2.65±0.06 | 1.14±0.11 |
| CHO 3A OSL 2 | 3.02–2.92 | $V_P$ | 15 | 15 | 100–200 | 1.05±0.12 | 2.92±0.83 | 3.60±0.22 | 3.01±0.13 | 7.35±0.31 | 1.58±0.06 | 2.54±0.05 | 1.42±0.09 |
| CHO 3A OSL 3 | 2.52–2.42 | $II_P$ | 1 | 19 | 100–200 | 0.98±0.11 | 4.22±1.06 | 2.10±0.11 | 1.48±0.07 | 4.17±0.18 | 0.42±0.02 | 1.22±0.03 | 1.72±0.10 |
| CHO 3A OSL 4 | 2.02 - 1.92 | $II_P$ | 1 | 16 | 100-200 | 1.02±0.09 | 2.80±0.75 | 2.00±0.11 | 1.34±0.07 | 3.48±0.17 | 0.49±0.02 | 1.19±0.03 | 1.68±0.10 |

Note: b.s. – below ground surface; a.s.l. – above sea level; unit – stratigraph-ical unit; W – water content; N – number of accepted aliquots ; OD – over dispersion (CHO 3A OSL 2 = 0.26; nil for the other samples); $D_e$ – equivalent dose; U – uranium; Th – thorium; K – potassium; D – dose rate; based on central age model (Galbraith et al. 1999).

## 2.6 Results

### 2.6.1 Sougia — stratigraphy and multi-proxy analyses

Five vibracores were drilled in the Sougia study area (SOU 4, SOU 5, SOU 6, SOU 7 and SOU 8; Fig. 2.2). Vibracore SOU 4 was drilled 160 m distant from the present coastline down to a depth of 10 m below surface (m b.s.). The overall stratigraphical record can be classified into four sedimentary units (Fig. 2.4).

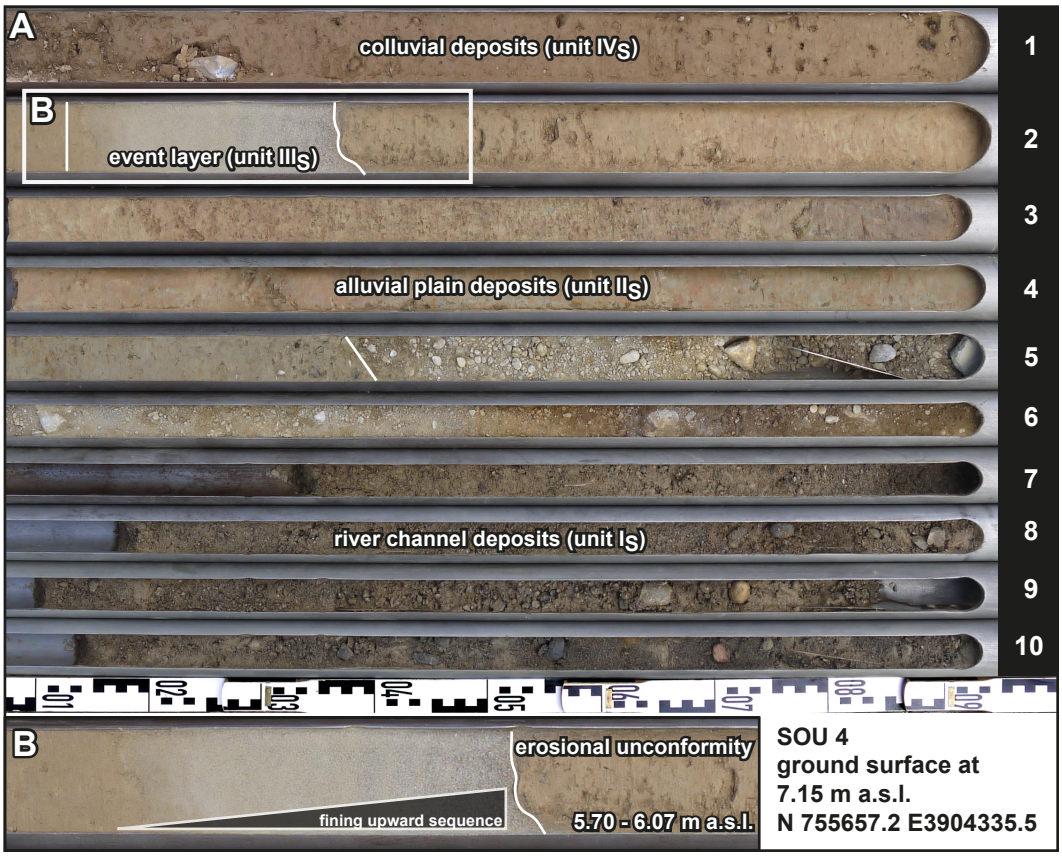


**Fig. 2.4:** (A) Sediment core SOU 4 drilled in the presumed area of the ancient harbour of Sougia with simplified stratigraphical information. For further information on sedimentary units see text. (B) Detailed view of the allochthonous high-energy sand layer found intersecting silty deposits in the upper part of the sediment core.

The lowermost unit $I_S$ reaches from 10 to 4.36 m b.s. (2.79 m a.s.l). Here, the sediment is dominated by dark brown to brown, partly unsorted, partly well-sorted sand including a high portion of gravel. Subsequent unit $II_S$ deposits first appear grey, then light brown in colour and predominantly consist of silt and clay. A distinct shift in depositional conditions at 1.37 m b.s. (5.70 m a.s.l.) marks the base of unit $III_S$. On top of a sharp erosional unconformity, formed within the silty and clayey sediments of unit $II_S$, a sand layer with fining upward of grain size and including marine shells was found. Unit $III_S$ sands reach up to 1.18 m b.s. (6.07

m a.s.l.). Unit $IV_S$ consists of light brown silt-dominated deposits covering unit $III_S$.

The stratigraphy of vibracore SOU 4 is reflected by selected sedimentological and geochemical parameters (Fig. 2.5). Grain size distribution data document the fourfold structure of the overall stratigraphy based on units $I_S$ to $IV_S$ and that changes from one unit to another are characterized by sharp breaks. The Ca/Fe ratio generally shows minor fluctuations but rapidly increases within unit $III_S$ while magnetic susceptibility shows slightly decreased values for this unit. Within the a*/b* ratio, the unit $III_S$ sand layer is neatly depicted by a maximum peak reflecting changing sediment colour. Findings of foraminifera species are strongly concentrated on the sand layer of unit $III_S$ (Fig. 2.6); foraminifera are completely absent in the lower units of the core.

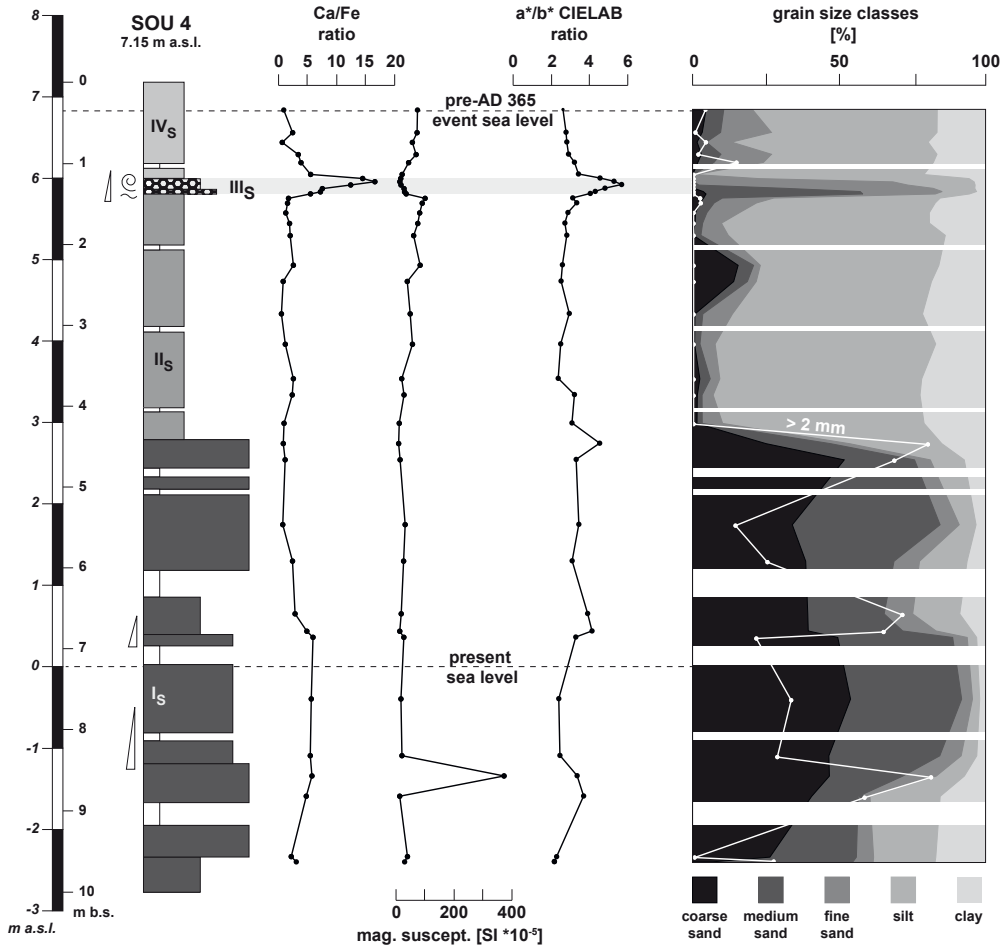


**Fig. 2.5:** Selected palaeoenvironmental proxies obtained for vibracore SOU 4. Ca/Fe ratio, magnetic susceptibility and a*/b* CIELAB ratio are compared to cumulative grain size distribution and stratigraphical units. Cumulative grain size data refer to fine sediment < 2 mm (shaded in grey, sum = 100%) and coarse sediment > 2 mm (white line; percentage referred to total mass of sample). The sheet of allochthonous sand at 5.70–6.07 m a.s.l. is depicted by a high Ca/Fe ratio, lower susceptibility values and a change in sediment colour accompanied by a distinctly increasing sand content. $I_S$–$IV_S$ indicate stratigraphical units, see text for explanations. For legend see Fig. 2.7.

Most foraminifera were encountered in the fine sand fraction (125–200 µm) and appear weathered and partly lithified due to uplift and subaerial weathering. Species typical of predominantly shallow marine conditions (e.g., *Cibicides* sp., *Bulimina* sp., *Rosalina* sp. and *Orbulina* sp.) are mixed with undetermined fragments of bryozoa and gastropods. The unit $II_S$ sample right below the unit $III_S$ sand layer includes a great many ostracods. Few reworked foraminifera from unit $III_S$ were found in the colluvial silts of the overlying unit $IV_S$.

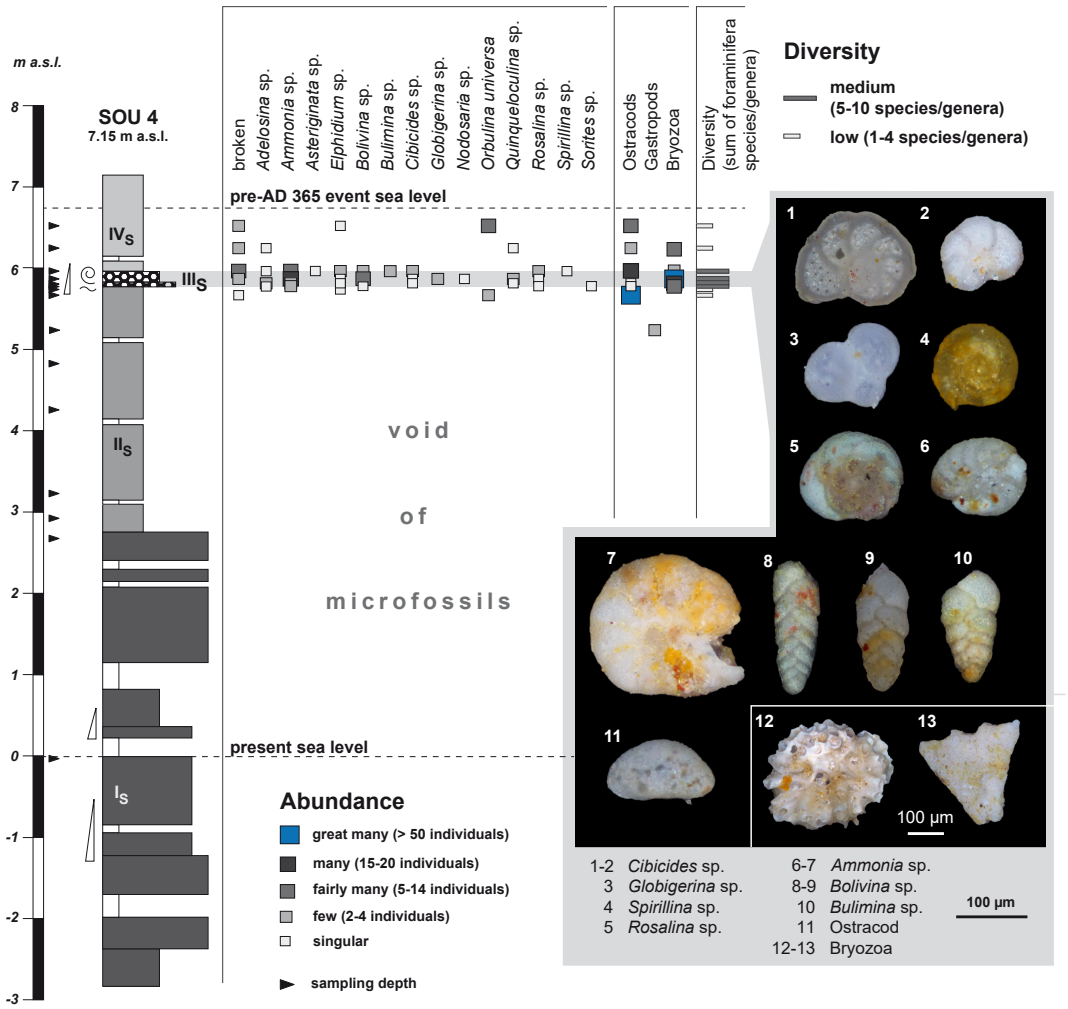


**Fig. 2.6:** Results of microfaunal analyses of selected sediment samples (triangles at vertical scale bar) from vibracore SOU 4. Foraminifera, indicating marine influence, are strongly concentrated on the intersecting layer of allochthonous high-energy sands in the upper part of the vibracore; a few reworked specimens were found in overlying colluvial units. Grey box to the right shows microscope photos of selected microfossil specimens. $I_S$–$IV_S$ indicate stratigraphical units, see text for explana-tions. For legend see Fig. 2.7.

A stratigraphical vibracore transect for the Sougia coastal plain is depicted in Fig. 2.7. The uplift of the study site during the AD 365 event, measured in the modern harbour at Sougia as the difference between the present sea level and the most elevated algal rim assigned to the pre-AD 365 event sea level (= 6.83 m a.s.l.), is marked as dashed line. The stratigraphi-

cal record of vibracores SOU 7 and SOU 6 is similar to the one described for vibracore SOU 4 also consisting of four sedimentary units. The base of the vibracores is characterised by coarse sand (unit $I_S$), partly mixed with gravel, followed by silt-dominated deposits (unit $II_S$). At 6.50 m a.s.l. (0.85 m b.s.) and at 7.20 m a.s.l. (0.41 m b.s.), a layer of medium and coarse sand and gravel (unit $III_S$) was found intersecting the silty unit at sites SOU 7 and SOU 6, respectively. At vibracoring site SOU 5, only 9 m away from site SOU 6, the coarse-grained unit $III_S$ layer lies almost 1.5 m deeper compared to sites SOU 6 and SOU 7.

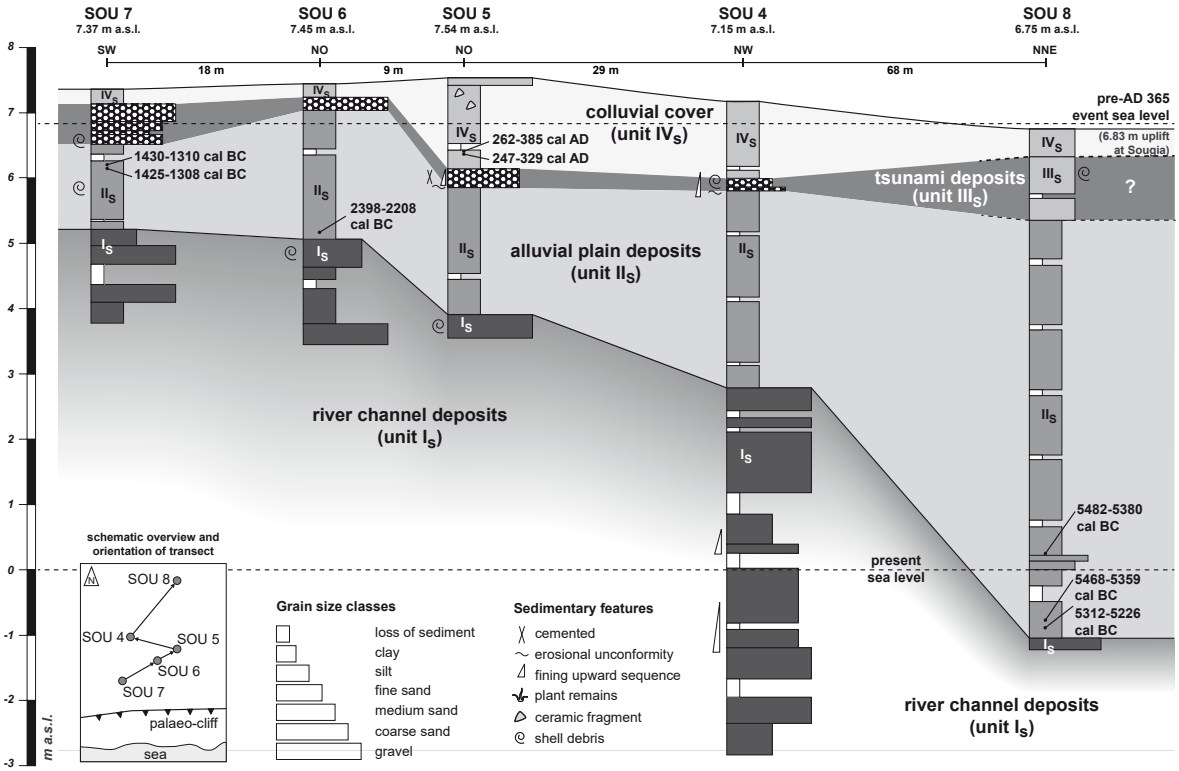


**Fig. 2.7:** Transect of vibracores drilled at the Sougia coastal plain. Tsunami sands intersecting alluvial silt deposits can be traced all along the transect. $I_S$–$IV_S$ indicate stratigraphical units, see text for explanations. For location of vibracoring sites see Fig. 2.2, for details on radiocarbon ages see Tab. 2.1.

At site SOU 5, the unit $III_S$ sand layer between 5.85 m and 6.14 m a.s.l. (1.69 to 1.40 m b.s.), appears well-sorted and partly cemented as beachrock-type calcarenite. Towards the top, silt-dominated colluvial deposits (unit $IV_S$) and a cover of gravel mixed with coarse sand and some ceramic fragments were documented. Vibracore SOU 8, drilled towards the northern part of the study site, is characterized by alternating coarse- and fine-grained deposits passing over into a thick homogenous fine-grained unit at 0.22 m a.s.l. (6.53 m b.s.). Grain size data show a remarkable increase of sand between 5.35 m to 6.29 m a.s.l. (1.40 to 0.46 m b.s.) which seems to be laterally equivalent to the sand-dominated unit $III_S$ encountered at coring sites further south. Also, numerous fragments of marine macrofauna were found restricted to this core section corroborating the marine fingerprint that was found typical of unit $III_S$ at the remaining Sougia vibracoring sites (Fig. 2.7).

### 2.6.2 Palaiochora — stratigraphy and multi-proxy analyses

In the Palaiochora study area, vibracoring sites CHO 1 and CHO 2 are situated at the present beach (Fig. 2.8). Vibracores CHO 3 and CHO 4 were drilled towards the northeast in the middle of the Palaiochora promontory. Here, pre-drilling stratigraphical information was obtained based on ERT transect CHO ERT 5 (Figs. 2.8 and 2.15).


**Fig. 2.8:** Overview of the Palaiochora coastal plain showing locations of vibracoring sites (CHO 1, CHO 2, CHO 3 and CHO 4) and ERT transect CHO ERT 5. Based on DGPS measurements, uplift during the AD 365 event was found to be ca. 7.75 m. The 8 m contour line together with the jagged palaeocliff line mark the pre-AD 365 event shoreline and the remaining Palaiochora Island that existed at that time. Map modified after Google Earth 2015 and IGME 2002.

Vibracore CHO 1 was drilled to a depth of 4 m b.s. where the Neogene bedrock was reached. Based on core log and grain size data, four sedimentary units can be differentiated (Figs. 2.9, 2.10 and 2.11). Basal unit $I_p$ consists of Neogene marl, bluish light grey (base) to light brown (top) in colour. Relative frequency distribution curves and the mean cumulative frequency curve show good sorting and a dominance of the silt fraction (Fig. 2.11a). The onset of unit $II_p$ (3.38–2.24 m b.s.; 1.38–0.24 m b.s.l.), brown to greyish brown in colour, is marked by an erosional contact on top of the Neogene marl. It is characterised by two distinct fining upward sequences both starting with dominating coarse and medium sands and ending up with silty fine sands.

Individual sediment samples from related subunits appear partly well sorted with a frequency maximum for fine or medium sand (Fig. 2.11 b). Also, the cumulated grain size data well reflect two impulses (Fig. 2.10). However, there are also samples with poor to moderate sorting covering several sand sub-fractions (Fig. 2.11 b). Specifically, the lowermost set of coarse-grained layers appear strongly unsorted showing highest amounts of gravel (Fig. 2.10). The mean relative frequency distribution curve and the mean cumulative frequency curve for unit $II_p$ samples indicate overall moderate to poor sorting. The latter forms a plateau between fine and coarse sand with a slight maximum in the medium sand fraction.

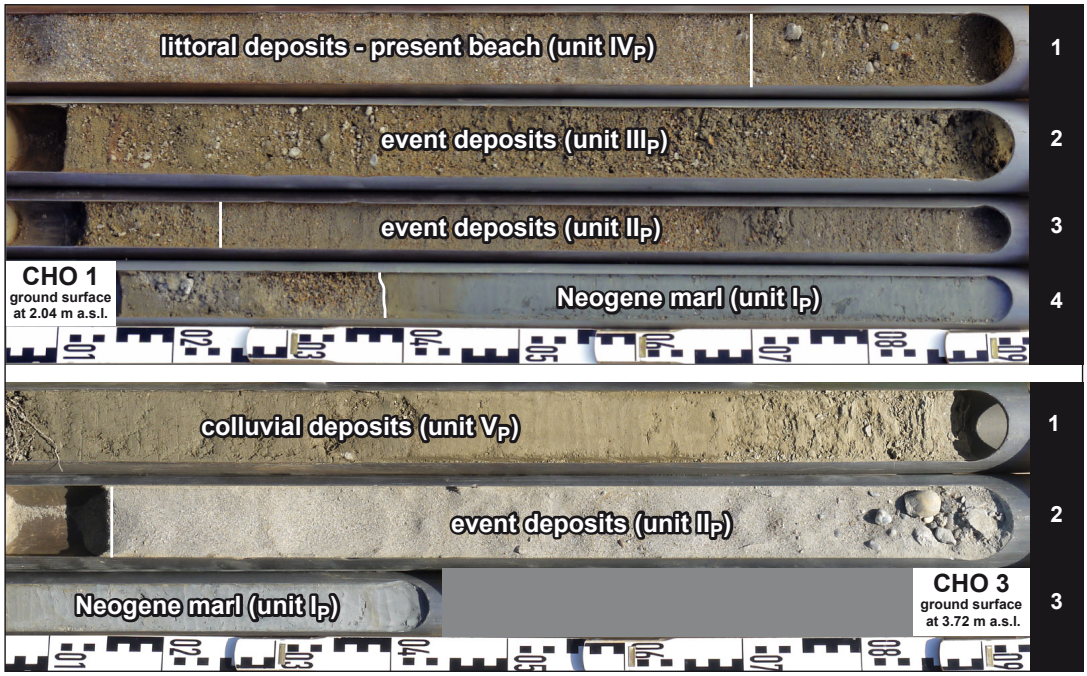


**Fig. 2.9:** Sediment cores CHO 1 and CHO 3 drilled at the present-day beach and in the middle of the Palaiochora promontory, respectively. For further information on sedimentary units see text.

Unit $III_p$ ranges from 2.24 to 0.70 m b.s. (0.20 m b.s.l. to 1.34 m a.s.l.). In contrast to unit $II_p$ it appears as thick layer of relatively unsorted coarse and medium sand with high amounts of gravel. A slight coarsening upward tendency can be observed, particularly for its upper part. Relative frequency distribution curves show a neat bimodal distribution; they underline

the dominance of coarse and medium sands, but also show a second maximum in the clay fraction. Both, the mean relative frequency distribution curve and the mean cumulative frequency curve, accentuate the poor sorting value (Fig. 2.11 c). Within both units ($II_P$ and $III_P$) numerous fragments of marine macrofossils, such as gastropods and molluscs indicate a marine character of the coarse-grained sand layers. Unit $III_P$ deposits are covered by the homogenous $IV_P$ sand layer, light beige in colour. Unit $IV_P$ sands, beginning at 0.7 m b.s. (1.34 m a.s.l.), appear very well sorted reflected by a distinct maximum in the medium sand fraction (Fig. 2.11 d). Unit $IV_P$ sands represent (sub-)recent beach deposits.

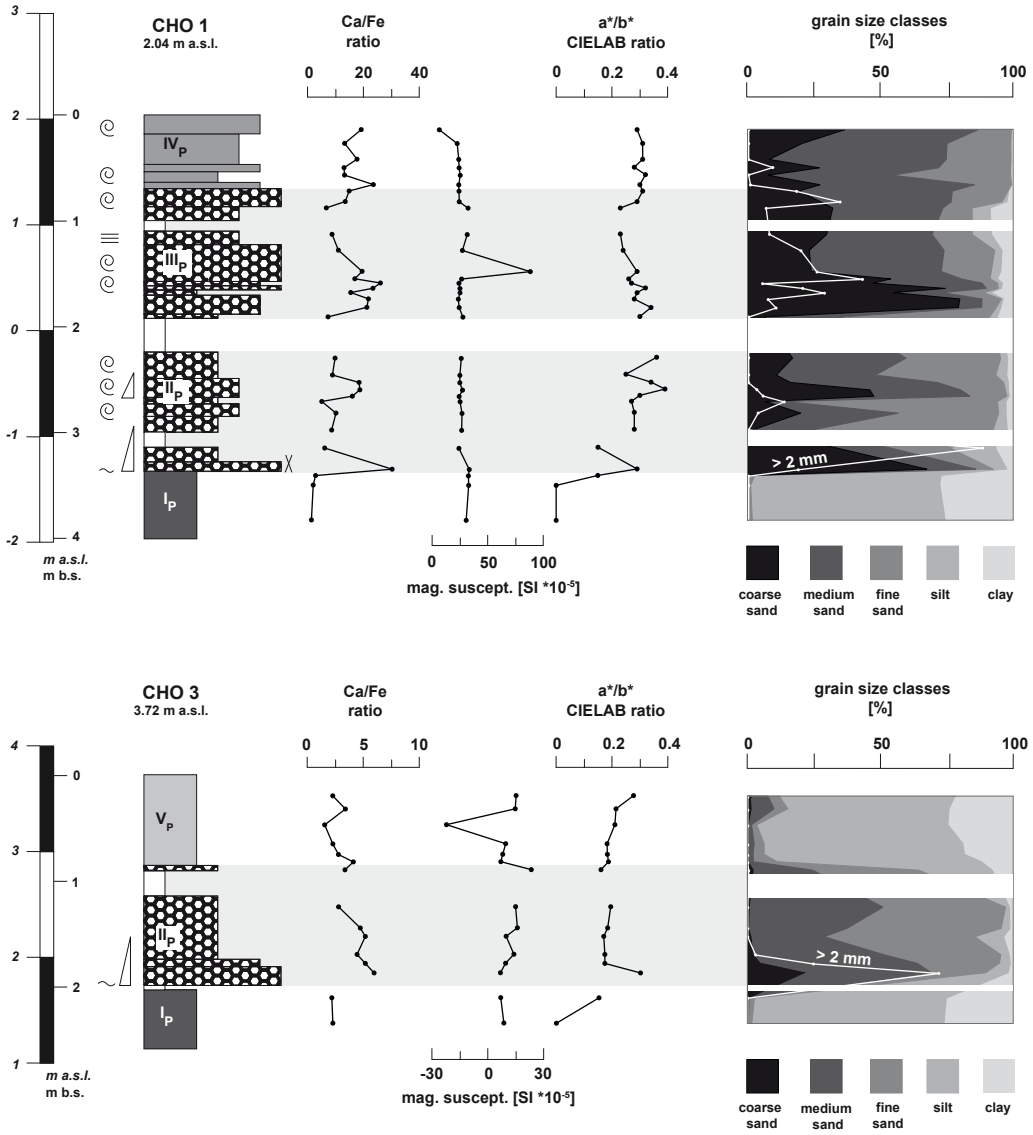


**Fig. 2.10:** Selected palaeoenvironmental proxies obtained for vibracores CHO 1 and CHO 3. Ca/Fe ratio, magnetic susceptibility and a*/b* CIELAB ratio are compared to cumulative grain size distribution and stratigraphical units. Grain size data refer to fine sediment < 2 mm (shaded in grey, sum = 100%) and coarse sediment > 2 mm (white line; percentage referred to total mass of sample). Note fining upward pulses depicted in the grain size data obtained for site CHO 1. $I_P$–$IV_P$ indicate stratigraphical units. See text for further explanations. For legend see Fig. 2.7.

Vibracore CHO 3 was drilled down to 2.5 m b.s. and shows three major sedimentary units (Figs. 2.9, 2.10, 2.12). Unit $I_P$ is characterized by Neogene marl, light grey in colour showing the same grain size characteristics (Fig. 2.12 a) as observed in core CHO 1 with maximum frequencies found for clay and silt fractions. At 2.04 m b.s. (1.68 m a.s.l.), the marl is covered by unit $II_P$, a thick sand layer. At its base, unit $II_P$ contains very high amounts of gravel, some gravel pieces showing features of coastal bioerosion bound to the littoral zone. Regarding the gravel and sand fractions, grain size data document a fining upward tendency for the lower part of unit $II_P$ (Fig. 2.10). Individual samples for material < 2 mm from the lower part show corresponding relative frequency distribution curves that cover the finest fine sand, fine and medium sand fractions thus indicating a low grade of sorting (Figs. 2.10 and 2.12).

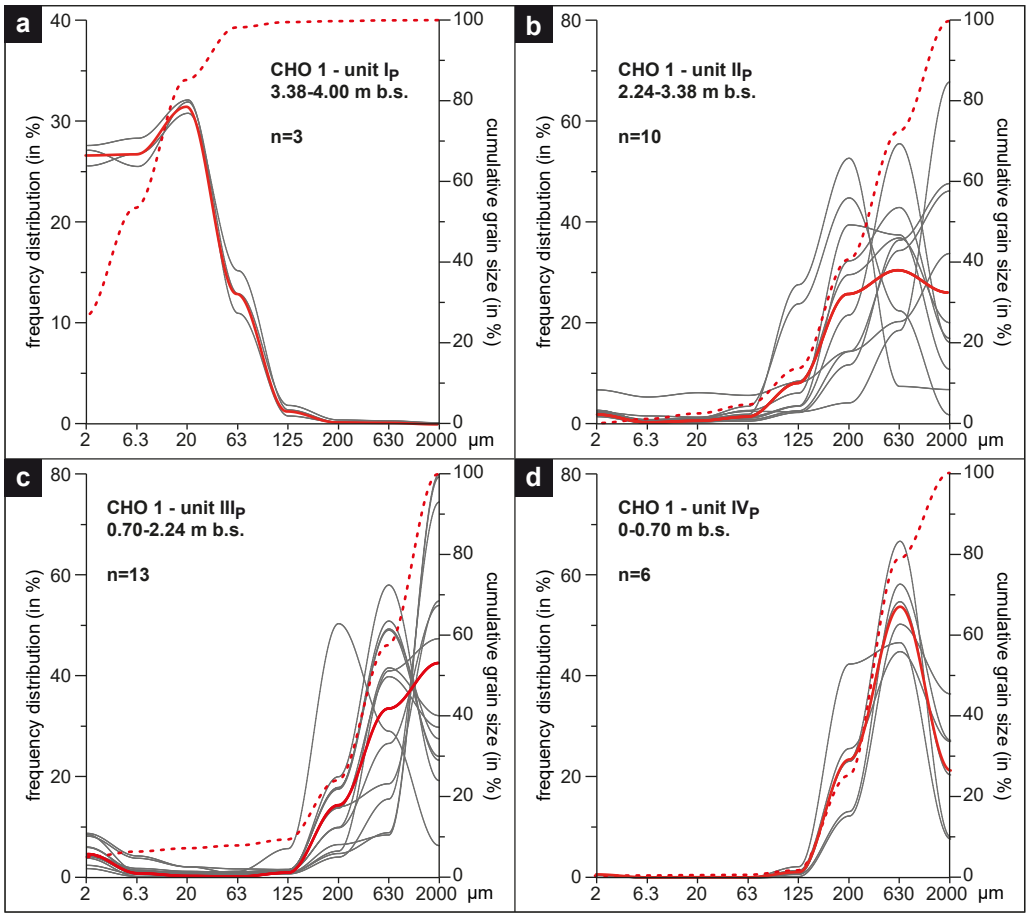


**Fig. 2.11:** Grain size data obtained for vibracore CHO 1 showing relative frequency distribution curves for each sample classified according to units $I_P$, $II_P$, $III_P$ and $IV_P$. Additionally, curves for the mean relative distribution frequency and the mean cumulative frequency are given for each sedimentary unit. For legend see Fig. 2.12.

In contrast, samples from the upper part of unit $II_P$ are slightly better sorted with maxima in the fine and medium sand fractions (Figs. 2.10 and 2.12). The medium cumulative frequency curve for unit $II_P$ (Fig. 2.12 b) shows a maximum in the medium sand fraction and a second, much lower maximum in the clay fraction documenting the overall unsorted character compared to recent beach deposits (Fig. 2.12 d). In contrast to core CHO 1, the upper

part of core CHO 3, starting at 0.86 m b.s. (2.86 m a.s.l.), consists of a layer dominated by clayey silt (Fig. 2.10). Grain size data for this unit $V_p$ show a multi-modal grain size distribution with a predominant maximum for the medium silt fraction, a second peak for the clay fraction and a third peak for the medium sand fraction (Fig. 2.12 c).

Unit $I_p$ of vibracores CHO 1 and CHO 3 shows a low Ca/Fe ratio and low magnetic susceptibility values (Fig. 2.10). At both coring sites, an abrupt change towards unit $II_p$ is represented by a strong increase of the Ca/Fe ratio and an obvious change of the a*/b* CIELAB ratio. Especially in core CHO 1, maximum peaks within the Ca/Fe ratio seem to be related with the input of coarse-grained material in both, unit $II_p$ and $III_p$, and might be associated with the concentration of shell debris. Magnetic susceptibility values do not allow for further differentiation of the sedimentary composition of core CHO 1. The maximum peak at 1.5 m b.s. may be caused by input of iron bearing or other heavy minerals. On the contrary, susceptibility values obtained for core CHO 3 show a slight increase on top of the Neogene marl within unit IIp and a decrease within unit $V_p$. The absolute minimum value is most probably bound to organic (diamagnetic) material measured within unit $V_p$.

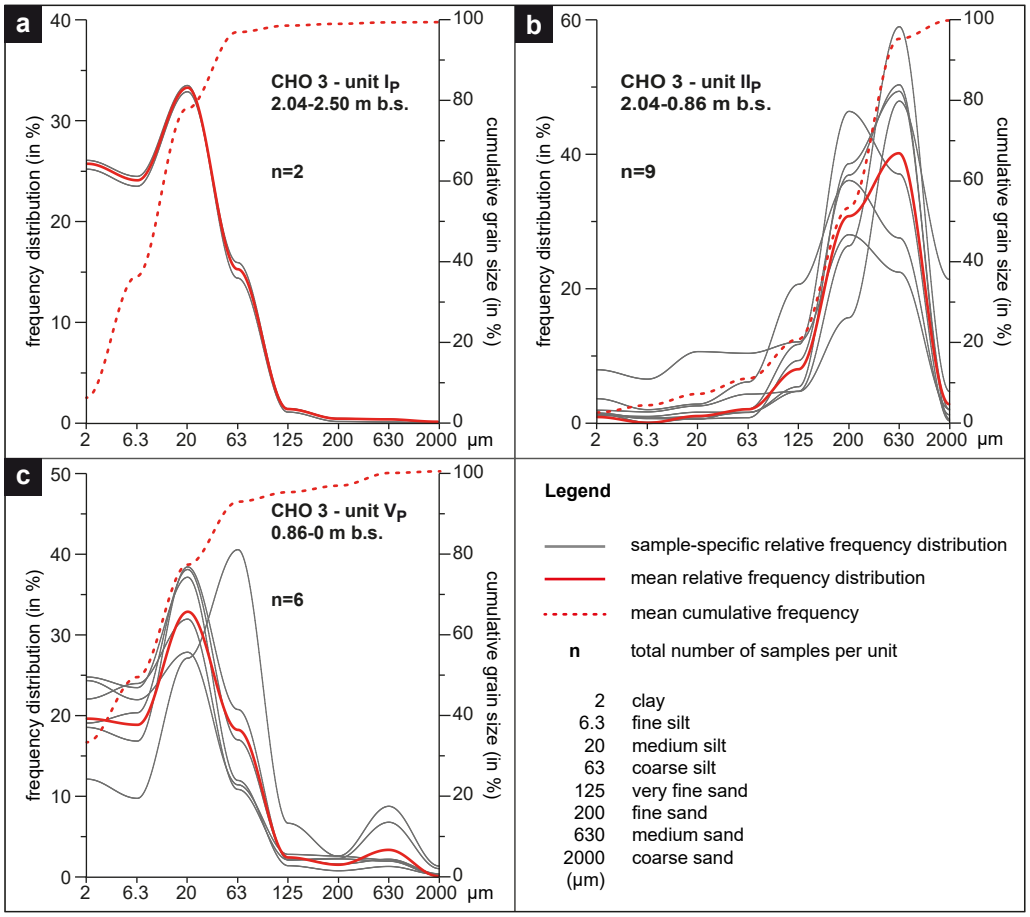


**Fig. 2.12:** Grain size data obtained for vibracore CHO 3 showing relative frequency distribution curves for each sample classified according to units $I_p$, $II_p$ and $V_p$. Additionally, curves for the mean relative distribution frequency and the mean cumulative frequency are given for each sedimentary unit.

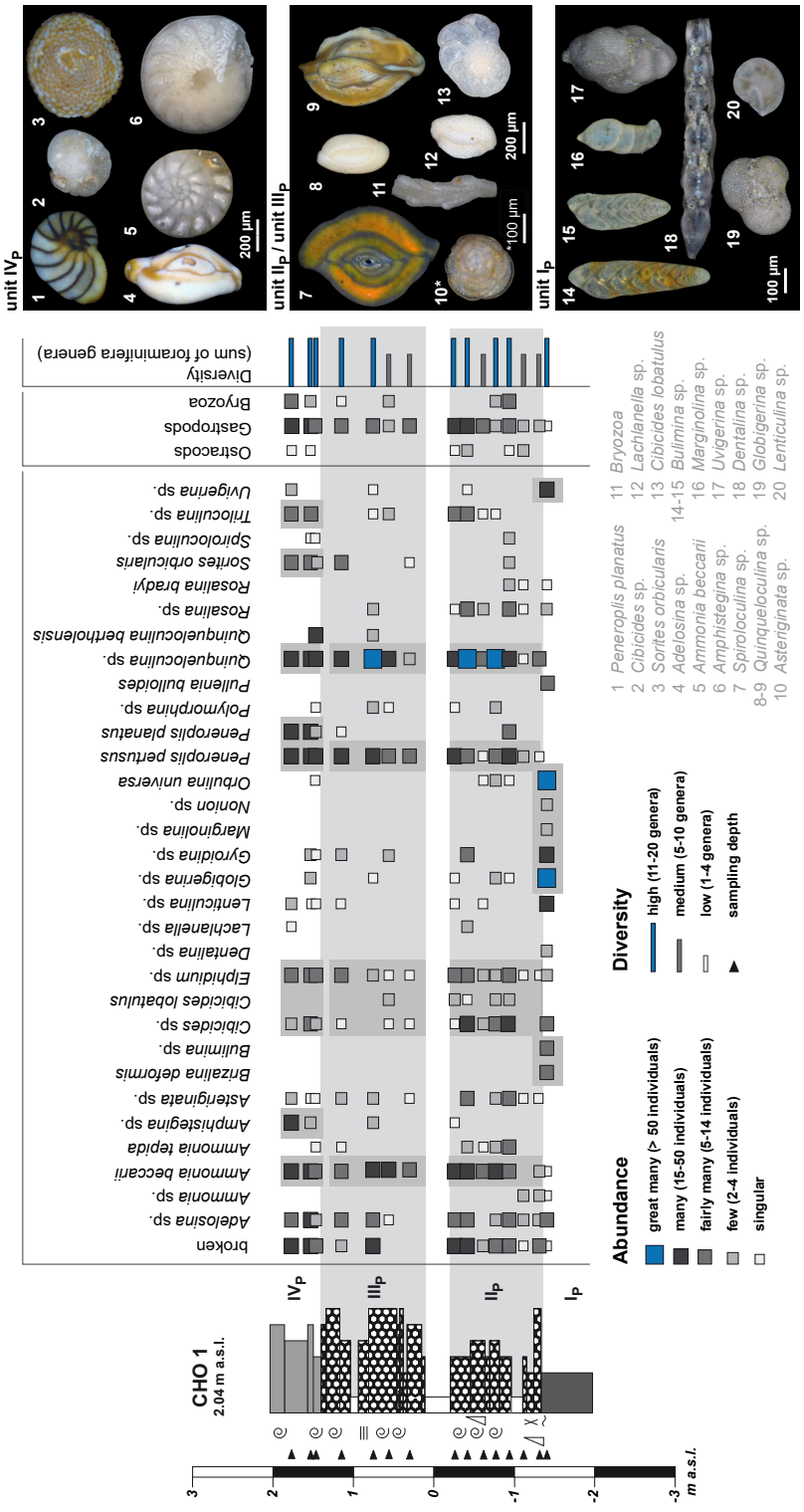


**Fig. 2.13:** Results of microfaunal analyses of selected sediment samples (triangles at vertical scale bar) from vibracore CHO 1. The foraminifera fingerprint of the local bedrock (unit $I_p$) is different from the signature of both high-energy event deposits (units $II_p$ and $III_p$, shaded in light grey) and beach sediments (unit $IV_p$). Differences in the distribution of foraminifera species/genera are highlighted by grey boxes. $I_p$–$IV_p$ indicate stratigraphical units. See text for further explanations. Boxes to the right show microscope photos of selected microfossil specimens.

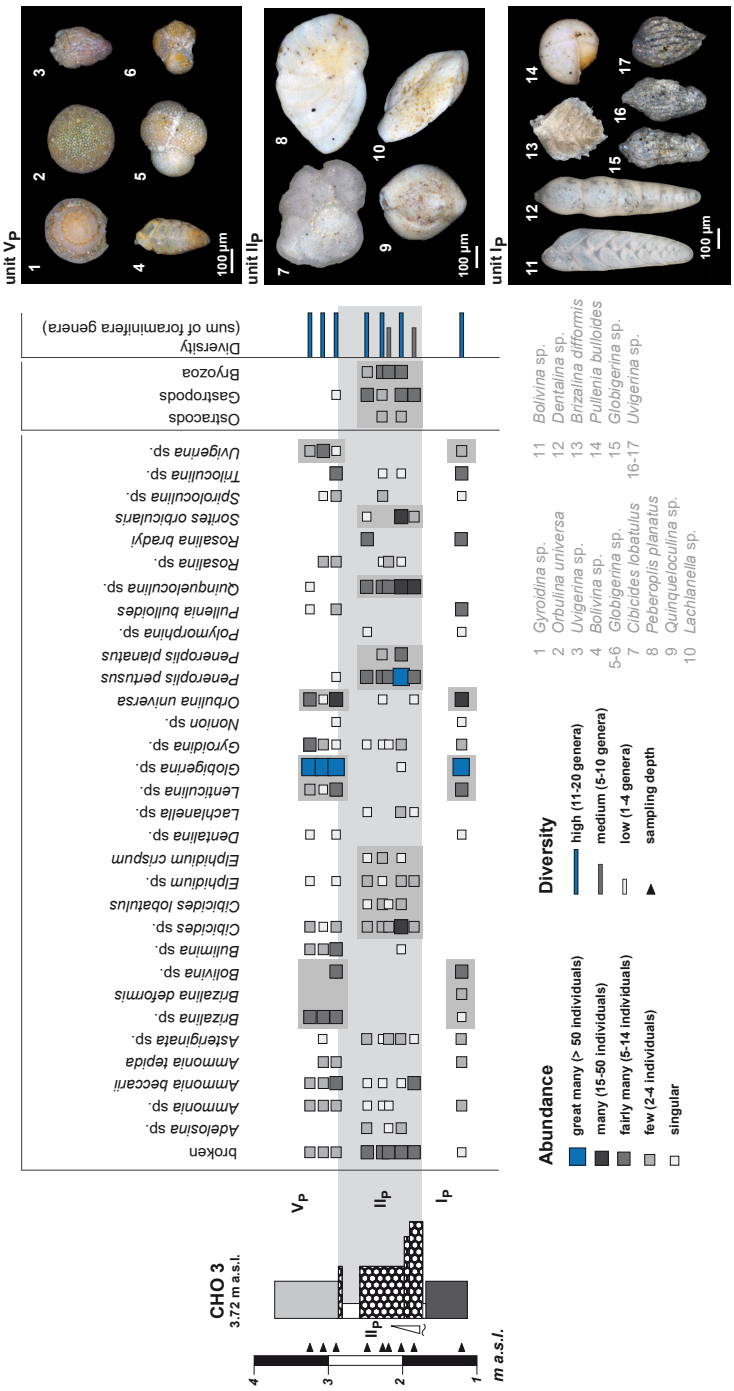


**Fig. 2.14:** Results of microfaunal analyses of selected sediment samples (triangles at vertical scale bar) from vibracore CHO 3. There are differences in the micro- and macrofossil signatures between local bedrock silts (unit $I_p$), high-energy event sands (unit $II_p$, shaded in light grey) and colluvial silts (unit $V_p$). Differences in the distribution of foraminifera species/genera are highlighted by grey boxes. $I_p$, $II_p$ and $V_p$ indicate stratigraphical units. See text for further explanations. Boxes to the right show microscope photos of selected microfossil specimens.

The sedimentary units encountered at site CHO 1 show differences in diversity and abundance of the microfaunal content (Fig. 2.13). Samples from the bedrock marl are dominated by highly abundant *Globigerina* sp., *Orbulina universa*, *Uvigerina* sp., *Gyroidinia* sp. and *Lenticulina* sp. mostly originating from open marine environments. Microfaunal signatures found in units $II_P$ and $III_P$ differ from the bedrock signatures. Within these units, we found *Quinqueloculina* sp., *Peneroplis pertusus*, *Cibicides* sp., *Cibicides lobatulus*, *Ammonia beccarii* and *Elphidium* sp. as dominating species (and genera). Additionally, numerous broken foraminifera tests were encountered in both units (Fig. 2.13). Sediment samples from the (sub-) recent beach (unit $IV_P$) showed highest abundance of *Peneroplis planatus*, *Sorites orbicularis* and *Amphistegina* sp. remains of which were underrepresented in units $II_P$ and $III_P$, and also revealed *Peneroplis pertusus*, *Elphidium* sp., *Triloculina* sp. and *Ammonia beccarii*. Specimens of *Rosalina* sp., *Rosalina bradyi* were almost completely restricted to units $I_P$ and $II_P$, i.e., almost absent in unit $III_P$ and not found at all in (sub-)recent beach deposits (unit $IV_P$). Maximum numbers of specimens of *Ammonia tepida*, *Gyroidina* sp. and *Polymorphina* sp. were also concentrated in units $II_P$ and $III_P$ compared to unit $IV_P$; these species appear underrepresented in unit $IV_P$ beach material. Overall, units $II_P$ and $III_P$ on the one hand and unit $IV_P$ on the other hand show differences in their microfossil signatures. Undetermined bryozoa, gastropod and ostracod specimens were found in all units overlying the bedrock.

Vibracore CHO 3 also revealed differences in the foraminiferal fingerprint of units $I_P$, $II_P$ and $V_P$ (Fig. 2.14). Unit $I_P$ bedrock samples are characterized by *Bolivina* sp., *Brizalina* sp., *Globigerina* sp., *Lenticulina* sp., *Orbulina universa*, *Pullenia bulloides* and *Uvigerina* sp. These species and genera also occur in medium to high numbers in the overlying silt-dominated cover sediments (unit $V_P$). In contrast, samples retrieved from unit $II_P$ show very high abundances of species and genera that were not at all encountered in units $I_P$ and $V_P$ or only found in very few numbers, namely of *Adelosina* sp., *Asteriginata* sp., *Cibicides lobatulus*, *Elphidium* sp., *Lachlanella* sp., *Peneroplis pertusus*, *Peneroplis planatus*, *Quinqueloculina* sp. and *Sorites* sp. Maximum abundances of *Cibicides* sp., *Quinqueloculina* sp., *Peneroplis pertusus*, broken foraminifera tests, gastropods and bryozoa are concentrated on unit $II_P$ sands; only few specimens were found in unit $V_P$ and almost none in unit $I_P$.

The ERT measurements were conducted prior to choosing vibracoring sites. ERT transect CHO ERT 5 runs in NNW-SSE direction in the northern part of the Palaiochora promontory and covers coring site CHO 3 (Figs. 2.8 and 2.15). The ERT depth section indicates a subdivision of the near-surface underground into two main units. The upper unit (from ca. 0 to 4 m a.s.l.) is characterised by comparatively high resistivity values ranging from approx. 24 Ωm to > 106 Ωm. The lower unit shows lower values between ~0.5 and 11.5 Ωm.

Stratigraphical information deduced from core CHO 3 was used for further interpretation of the depth section. Colluvial sediments of unit $V_P$ are associated with low resistivity values compared to underlying units $II_P$ and $I_P$ indicating a shallow depression. The vertical resolution of the ERT depth section is not high enough to allow an unambiguous differentiation between event deposits and underlying bedrock. However, it cannot be excluded so far that coarse-grained unit $II_P$ deposits encountered at site CHO 3A are, at least partly responsible for the ellipsoidal zone of maximum resistivity values depicted in Fig. 2.15. Resistivity values modelled for elevations below 0 m a.sl. are most likely bound to the groundwater influence.

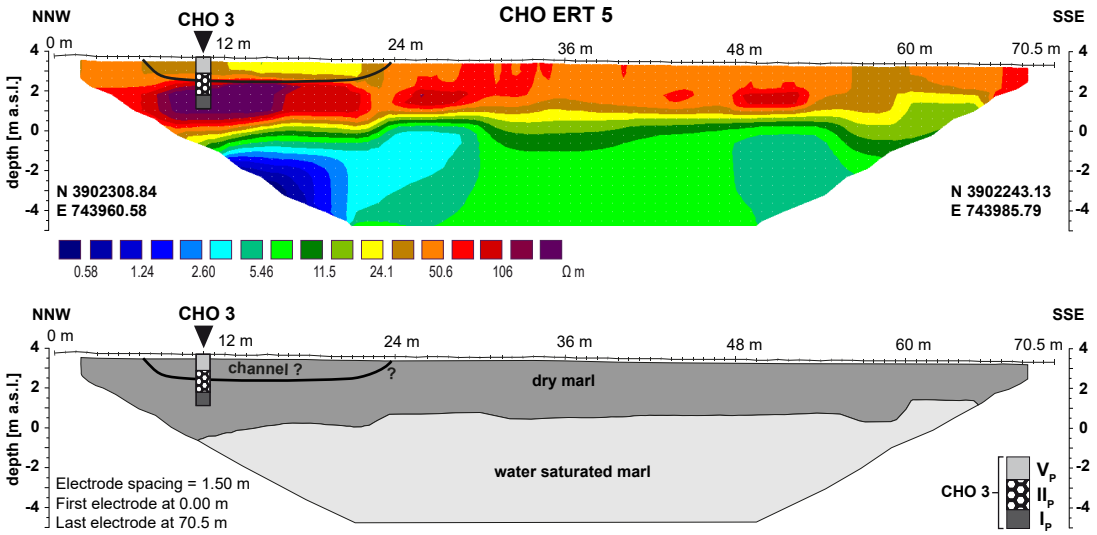


**Fig. 2.15:** Depth section of CHO ERT 5 based on ERT measurements (upper) and interpretation based on core log data from vibracore CHO 3 (lower). See text for explanation.

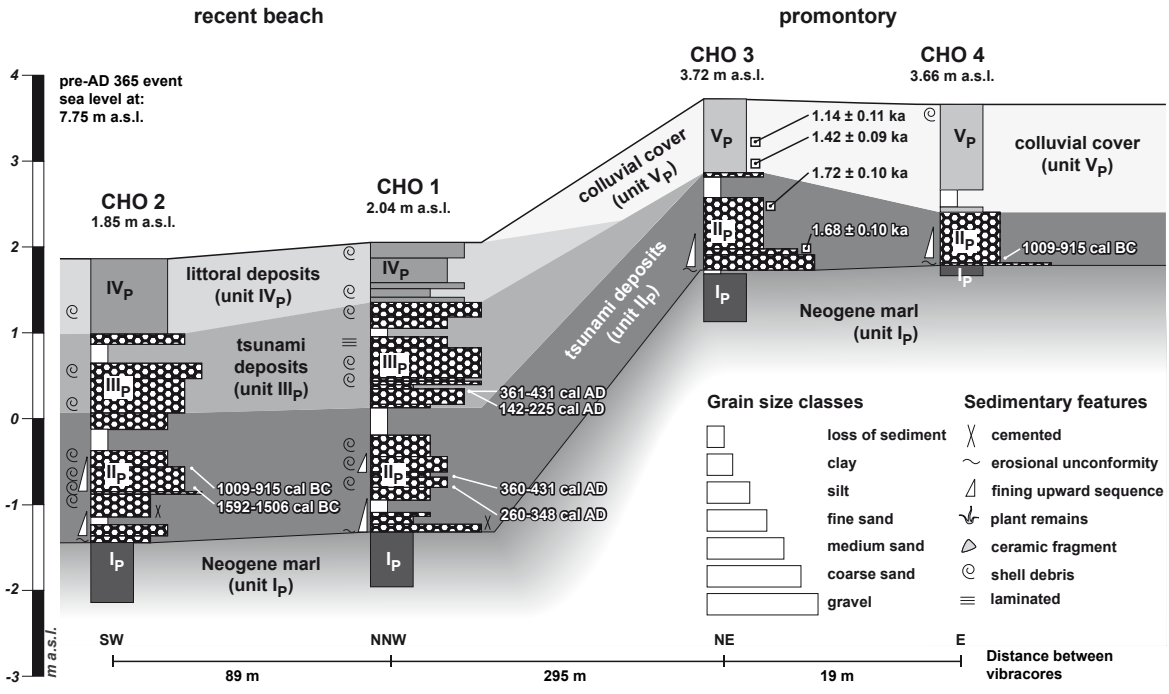


**Fig. 2.16:** Transect of vibracores drilled at the Palaiochora promontory. Event deposits found at sites CHO 1 and CHO 2 show two fining upward sequences representing the passage of two tsunami waves. Note thinning inland tendency of tsunami-related gravel and sand layer. $I_P$–$IV_P$ indicate stratigraphical units. See Figs. 2.10, 2.11 and 2.12 for grain size data and text for further explanations. For details on radiocarbon ages and OSL ages see Tab. 2.1 and Tab. 2.2.

The Fig. 2.16 summarizes stratigraphical information obtained along the vibracore transect across the Palaiochora peninsula. Unit $II_P$ sands are lying directly on top of the Neogene bedrock at sites CHO 3 and CHO 4, marked by an erosional unconformity. Unit $II_P$ sands were also found at sites CHO 1 and CHO 2 drilled in present beach position. In contrast, unit $III_P$ is restricted to sites CHO 1 and 2. Please note that coring site CHO 4 is located ca. 360 meters inland from the present-day shoreline. ERT measurements conducted along transects on the beach, not shown in this paper, and differences in the elevation of coring sites measured by DGPS document a step of approximately 2.5 m in bedrock topography between coring sites CHO 1 and 2 at the beach and sites CHO 3 and 4 in the midst of the Palaiochora plain (Figs. 2.8 and 2.16).

### 2.6.3 Geochronology

We present $^{14}C$ AMS radiocarbon ages of 15 samples retrieved from seven vibracores (Tab. 2.1). Where possible, we preferred non-marine plant material for dating in order to avoid uncertainties caused by the marine reservoir effect (MRE) that leads to considerable age deviations. However, especially in the Palaiochora site, plant material was rare. As a result, six out of 15 samples consist of articulated specimens of marine molluscs. We chose articulated specimens in order to guarantee that specimens were found in living position or were transported alive during sedimentation process. Results of radiocarbon analyses are summarized in Tab. 2.1.

For OSL dating, we used plastic inliner core CHO 3A drilled at site CHO 3. Two samples were taken directly from the unit $II_P$ sand layer and two samples were retrieved from the overlying silt-dominated unit $V_P$ deposits. Results of OSL dating and sample properties are summarized in Tab. 2.2. OSL dating results do not show any age inversions. OSL ages obtained for unit $II_P$ sands are considered identical within the range of error. The calculated $D_e$ values showed a normal distribution for each sample and low overdispersion and thus allowed for the application of the common or central age model (see Galbraith & Roberts 2012).

However, the number of aliquots for sample CHO 3A OSL 1 that passed the acceptance criteria is quite low (n = 7). The small number of aliquots may be explained by poor and incomplete bleaching during sediment deposition or by a weak signal due to the young age of the sediments. Thus, the OSL age retrieved from sample CHO 3A OSL 1 has to be considered with reservation.

The equivalent concentrations of the daughter nuclides of $^{238}U$ were measured in order to check for radioactive disequilibria within the measured samples. Doing so, we applied the method described by Rieser (1991) based on $^{214}Pb$ and $^{214}Bi$ (see also Lang 1996) and found only very small deviations from the equivalent uranium content for all samples. All samples are considered to be within the radioactive equilibrium besides sample CHO 3A OSL 4 with minor deviations. The latter, according to Olley et al. (1999), are considered to be of minor importance and only influence the error range of the determined OSL age.

## 2.7 Discussion

### 2.7.1 Establishing a facies model

Combining vibracore stratigraphies, multi-proxy datasets and spatial information obtained by geomorphological site prospection, we were able to differentiate between different facies types and to reconstruct the development of the Sougia and Palaiochora coastal zones.

**Sougia**. Unit $I_S$ deposits encountered along the Sougia vibracore transect (Fig. 2.7) are poorly sorted, consisting of medium to coarse sand with a high amount of gravel. Due to the poor sorting and the fact that no microfaunal evidence showing marine influence was found, we interpret unit $I_S$ as river channel facies deposited by the Kamarianos River. In its upper reaches, the river has incised a deep valley and steep gorge sections; with decreasing flow velocity, the eroded fluvial material was then accumulated in the bay of Sougia. The main channel of this lower course fluvial system seemed to have shifted over time towards the southwest where the corresponding facies was found in much higher stratigraphical positions (Fig. 2.7).

Compared to underlying unit $I_S$, unit $II_S$ shows a much lower depositional energy; the homogenous, greyish clayey silts do not include any microfaunal remains. We conclude that depositional energy strongly decreased from unit $I_S$ to unit $II_S$, maybe caused by tectonic factors, abrupt sea level changes or decrease of fluvial dynamics, or by a combination of these factors. Based on our geochronological data (Tab. 2.1), fine-grained material was subsequently accumulated in the Sougia plain over thousands of years documenting more or less stable tectonic conditions and low braiding dynamics of the main river channel. The occurrence of unit $III_S$ sands, however, marks a sudden interruption of these conditions reflecting abrupt, temporary and strong increase of flow velocity and energetic potential. Unit $III_S$ sands show an erosional contact at their base and can be traced over a distance of 120 m along the Sougia vibracore transect (SOU 7 to SOU 8).

The microfossil signature of unit $III_S$ sands at site SOU 4 documents a marine character and proves that the sand unit was laid down associated with a strong inundation event. It is considered a key indicator for high-energy wave impact from the seaside (see Mamo et al. 2009; Pilarczyk et al. 2014; Quintela et al. 2016). Sedimentological and geochemical properties underline the abrupt high-energy nature of this inundation. Unit $IV_S$ silts represent colluvial deposits, partly including ceramic fragments. This material originates from the surrounding hillslopes and covers the high-energy sand layer of unit $III_S$. **Palaiochora.**

For the Palaiochora study area, our results revealed the Neogene marl forming a shallow bedrock platform (unit $I_P$, Fig. 2.16). Marked by an erosional contact, bedrock silts are covered by unit $II_P$ sediments consisting of coarse and medium sands, partly mixed with gravel. Similar to our findings at Sougia, unit $II_P$ shows a marine character reflected by its allochthonous Holocene microfaunal fingerprint which can be neatly discerned from the geogenic background produced by reworked fossils out of the Neogene marl. Moreover, there are differences in the microfossil signature between unit $II_P$ and $III_P$ on the one hand and (sub-) recent beach sands of unit $IV_P$ on the other hand (section 2.6.2).

Sedimentary data document a three-pulsed inundation from the seaside associated with a high-energy event (Fig. 2.10) that obviously mixed allochthonous marine sediments with reworked local bedrock material (Figs. 2.11 and 2.12). The first two wave pulses (unit $II_P$) are characterised by fining upward sequences each indicating decreasing flow velocities with time and transition to laminar flow conditions (section 2.6.2). Overlying unit $III_P$ consists of poorly sorted deposits showing a bimodal grain size distribution (Fig. 2.11 c) typical of high-energy tsunami-type inundation (Scheffers & Kelletat 2004; Scheffers & Scheffers 2007). Thus, we hypothesize that unit $III_P$ rather reflects turbulent flow conditions in a later phase of the extreme wave event caused by local vortices, wave reflection and wave refraction dynamics.

At sites CHO 1 and CHO 2, unit $II_P$ and $III_P$ event deposits are covered by (sub-)recent beach deposits that are much better sorted (unit $IV_P$, Figs. 2.11c and 2.11d). Apart from obvious differences in the grain size distribution, beach deposits differ from underlying event units with regard to microfossil content, colour and Ca/Fe ratio (section 2.6.2).

Further inland, at sites CHO 3 and CHO 4, unit $II_P$ event deposits are subsequently covered by a silt-dominated colluvial facies showing typical multi-modal grain size distribution (unit $V_P$). At coring sites CHO 3 and CHO 4, only one wave pulse is recorded showing one singular fining upward sequence. Unit $II_P$ deposits at sites CHO 3 and CHO 4 differ from littoral deposits concerning grain size distribution and sorting (Figs. 2.11d and 2.12b). Analogous to coring sites CHO 1 and CHO 2, we interpret unit $II_P$ as high-energy overflow deposit showing decreasing flow velocity with time. We do not know why, on top of the Palaiochora plateau, only one wave pulse is recorded in the geological archive but hypothesize that parts of the high-energy sequence may have been eroded and/or reworked. To solve this question further investigation is necessary.

### 2.7.2 Detecting the ancient harbour of Sougia?

According to the Stadiasmus, a Roman guidebook for sailors including detailed information about Mediterranean harbours, the ancient city of Sougia (Syia) possessed a well-protected and spacious harbour. Extensive archaeological remains of ancient Sougia are located in the eastern part of the Sougia coastal plain, but no harbour infrastructures have yet been found (Pashley 1837; Markoulaki 1982; Andrianakis 1982; Sanders 1982; Christodoulakos & Markoulaki 2006). From the western part of the plain, Spratt (1865) described wall remains and supposed harbour installations still visible at the surface at his time. Thus, the western plain seemed a suitable candidate for the ancient harbour basin, potentially useful for the detection of tsunami deposits.

Unit $II_S$ found in vibracore SOU 4 resembles sediment fill of the uplifted ancient harbour at Phalasarna with regard to sediment texture, grain size distribution and sediment colour (section 2.7.1). Coseismic uplift reconstructed for the Sougia study site (6.83 m) is in the same range as the uplift known for Phalasarna (6.6 m). Both Pirazzoli et al. (1992) and Dominey-Howes et al. (1998) found continuous influence of saltwater to the Phalasarna harbour basin until the harbour was hit by the AD 66 tsunami as reflected by the foraminifera fingerprint of the corresponding deposits. At Sougia, however, we did not find any traces of foraminifera in the corresponding section of the sedimentary record, namely in unit $II_S$

deposits at site SOU 4 below the event layer, which would serve as reliable evidence of a former harbour. At site SOU 4, findings of foraminifera are strongly restricted to high-energy unit $III_S$ sands and underline their allochthonous nature. Even if one assumes that the ancient harbour of Sougia, due to its presumed proximity to the Kamarianos River, was strongly influenced by freshwater, a slight saltwater influence must be expected for a harbour used by sea ships. Based on these findings, there is no geoscientific evidence that the ancient harbour of Sougia was located in the western part of the Sougia coastal plain.

### 2.7.3 Tsunami nature of event deposits

High-energy sands encountered at the Sougia and Palaiochora sites show sedimentary, geochemical and microfaunal characteristics typical of abrupt and temporary high-energy inundation from the sea side. In Tab. 2.3, we summarized the most important criteria for extreme wave impact from the sea for each unit, amongst others basal erosional contacts, fining upward trends in grain size, impulse-controlled multiple layer sequences, peaks in the Ca/Fe ratio and evidence of allochthonous marine microfauna. Searching for the potential triggering mechanisms within the framework of (palaeo-) geographical conditions for SW Crete, we take both extreme storm surges and tsunamis into account.

The overall wind and wave climate of the Hellenic Seas is regarded as considerably mild, on a mean annual basis (Soukissian et al. 2008). However, during winter season, strong storms may occur with decreasing frequencies in W-E direction, namely from the Ionian to the Libyan Seas, associated with cyclones of the west wind zone and sometimes related to so-called medicanes (Cavicchia et al. 2014). Still, due to the prevailing westerly winds and the relatively long fetch, it is mainly the western coast of Crete facing highest open sea dynamics. Most intense wind and wave conditions appear in the straits between the islands of Kythira and Crete located to the west of the study site of this paper. Soukissian et al. (2008) found, on average for the entire Hellenic Seas, maximum wind speeds of over 8 m/s and mean significant wave heights over 1.7 m during winter months (see also Menendez et al. 2014).

During winter, the area around Palaiochora and Sougia experience maximum wind speeds and mean significant wave heights below these average values, namely reaching ≤ 6 m/s and ≤ 1.2 m, respectively (Soukissian et al. 2008: Figs. 2.6 and 2.8). These conditions are, for example, even slightly milder than those of the northern Ionian Sea where a weak to medium wind and wave climate with mean significant wave heights of 1.2–1.6 m and very low annual wave energy flux (Cavaleri et al. 1991; Karathanasi et al. 2015) exists. In the open Ionian Sea, the maximum observed storm wave height does not exceed 6–7 m (Scicchitano et al. 2007). Moreover, such extremely high waves are always strongly reduced in height by wave shoaling when propagating towards the coasts. It has to be pointed out that catalogues registering historical extreme storms do not exist for the Mediterranean. In contrast, there is manifold information on extreme tsunami inundation (Hadler et al. 2012).

**Tab. 2.3:** Compilation of sedimentary, geophysical, geochemical and microfaunal features encountered in vibracores from Sougia and Palaiochora documenting sediment deposition associated with a high-energy event.

| | | | Sedimentological and geochemical features | | | | | | Fossil signature | | |
|---|---|---|---|---|---|---|---|---|---|---|---|
| Vibracores | | Units | Basal erosional contact | Fining upward sequence | lamination trend, material well sorted | Bimodal grain size distribution | Partly cemented, beachrock-type | Max. Ca/Fe ratio | Allochthonous microfauna | Marine macrofauna | Shell debris |
| **Sougia** | SOU 4 | $III_S$ | + | + | + | – | – | + | + | + | + |
| | SOU 5 | $III_S$ | + | + | + | – | + | + | + | + | + |
| | SOU 6 | $III_S$ | – | – | – | – | – | + | + | + | + |
| | SOU 7 | $III_S$ | – | – | – | – | – | + | + | + | + |
| | SOU 8 | $III_S$ | – | – | – | – | – | – | no data | no data | no data |
| **Palaiochora** | CHO 1 | $III_P$ | – | – | – | – | – | – | + | + | + |
| | | $II_P$ | + | + | + | – | + | + | + | + | + |
| | CHO 2 | $III_P$ | – | – | – | + | – | – | no data | no data | no data |
| | | $II_P$ | + | + | + | – | + | + | no data | no data | no data |
| | CHO 3 | $II_P$ | + | + | + | + | – | + | + | + | + |
| | CHO 4 | $II_P$ | + | + | + | – | – | + | no data | no data | no data |

Note: + existing; - absent.

Sedimentary structures such as fining upward sequences, erosional unconformities, translocated microfauna and stratigraphical subunits with bimodal grain size distribution were documented as key identifying issues with regard to recent tsunami sediments (e.g., Bahlburg & Weiss 2007; Chagué-Goff et al. 2011; Goto et al. 2011) as well as associated with palaeotsunami deposits encountered along the coasts of the Aegean, Ionian and Adriatic Seas (e.g., De Martini et al. 2003; Scheffers & Kelletat 2004; Kortekaas et al. 2011; Mastronuzzi & Sansò 2012; Mathes-Schmidt et al. 2013; Koster et al. 2015; Vött et al. 2009a, 2011a, 2015; Willershäuser et al. 2015) and the Portuguese coast of the Algarve (e.g., Quintela et al. 2016). Grain size data obtained for core CHO 1 from Palaiochora revealed two identifiable fining upward sequences (unit $II_P$) that indicate two wave pulses. Additionally, covering unit $III_P$ represents another pulse characterised by predominantly turbulent flow conditions (section 2.6.2 and 2.7.1; Figs. 2.10, 2.11).

High-energy sands are different from (sub-)recent beach deposits with regard to both, grain size distribution and foraminifera spectrum (section 2.6.2). Input of coarse sand was observed, for example, by several tsunami waves associated with the Boxing Day Indian Ocean tsunami in 2004 in Thailand (Hori et al. 2007). Also, at the Sougia coastal plain, geochemical analyses of sediment samples from vibracore SOU 4 revealed a maximum Ca/Fe value for high-energy unit $III_S$ sands. In the context observed, this phenomenon is associated with the input of abundant marine biogenic carbonate, such as shell debris or microfaunal remains and represents a fingerprint which has been successfully applied in (palaeo-)tsunami studies (Vött et al. 2011a, 2014; Chagué-Goff et al. 2015; Judd et al. 2017).

Vibracores from the Palaiochora coastal plain show a complex layering within the defined high-energy event deposits. Fining upward sequences in unit $II_P$ document high-energy overflow with decreasing flow velocities for two wave pulses at sites CHO 1 and CHO 2, and one wave pulse at site CHO 3. In contrast, poorly sorted deposits with bimodal grain size distribution associated with unit $III_P$ at sites CHO 1 and CHO 2 are interpreted as the result of turbulent flow conditions and the influence of wave reflection and refraction and local vortices.

In the central Palaiochora plain, unit $II_P$ abruptly covers the underlying bedrock marl (unit $I_P$). High-energy deposits of unit $II_P$ can be traced over a distance of at least 360 meters across the Palaiochora promontory following a landward thinning trend (Fig. 2.16). The latter is considered typical of tsunami imprint in the eastern Mediterranean where extreme storms are absent (e.g., Gianfreda et al. 2001; Luque et al. 2002, Vött et al. 2011a). Vibracoring sites CHO 3 and CHO 4 are located towards inland, some 250–300 m distant from a distinct pre-AD 365 underwater reef formed in Neogene marls (Fig. 2.8, see also section 2.6.2) so that storm waves would have experienced strong deceleration and shoaling before arriving at these sites.

Based on geophysical measurements and vibracoring conducted on top of today's Palaiochora promontory, we cannot decide whether or not high-energy deposits encountered at sites CHO 3 and CHO 4 were accumulated in the form of a widespread sediment sheet or associated with shallow channels that may have been eroded into the relatively soft bedrock within the course of the inundation event. ERT data and vibracore stratigraphy are only partly consistent (section 2.6.2) what might be caused by methodological problems of ERT measurements such as the loss of sensitivity with depth (Fischer et al. 2016b) or a missing contrast between bedrock and overlying coarse-grained deposits. Erosion channels, incision features and scours were observed in conjunction with studies on the geomorphological effects of in- and outflowing tsunami water masses, for example by Matsumoto et al. (2010), Scheuer & Vortisch (2011), Richmond et al. (2012), Goto et al. (2014) and Koster & Reicherter (2014). With respect to Greece, the formation of erosional channels in pre-existing sedimentary units by palaeotsunami overflow dynamics are described by Vött et al. (2009b) for the Lake Voulkaria (northern Akarnania), by Koster et al. (2013) and Hadler et al. (2013) for the eastern Gulf of Corinth, and by Willershäuser et al. (2015) for the lowlands around Pyrgos at the shore of the Gulf of Kyparissia.

For the Palaiochora site, however, further studies are required to clarify if high-energy overflow actually eroded shallow channels in the bedrock marl. For example, ERT studies could be performed with a much higher resolution. Findings of allochthonous Holocene marine microfauna at coring site SOU 4 are strongly concentrated on high-energy sands (unit $III_S$); few specimens were also found in overlying colluvial deposits which is due to reworking effects (Fig. 2.6). For outer-Mediterranean areas, it was found that tsunami and storm deposits may be very similar in their appearance (e.g., Switzer & Jones 2008). As it should be expected for common winter storms in the Mediterranean, storms are high-frequency events so that geological archives affected by storm-prone inundation should comprise a long record of repeated input of more or less thin storm-generated sand layers (e.g., Maas & Macklin 2002).

However, the sedimentary record of core SOU 4 and of neighbouring vibracores show only one single high-energy signal related to marine inundation that is embedded within low-energy fine-grained deposits. Moreover, following the principle of uniformitarianism, it is assumed that the allochthonous SOU 4 sand layer was laid down by post-uplift depositional processes (see section 2.7.5) resulting in an approximate lateral transport distance of minimum 160 m with regard to the present coastline and overflowing a pre-AD 365 palaeo-cliff. These arguments are not in favour of a storm-related marine inundation but speak for a tsunami-related deposition of the allochthonous sand layer at Sougia.

Findings from Palaiochora allow discriminating between the foraminiferal signatures of the local Neogene marine marl, deposits related with high-energy inundation from the sea side and (sub-)recent littoral deposits (section 2.6.2). At site CHO 3, for example, species and genera found typical of bedrock units are not or only negligibly present in samples from high-energy sands of unit $II_P$ (Fig. 2.14), whereas these species play a major role in post-event colluvial deposits indicating strong erosion of neighbouring hill slopes. The marine imprint of the high-energy sand layer goes far beyond the microfossil signature of the local bedrock. At site CHO 1, the foraminifera fingerprint of the local bedrock is also different from the thick unit $II_P$ and $III_P$ high-energy deposits (Fig. 2.13); (sub-)recent littoral processes obviously caused reworking of event deposits as mirrored by similar microfaunal fingerprints of units $II_P$, $III_P$ and $IV_P$.

However, there are also species and genera typical of (sub-)littoral environments that were almost exclusively found in samples retrieved from littoral unit $IV_P$ sands, such as *Amphistegina* sp., *Peneroplis planatus* and *Quinqueloculina bertholensis* (Fig. 2.13; for details see section 2.6.2). In addition, grain size data obtained for site CHO 1 (Fig. 2.11) underline that there are differences between (sub-)recent beach deposits and event deposits. Beach deposits are well sorted, show a more homogenous grain size distribution (Fig. 2.11 d) predominantly out of medium sand, whereas event deposits appear partly layered (unit $II_P$) with fining upward sequences, and partly unsorted with a bimodal grain size distribution (unit $III_P$; see Fig. 2.11 b, c) and rich in broken mollusc fragments.

Considering sedimentary traces, microfaunal evidence and the overall geomorphological settings for the time right before the AD 365 event and for today, event layers found at Palaiochora and Sougia seem to be out of reach of storms. We argue that storms may not explain the singular event signals at Sougia and Palaiochora. Storms may also not explain the considerable reach of event deposits and the multi-pulse character reflected by event deposits at sites CHO 1 and CHO 2 at Palaiochora. Conclusively, we interpret distinct high-energy signatures encountered at both Sougia and Palaiochora as caused by tsunami impact.

### 2.7.4 Event geochronology for Sougia and Palaiochora

Radiocarbon and OSL ages obtained for samples from Sougia and Palaiochora were used to establish local event geochronologies and to assess palaeoenvironmental changes.

Massive input of coarse-grained fluvial sediments at Sougia, namely at site SOU 8 already ceased in the 6$^{th}$ mill. BC (Fig. 2.7, Tab. 2.1). At site SOU 6, considerable input of fluvial gravel took place until the 3$^{rd}$ mill. BC documenting a shift of the main river channel towards the southeast. Radiocarbon data do not give any information on the onset of alluvial silt accumulation at sites SOU 4 and SOU 5. Regarding grain size data, however, strongly increasing deposition of silt at site SOU 4 occurred at ca. 4.30 m below present surface (2.85 m b.s.l.).

Radiocarbon samples SOU 5/5 HK2 and SOU 5/5 HK 3 that were retrieved from right above the tsunami sand layer found on top of alluvial plain deposits yielded radiocarbon ages between 247–329 cal AD and 262–385 cal AD, respectively, almost identical within the ranges of error. These ages give minimum ages or termini ante quos for the tsunami event recorded in the consistent geological archives of SOU 5 and SOU 4. Samples SOU 7/13 HK 1 and SOU 7/13 HK 2 were retrieved from below the tsunami deposits at site SOU 7 and yielded radiocarbon ages of 1430–1310 cal BC and 1425–1308 cal BC, respectively. These ages represent termini post quos for the event. Considering potential tsunami-related erosion of basal layers known to be a feature typical of tsunami landfall, the termini ante quos have to be regarded as a more reliable age estimate lying closer to the actual event than the termini post quos. We conclude that the tsunami layer, identified in the archive of the Sougia coastal plain, is to be seen in direct relation with the earthquake and tsunami event that occurred on 21 July AD 365.

On the beach of Palaiochora, three out of four samples from site CHO 1 (CHO 1/16 M2, CHO 1/25 M and CHO 1/26 M) taken from the two-partite tsunami layer, yielded almost identical ages (361–431 cal AD, 360–431 cal AD and 260–348 cal AD, respectively). These three ages are considered more as termini ad quos than as termini post quos for the tsunami event because of their quasi-identical range. Another sample (CHO 1/16 M2) rendered a slightly older age, namely 142–225 cal AD (Tab. 2.1). We conclude that the event deposits found at site CHO 1 are best-fit candidates for being caused by the AD 365 earthquake and tsunami event. Samples CHO 2/13 M and CHO 2/12 M1, retrieved from the correlating stratigraphical layer in core CHO 2, yielded much older ages, namely 1592–1506 cal BC and 1009–915 cal BC, which we consider as being reworked by the tsunami event.

For the Palaiochora study site, we undertook a geochronological cross-check based on OSL age determination for four samples retrieved from core CHO 3A (Tab. 2.2). Samples CHO 3A OSL 4 and CHO 3A OSL 3 were taken directly from the tsunami sand layer (unit $II_p$) yielding depositional ages of 1.68 ± 0.1 ka and 1.72 ± 0.1 ka, respectively. Two OSL samples taken from the overlying colluvial unit (unit $V_p$), namely samples CHO 3A OSL 2 and CHO 3A OSL 1, yielded ages of 1.42 ± 0.01 ka and 1.14 ± 0.1 ka, respectively (Tab. 2.2). It can be concluded that, first, the two depositional ages obtained for the CHO 3A tsunamite are identical within the statistical error ranges, and, second, that they represent best-fit candidates for the AD 365 tsunami. Subsequent to the event, site CHO 3A was subject to strong colluviati-

on, which we explain by considerable input of material eroded from adjacent hillslopes and accumulated on top of the event deposits (Figs. 2.15 and 2.16).

From the uplifted harbour of Phalasarna on the west Cretan coast, Pirazzoli et al. (1992) and Dominey-Howes et al. (1998) identified a layer of coarse-grained deposits as tsunami layer and associated it with the AD 66 tsunami event (section 2.2). However, AD 365 tsunami candidate deposits were so far not identified at Phalasarna. Scheffers & Scheffers (2007) described, without age control, tsunami-related boulder-dislocation from Phalasarna and the Gramvousa Peninsula in northwestern Crete. For the southern coast of Crete, Boulton & Whitworth (2017) recently presented evidence for block and boulder accumulations which is associated with the AD 365 event by these authors. In this contribution, we present for the first time geoscientific evidence of a strong AD 365 tsunami imprint on fine-sedimentary archives along the coasts of Crete. Both, Sougia and the Palaiochora, were hit by the 21 July AD 365 tsunami.

### 2.7.5 Reconstructing tsunami landfall at Sougia and Palaiochora

Tsunami models for the AD 365 event considering the seismic potential of appropriate fault candidates offshore western Crete (e.g., Shaw et al. 2008; Flouri et al. 2013; Tiberti et al. 2014; Valle et al. 2014) show that the simulated waves reach the southwestern coast of Crete several minutes after the main shock. Pirazzoli et al. (1992) assumed that the ancient harbour of Phalasarna was already uplifted by 6.6 m before the first tsunami waves arrived. This post-uplift inundation scenario is also plausible with regard to the principles of uniformitarianism as sudden pre-tsunami coseismic uplift of several meters was, for example, reported from the great Sumatra-Andaman earthquake in 2004 (e.g., Meltzner et al. 2006; Subarya et al. 2006). Based on this 'first uplift then tsunami inundation' effect, we present tsunami landfall scenarios for the study sites at Sougia (A) and Palaiochora (B) (Fig. 2.17). n.

Right before the AD 365 earthquake took place, the Sougia coastal plain was characterized by an alluvial flood plain with the main river channel located in the eastern part of the plain approximately at its current position (Fig. 2.17, scenario A1). Also, a small cliff is assumed to have existed at the seaward front of the plain. At that time, local relative sea level was 6.83 m higher than today (section 2.4.1). During the AD 365 earthquake, the site was first coseismically uplifted resulting in a falling sea level. Then, maybe just a few minutes later, seismically triggered tsunami waves hit and inundated the Sougia area and led to the deposition of a tsunami sand sheet (scenario A2).

According to existing models (e.g., Shaw et al. 2008; Flouri et al. 2013) this inundation occurred from southerly or southwesterly directions. Subsequent to the uplift and tsunami landfall, colluvial sediments were eroded from the surrounding hill slopes and covered the AD 365 tsunami layer (scenario A3). Due to the coseismic uplift, the pre-AD 365 cliff got out of range of wave erosion, became inactive and is still visible today as a prominent feature of the Sougia coast.

The central Palaiochora coastal plain around coring sites CHO 3 and CHO 4 was situated around 4.25 m below the pre-AD 365 earthquake sea level, considering an approximate elevation of the Neogene marl platform of around 3.5 m a.s.l. and a coseismic uplift during

the AD 365 event of approximately 7.75 m (section 2.4.2). Only the southern part of the peninsula, where a medieval castle is situated, was lying above the sea level at that time fringed by a cliff (Fig. 2.17 B, scenario 1). Following our scenario, the central Palaiochora coastal plain was uplifted during the AD 365 earthquake from around 4.25 m below present sea level to around 3.5 m above present sea level by 7.75 m prior to tsunami inundation. Tsunami waves reaching Palaiochora heavily shoaled and overflowed at least the uplifted central part of the promontory.

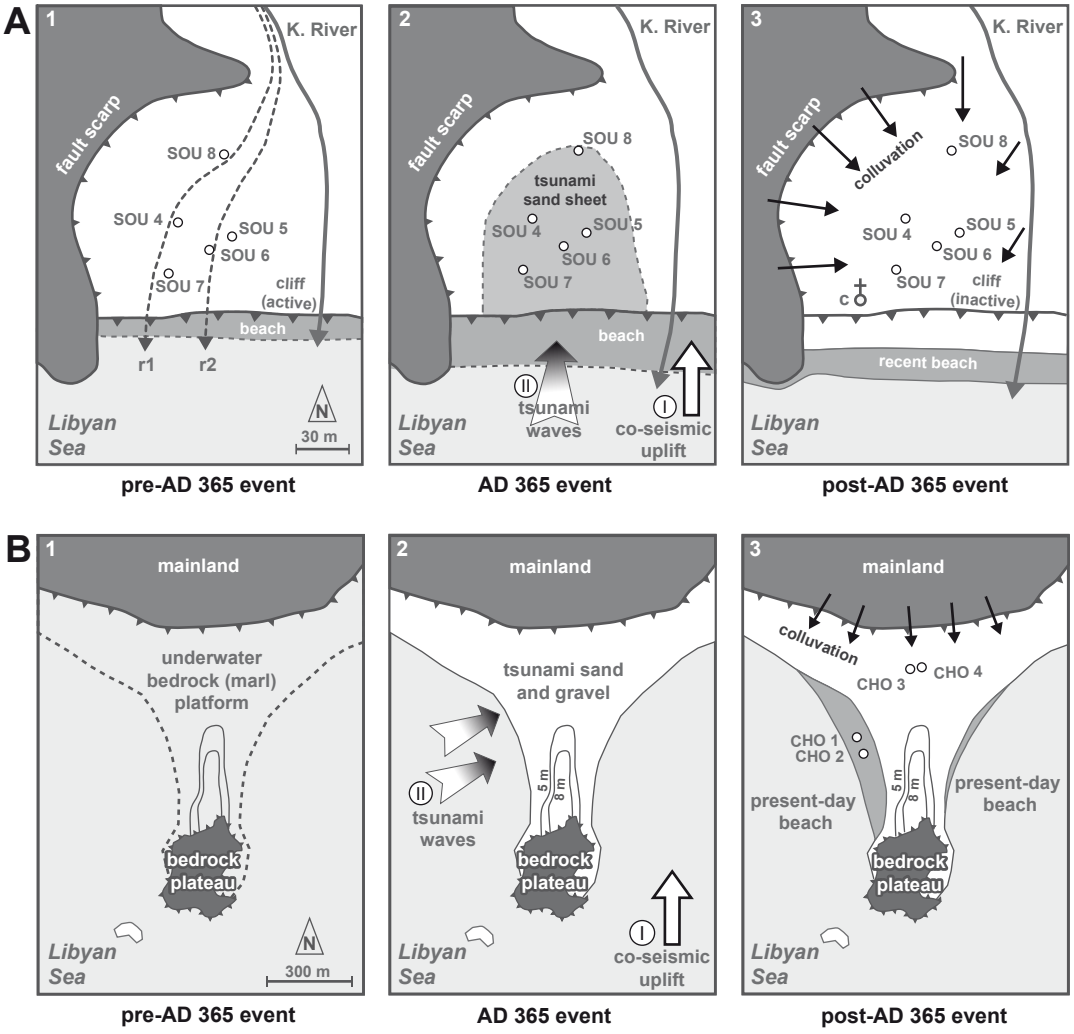


**Fig. 2.17:** Reconstruction of tsunami landfall scenarios for (A) the Sougia coastal plain (1–3; note: K. River – Kamarianos River; r1–2 – older river channel generations 1 and 2; c – chapel of Aghios Pande-leimon) and (B) the Palaiochora peninsula (1–3) associated with the AD 365 earthquake. See text for further explanation.

A minimum of two tsunami waves overflowed sites CHO 1 and CHO 2 at the present beach and most possibly also the Palaiochora peninsula. We argue that the sedimentary archives of the central promontory record only one overflow pulse because parts of the high-energy sequence may have been eroded and/or reworked. Further investigations are necessary

to solve this question. The fact that tsunami deposits at the beach of Palaiochora (units $II_P$ and $III_P$) are extremely thick is explained (i) by the N-S trending shallow promontory representing a major barrier to tsunami waters propagating from western directions, (ii) by the step-like increase in elevation of the Neogene platform from around 1.5 m b.s.l. to 1.5 m a.s.l. between the beach and the central promontory, respectively (see sections 2.6.2 and 2.7.3), which partly worked as barrier with regard to sediment transport and (iii) probably by the input of multiple tsunami waves.

Obviously, pre-uplift littoral deposits lying in front and on top of the promontory surface were swirled up and mixed with allochthonous tsunami sediments (section 2.6.2). Most likely, overflow of the promontory was so strong that entrained tsunami sediments were mainly deposited in the immediate front of the platform serving as obstacle, as encountered at sites CHO 1 and CHO 2, and as thinner unit of tsunami gravels and sands on top of the promontory, as encountered at sites CHO 3 and CHO 4. After the coseismic uplift and the subsequent tsunami passage, colluvial deposits from adjacent hill slopes were accumulated. As a result, the present-day beach along the Palaiochora coastal plain has developed out of AD 365 tsunami deposits reworking and sorting their uppermost parts in the present littoral zone (Fig. 2.11; section 2.6.2).

## 2.8 Conclusions

According to historical accounts and based on geotectonic studies, a tsunami associated with the 21 July AD 365 mega-earthquake hit the western and southwestern coasts of Crete. Detailed review of literature reveals that, so far, there is no geoscientific evidence of this AD 365 tsunami in the fine-sedimentary record of Crete. We investigated near-coast geological archives along the southwestern coast of Crete in search of the AD 365 tsunami fingerprint based on vibracores. Pre-coring prospection of the study area was accomplished by multi-electrode electrical resistivity tomography in order to obtain the thickest possible Holocene record of fine material. Associated with the mega-earthquake from 21 July AD 365, the western part of Crete experienced vertical crust uplift of up to 9 m which has, since then, led to strong erosion of fine material. Therefore, sedimentary records covering the Holocene are mostly destroyed. However, we were able to detect two appropriate geological archives, namely the coastal plain at Sougia and the Palaiochora promontory.

At Sougia, a sand sheet was found embedded into alluvial plain deposits, associated with basal unconformities and fining upward of grain size. The foraminifera fingerprint of this sand layer revealed a marine origin of the sediments. The underlying material was void of microfossils documenting the abrupt input of marine deposits. Radiocarbon data indicate that deposition of the allochthonous sands took place associated with the AD 365 tsunami impact. We present a post-uplift scenario for tsunami inundation reaching at least 160 m inland and overflowing today's palaeo-cliff. From a geoarchaeological point of view, the hypothesis that Sougia's ancient harbour existed in the western part of the plain was falsified due to the absence of corresponding microfauna.

At the Palaiochora promontory, tsunami deposits were detected both along the present beach underneath (sub-)recent littoral deposits, and up to 360 m inland from the present shore on top of today's central Palaiochora peninsula. High-energy deposits were found associated with basal erosional surfaces, multiple sequences of fining upward of grain size and specific patterns of grain size distribution and sorting (see section 2.6.2). Based on foraminiferal analyses, tsunami-related sands and gravels show a foraminifera signature different from both, the signature of the marine bedrock and the signature of littoral deposits documenting that the site was inundated from the seaside within the course of a high-energy event.

A thorough geochronological framework based on $^{14}C$ AMS and OSL ages documents that high-energy overflow was related to the AD 365 tsunami event. Prior to the AD 365 event, today's Palaiochora promontory was submerged under 4.25 m deep water and thus part of the (sub-)littoral zone. Our scenarios show that the platform was overflowed by tsunami waters after the coseismic vertical crust uplift by 7.75 m. Based on sedimentary findings, two wave pulses were identified for the area of the present beach, characterised by fining upward sequences each indicating laminar flow conditions and decreasing flow velocities. A third wave pulse is assumed to be associated with turbulent flow conditions leaving deposits with a bimodal grain size distribution. We interpret this as having taken place during a later phase of the extreme wave event related to wave reflection and refraction and local vortices. In contrast, the archives of the central promontory only show one wave pulse with a singular fining upward trend, most probably because parts of the high-energy sequence were eroded and/or reworked.

Further investigations are necessary to solve this question. Storms were discussed as potential causes for the allochthonous marine deposits encountered at Sougia and Palaiochora, but geoscientific, geographical and historical data are in favour of interpreting them as being related to the AD 365 tsunami event. This is the first study that presents reliable geoscientific traces of the AD 365 tsunami impact in fine-sedimentary coastal archives of western and southwestern Crete.

# 3 Mid-Holocene tectonic geomorphology of northern Crete deduced from a coastal sedimentary archive near Rethymnon and a Late Bronze Age Santorini tsunamite candidate

**Abstract**. The Late Bronze Age (LBA) tsunami and the AD 365 tsunami are supposed to have affected the northern coasts of Crete. However, near-coast sedimentary archives have been rarely investigated in this area, and sedimentary archives including palaeotsunami fingerprints are still unknown. The main objective of our research was to search for appropriate tsunami sediment traps in order to gain detailed insights into the Holocene palaeotsunami history of northern Crete. We found an excellent fine sediment archive near Pirgos, located to the west of Rethymnon. Based on a multi-electrode geoelectrical survey and an 11-m-deep sediment core, we analysed the event-geochronostratigraphical record by means of sedimentological, geochemical, geochronological, geomorphological, and microfossil investigations. The Pirgos record revealed a thick unit of homogeneous mud of a lagoonal environment starting ~ 6000 years ago. The lagoon was affected by five high-energy events, leaving layers of allochthonous sand. Microfossil analyses of these layers revealed a mixed foraminiferal assemblage including species from brackish habitats but also displaced and transported species from open marine and deep-water environments. Considering sedimentary characteristics, the local wave climate of the Cretan Sea, and the overall geomorphological setting, we interpret these layers as related to extreme wave events (EWE). Based on a local radiocarbon age-depth-model, we identified one EWE layer as a reliable candidate for the LBA Santorini tsunami. Another EWE layer is most probably associated with the AD 365 tsunami. This EWE ended abruptly the lagoonal conditions at Pirgos because of to the 1.64 m coseismic uplift at the site. The Pirgos lagoon existed between the first half of the 6$^{th}$ mill. BC and (at least) the end of the 2$^{nd}$ mill. BC We found that the area around Pirgos has continuously subsided over 3000 or so years, reflecting constant tectonogeomorphological conditions dominated by the nearby subduction zone between the Aegean and African plates.

This section is based on Werner et al. 2018b, published in Geomorphology 326, 167–198.

## 3.1 Introduction

The high tectonic potential of the Hellenic Subduction zone, reaching from the Ionian Islands to the west coast of Turkey, is known to have generated several major thrust earthquakes in historical and prehistorical times. For example, the AD 365 M ~ 8.3 earthquake that coseismically uplifted the western part of Crete up to 9 m and also triggered a catastrophic tsunami that affected the Mediterranean world (e.g., Thommeret et al. 1981; Kelletat 1991; Guidoboni et al. 1994; Pirazzoli et al. 1996; Stiros 2001; Shaw et al. 2008; Papadopoulos

et al. 2014; Werner et al. 2018a). Since this event, the entire southwestern coast of Crete has experienced strong erosion. Near-coast sedimentary archives covering major parts of the Holocene are thus rare, less investigated, or do not contain relevant information on the tectonogeomorphological evolution of western Crete before AD 365.

In search of appropriate geoarchives that include signals of the palaeotsunami history of Crete, we focused on the northwestern part of Crete. Here, the seismotectonic uplift by the AD 365 event reached only 1–2 m (Kelletat 1991), suggesting less intense post-erosional processes and the presence of thick near-coast pre- AD 365 Holocene sedimentary sequences. This is confirmed by the fact that Bottema & Sarpaki (2003) retrieved the longest continuous vegetation record for Crete from near Lake Kournas.

Crete is exposed to the Hellenic subduction zone to the south and west of the island and to the Aegean volcanic arc to the north of the island. The volcanic arc includes five still active volcanic centres. One of the largest volcanic eruptions during Holocene was the eruption of the Santorini (Thera) volcano during the Late Bronze Age (LBA). The LBA Santorini eruption, dated by AMS-radiocarbon dating to 1621–1605 cal BC (Friedrich & Heinemeier 2009; Friedrich 2013) is associated with a supraregional tsunami that affected the eastern Mediterranean (Hammer et al. 1987; Druitt & Francaviglia 1992; McCoy & Heiken 2000). LBA Santorini tsunamites have already been detected at several sites along the coasts of the Aegean Sea and the eastern Mediterranean. At Santorini itself, McCoy & Heiken (2000) found evidence for tsunamigenically reworked volcanic tephra near Pori.

Near Didim and Fethye (SW Turkey), Minoura et al. (2000) identified LBA Santorini tephra deposited on top of a marine sand layer. In four sediment cores drilled offshore ancient Caesarea (Israel), Goodman-Tchernov et al. (2009) found several tsunami layers, the lowermost dating to the LBA Santorini eruption.

On northwestern Crete, Minoura et al. (2000) found a unit of pumice deposited on a floor of a Late Minoan workshop near Gouves, which was overlaid by a thin marine sand layer. At the east coast of Crete, Bruins et al. (2008) found a chaotic geoarchaeological tsunamite situated at a promontory near Palaikastro that showed typical tsunami signatures, e.g., erosional contact, volcanic Santorini ash intraclasts, and marine macro- and microfauna. Inferred from radiocarbon dating and stratigraphical background, Bruins et al. (2008) related the tsunamite to the LBA Santorini eruption.

Therefore, near-coast sedimentary archives along the northwestern coasts of Crete are supposed to contain signals of palaeotsunami impact, specifically signals of the LBA Santorini tsunami. Numeric simulations of tsunami wave propagation triggered by the LBA Santorini eruption (e.g., by Minoura et al. 2000; Pareschi et al. 2006; Bruins et al. 2008; Novikova et al. 2011; Sakellariou et al. 2012; Periañez & Abril 2014) support this assumption.

The main objectives of this study, focusing on the northwestern coasts of Crete, were:

- to search for appropriate near-coast fine sediment geological archives with sufficient accommodation space for the past 6000 or so years,
- to investigate the palaeogeographical and palaeoenvironmental evolution since

the mid-Holocene using stratigraphical, geochronological, and palaeoenvironmental multi-proxy data,

- to reconstruct the tectonogeomorphological development of the study area against the background of the seismotectonically induced uplift of ca. 1–2 m associated with the AD 365 event, and
- to search for the LBA Santorini tsunami impact on the study site and reconstruct the palaeotsunami history of the area.

## 3.2 Natural setting and state of the art of research on LBA Santorini tsunami impact

### 3.2.1 Geotectonic background

Crete is exposed to the Hellenic Trench (Fig. 3.1) – the tectonic key element of the eastern Mediterranean region, where the African Plate is being subducted with 35–40 mm/yr (McClusky et al. 2000; Reilinger et al. 2006; Hollenstein et al. 2008) beneath the overriding Aegean microplate. To the immediate south of Crete, three marine trenches more than 3000 m deep mark this plate boundary. In front of the subduction zone, the Mediterranean Ridge, a compressive accretionary prism, has been developed (McKenzie 1972; Le Pichon & Angelier 1979; Doutsos & Kokkalas 2001).

Within the last 13 million years, subduction and associated coseismic processes caused a cumulative uplift of Crete in several different phases of approximately 2–3 km (McKenzie 1978; Meulenkamp et al. 1994; Jolivet et al. 1996). Recent studies by Tiberti et al. (2014) for western Crete showed that this net uplift results from a sequence of periods dominated by either uplift or subsidence. Crustal extension started during Miocene and lead to a fragmentation of Crete into fault-bounded blocks creating a prominent horst-graben structure (Peterek & Schwarze 2004; Seidel et al. 2007; Caputo et al. 2010; Mason et al. 2016).

Induced by the rollback effect of the subducting plate and the movement of the trench towards the south the Cretan Sea, a broad back-arc basin with an average water depth of 1000 m has formed to the north of Crete (McKenzie 1972; Angelier et al. 1982; Doutsos & Kokkalas 2001; Reilinger et al. 2006; Seidel et al. 2007; Royden & Papanikolaou 2011). The Hellenic subduction interface dips northward at 10° to 15°, whereas the subducted slab reaches depths of 35 to 45 km beneath Crete and several hundreds of kilometres beneath the central Aegean (e.g., Bohnhoff et al. 2001; van Hinsbergen et al. 2005; Hollenstein et al. 2008). A well-defined Benioff seismic zone reaches a maximum depth of 200 km and ends beneath the volcanic back-arc of the Cyclades, including the still active Colombo-complex near Santorini and Milos (Le Pichon & Angelier 1979; Hollenstein et al. 2008).

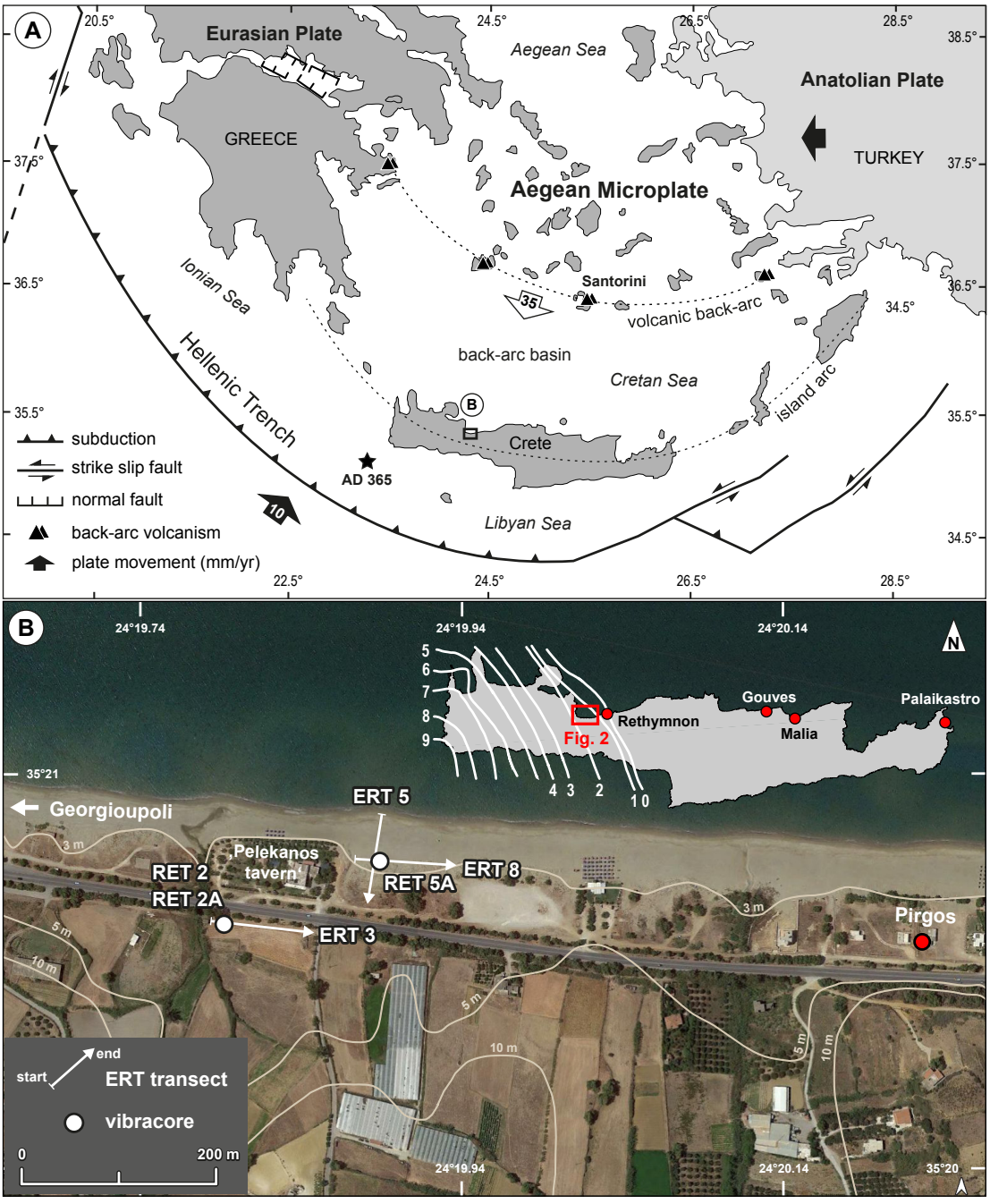


**Fig. 3.1:** Overview of the study area near Pirgos, Crete. (A) Tectonic background of the eastern Mediterranean with the Hellenic Trench in the south and the volcanic back-arc to the north of Crete (adapted from DOUTSOS & KOKKALAS 2001). Star indicates epicentre of the AD 365 earthquake (after SHAW et al. 2008). (B) North coast of Crete to the west of Pirgos with location of vibracores and ERT transects. Isolines in inset map depict coseismic uplift associated with AD 365 earthquake in meters (after KELLETAT 1991; SHAW et al. 2008) (map modified after Google Earth 2015).

### 3.2.2 Earthquakes, volcanism, and tsunami history of Crete

Frequent shallow earthquakes along the Hellenic Trench are characteristic and are linked to the extensional faulting of the overriding Aegean microplate. Deeper earthquakes accompany the descent of the subducted plate (Taymaz et al. 1990; Papazachos & Papazachou 1997). Most earthquakes occur on the interface of the Hellenic subduction zone up to a medium depth of 45 km and may reach maximum magnitudes of Mw = 8.5 (Hollenstein et al. 2008; Shaw et al. 2008; Shaw & Jackson 2010; Stiros 2010). In history, several catastrophic seismic events hit Crete that often induced tsunami waves as well, as for example the prominent earthquake on 21 July AD 365. As suggested by Shaw et al. (2008; see also Lorito et al. 2008; Flouri et al. 2013), this tsunamigenic earthquake was triggered on a N-E dipping reverse fault located within the overriding plate in the south of Crete (Fig. 3.1A). The earthquake reached an estimated magnitude of Mw = 8.3 (Stiros 2001; Shaw et al. 2008; Shaw & Jackson 2010). During this event the western part of Crete experienced coseismic crust uplift of up to 9 m and the former sea level stand, visible as well-preserved bio-erosive markers and algal rims, still fringes the coast of western Crete (e.g., Spratt 1865; Pirazzoli et al. 1982, 1996; Shaw et al. 2008; Mouslopoulou et al. 2015a).

Based on historical accounts (e.g., by the historian and geographer *Ammianus Marcellinus*; Kelly 2004) and on numeric modelling (e.g., Lorito et al. 2008; Flouri et al. 2013; Valle et al. 2014), the AD 365 earthquake is known to have been associated with a catastrophic tsunami that affected the eastern Mediterranean region (e.g., Thommeret et al. 1981; Kelletat 1991; Guidoboni et al. 1994; Pirazzoli et al. 1996; Stiros 2001; Shaw et al. 2008; Papadopoulos et al. 2014). Recently, sedimentary traces of this tsunami were, for the first time, identified in fine-sedimentary archives along the southwestern coast of Crete (Werner et al. 2018a). On 8 August AD 1303, a strong earthquake (Mw = 8.0) ruptured the eastern part of the Hellenic Arc between Crete and Rhodes. As reported by several historical documents, an associated tsunami reached Crete's northeastern coast and struck the capital city of Heraklion (Papadopoulos et al. 2014). The largest tsunamigenic earthquake in Greece during the last century took place on 9 July 1956 at the Amorgos Island area located in the south Aegean Sea. It reached a magnitude of Mw = 7.5, and it was generated by an offshore 40-km-long active fault (Nomikou et al. 2018).

One of the largest volcanic eruptions during the Holocene was the caldera-forming eruption of Santorini during the Late Bronze Age (LBA) (Hammer et al. 1987; Druitt & Francaviglia 1992; McCoy & Heiken 2000). Similar to the eruption of Krakatau and Tambora, the LBA Santorini eruption is supposed to have generated strong earthquakes and a catastrophic tsunami that affected not only the surrounding islands but also at least the northeastern coast of Crete (Bruins et al. 2008). A detailed description of the LBA Santorini eruption is given in section 3.2.4. The last eruption of Santorini occurred in AD 1950 (Georgalas 1953, 1962). A detailed overview of all known historical and prehistorical tsunami records in the Mediterranean are listed in earthquake and tsunami catalogues (e.g., Galanopoulos 1960; Papadopoulos & Chalkis 1984; Tinti 1991; Guidoboni et al. 1994; Soloviev et al. 2000; Papadopoulos et al. 2007, 2014; Ambraseys 2009; Hadler et al. 2012).

### 3.2.3 Study area characteristics

The study site is located near the small village of Pirgos at the northwestern coast of Crete, ~ 13 km westwards of the City of Rethymnon (Figs. 3.1 and 3.2). Located at Almiros Bay, the study site is characterized by a subbasin structure between the cities of Georgioupoli in the west and Petres in the east where it is bound to N-S trending faults (VAN HINSBERGEN & MEULENKAMP 2006). Therefore, this is a local tectonic graben, where young post-Alpine sediments are bounded by N-S trending normal faults, separating them from the older Alpine rocks (Fig. 3.2). Here, a distinctive sandy beach, partly mixed with gravels, has developed. The coastal plain (Fig. 3.2) is fringed by Pliocene marls and bioclastic limestone (IGMR 1977; MEULENKAMP 1969; VAN HINSBERGEN & Meulenkamp 2006) that rise gently in the northward direction, representing finger-like extensions close to the present shoreline. These post-Alpine sediments rest through a major unconformity on top of the geotectonic units deformed by the Alpine orogeny.

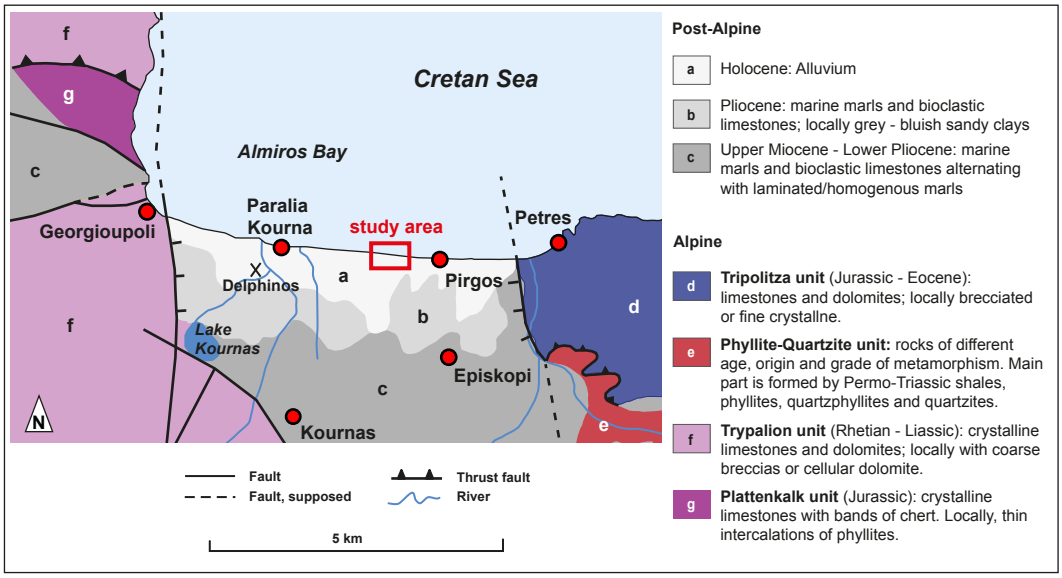


**Fig. 3.2:** Geological map of the Almiros Bay area, northern Crete geotectonic units and location of the study area (adapted from MEULENKAMP 1969; IGMR 1977; PAPANIKOLAOU & VASSILAKIS 2010).

In the study area, three of these units occur, namely the Gavrovo-Tripolitsa unit (with the Jurassic-Eocene limestones overlying the Tyros or Ravdoucha beds comprising Permo-Triassic shales, phyllites, and quartzites), the Trypalion unit (or the upper part of the Western Crete unit, comprising crystalline limestone and dolomite), and the Plattenkalk or metamorphic Ionian/Mani unit (consisting of crystalline limestone with bands of chert; PAPANIKOLAOU & VASSILAKIS 2010). Crystalline limestone and dolomites locally associated with coarse breccia or cellular dolomite of the Trypalion unit border the coastal plain in the west (IGMR 1977; VAN HINSBERGEN & MEULENKAMP 2006). A major N-S fault runs near Georgioupoli to Lake Kournas in the south where it changes its direction to NW-SE and separates this unit from the coastal plain (MEULENKAMP 1969). In the east, Jurassic to Eocene limestones and dolo-

mites of the Gavrovo-Tripolitza series follow (IGMR 1977). The coseismic uplift associated with the AD 365 earthquake (Fig. 3.1) is 1 m in the west of Rethymnon and 2 m in the west of Georgioupoli (Pirazzoli et al. 1982; Kelletat 1991; Shaw et al. 2008; Mouslopoulou et al. 2015a).

### 3.2.4 LBA Santorini eruption and associated tsunamites

The LBA Santorini eruption is often compared to huge historical volcanic eruptions such as the Tambora eruption in 1815 or the eruption of Krakatau in 1883. Tephra from the LBA Santorini eruption has been spread throughout the eastern Mediterranean region. McCoy & Dunn (2002) estimated by means of GIS visualisation of known deposits an ejected volume of 100 $km^3$. The volcanic explosivity index (VEI) of the LBA Santorini eruption is estimated between 6.9 and 7.1 (McCoy & Heiken 2000; Sigurdsson at al. 2006). In comparison, the well-documented eruption of Krakatau lasted several months and reached a VEI of 6 during the final stage of its explosion (Newhall & Self 1982). The latter induced a catastrophic tsunami with an average wave height of 15 m and a maximum run up of 42 m, hitting the neighbouring coasts of Java and Sumatra (Choi et al. 2003). Inspired by the huge impact of the Krakatau tsunami, first Marinatos (1939) supposed a connection between well-distinct archaeological destruction layers of Minoan age found at numerous sites along Crete's northern coast (e.g., the palaces of Amnissos, Malia, and Knossos) and a catastrophic tsunami that was supposed to have been generated by the LBA Santorini eruption. The explosive main stage of the LBA Santorini eruption ended in the collapse of the volcano complex, forming a huge caldera that is often suggested as one main tsunami trigger (e.g., Marinatos 1939; McCoy & Heiken 2000).

In contrast, the latest research of Nomikou et al. (2016) assumed that the caldera formation of the LBA Santorini eruption occurred 'syn-eruptively' (Nomikou et al. 2016) and was not open to the sea during the main eruption stage. Instead, they proposed pyroclastic flows as the main tsunami escapement, which moved down the inner and the outer flanks of the island into the sea, and submarine slumping (Nomikou et al. 2016). Hence, the generated tsunami wave(s) would have spread toward all directions and must have affected at least the neighbouring islands. The LBA tsunami deposits were reported from several sites along the coasts of the Aegean Sea and the eastern Mediterranean region. On Santorini, McCoy & Heiken (2000) found evidence for tsunamigenically reworked volcanic tephra near Pori and estimated a wave amplitude of 8 m a.s.l.

Regarding the supraregional context, Goodman-Tchernov et al. (2009) recovered four sediment cores offshore ancient Caesarea (Israel). They dated a 40-cm-thick sand layer and identified it to be caused by the LBA Santorini tsunami. Minoura et al. (2000) reported LBA Santorini tsunami deposits from Didim and Fethye (SW Turkey) and from Gouves (northern Crete). At Didim and Fethye, a layer of LBA tephra was deposited on top of a marine sand layer, indicating the LBA Santorini tsunami propagating toward the east. At Gouves (NW Crete), Minoura et al. (2000) identified a 10–20 cm thick layer of pumice that was deposited on top of a marine sand layer at 2–3 m a.s.l. Because of its position on top of a Late Minoan workshop floor and the associated tephra, they related the tsunamite to the LBA Santorini eruption and inferred that the tsunami waves propagated to the southwest as

well. Dominey-Howes (2004), however, criticized that the assumed LBA tsunami deposits at Gouves provided 'neither stratigraphic description nor exact altitudinal measurements and distance' (Dominey-Howes 2004) and that they are therefore not convincing.

In a detailed field campaign, Dominey-Howes (2004) surveyed more than 40 sites along the northern coast of Crete in search of onshore tsunami deposits. However, he found no evidence for supraregional onshore tsunami flooding and sediment deposition. Four years later, however, tsunami-related impact on the northeastern coast of Crete triggered by the LBA Santorini eruption was proven by Bruins et al. (2008). Massive chaotic tsunami deposits were found at the promontory of Palaikastro showing typical tsunami sedimentary signatures, e.g., erosional contact with underlying strata, volcanic ash intraclasts, marine macro- and microfauna, and imbrication of rounded beach pebbles, ceramic sherds and bones. Deduced by field evidence, Bruins et al. (2008) suggested that the tsunami wave at Palaikastro reached a wave height of at least 9 m a.s.l.

Approximately 3.5 km distant from the Pirgos study area of this paper, Bottema & Sarpaki (2003) drilled the longest continuous vegetation record of Crete near Delphinos (see Fig. 3.2). Detailed pollen analysis revealed the vegetation history of northern Crete. They also encountered a distinct pumice layer that was chemically proven to be related to the LBA Santorini eruption. The authors suggested that the deposition was caused by seawater currents but no sedimentary evidence of a direct LBA Santorini imprint was found. Based on pollen data, Bottema & Sarpaki (2003) concluded that neither the influence of the LBA eruption on vegetation and crop cultivation nor major climate changes throughout the Holocene are visible. However, climatic effects can be masked by human impact and thus can not be excluded.

## 3.3 Material and methods

### 3.3.1 Field work

Geophysical prospection was carried out using electrical resistivity tomography (ERT) in order to examine the bedrock topography and main stratigraphical structures of the near-surface underground. We used a multi-electrode Syscal R1 switch 48 device (type Iris Instruments) with an electrode spacing of 2 m and a Wenner-Schlummberger electrode array. Measured data were inverted to depth sections using the RES2DINV software (Geotomo Software). Local stratigraphical data were obtained by three vibracores and were used to calibrate results of ERT measurements. Two vibracores (RET 2A and RET 5A) were drilled using a Cobra Pro handheld coring device (type Atlas Copco) with a closed auger system and plastic inliners, 50 mm in diameter. Vibracore RET 2 was drilled using an open auger system. Position and elevation data of ERT electrodes and vibracoring sites were measured using a differential GPS (type Topcon Hiper Pro FC-250) with a minimum horizontal and vertical precision of 2 cm.

### 3.3.2 Laboratory analyses

Plastic inliners filled with sediment were cut into two halves at the geolaboratory of Johannes Gutenberg-University Mainz, Germany, then cleaned, photographically documented and analysed using sedimentological and geomorphological methods according to Ad hoc-AG Boden (2005) and Schrott (2015). Selected samples (RET 2A: 50 samples; RET 5A: 36 samples) were retrieved from representative stratigraphical units for further sedimentological, geochemical, and microfaunal analyses.

Grain size analyses of sediment samples were conducted using the sieve and pipette method after Köhn (Köhn 1929; DIN/EN ISO 11277 2002). Prior to wet-sieving and pipette analyses, standard pretreatment included dry-sieving in order to determine the amount of coarse particles with diameter >2 mm, followed by peptisation of the fraction <2 mm in sodium pyrophosphate for 12 hours. Percentages of eight grain size classes (clay: < 2 µm, fine silt: 2–6.3 µm, medium silt: 6.3–20 µm, coarse silt: 20–63 µm, finest fine sand: 63–125 µm, fine sand: 125–200 µm, medium sand: 200–630 µm, coarse sand: 630–2000 µm) were determined. For each sample, we calculated (mean) relative frequency distribution curves as well as cumulative frequency curves based on a 99-step cosine interpolation function over the grain size classes.

A spectrophotometer (type Konica Minolta CM-600 d) was used to quantify changes in sediment colour based on the chromaticity values a* and b* of the CIELAB colour space (L*a*b*) with an interval of 2 cm. The variables a* and b* specify the content of red (+a*) and green (–a*) and yellow (+b*) and blue (–b*) of the sediments respectively. Sediment colour can be used as an additional tool to discriminate between sedimentary facies, e.g., for differentiating between sediments that were accumulated under oxic or anoxic conditions or between sediments with different organic content. The geochemical element composition of sediments (in total 32 elements) was analysed using a portable Niton XL3t 900 S GOLDD XRF handheld analyser (calibration mode SOIL) with a vertical resolution of 2 cm. Results of the portable XRF (PXRF) technique are semiquantitative and commonly used to identify trends and changes in geochemical composition between different sediment units (Chagué-Goff et al. 2015, 2017; Judd et al. 2017).

We used the Zr/K ratio as a grain size proxy in order to identify less visible changes in the sedimentation process. Zirconium (Zr) ranks among heavy minerals and relates to coarser sediments and high-energy environments (Chagué-Goff et al. 2017). Potassium (K) relates to terrestrial environments as it is strongly bound to clay minerals. Magnetic susceptibility of sediments, the content of diamagnetic and magnetic materials of the sediment, was measured using a Bartington MS2K surface sensor.

Semiquantitative microfossil analyses were conducted for selected sediment samples (RET 2: 40 samples; RET 5A: 20 samples) in order to reconstruct palaeoenvironmental changes and to differentiate between autochthonous and allochthonous deposits. For that purpose, 15 ml of sediment was sieved in the fractions > 400, 400–200, 200–125 and < 125 µm and analysed with the help of a stereo microscope (type Nikon SMZ 745T). The Z-series photos of foraminifera specimens were taken using a light-polarizing microscope (type Nikon Eclip-

se 50i POL with Digital Sight DS-FI2 digital camera). Genera and, if possible, species of foraminifera were determined after Cimerman & Langer (1991), Murray (2006) and Rönnfeld (2008). In some cases, foraminifera were strongly calcified and worn and the species was not determinable.

For geochronological information, ten samples underwent $^{14}C$ AMS radiocarbon analysis. Conventional radiocarbon ages were calibrated using the calibration software Calib Rev 7.10 and the Marine13 and IntCal13 data sets (Reimer et al. 2013).

## 3.4 Results

### 3.4.1 Pre-drilling ERT survey

We present depth sections of three selected transects (Fig. 3.3, A–C) along which ERT measurements were carried out for preboring exploration of the near-surface underground. Localisation and orientation of these ERT transects are depicted in Fig. 3.1B.

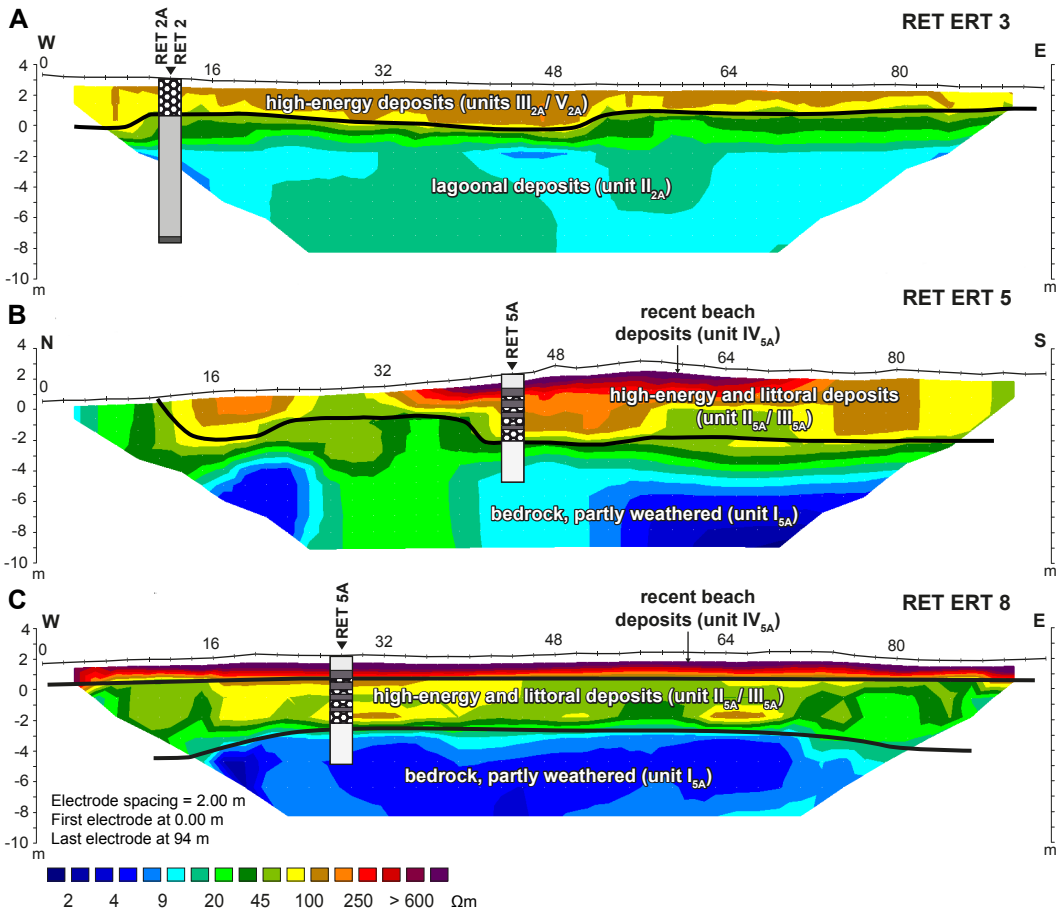


**Fig. 3.3:** Depth sections of ERT transects RET ERT 3, RET ERT 5 and RET ERT 8 based on ERT measurements (see Fig. 3.1 for locations). Figure also shows location of vibracoring sites. Interpretation of depth sections is based on core log data from vibracores RET 2/2A and RET 5A. See text for explanation.

In general, high resistivity values reflect coarse-grained sand and gravel, partly (very) dry. Low resistivity values document sediments dominated by fine-grained material, mostly silt and clay. All three ERT depth sections were converted to the same scale that comprises electrical resistivity values from 0 (dark blue) to > 600 Ωm (purple).

The ERT sections additionally include the position and simplified stratigraphy of related vibracores (Fig. 3.3, A–C). Transect RET ERT 3 runs from W to E parallel to the road in the south of the study area. The depth section shows a two-part horizontal composition with low-resistivity deposits at the bottom (9–78 Ωm), reaching up to around 2 m b.s.l, and medium to high-resistivity (78–175 Ωm) deposits at the top. The ERT transect RET ERT 5 runs perpendicularly to transect RET ERT 8 from N to S. The lower unit of the two-part composition reaches values in the range of 2–78 Ωm. The upper unit reaches values > 78 Ωm. The depth section of transect RET ERT 8 again trends in the W-E direction and runs at the present beach, ~ 70 m distant to RET ERT 3. Inversion results help to differentiate between three different units. The lowermost unit shows low-resistivity deposits (> 2–15 Ωm). The intermediate unit is characterized by resistivity values of 15–78 Ωm and highest resistivity values (> 78 to >600 Ωm) were found for the top layer. Two vibracores were drilled in order to determine sedimentary characteristics for the different ERT units detected and correlated ERT units with sedimentary units. Vibracoring sites RET 2/2A and RET 5 were chosen to obtain maximum possible thickness of low-resistivity sedimentary units.

### 3.4.2 Multi-proxy analysis of vibracore RET 2/2A

Vibracores RET 2/2A were drilled at 3.17 m a.s.l. (a.s.l. = above sea level) ca. 135 m inland (Fig. 3.1; RET 2A closed auger using plastic inliners; RET 2 with open auger system) reaching a maximum depth of 10 m below surface (b.s.). We classified five stratigraphical units (see Tab. 3.1) according to the main sedimentary characteristics deduced from grain size (Figs. 3.5 and 3.6) and sediment colour data (Fig. 3.5) and visible macrofossil content (Fig. 3.7). Minor stratigraphical differences between cores RET 2 and RET 2A are evoked by differences in drilling technique and compression.

**Tab. 3.1:** Stratigraphical units found for vibracores RET 2A/2 and RET 5A based on grain size data, sediment colour and macrofossil content.

| | Unit | Sediment character (grain size, colour, macrofossil content) |
|---|---|---|
| **RET 2 / RET 2A** | $I_{2A}$ | medium sand, grey |
| | $II_{2A}$ | silt and clay dominated, dark grey to light grey, Cerastoderma glaucum shells in the lower parts |
| | $III_{2A}$ | medium sand, ferruginous-beige to dark ferruginous, marine shell fragments |
| | $IV_{2A}$ | clay and silt dominated, ferruginous-beige locally with dark intersections |
| | $V_{2A}$ | medium sand with gravel, dark beige, marine shell fragments |
| **RET 5A** | $I_{5A}$ | clay and silt dominated bed rock, partly weathered, locally with higher sand and gravel content, light grey |
| | $II_{5A}$ | gravel dominated medium sand matrix (similar to $III_{2A}$), ferruginous-beige, marine shell fragments |
| | $III_{5A}$ | medium sand, well sorted, beige, marine shell fragments |
| | $IV_{5A}$ | similar to $III_{5A}$ but without any material > 2mm |

From 10.00 m b.s. (–6.83 m below sea level (b.s.l.)) to 9.81 m b.s. (–6.64 m b.s.l.), sediment core RET 2A is characterised by greyish medium sand (unit $I_{2A}$) (Fig. 3.4). From 9.81 to 2.33 m b.s. (0.84 m a.s.l.), a thick light grey to dark grey layer (unit $II_{2A)}$ predominantly consisting of clay and silt follows. Unit $II_{2A}$ is partly enriched with plant remains and diverse mollusc fragments. In the lower parts of the sediment core, intact valves of Cerastoderma glaucum are embedded (9.40, 8.96, 8.54, 8.28 and 8.24 m b.s.). Two thin layers between 8.80 and 8.75 m b.s. (–5.63 to –5.58 m b.s.l.) and between 8.55 and 8.53 m b.s. (–5.38 to –5.36 m b.s.l.) show a high percentage of shell debris. Three layers showing sedimentary characteristics similar to unit $I_{2A}$ intersect unit $II_{2A}$ between 5.71 and 5.65 m b.s. (–2.54 to –2.48 m b.s.l.) followed by a major loss of sediment (l.o.s.), between 4.82 and 4.58 m b.s. (–1.65 to –1.41 m b.s.l.) and between 3.93 and 3.71 m b.s. (–0.76 to –0.54 m b.s.l.).


**Fig. 3.4:** Stratigraphy of sediment core RET 2A drilled ca. 135 m distant to the present-day shoreline with basal information on sediment character (grain size, colour, macrofossil content). See text and Tab. 3.1 for explanation.

The uppermost part of unit $II_{2A}$ between 2.38 and 2.33 m b.s. (0.84 m a.s.l.) shows deposits still dominated by silt, but with a change in colour to ferruginous-beige. Following a sharp erosional contact, we found medium sand with a low percentage of clay and silt (unit $III_{2A}$; Fig. 3.4) with a ferruginous-beige to dark ferruginous colour between 2.33 and 1.76 m b.s. (1.41 m a.s.l.). Between 1.76 and 1.45 m b.s. (1.41 to 1.72 m a.s.l.), deposits are again dominated by clay and silt (unit $IV_{2A}$) but, in contrast to unit $II_{2A}$, are solely ferruginous-beige in colour. Another erosive contact was found at 1.45 m b.s. (1.72 m a.s.l.), where a thick layer of unit $III_{2A}$ ferruginous-beige to dark ferruginous medium sand reaches up to 1.35 m b.s. (1.82 m a.s.l.). Following a section with minor loss of sediment, these sands are covered by dark beige gravel, incorporated in a medium sand matrix from 1.32 to 1.18 m b.s. (1.85 to 1.99 m a.s.l.; unit $V_{2A}$). On top, again unit $III_{2A}$ deposits follow up to 0.46 m b.s. (2.71 m a.s.l.), finally covered by anthropogenic infill.

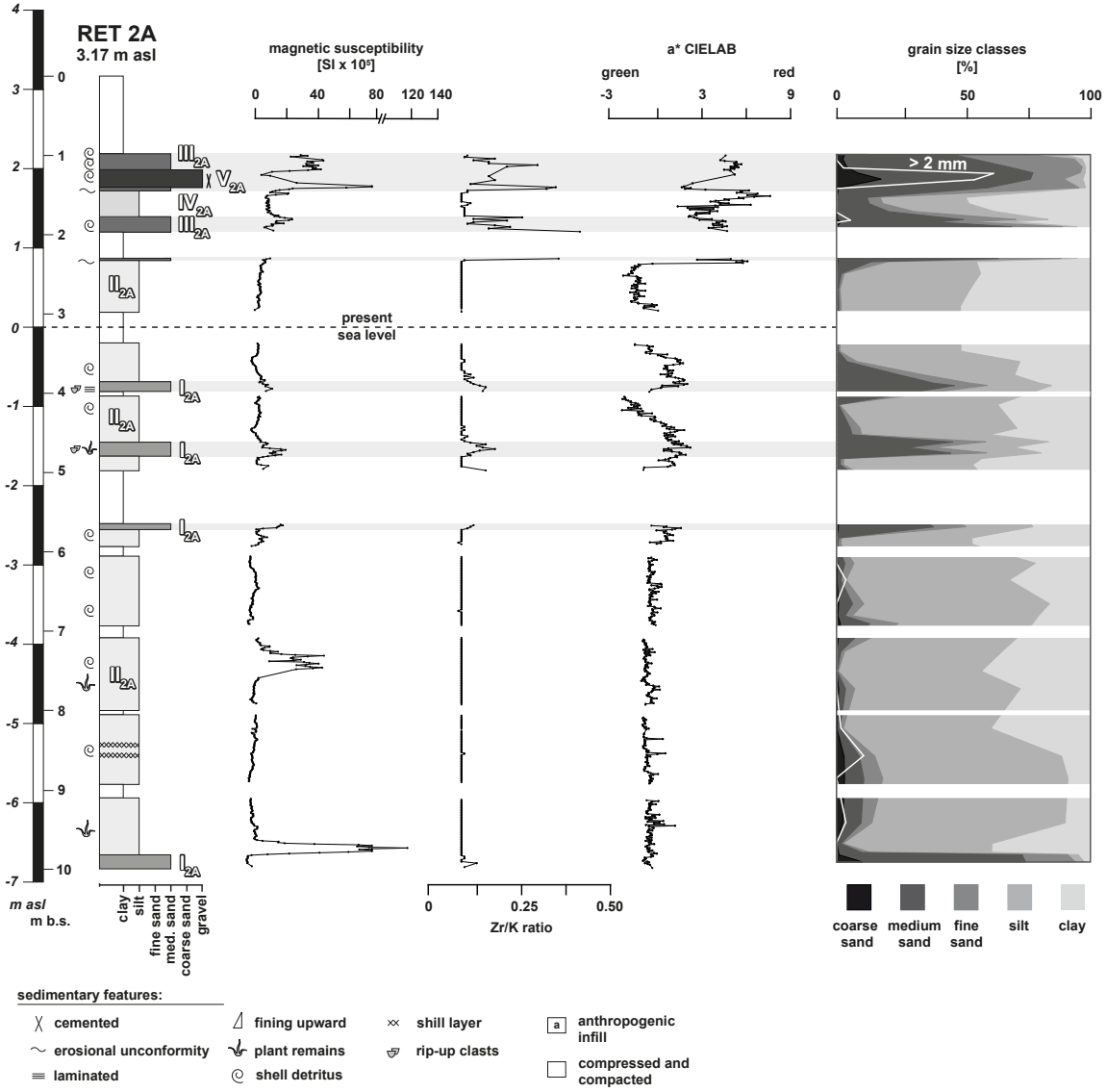


**Fig. 3.5:** Selected palaeoenvironmental proxies obtained for vibracore RET 2A by multi-proxy analyses. Magnetic susceptibility, Zr/K ratio, and a* CIELAB are compared to cumulative grain size data and stratigraphical units ($I_{2A}$ to $V_{2A}$; see Tab. 3.1). Cumulative grain size data refer to fine sediment < 2 mm (sum = 100 %) and coarse sediment > 2 mm (white line; percentage referred to total mass of sample).

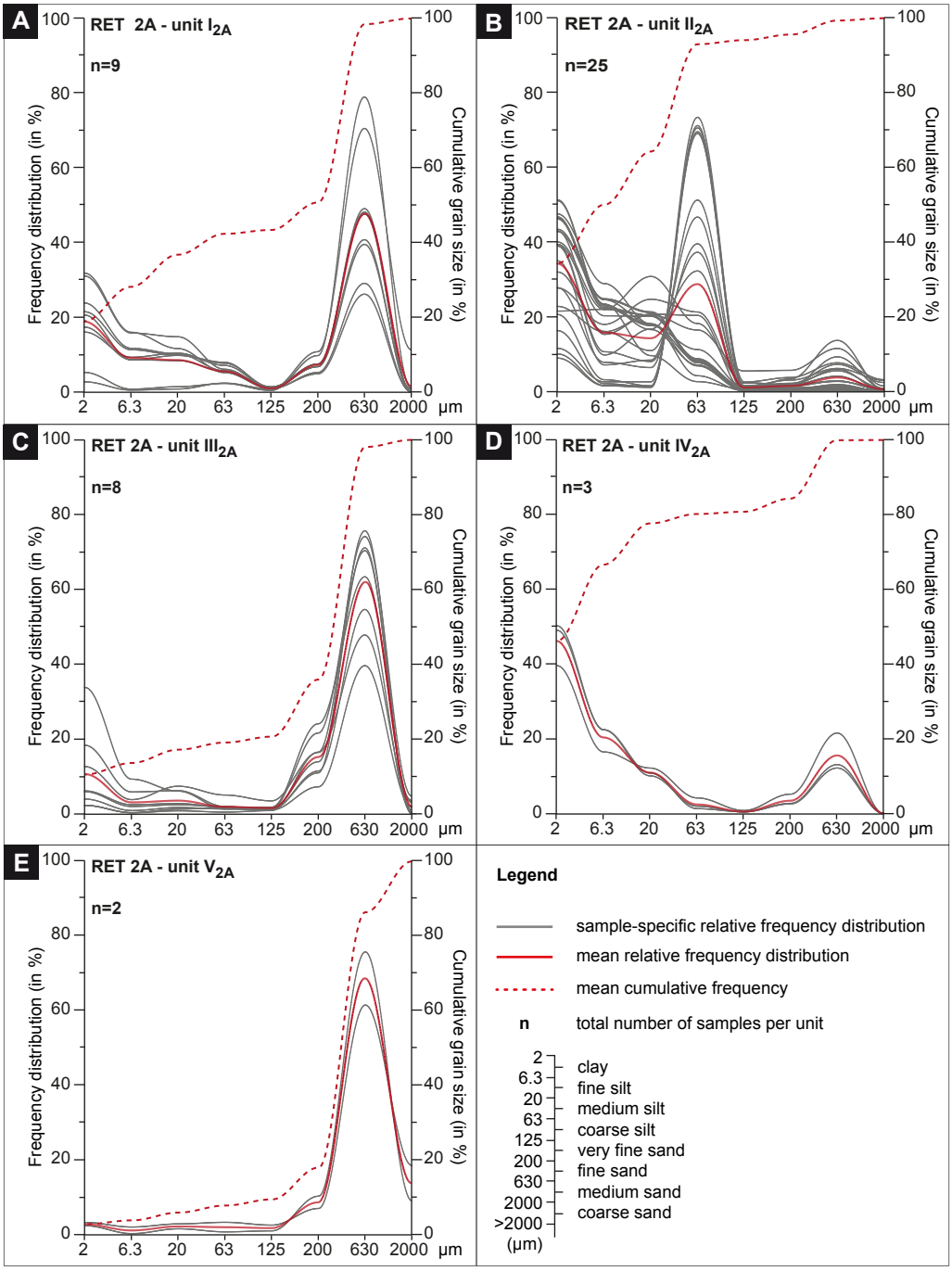


**Fig. 3.6**: Relative frequency distribution curves of grain size data obtained for sediment samples from vibracore RET 2A classified by stratigraphical units $I_{2A}$, $II_{2A}$, $III_{2A}$, $IV_{2A}$ and $V_{2A}$ (see Table 3.1 for explanation). Curves for the mean relative frequency distribution and the mean cumulative frequency are given for each stratigraphical unit.

Figure 3.5 depicts selected sedimentary and geochemical parameters deduced from multi-proxy analyses of vibracore RET 2A. Magnetic susceptibility measurements show distinct peaks at the base, in mid- and top-core position. The upper half of the vibracore shows peaks in units $I_{2A}$, $III_{2A}$ and $V_{2A}$. These units are consistent with peaks in the Zr/K ratio. Down-

and mid-core sections show more or less homogeneous a* values of the CIELAB colour space indicating predominant green colour aspects. Peaks toward higher content of red colour are associated with mid- and top-core units $I_{2A}$. At ca. 2.38 m b.s., a shift from grey deposits with mostly negative a* values toward brown sediments is visible. Grain size data reflect stratigraphical changes with units $I_{2A}$, $III_{2A}$ and $V_{2A}$ showing maximum percentages of sand. Unit $V_{2A}$ is characterised by a maximum amount of gravel. Mean relative frequency distribution of grain sizes for each sedimentological unit are depicted in Fig. 3.6. Units $I_{2A}$ and $III_{2A}$ show a bimodal grain size distribution with high amounts of fine- (clay and silt) and coarse-grained (sand) mineral grains. Predominantly fine-grained deposits (≤ 63 µm) characterize unit $II_{2A}$. Unit $IV_{2A}$ shows predominantly fine-grained (≤ 20 µm) deposits with a secondary peak of medium sand. Unit $V_{2A}$ is characterized by well-sorted material < 2 mm, nearly exclusively medium sand, but also contains more than 50 % gravel, resulting in a bimodal grain size distribution as well.

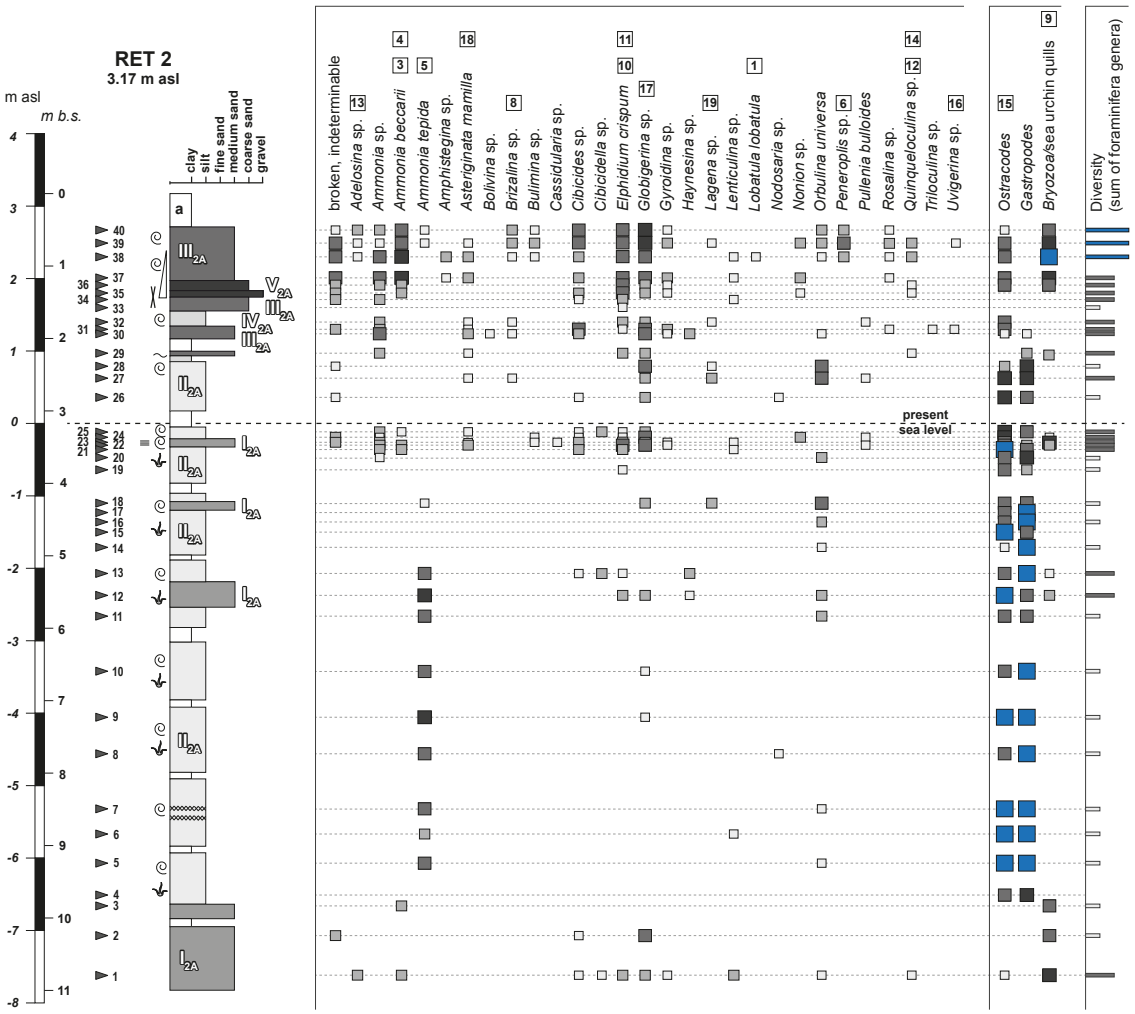


**Fig. 3.7:** Results of microfaunal analysis of sediment samples from vibracore RET 2 based on a semiquantitative approach. Black triangles near scale bar indicate sampling depth of individual samples numbered consecutively from base to top (1 to 40). $I_{2A}$ to $V_{2A}$ indicate stratigraphical units. See text and Tab. 3.1 for explanation. Numbers above biological names refer to numbers and specimens depicted in Fig. 3.8. For legend, see Fig. 3.12.

Samples for microfossil analyses were retrieved from vibracore RET 2. The semiquantitative evaluation of the microfossil content is depicted in Fig. 3.7. An overview of selected foraminifera species and further microfossils is shown in Fig. 3.8. Studied samples (black triangles to the left of the scale bar) are consecutively numbered from base to top. The results show that the down- and mid-core sections up to ca. 3.50 m b.s. contain fewer foraminifera tests than the top-core section, where the diversity (sum of different foraminifera genera) rises abruptly. Both diversity and abundance of foraminifera genera in basal and intersecting units $I_{2A}$ are always higher than in directly over- or underlying neighbouring units. Samples (1, 2, 12, 18, 22, 23, 24) retrieved from unit $I_{2A}$ contain multiple tests of *Ammonia* sp., *Ammonia beccarii*, *Elphidium crispum*, *Globigerina* sp., *Cibicides* sp., *Orbulina universa* and *Asteriginata mamilla* and lower numbers of *Cibicidella* sp. and *Pullenia bulloides*. In contrast, low abundance and low diversity of foraminifera genera are always associated to sedimentary unit $II_{2A}$. Here, the microfaunal signature of the upper part (samples 14–17, 19–21, 24–28) differs from down- and mid-core sections (samples 4–11). We found a relatively higher biodiversity and abundance and a shift from *Ammonia tepida* dominated assemblage (down- and mid-core) to an assemblage dominated by *Globigerina* sp. and *Orbulina universa* (top-core section). Additionally, samples from unit $II_{2A}$ in down- and mid-core sections contain very high numbers of ostracoda and gastropoda (both not determined).

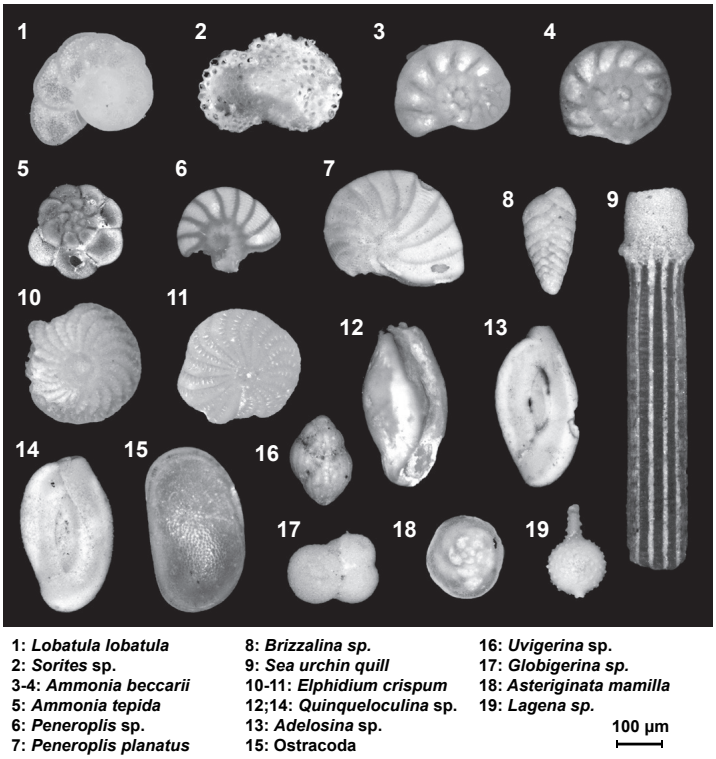


**Fig. 3.8:** Selected specimens of foraminifera and other microfossils found in samples from vibracores RET 2/2A and RET 5A. Species and genera were determined after Cimerman & Langer (1991), Murray (2006) and Rönnfeld (2008).

Maximum diversity and abundance of foraminifera genera are associated with intersecting sand layers in the top-core section at ca. 3.5 m b.s. (unit $I_{2A}$), comprising sample numbers 22–24, and with sand and gravel layer from ca. 2.3 m b.s. to the present surface (units $III_{2A}$ and $V_{2A}$; sample numbers: 29–31, 33–40). *Ammonia beccarii*, *Cibicides* sp., *Elphidium crispum*, *Globigerina* sp. and *Peneroplis* sp. dominate the foraminiferal composition of these units. Furthermore, they include some individuals of *Brizalina* sp., *Bulimina* sp. and *Quinqueloculina* sp. Unit $IV_{2A}$, intercalated between unit $II_{2A}$ and $V_{2A}$ deposits, contains sporadic foraminifera tests of *Ammonia* sp., *Asteriginata mamilla*, *Brizallina* sp. and *Elphidium crispum* but is characterized by a slightly decreased abundance (sample 32) compared to overlying and underlying units.

### 3.4.3 Multi-proxy analysis of vibracore RET 5A

Vibracoring site RET 5A is located ca. 60 m distant from the present-day shoreline in the upper supralittoral zone in front of a small dune belt at 2.19 m a.s.l. and ca. 160 m to the NE of vibracoring site RET 2/2A (Fig. 3.1). Vibracore RET 5A was drilled to 7 m b.s. using plastic inliners (Fig. 3.9). From 4.40 m b.s. (–2.21 m b.s.l.) downward, we used an open coring system because of strongly increased sediment consistency. Four stratigraphical main units can be distinguished (Tab. 3.1) based on grain size data, sediment colour and visible macrofossil content.

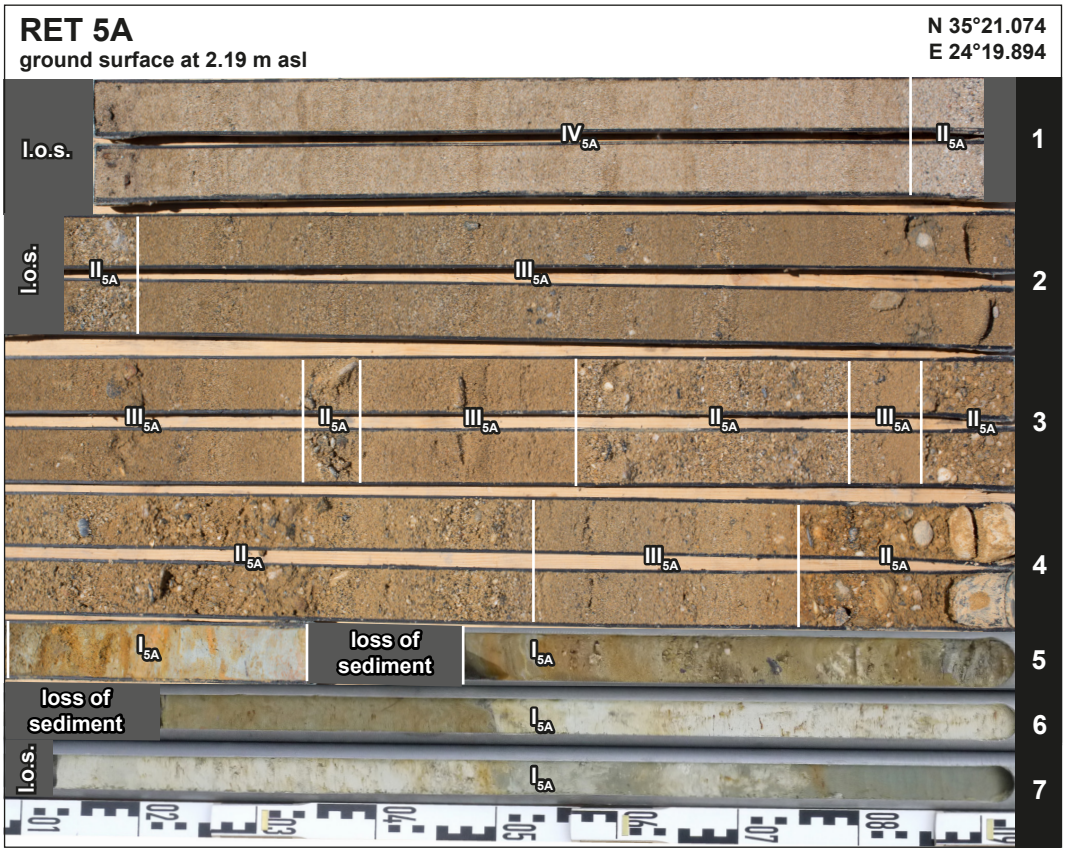


**Fig. 3.9:** Stratigraphy of sediment core RET 5A drilled ca. 60 m distant to the present-day shoreline with basal information on sediment character (grain size, colour, macrofossil content). See text and Tab. 3.1 for explanation.

Between 7.00 and 4.10 m b.s. (–4.81 to –1.91 m b.s.l.), core RET 5A is characterised by clay-dominated bedrock marl of a light greyish colour (unit $I_{5A}$), partly weathered, and locally showing considerable contents of medium sand and gravel (Figs. 3.9 and 3.10). Subsequently follows a layer characterised by a high portion of gravel and marine shell debris imbedded in a matrix out of primarily medium and coarse sand and secondarily fine sand (unit $II_{5A}$). This material, ferruginous in colour, poorly sorted and reaching up to 3.75 m b.s. (–1.56 m b.s.l.), is covered by a thick sequence of mostly sandy deposits (unit $III_{5A}$). These sands are partly laminated and well sorted and reach up to 1.20 m b.s. (0.99 m a.s.l.). Unit $III_{5A}$ sands are intersected by four coarse-grained layers out of type-unit $II_{5A}$ material, namely between 3.53 and 2.85 m b.s. (–1.34 to –0.66 m b.s.l.), between 2.79 and 2.56 m b.s. (–0.60 to –0.37 m b.s.l.), between 2.39 and 2.34 m b.s. (–0.20 to –0.15 m b.s.l.), and between 1.20 and 0.84 m b.s. (0.99 to 1.35 m a.s.l.). The uppermost part of the sediment core consists of well-sorted medium to coarse sand (unit $IV_{5A}$), does not include any material with diameters over 2 mm, and shows several fine sand laminae.

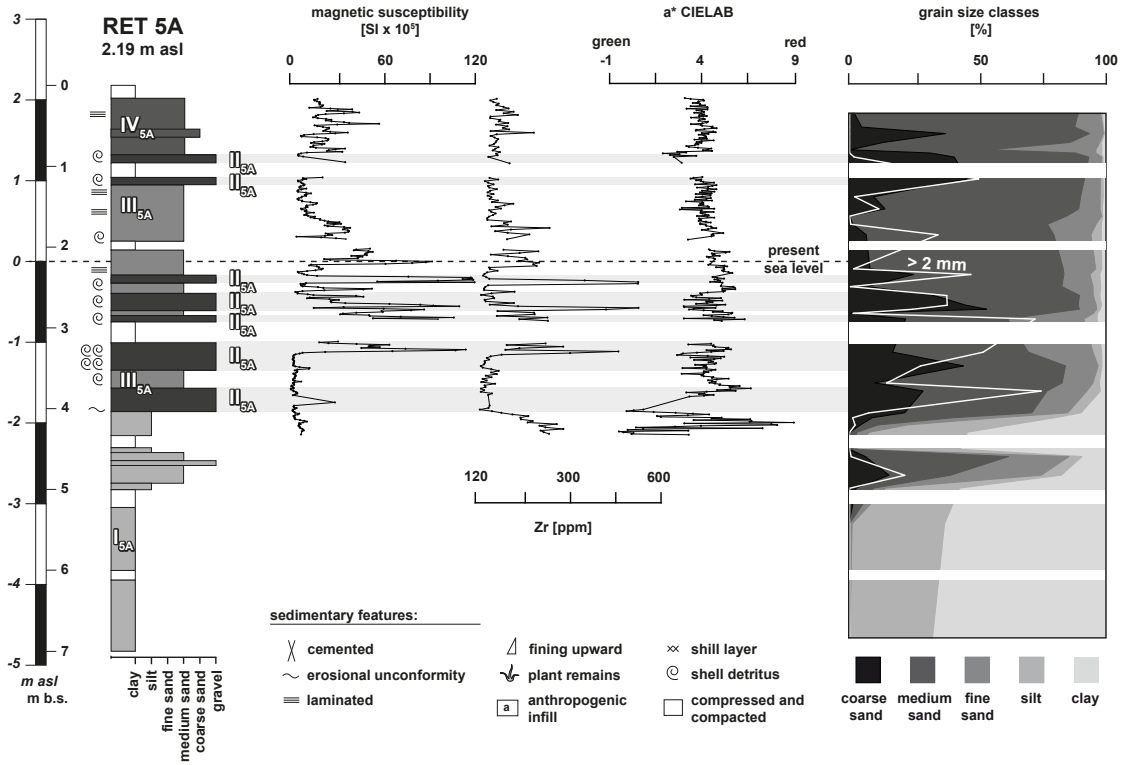


**Fig. 3.10:** Selected palaeoenvironmental proxies obtained for vibracore RET 5A by multi-proxy analyses. Magnetic susceptibility, Zr/K ratio and a* CIELAB are compared to cumulative grain size data and stratigraphical units ($I_{5A}$ to $IV_{5A}$; Tab. 3.1). Cumulative grain size data refer to fine sediment < 2 mm (sum = 100 %) and coarse sediment > 2 mm (white line; percentage referred to total mass of sample).

Results of multi-proxy analyses of vibracore RET 5A are depicted in Fig. 3.10. Basal unit $I_{5A}$ and intermediate unit $III_{5A}$ show low magnetic susceptibility values. Relative maxima are associated with unit $II_{5A}$ (except uppermost unit $II_{5A}$ layer). Unit $IV_{5A}$ shows intermediate

magnetic susceptibility values. Maximum peaks of the heavy mineral zirconium are bound to units $I_{5A}$ and $II_{5A}$ (except lowermost unit $II_{5A}$ layer). Minima are associated with units $III_{5A}$ and $IV_{5A}$. The sediment colour, represented by a* of the CIELAB colour space (Fig. 3.10), is more or less homogenously brown in top- and mid-core positions. In contrast, the lower core section (unit $I_{5A}$) shows variable colours mostly dominated by grey.

Grain size data show that unit $I_{5A}$ is dominated by silt and clay, locally including sand and gravel (Fig. 3.10). In contrast, unit $II_{5A}$ predominantly shows medium and coarse sand and gravel, the latter reaching a percentage of up to 50%. Unit $III_{5A}$ is primarily characterized by medium sand and reduced amounts of coarse sand and gravel (gravel still up to > 25 %). Unit $IV_{5A}$ contains predominantly medium sand but gravel tends toward nil. The mean relative frequency distribution of grain sizes are depicted in Fig. 3.11 for each sedimentological unit. Some samples of unit $I_{5A}$ show a bimodal grain size distribution. Units $II_{5A}$ and $III_{5A}$ appear poorly sorted and show bimodal grain size distributions. In contrast, the material of unit $IV_{5A}$ is very well sorted.

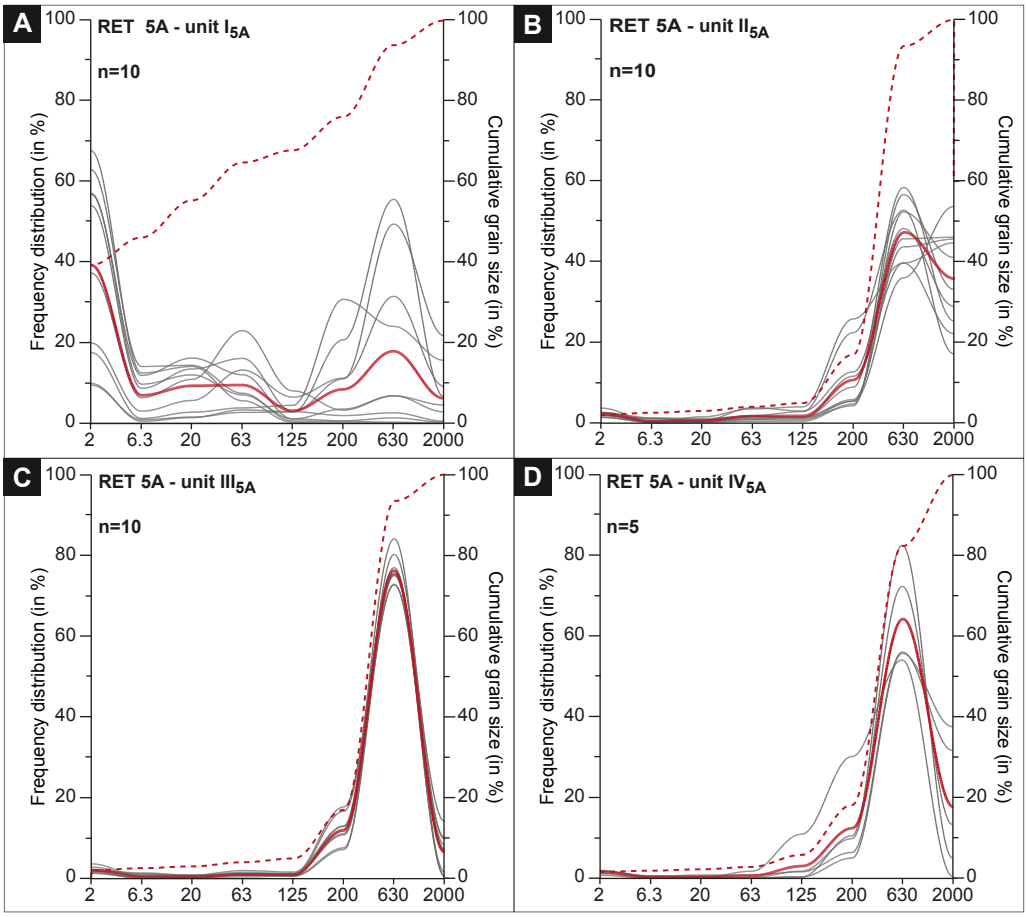


**Fig. 3.11:** Relative frequency distribution curves of grain size data obtained for sediment samples from vibracore RET 5A classified by stratigraphical units $I_{5A}$, $II_{5A}$, $III_{5A}$ and $IV_{5A}$ (see Tab. 3.1 for explanation). Curves for the mean relative frequency distribution and the mean cumulative frequency are given for each stratigraphical unit. For legend, see Fig. 3.6.

Results of microfaunal analyses are summarized in Fig. 3.12. Studied samples are consecutively numbered from base to top (black triangles to the left of the scale bar). Material from the lowermost unit $I_{5A}$, belonging to the local bedrock (marl), neither includes foraminifers nor other microfossils (samples 1–3). On the contrary, maximum abundance and biodiversity of foraminifera genera were found associated with unit $II_{5A}$ in mid-core position; abundance and biodiversity appear slightly lower for unit $III_{5A}$ and relatively lowest for unit $IV_{5A}$. Highest numbers of the foraminifera genera *Asteriginata mamilla*, *Cibicides* sp., *Elphidium* sp. and *Gyroidina* sp. were found in sediments from unit $II_{5A}$, also a high number of *Globigerina* sp. Other foraminifera genera such as *Ammonia beccarii*, *Globigerina* sp. and *Quinqueloculina* sp. occur as a kind of background noise, showing no specific change in abundance. Other genera, such as *Brizalina* sp., *Bulimina* sp., *Lenticulina* sp., *Rosalina* sp. and *Rosalina bradyi* are mostly restricted to units $II_{5A}$ and $III_{5A}$ but only sporadically included. *Sorites* sp., *Peneroplis planatus*, *Haynesina* sp., *Rosalina* sp. and *Rosalina bradyi* show maximum abundance associated with unit $III_{5A}$. Highest abundance of Cibicides refulgens and *Melonis* sp. is noticeable for unit $IV_{5A}$ (samples 19–20). Units $II_{5A}$ to $IV_{5A}$ also include a high abundance of marine gastropods and bryozoa, both not determined.

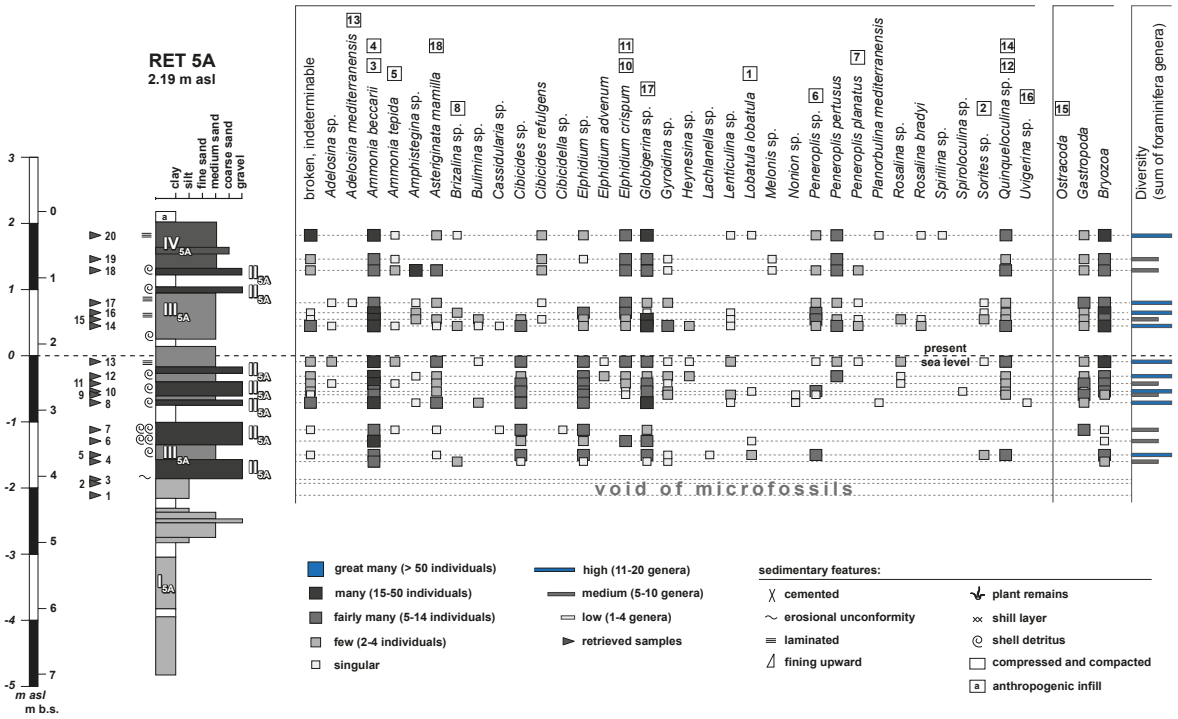


**Fig. 3.12:** Results of microfaunal analysis of sediment samples from vibracore RET 5A based on a semiquantitative approach. Black triangles near scale bar indicate sampling depth of individual samples numbered consecutively from base to top (1 to 20). $I_{5A}$ to $IV_{5A}$ indicate stratigraphical units. See text and Tab. 3.1 for explanation. Numbers above biological names refer to numbers and specimens depicted in Fig. 3.8.

### 3.4.4 Geochronology

Ten samples were retrieved from vibracore RET 2 for $^{14}C$ AMS radiocarbon dating in order to establish a local event-geochronology for the Pirgos study site. Five samples consisted of undetermined plant remains; five samples of wood remains. Conventional radiocarbon ages were calibrated using the Calib 7.10 software. Radiocarbon dating results are summarised in Tab. 3.2.

**Tab. 3.2:** Stratigraphical units found for vibracores RET 2A/2 and RET 5A based on grain size data, sediment colour and macrofossil content.

| Sample | Lab. no. (CEZ) | Depth m b.s. | Depth m a.s.l. | Sample description | Unit | $^{14}C$ Age (BP) | $\delta^{13}C$ (‰) | 1σ max; min (cal BC/AD) | 2σ max; min (cal BC/AD) |
|---|---|---|---|---|---|---|---|---|---|
| RET 2/22 PR 3.38 | 24922 | 3.38 | –0.21 | plant remains | $II_{2A}$ | 3690 ± 25 | –35.5 | 2133;2033 BC | 2192;1980 BC |
| RET 2/25 PR2 3.53 | 24923 | 3.53 | –0.36 | plant remains | $II_{2A}$ | 3828 ± 23 | –28.6 | 2331;2206 BC | 2431;2154 BC |
| RET 2/30 PR 4.58 | 24924 | 4.58 | –1.41 | plant remains | $II_{2A}$ | 4220 ± 24 | –29.1 | 2893;2777 BC | 2900;2703 BC |
| RET 2/33 HR 5.29 | 24925 | 5.29 | –2.12 | wood remain | $II_{2A}$ | 4485 ± 24 | –30.1 | 3329;3100 BC | 3340;3092 BC |
| RET 2/35 PR 5.54 | 24926 | 5.54 | –2.37 | plant remains | $II_{2A}$ | 4864 ± 25 | –20.8 | 3691;3638 BC | 3699–3636 BC |
| RET 2/36 HR 5.87 | 24927 | 5.87 | –2.70 | wood remain | $II_{2A}$ | 4755 ± 25 | –32.2 | 3632;3522 BC | 3637–3384 BC |
| RET 2/40+ HR 7.25 | 24928 | 7.25 | –4.08 | wood remain | $II_{2A}$ | 5580 ± 26 | –34.9 | 4449;4369 BC | 4457–4357 BC |
| RET 2/48 PR 9.57 | 24929 | 9.57 | –6.40 | plant remains | $II_{2A}$ | 6535 ± 27 | –29.6 | 5512–5478 BC | 5543–5471 BC |
| RET 2/49 HR 9.72 | 24930 | 9.72 | –6.55 | wood remain | $II_{2A}$ | 6643 ± 27 | –28.6 | 5618;5559 BC | 5626–5527 BC |
| RET 2/50 PR 2 9.80 | 24931 | 9.80 | –7.25 | plant remains | $II_{2A}$ | 6628 ± 27 | –28.3 | 5615–5539 BC | 5622–5514 BC |

Note: Lab. No. – laboratory number, CEZ – Curt-Engelhorn-Zentrum für Archäometrie, Mannheim, Germany; b.s. – below ground surface; asl – above sea level; unit – stratigraphical unit; 1σ max; min (cal BC/AD) – calibrated ages, 1σ range (; – several possible age intervals); 2σ max; min (cal BC/AD) – calibrated ages, 2σ range (; – several possible age intervals). Calibration based on Calib Rev 7.1 with IntCal 13 dataset (Reimer et al. 2013).

## 3.5 Discussion

### 3.5.1 Establishing a facies model

Based on multi-proxy analyses, we differentiated between different sedimentary facies, which we used to reconstruct the palaeogeographical development of the Pirgos study site (Fig. 3.13). The base of vibracore RET 2/2A is made out of shallow marine to littoral deposits consisting almost exclusively of medium sand. A small peak in Zr is probably associated with marine input of heavy minerals (Chagué-Goff et al. 2017). The foraminiferal assemblage encountered is typical of a shallow marine environment. In contrast, thick silty and clayey unit $II_{2A}$ deposits are associated with homogenous and low-energy sedimentation proces-

ses in a sheltered water body. The multiplicity of embedded plant remains, ostracoda and stress tolerating foraminifera species, for instance *Ammonia tepida* and *Haynesina* sp., correspond well with a brackish environmental condition typical of lagoonal systems (Murray 2006; Avnaim-Katav et al. 2013).

Fragments of marine molluscs, especially *Cerastoderma glaucum*, two prominent shell debris layers and sporadic occurrence of marine foraminifera species, which do not derive from the local bedrock, point to a clear but restricted saltwater inflow. Encountered lagoonal deposits of unit $II_{2A}$ are consistent with the lower horizontal unit of ERT transect RET ERT 3. Coarse-grained unit $I_{2A}$ deposits (except basal unit $I_{2A}$ layer), $III_{2A}$ and $V_{2A}$ document increased depositional energy and interrupt stable lagoonal depositional conditions several times. High-energy layers, including muddy rip-up clasts, show an abrupt increase in sand content and contain high values of the heavy mineral zirconium, which is related to marine input (Chagué-Goff et al. 2017). Furthermore, the microfaunal signature shows a marine character by comprising lagoonal (e.g., *Ammonia tepida*, *Heynesina* sp.), shallow water (e.g., *Elphidium crispum*, *Ammonia beccarii*, *Peneroplis pertusus*) and deep water species (e.g., *Brizalina* sp., *Cibicides* sp.) resulting in a signature far beyond marine signals of basal sands and the signature of lagoonal muds.

The mixed foraminiferal assemblage underlines the marine origin of the allochthonous sand layers, which we associate with extreme wave events (EWE) from the seaside that affected the lagoonal system. Additionally, the middle layer of unit $III_{2A}$ features a distinct basal erosional unconformity and consist of poorly sorted and partly cemented sediments that are characteristics of beachrock-type high-energy deposits (Vött et al. 2010). Stable lagoonal depositional conditions were reestablished again after this EWE layer and lasted until the upper limit of unit $IV_{2A}$, namely at 1.45 m b.s. (1.72 m a.s.l.). Nevertheless, compared to unit $II_{2A}$ lagoonal mud, unit $IV_{2A}$ sediments show influence of post-sedimentary oxidation, such as iron and manganese spots, which we interpret as evidence for post-sedimentary uplift.

In vibracore RET 5A, basal unit $I_{5A}$ belongs to weathered Neogene marl. This bedrock unit reaches the surface a little farther to the south in the nearby hinterland of the study site and forms the local hillside (Meulenkamp 1969; Fig. 3.2). Neogene marls in vibracore RET 5A are partly reworked with intermingled sandy and gravelly sections. They can be easily identified in ERT transects RET ERT 5 and 8 (Fig. 3.3) where they induce low electrical resistivity values because of the prevailing fine-grained texture. Subsequent unit $II_{5A}$ represents a poorly sorted high-energy deposit, dominated by chaotically embedded gravel in a sandy matrix. A high content of marine shell fragments and the foraminifera signature reflect strongly its marine character. Sediments of unit $II_{5A}$ contain a mixed foraminiferal assemblage that include foraminifera genera of near-shore habitats (e.g., *Ammonia* sp., *Brizalina* sp. and *Elphidium* sp.) and benthic species preferring deep water habitats (e.g., *Cibicides* sp. and *Gyroidina* sp.; De Rijk et al. 1999; Murray 2006; Avnaim-Katav et al. 2013). Therefore, we interpret unit $II_{5A}$ as a high-energy EWE deposit that was laid down by predominantly turbulent flow dynamics, which caused poor sorting and missing layering features.

In unit $III_{5A}$, depositional energy and grain size decrease but foraminiferal assemblage still reflects a clear marine character with increasing occurrence of genera such as *Peneroplis* sp. and *Sorites* sp., which are often associated with carbonate-rich sandy beach sediments

(Murray 2006; Avnaim-Katav et al. 2013). This sedimentary unit comprises partly well-laminated former EWE deposits of unit $II_{5A}$, which were reworked over the years by all-day littoral processes. Unit $IV_{5A}$ material represents well-sorted and clearly layered recent beach deposits showing no coarse material with diameters >2 mm.

### 3.5.2 Identification and characterisation of extreme wave events

The Pirgos geological archive (Fig. 3.13) records five high-energy extreme wave events (EWE; labeled with Greek letters from α to ε). Associated deposits show sedimentary, geochemical and microfaunal characteristics typical of abrupt and temporary water inundation from the seaside. Searching for the potential trigger mechanisms within the framework of (palaeo)geographical conditions, extreme storm surges and tsunamis must be taken in account for the northern coast of Crete. On a global scale, tsunami and storm deposits may be very similar in their sedimentological characteristics (summarised, e.g., by Dominey-Howes et al. 2006; Switzer & Jones 2008; Smedile et al. 2011; Rodríguez-Ramírez et al. 2016).

Tsunamis and high-energy storm surges are often associated with the input of coarse-grained allochthonous sands and gravel to sheltered low-energy sedimentary environments such as lagoons, beach lakes or harbour basins (Marriner & Morhange 2007; Vött & May 2009). Sediments deposited by storm surges generally comprise nearshore material, for example, beach and nearshore sands; whereas tsunami deposits are characterised by a wide range of source material because of its bigger wavelength affecting open marine, shelf, littoral and terrestrial environments (Switzer & Jones 2008; Röbke & Vött 2017).

Studies on modern mega tsunami events, such as the Boxing Day Tsunami in 2004 and the Tōhoku-oki tsunami in 2011, illustrate that tsunamis are capable of transporting high amounts of sediment with a wide spectrum of grain sizes for a long distance landward, often accompanied by a landward thinning (Bahlburg & Weiss 2007). Moreover, sedimentary structures – such as fining upward sequences of grain size, a broad spectrum of different grain sizes, rip-up clasts, erosional unconformities and poor sorting – were documented for tsunami deposits (e.g., Dominey-Howes et al. 2004, 2006; Bahlburg & Weiss 2007; Switzer & Jones 2008; Röbke & Vött 2017).

Geochemical signatures of event deposits, for example the input of marine calcium and strontium, can also be used to identify tsunami fingerprints. Chagué-Goff et al. (2015, 2017) gave an overview of different element ratios that were most recently applied successfully in palaeotsunami research. Microfaunal analyses, especially analyses of foraminiferal assemblage, are often used as a proxy for marine inundation events in coastal areas and are useful tools to indicate palaeoenvironmental changes (Dominey-Howes et al. 2006; Pilarczyk et al. 2014). Within the framework of palaeotsunami studies in the Mediterranean (Reinhardt et al. 1994; Goodman et al. 2008; Hadler et al. 2013; Mathes-Schmidt et al. 2013; Fischer et al. 2016a; Finkler et al. 2018a), a mixed assemblage of foraminifera with differing ecological habitats and preservation states was found to be typical of tsunami deposits. The 'typical tsunami foraminiferal assemblage', if ever existing, differs from study to study and is related to local geomorphological and bathymetrical conditions. Best results of identifying tsunami influence are given by displaced and transported species, for example,

deep water species found in lagoonal or marsh settings (Mamo et al. 2009; Pilarczyk et al. 2014).

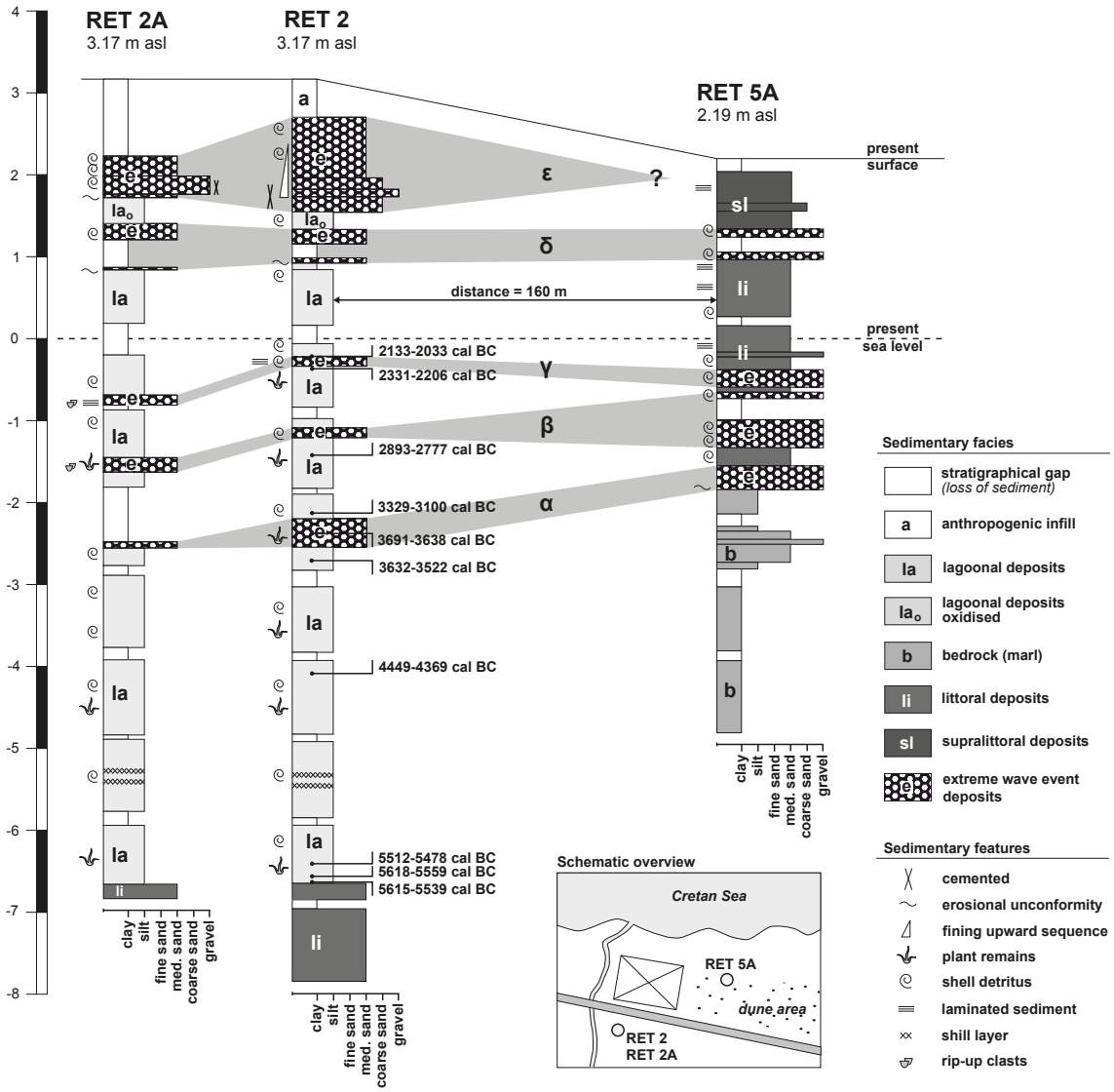


**Fig. 3.13:** Vibracore transect of cores RET 2, RET 2A and RET 5A drilled near Pirgos. The sedimentary record of vibracores RET 2/2A reveals five extreme wave event (EWE) deposits shaded in grey and labelled with Greek letters α to ε. At site RET 5A, the uppermost EWE layer ε is supposed to be reworked by all-day littoral processes. For location of vibracoring sites see Fig. 3.1. Stratigraphical units are explained in Tab. 3.1. For details on radiocarbon ages see Tab. 3.2 and Fig. 3.14. See text for further explanation.

Numerous palaeotsunamites detected in sedimentary archives all over the Mediterranean point out the high tectonic potential of this region and the supraregional impact of major tsunami events. Tsunamites were identified, for instance, along the coasts of the Aegean, Ionian and Adriatic seas and along the northeastern and southwestern coasts of Crete (e.g., De Martini et al. 2003; Bruins et al. 2008; Vött et al. 2009a, 2011b, 2014, 2015; Kortekaas et al. 2011; Mastronuzzi & Sansò 2012; Koster et al. 2015; Willershäuser et al. 2015;

Quintela et al. 2016; Werner et al. 2018a). Recent attempts to reinterpret geological evidence of tsunami impact in the Mediterranean as rather associated to storm events manipulated original data and revealed basic methodological flaws. The validity of geological evidence for Mediterranean extreme wave events and their interpretation as caused by palaeotsunami impacts is untouched (for further details, see Vött et al. 2018b).

In our study, vibracore RET 2/2A records five extreme wave events associated with the input of poorly sorted coarse-grained marine material varying from fine sand to gravel into a lagoonal environment. Intersecting coarse-grained layers are in contrast with the under- and overlying fine-grained lagoonal deposits and partly show a basal erosional contact (Fig. 3.13, α to ε). The sedimentary records of cores RET 2A and RET 5A do not show general evidence for fining upward sequences; only vibracore RET 2 shows a decrease of grain sizes for EWE ε. In addition, landward thinning tendencies of EWE sediment layers cannot be recognized; locally, they might fall into sections of sediment loss, particularly in vibracore RET 2A. However, EWE layers β and γ include intraclasts that were most likely reworked from the underlying silty lagoonal deposits.

Vibracore 5A gives evidence of four EWE layers that show even more contrasting changes in grain sizes and include a high content of marine shell debris. Their stratigraphical position is in good accordance with EWE layers α, β, γ and δ encountered at vibracoring site RET 2/2A. The EWE deposits α to ε found in vibracore RET 2/2A reveal a clear fingerprint of allochthonous marine foraminifera (Fig. 3.7), events γ, δ and ε showing maximum diversities. Event layers are characterised by a mixture of species and genera from different ecological habitats including benthic and shallow marine environments and thus strongly differing from microfossil assemblages typical of lagoonal environments (dominated by e.g., *Ammonia tepida* and numerous ostracods). Shallow marine foraminifera species and genera (e.g., *Ammonia beccarii*, *Asteriginata mamilla*, *Elphidium* sp., *Gyroidina* sp. and planktonic *Globigerina* sp.) mixed with benthic species (e.g., *Cibicides* sp.), particularly abundant in high-energy EWE layers of vibracore RET 5A, were also found within EWE layers of vibracore RET 2/2A, albeit with decreasing abundance. This suggests a landward sediment transport of sediment over a distance of at least 160 m between the two sites.

In littoral systems, the element zirconium is mostly associated with the input of marine heavy minerals generally bound to fine sand deposits (Cuven et al. 2013). The Zr/K ratio turned out to be a useful grain size indicator, especially for vibracore RET 2/2A where it reflects slightly increased sand content. However, both coring sites are situated relatively close to the present shore and might be in the potential range of (palaeo-)storm events so that overall marine signals independent from tsunami signals cannot be excluded. Considering sedimentary character, microfaunal evidence, geochemical signals and the overall geomorphological setting of Pirgos study site, the encountered EWE layers show some signals typical of tsunami events, but these signals alone do not allow us to exclusively attribute EWE layers to either storm or tsunami events.

On an annual basis, Crete's northern coasts are exposed to a considerably mild wind and wave climate (Soukissian et al. 2008; Alexandrakis et al. 2011). Waves mainly approach from the west and northwest, or less frequently from the north, which conform to predominant winds in the open Aegean Sea (Athanassoulis & Skarsoulis 1992; Soukissian et al.

2008; Alexandrakis et al. 2011). During the winter season, often accompanied by strong storm winds or Etesian winds, the mean wave heights along the northern coast of Crete vary between 0.8 and 0.9 m (Soukissian et al. 2008), being lower in sheltered areas such as the Almiros Bay. Extreme wave heights of over 4 m occur with a statistical annual frequency of 0.5% (Soukissian et al. 2007), and wave shoaling in the foreshore area considerably reduces wave heights.

Winter storms in the Mediterranean are high-frequency events. Consequently, near-coast geological archives prone to frequent storm-caused inundation are supposed to comprise a long record of repeated storm influence in the form of more or less thin storm-generated sand layers (e.g., Maas & Macklin 2002). However, vibracore RET 2/2A records only five and RET 5A only four high-energy inundation events over several thousands of years resulting in a low-frequency signature of high-magnitude events. In contrast, vibracore 5A, between major EWE layers, reveals hardly visible thin sediment layers with alternating grain sizes (Fig. 3.9); such lamination (for example, in unit $III_{5A}$ at 1–2 m b.s. and in unit $IV_{5A}$) might be associated with more frequent storm surges in the Mediterranean region. More detailed research on these issues is, however, needed to solve this question.

In a summary view, major EWE layers encountered in vibracores RET 2/2A and RET 5A show low-frequency, high-magnitude characteristics typical of tsunamis in the Mediterranean. Typical sedimentary tsunami signatures were found, but because of the overall constellation with vibracoring sites lying relatively close to the present shore (max. 135 m), these arguments alone are not sufficient to completely exclude alternative, storm-related inundation events. Also from a climatological point of view, it remains difficult to differentiate between storm and tsunami event deposits.

### 3.5.3 Age-depth relations

We established an age-depth model as a base for the reconstruction of the palaeoenvironmental evolution of the Pirgos study site (Fig. 3.14a). Doing so, we compared the stratigraphical log with sedimentary units of vibracore RET 2 to calibrated radiocarbon ages (1σ intervals and mean ages; Calib 7.1). From the top of the shallow marine basal sands to the uppermost limit of the lagoonal sequence represented by sedimentary units $II_{2A}$ and $IV_{2A}$, all age-depth points are lying on a straight line with almost no relevant deviations between individual data points and trend curve. According to the age-depth model, the Pirgos lagoonal environment started to exist in the first half of the 6$^{th}$ mill. BC and continuously persisted until the first half of the 2$^{nd}$ mill. cal BC, i.e., during a period of about 3000 years. We calculated a stable sedimentation rate of S = 1.853 m/ka for the lagoonal environment during this period.

The local sedimentation rate can be considered as the result of relative sea level changes (as the depositional environment/lagoon is connected to the Cretan Sea) meaning that eustatic and tectonic components were not subject to major abrupt changes but remained in balance over time. We interpret these results as the consequence of continuous subsidence of the near-coast environment at Pirgos, thus reflecting stable tectonogeomorphological conditions over 3000 or so years.

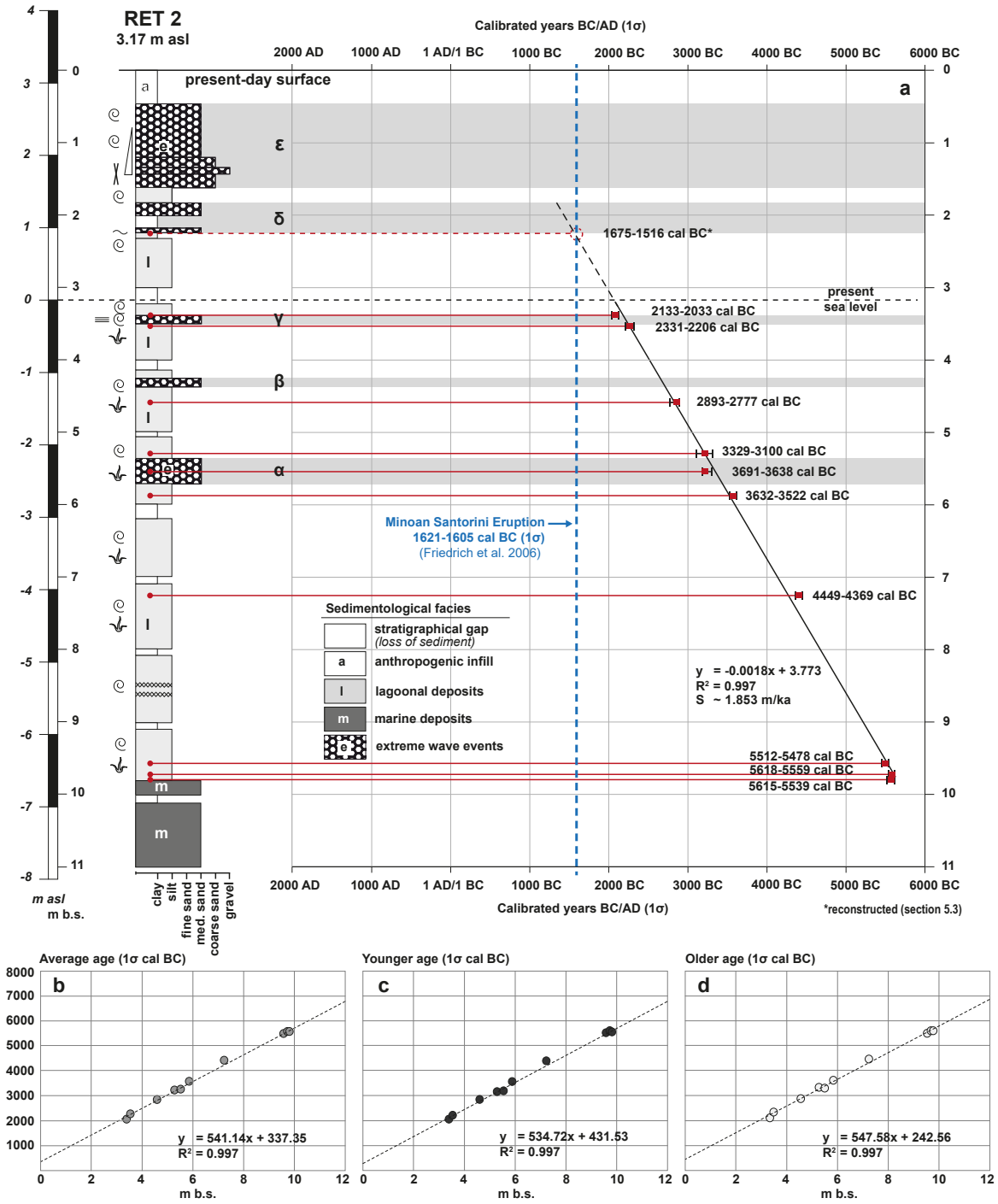


**Fig. 3.14:** Age-depth model for vibracore RET 2 based on stratigraphical and radiocarbon data and statistic age-depth relation. (a) Age-depth model showing stratigraphical units and calibrated radiocarbon ages (1σ intervals and mean age; Calib 7.1). Dashed blue line marks the age of the LBA Santorini eruption derived from radiocarbon dating by FRIEDRICH et al. (2006: 1621–1605 cal BC, 1σ). (b–d) Calibrated 1σ ages were used to calculate linear regression trends for age-depth relations, namely for the average (b), the younger (c) and the older (d) age limits of radiocarbon age intervals obtained for each sample. Resulting linear equations (b–d) show very high coefficients of determination with $R^2$ = 0.997. Based on the linear regression equations, we reconstructed the age of EWE δ to the timeframe of 1675–1516 cal BC. See text for further explanations.

Intersecting high-energy sand layers (Fig. 3.13, α to δ) represent extreme wave events and were obviously not related to local/regional changes in relative sea level. In contrast, each EWE caused a temporary interference of the lagoonal environment but with the lagoonal system completely reestablished soon after the corresponding event.

Calibrated 1σ-ages were used to calculate linear regression trends for age-depth relations at the Pirgos site, namely for the upper and lower age limits of radiocarbon age intervals and the average ages (see Figs. 3.14b to 3.14d). All linear equations show very high coefficients of determination ($R^2 = 0.997$):

| | |
|---|---|
| (1) Average age: | y = 541.14 x + 337.35 (Fig. 3.14b) |
| (2) Upper (younger) age limit: | y = 547.58 x + 242.56 (Fig. 3.14c) |
| (3) Lower (older) age limit: | y = 534.72 x + 431.53 (Fig. 3.14d) |

Linear regression equations were used to calculate the point in time when EWE δ hit the study site and left high-energy deposits in the top-core position, namely sedimentary unit $III_{2A}$ at 2.33 and 2.32 m b.s. at sites RET 2A and RET 2 respectively. Based on the linear regression Eqs. (1–3), EWE δ can be dated (rounded up) to a lower age limit of 1675 cal BC, an upper age limit of 1516 cal BC and an average age of 1596 cal BC. The resulting calibrated timeframe of 1675–1516 cal BC is highly consistent with ages obtained for LBA Santorini tsunamites found in the literature (Fig. 3.15) and with the age of the LBA Santorini eruption radiocarbon dated by Friedrich et al. (2006) to 1621–1605 cal BC (1σ; see also Friedrich & Heinemeier 2009).

Abrupt high-energy impact associated with an EWE of possibly tsunami-related nature (section 3.5.2) is already proven by corresponding sedimentary features, for example the presence of an erosional unconformity and microfossil evidence, namely the abrupt increase of shallow marine foraminifera such as *Ammonia* sp., *Asteriginata mamilla*, *Elphidium crispum*, *Triloculina* sp. and *Uvigerina* sp. At this point, we consider the strong geochronological consistency between Pirgos EWE δ and published LBA Santorini data as a crucial argument to conclude that EWE δ at site RET 2/2A is a reliable tsunamite candidate for the LBA Santorini tsunami.

After this EWE δ, it seems as if the lagoonal environment persisted up to 1.44 and 1.62 m b.s. at sites RET 2A and RET 2 respectively (mean: 1.53 m b.s.), when the subsequent EWE ε occurred. Linear regression Eqs. (1–3) result in a corresponding age of 1250–1080 cal BC. However, the unconformity found on top of unit $IV_{2A}$ lagoonal deposits suggest erosion effects by EWE ε so that the obtained age of 1250–1080 cal BC must be considered as the minimum age. We do not suggest that mud-dominated unit $IV_{2A}$, slightly sandy, represents a thick mud cap section between two individual waves of EWE δ because grain size data (Figs. 3.5 and 3.6) do not show any (secondary) fining upward trends which should be expected. Additionally, considering the local stratigraphy, the mud section seems to be too thick to represent a mud cap between two waves of an EWE δ wave train. Thus, we are able to expand the life time of the Pirgos lagoonal environment to at least the second half of the 2$^{nd}$ mill. cal BC.

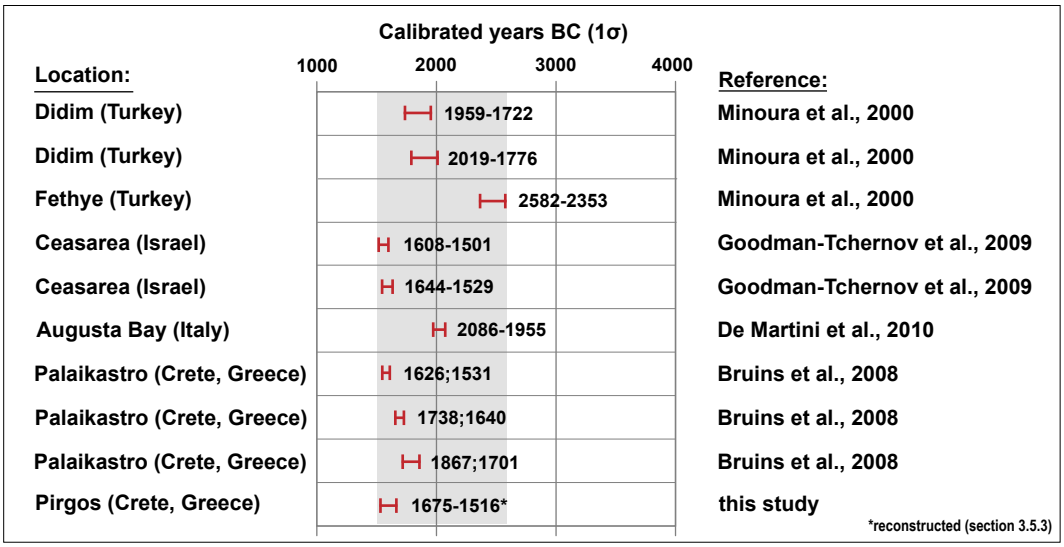


**Fig. 3.15:** Radiocarbon ages of LBA Santorini tsunamites found at different study sites all over the eastern Mediterranean (recalibrated ages, see Tab. 3.3, based on Calib Rev 7.1 with Intcal13 data set, Reimer et al. (2013), calibrated ages, 1σ range (; – several possible age intervals). The time interval found for the age of EWE δ at Pirgos (this paper; 1675–1515 cal BC) is highly consistent with ages obtained for LBA Santorini tsunamites found in the literature and the radiocarbon age of LBA Santorini eruption published by Friedrich et al. (2006: 1621–1605 cal BC, 1σ).

### 3.5.4 Local event-geochronostratigraphy

The five EWE α to γ that hit the Pirgos lagoonal environment were radiocarbon dated using the sandwich dating approach (Fig. 3.14, Tab. 3.2).

The EWE α most probably affected the Pirgos lagoon between 3309 and 3100 cal BC as a best-fit age interval (Tab. 3.2: terminus post quem: 3691–3638 cal BC; terminus ad or post quem: 3309–3178 cal BC; terminus ante quem: 3229–3100 cal BC). For EWE β, we found a terminus post quem of 2893–2777 cal BC and a terminus ante quem of 2331–2206 cal BC, resulting in a best-fit age interval of 2893–2206 cal BC. The age of EWE γ is defined by the terminus post quem of 2331–2206 cal BC and the terminus ante quem is 2133–2033 cal BC, resulting in a best-fit age interval of 2331–2033 cal BC. We interpret EWE δ as a reliable LBA Santorini tsunami candidate. Based on linear regression equations calculated from the Pirgos age-depth model (Fig. 3.14a), its best-fit age is 1675–1516 cal BC (section 3.5.3). Continuous lagoonal depositional conditions persisted until the impact of EWE ε, the youngest out of five EWEs recorded at Pirgos, with a minimum age of 1250–1080 cal BC. After EWE ε, lagoonal conditions stopped existing at the Pirgos site.

At the northeastern coast of Crete, Lespez et al. (2003) investigated several sediment cores from a marsh near the excavation site of Minoan Malia. Core C6 included a significant layer of clayey marine sand, 40 cm thick, with pumice on top that was embedded in marsh deposits. This layer was radiocarbon dated to 1739–1513 cal BC (2σ) so that Lespez et al. (2003) suggested a relation to the LBA Santorini eruption and assumed a tsunami origin. This tsu-

nami candidate layer is highly consistent in age with EWE δ, i.e., the reliable LBA Santorini tsunami candidate found near Pirgos. Goodman-Tchernov et al. (2009) also identified a corresponding LBA Santorini tsunamite candidate within sediment cores drilled offshore Caesarea at the Israeli coast.

**Tab. 3.3:** Radiocarbon ages of LBA Santorini tsunamites published by different authors recalibrated using Calib 7.1 with IntCal 13 dataset (Reimer et al. 2013).

| Location | Country | Reference | Sample | Position | Material | $\delta^{13}C$ (‰) | $^{14}C$ Age (YBP) | Calibration by authors | | Recalibration (Calib 7.10) | |
|---|---|---|---|---|---|---|---|---|---|---|---|
| | | | | | | | | 1σ max; min | 2σ max; min | 1σ max; min | 2σ max; min |
| Didim | Turkey | Minoura et al. 2000 | Didim | w | foraminifera | –2.2 | 3837 ± 88 | 1930–1706 cal BC | - | 1959–1722 cal BC | 2094–1617 cal BC |
| Didim | Turkey | Minoura et al. 2000 | Didim | b | foraminifera | 0.1 | 3886 ± 86 | 1991–1759 cal BC | - | 2019–1776 cal BC | 2142–1670 cal BC |
| Fethye | Turkey | Minoura et al. 2000 | Fethye | b | marine gastropodes | –7.6 | 4303 ± 79 | 2562–2351 cal BC | - | 2582–2353 cal BC | 2729–2239 cal BC |
| Palaikastro | Greece/ Crete | Bruins et al. 2008 | PK-PR-1 | w | cattle bone | –20.81 | 3310 ± 35 | - | - | 1626;1531 cal BC | 1682;1505 cal BC |
| Palaikastro | Greece/ Crete | Bruins et al. 2008 | PK-PR-2 | w | cattle bone | –18.71 | 3390 ± 35 | - | - | 1738;1640 cal BC | 1860;1612 cal BC |
| Palaikastro | Greece/ Crete | Bruins et al. 2008 | BC-1-10 | w | patellidae | 2.48 | 3790 ± 60 | - | - | 1867;1701 cal BC | 1936–1616 cal BC |
| Ceasarea | Israel | Goodman-Tchernov et al. 2009 | Core 1 | w | foraminifera | 3.0 | 3610 ± 40 | - | 1660–1460 cal BC | 1608–1501 cal BC | 1664–1445 cal BC |
| Ceasarea | Israel | Goodman-Tchernov et al. 2009 | Core 2 | w | foraminifera | 2.2 | 3640 ± 40 | - | 1680–1490 cal BC | 1644–1529 cal BC | 1714–1484 cal BC |
| Augusta Bay | Italy | De Martini et al. 2010 | OPR-S1 | w | bivalve | 0.7 | 3970 ± 35 | - | 2100–1635 cal BC | 2086;1955 cal BC | 2131–1904 cal BC |

Note: Calibrated ages, 1σ range (; – several possible age intervals); b – below tsunami layer, w – within tsunami layer. For details, see Tab. 3.2.

Another 'exceptional marine inundation' event found in the lower part of core C6 at Malia was dated to ca. 2500–2040 cal BC (Lespez et al. 2003, p. 449). This age interval is in very good accordance with the best-fit age interval for EWE γ at Pirgos (2331–2033 cal BC), emphasising that deposits of EWE γ were laid down in the course of a supraregional tsunami event as well.

Searching for (supra)regional event(s) possibly corresponding to EWE ε, a first possible candidate is the many discussed AD 365 earthquakes that generated a strong tsunami that was, according to historical accounts, similar to the Boxing Day tsunami 2004 in southeast Asia (Kelly 2004; Vött & May 2009; Werner et al. 2018a). This tsunami was triggered offshore southwestern Crete and was related to a mega-earthquake along major reverse faults in the overriding Aegean microplate (Mouslopoulou et al. 2015b). Numerical simulations (e.g., Shaw et al. 2008: Fig. 4) showed, that the central and southern Aegean and Cretan Seas were actually affected by the AD 365 tsunami. However, no sedimentary evidence of the AD 365 event was found on the north coasts of Crete so far.

Event-geochronostratigraphies by Ntageretzis et al. (2015a) revealed multiple tsunami impacts at Limnothalassa Moustou, Argolid Gulf, ca. 270 km to the NW of the Pirgos site. The

youngest tsunami impact was dated to the time between the seventh and fifteenth cent. AD. In the Evratos River delta, ca. 220 km to the NW of Pirgos, Ntageretzis et al. (2015b) found sedimentary and microfossil evidence of a tsunami event that was also dated to the time between the seventh and fifteenth centuries AD. Both tsunami events most possibly refer to the historically well-known tsunami that affected wide parts of the eastern Mediterranean in AD 1303. This event must therefore be taken into account as a second possible EWE candidate for ε.

Historical catalogues reported severe destruction from northeastern Crete where the tsunami of AD 1303 hit the capital city of Heraklion (Papadopoulos 2014). Scheffers et al. (2008) found dislocated boulders at the Bay of Vatika, SE Lakonia, ca. 180 km to the NW of the study site, that refer to a transportation age around 1300 cal AD. Sedimentary, geomorphological and micro- and macrofaunal evidence of younger tsunami events is presented by Ntageretzis et al. (2015c) for the Bay of Vatika. Here, an event layer was dated to 1467–1618 cal AD (maximum age) representing a third possible EWE candidate.

Another younger event, thus the fourth possible tsunami candidate, affected the Bay of Vatika after the beginning of the seventeenth century AD. However, without further age control, it remains impossible to correlate Pirgos EWE ε with one of these tsunami events or with other, potentially even younger EWEs.

### 3.5.5 Palaeogeographical reconstruction

Stable lagoonal environmental conditions at site RET 2A/2 near Pirgos lasted from the first half of the 6$^{th}$ mill. BC until (at least) the end of the 2$^{nd}$ mill. BC. Until the end of the 4$^{th}$ mill. BC, the lagoon was, at least locally, separated from the Cretan Sea by a bedrock sill out of Pliocene marl, the surface of which was drilled at 1.99 m b.s.l. in vibracore RET 5A (Fig. 3.13). Later, the lagoon was bound to a sandy littoral system and was probably sheltered by a beach barrier, remains of which were also found in sediment core RET 5A.

The Pirgos vibracore transect (RET 2/2A and RET 5A) shows consistent stratigraphical patterns with regard to EWE layers α to δ. However, no sedimentary evidence of EWE ε was found at site RET 5A (Fig. 3.13). Nevertheless, cemented sand and gravel similar to beachrock was found at the northeastern fringe of the beach area of the neighbouring Pelekanos tavern and seems to be consistent with EWE ε at site RET 2/2A (Fig. 3.1; see Vött et al. 2010). We thus believe that EWE ε deposits were originally present at site RET 5A but were reworked by littoral processes.

The sedimentary record of Delphinos (Fig. 3.2) drilled by Bottema & Sarpaki (2003) comprises a thick lagoonal sequence enriched with plant remains and individuals of *Cerastoderma glaucum*, specifically in the lower parts of the core as well. In a depth similar to the one of the EWE δ layer at Pirgos, namely from 2.40 to 2.09 m b.s., volcanic deposits in the form of pumice were found but, unfortunately, without further descriptions of the stratigraphical context. However, this consistency underlines the hypothesis of a large near-coast lagoonal system or several smaller lagoons that were located in today's Almiros Bay.

These lagoons were most likely separated from the open sea by beach barriers that evolved

where Neogene marl reached or came close to the surface generating an obstacle that initiated littoral sediment accumulation.

### 3.5.6 Uplift indicators

During the strong earthquake of AD 365, the western part of Crete was coseismically uplifted by up to 9 m (Pirazzoli et al. 1992). Geomorphological indicators of coseismic uplift, such as uplifted notches, are well known for the area between Georgioupoli and Petres. Here, the coseismic uplift amounts to 1–2 m and is associated with the AD 365 event according to geomorphological literature (Kelletat 1991; Shaw et al. 2008; Mourtzas et al. 2015; Mouslopoulou et al. 2015a).

Vibracore RET 2/2A reveals evidence of post-sedimentary oxidation of upper unit $II_{2A}$ and $IV_{2A}$ deposits in the top-core position. Based on the sedimentary facies, lagoonal sediments were originally deposited at or, more probably, below sea level. Their uppermost occurrence at (average) 1.53 m b.s. (= 1.64 m a.s.l.) requires a minimum coseismic uplift of 1.64 m. This amount of crust uplift is well consistent with literature data mentioned above.

Lagoonal sedimentary conditions were reestablished after the LBA Santorini tsunami candidate δ hit the Pirgos study site, as evidenced by the local stratigraphy and the age-depth model of RET 2 (Fig. 3.14a). The EWE ε finally ended lagoonal conditions, most probably because of the abrupt coseismic crust uplift related to earthquake and tsunami effects. This scenario indicates that it is the combined AD 365 earthquake, tsunami, and crust uplift event that is the most favourable scenario for the formation of the EWE layer ε at Pirgos (see section 3.5.4).

Regarding the overall tectonogeomorphological development of Crete since the mid-Holocene, the results of this study allow further substantial contributions. In Fig. 3.16, we present age-depth data from this study compared to age-depth data from Malia, eastern Crete, collected within the framework of the study by Lespez et al. (2003). Original radiocarbon age data were recalibrated (1σ intervals and mean ages; Calib 7.1) and plotted against sampling depths. As already described for the study area of this paper, the Malia site is also characterized by more or less constant sedimentation rates over more than 7000 years (ca. 6300 cal BC to 1300 cal AD; see Fig. 3.16). However, compared to the Pirgos site, the slope of the age-depth-curve is considerably shallower. We can, therefore, conclud that both sites reflect steady subsidence of Crete at least since the 7$^{th}$ mill. BC but with different subsidence rates. Crust downwarp in the west (Pirgos) was much stronger than farther east (Malia), leading to different deposition velocities ($v_{depos\ Malia} < v_{depos\ Pirgos}$) concerning the filling of the locally available accommodation space. Obviously, the rate of crust subsidence during interseismic periods is much higher in the west than in the east, possibly because of the stronger influence by the subduction processes bound to the Hellenic Subduction Trench (Mouslopoulou et al. 2015b). These observations are highly consistent with the model presented by Shaw (2012: Fig. 2.8) that described crust subsidence during an interseismic period in the overriding plate in a proximal part, whereas (separated by a hinge) there is predominant crust uplift in the flexural bulge in the more distal part of the overriding plate. Based on this model, the Pirgos site is located much closer to the subduction interface.

Moreover, our data nicely document that the Pirgos site experienced crust uplift during an earthquake, whereas the Malia site was not affected by upward crust movements. This is also highly consistent with SHAW's model (2012: Fig. 2.8) in so far as the region above the seismogenic part of the interface is now uplifted and points landward of the hinge are now subject to subsidence. Thus, the hinge must be located somewhere between Malia in the east and Pirgos in the west, most probably right near Rethymnon where the AD-365-associated uplift is null (Fig. 3.1 B).

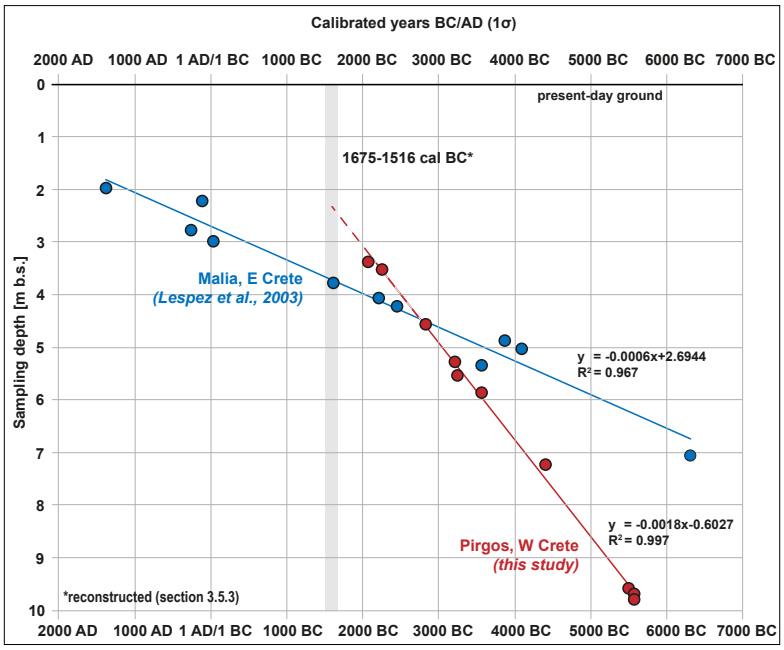


**Fig. 3.16** Age-depth relations reconstructed for Pirgos, western Crete (this study), compared to age-depth relations for Malia, eastern Crete (LESPEZ et al. 2003; radiocarbon data recalibrated). The vertical grey bar illustrates the calculated time interval of EWE δ found at Pirgos (this paper; 1675–1515 cal BC). The curves document continuous subsidence at different rates during long-enduring interseismic periods. The Pirgos depositional environment came out of function at a much earlier point in time because of crust uplift associated with seismic event(s). For further explanations, see text.

## 3.6 Conclusions

The Hellenic subduction zone and the Aegean volcanic arc are well-known tsunami triggers, such as for example the AD 365 or the LBA Santorini events. During the AD 365 earthquake, the (south)western part of Crete was coseismically uplifted by up to 9 m. Since then, erosion processes have intensified and reduced or even erased potential fine sediment archives comprising relevant Holocene event signals.

In search of potential Holocene tsunami sediment traps along the northwestern coasts of Crete, we found an excellent fine sediment archive near Pirgos, located to the west of Rethymnon. Geophyscial prospection by means of multi-electrode electrical resistivity to-

mography helped to select appropriate vibracoring sites. Vibracores RET 2/2A were drilled ca. 135 m distant to the present-day shore, revealing a thick sequence of lagoonal deposits. The Pirgos lagoon existed between the first half of the 6th mill. BC and (at least) the end of the 2nd mill. BC. We found that the area around Pirgos has continuously subsided over 3000 or so years, reflecting stable tectonogeomorphological conditions. Based on sedimentary and micropalaeontological analyses, we identified four EWE layers intersecting the Pirgos lagoonal sequence (α–γ) and a fifth EWE (ε) that ended the lagoonal environment. The EWE α–γ were also identified in vibracore RET 5A drilled ca. 160 m distant from RET 2/2A.

The EWE layers encountered in vibracores RET 2/2A and RET 5A show low-frequency, high-magnitude characteristics typical of tsunamis in the Mediterranean. Sedimentary and microfossil signatures typical of Mediterranean tsunamis were found, but because of the fact that vibracoring sites are located relatively close to the present shore, these arguments alone are (in the absence of additional data) considered not sufficient to completely exclude alternative, storm-related inundation events.

Using the sandwich dating approach, EWE α was radiocarbon dated to the time interval 3309–3100 cal BC, event β to 2893–2206 cal BC and event γ to 2331–2033 cal BC. The age of EWE δ was reconstructed based on an age-depth model and linear regression trends calculated for radiocarbon ages; doing so resulted in an age of 1675–1516 cal BC. We consider the strong geochronological consistency between Pirgos EWE δ and published LBA Santorini ages (Friedrich et al. 2006: 1621–1605 cal BC, 1σ) as solid (or valid) argument to conclude that EWE δ at site RET 2/2A is a reliable tsunamite candidate for the LBA Santorini tsunami.

After the LBA Santorini tsunami hit the Pirgos site, it seems as if the lagoonal system was re-established again and persisted up to 1.54 m b.s. (mean depth) when the subsequent EWE ε occurred at 1250–1080 cal BC or later. The EWE ε, probably triggered by an earthquake- and tsunami-related coseismic uplift of 1.64 m, ended lagoonal conditions, which led to oxidation of older lagoonal sediments. Consistent amounts of coseismic uplift in the area between Georgioupoli and Petres by 1–2 m are described in the literature and related to the AD 365 earthquake and tsunami events (Kelletat 1991; Pirazzoli et al. 1992). This scenario indicates that the combined AD 365 earthquake and tsunami events, and the crust uplift event that is most probably responsible for the formation of EWE layer ε at Pirgos.

We finally conclude that, since the mid-Holocene, the local tectonogeomorphological evolution was dominated by relative subsidence until the time when, most probably, the AD 365 event triggered strong coseismic crust uplift and thus invalidated the Pirgos basin as accommodation space for sediment deposition. On a local scale, subsidence may be seen in conjunction with the neotectonic behaviour of the graben structure between Georgioupoli and Petres (Fig. 3.2). On a more regional scale, our results clearly document the tectonic influence of the nearby subduction zone between the Aegean and African plates on the geomorphological evolution of Crete.

For the study area, we further identified five EWE that hit the Pirgos lagoon, namely three EWE (α, β, γ) for which a tsunami-origin is probable but not proven, a reliable LBA Santorini tsunami candidate (δ) and a candidate for the AD 365 tsunami (ε).

# 4 Extreme wave events recorded in sedimentary archives of the Geropotamos River (north-central Crete, Greece)

**Abstract.** Recent tsunami events have shown that tsunamis may propagate far inland by entering rivers mouths and may cause massive damage along the river banks. However, so far, only a few studies have been conducted such a search for studying tsunami signals in incised valley systems along the Mediterranean coasts although the tsunami hazard is high. The island of Crete is known to have been affected several times by strong tsunamis, e.g., by the AD 365 and the Late Bronze Age (LBA) Santorini tsunami. The narrow Geropotamos River valley, distinctly incised into local bedrock and located at the northern coast of Crete and fully exposed to the Cretan Sea, was selected as a promising natural setting to search for palaeotsunami signatures in fluvial sedimentary archives. Based on a multi-electrode geoelectrical survey and a set of sediment cores, we investigated the event-geochronostratigraphic record of both the Geropotamos River mouth area and the river valley ca. 1 km upstream by means of sedimentological, geochemical, geochronological, geomorphological and micropalaeontological methods. The sedimentary environment towards the present-day river mouth is dominated by (fluvio-)lagoonal muds since the mid-Holocene. These lagoonal sediments are intersected successively by six coarse-grained sand layers each representing an extreme wave event (EWE). EWE layers are up to several decimetres thick and are characterized by an allochthonous foraminiferal assemblage comprising shallow marine to open marine species. Also ca. 1 km further upstream, the sedimentary record revealed grain size and microfossil evidence of two high-energy events showing a clear marine imprint. Based on this, we suggest inundation from the seaside that reached minimum 1 km inland and left EWE signatures in a presently inactive external bank position of the Geropotamos River. Considering the sedimentary characteristics, the local wind and wave climate of the Cretan Sea and the overall geomorphological setting, we interpret these EWE layers as tsunami-related. A major hiatus identified in the Geropotamos River mouth sediments seems to be related to the LBA Santorini tsunami as can be inferred based on local age-depth relations. The LBA tsunami is known to have severely hit the northern coast of Crete. However, the hiatus may also reflect changes in the subsidence rate and the local accommodation space architecture. The youngest EWE signal in the Geropotamos River archive appears to have been caused by the AD 365 tsunami event. Candidate deposits for both tsunami deposits were identified ca. 1 km further inland. Evidence of EWE impact documents channelling and acceleration effects of intruding water masses caused by the narrow and steeply incised Geropotamos River valley in an upstream direction. Further geochronological studies based on OSL dating are necessary for a reliable age control of these EWE candidate layers.

This section is based on Werner et al. 2019, submitted in Zeitschrift für Geomorphologie.

## 4.1 Introduction

The Greek island of Crete has been affected by numerous major tsunami events during historical and pre-historical times (e.g., Kelletat 1991; Pirazzoli et al. 1992; Stiros 2001; Shaw et al. 2008; Bruins et al. 2008). Crete is exposed to the Hellenic subduction zone in the south (Libyan Sea) and in the west (Ionian Sea) as well as to the Aegean volcanic arc and the Cretan Sea in the north. The Hellenic subduction zone has generated strong earthquakes, for example in AD 365 and AD 1303. Both earthquakes generated catastrophic supra-regional tsunamis that hit Crete's coasts as documented by geological evidence (Pirazzoli et al. 1992; Papadopoulos et al. 2007; Scheffers & Scheffers 2007; Bruins et al. 2008; Boulton & Whitworth 2017; Werner et al. 2018a, 2018b).

Also during the Late Bronze Age (LBA), one of the largest volcanic eruptions in the Mediterranean took place on the Santorini (Thera) volcano. The eruption generated a tsunami that impacted the northern coast of Crete (Bruins et al. 2008; Werner et al. 2018b). These examples underline the high tsunami risk for the island. Tsunami events similar to the AD 365-type magnitude along the entire Hellenic subduction zone are supposed to reach a recurrence interval of 800 years (Shaw et al. 2008). Today, coastal areas of the Mediterranean are densely populated. Therefore, studying traces of palaeotsunami events is important to understand their impact on the Holocene coastal evolution and helps to assess the impact of possible future tsunami events.

Palaeotsunami traces in the Mediterranean have been identified as high-energy signatures in various types of sedimentary archives. First, sheets of translocated marine sands were found in near-coast silt-dominated lagoons or freshwater lakes (e.g., Aliki Lagoon, Greece: Kontopoulos & Avramidis et al. 2003; Voulkaria Lake, Greece: Vött et al. 2009b; Thermaikos Gulf, Greece: Reicherter et al. 2010), locally associated with geomorphological forms of washover fans (Gargano coast, Italy: Gianfreda et al. 2001) or chevrons in case of high flow velocities and negligible influence of backflow erosion (e.g., Lefkada Lagoon, Greece: May et al. 2012; Gialova Lagoon, Greece: Willershäuser et al. 2015). Second, sheets of translocated marine sands are embedded in peat units deposited in paralic swamps (e.g., Cefalonia Island, Greece: Willershäuser et al. 2013; Evrotas River delta, Greece: Ntageretzis et al. 2015a). Third, mixed sedimentary units out of allochthonous and autochthonous material were identified in ancient harbour areas and corresponding deposits (e.g., Byzantine harbour of Yenikapı, Turkey: Bony et al. 2012; ancient harbour of Corinth, Greece: Hadler et al. 2013, Vött et al. 2018a; ancient harbour of Phalasarna, Greece: Pirazzoli et al. 1992; ancient harbour of Corfu, Greece: Finkler et al. 2018a, 2018b). Fourth, mixed, poorly sorted geoarchaeological units were identified as tsunami-related sediments deposited in archaeological contexts on land (e.g., Palaikastro, Greece: Bruins et al. 2008; Palairos/Pogonia, Greece: Vött et al. 2011a). Fifth, beachrock-type calcarenite in coast or near-coast positions turned out to have been deposited within the course of tsunami landfall and the sediments have been subject to post-depositional cementation (e.g., ancient harbour of Olympia at Pheia, Greece: Vött et al. 2011b; ancient harbour of Kyllini, Greece: Hadler et al. 2015; ancient harbour of Corinth and in the Diolkos area, Greece: Hadler et al. 2013). Finally, high-energy coarse-grained tsunami layers out of allochthonous material were also encountered in offshore sub-littoral and marine environments where they were entrained

by local backwash currents (e.g., Caesarea, Israel: Goodman-Tchernov et al. 2009, Tyuleneva et al. 2018; Augusta Bay, Italy: De Martini et al. 2010; Smedile et al. 2011; Mediterranean megaturbidite: Polonia et al. 2013).

However, despite this large variety of different tsunami traces, only few studies have been conducted so far in narrow, deeply incised valley systems, as for example at the Boca do Rio estuary, Portugal (e.g., Hindson et al. 1996 and Font et al. 2010 and references therein), although these valley systems are known to represent priority regions with regard to the maximum landward intrusion of tsunami waves. The latter was painfully experienced during the Indian Ocean 2004 and the Japan 2011 tsunami events (Adityawan et al. 2012; Tanaka et al. 2012, 2014; Tolkova & Tanaka 2016). In the Mediterranean, Ntageretzis et al. (2015b) detected palaeotsunami evidence in a valley to the northwest of Neapoli Vion, Vatika Bay (Greece) incised into older lithified Pleistocene fans and marine terraces. The inundation line was found to reach at least 400 m inland and Ntageretzis et al. (2015b) assumed funnelling and acceleration effects of the intruding tsunami waters. More recent observations from the Tōhoku-oki tsunami in 2011 documented that tsunamis following rivers and channels caused massive damage deep inland and are an important tsunami risk evaluation factor (Tanaka et al. 2014).

Focusing on the northern coast of Crete, the narrow and deeply incised Geropotamos River valley – facing the open Cretan Sea – was selected as a promising natural setting to search for palaeotsunami signatures in fluvial sedimentary archives. The main objectives of our study were

(i) to search for extreme wave event (EWE) traces in the Geropotamos River sedimentary archives,

(ii) to analyse EWE candidate deposits by using a multi-proxy geomorphological and sedimentological approach,

(iii) to reconstruct potential EWE impacts and their flow dynamics in interaction with the Geropotamos River valley and finally

(iv) to compare the Geropotamos EWE signatures with signatures known from other coastal sites in search of supra-regional impacts along the northern coasts of Crete.

## 4.2 Geography and tectonic setting

### 4.2.1 Tectonic setting

Crete is located in close proximity to the Hellenic subduction zone. Here, the African plate is being subducted with 35-40 mm/y on average (McClusky et al. 2000; Reilinger et al. 2006; Hollenstein et al. 2008) beneath the Aegean microplate. A compressive accretionary wedge, the Mediterranean Ridge, has been developed above the subduction interface (McKenzie 1972; Le Pichon & Angelier 1979; Doutsos & Kokkalas 2001, Shaw & Jackson 2010). After Shaw & Jackson (2010), splay faults located in the accretionary wedge control the growth of Crete's topography by uplifting the overriding Aegean microplate. Within the last 13 million years, subduction and associated coseismic processes caused a cumulative uplift of Crete of approximately 2-3 km (McKenzie 1978; Meulenkamp et al. 1994; Jolivet et al. 1996). The central Iraklion ridge emerged first some 4 million years ago and the outer island parts followed ca. 1 million years later (Shaw & Jackson 2010). Studies by Tiberti et al. (2014) showed that in western Crete this net uplift includes periods of both uplift and subsidence.

Induced by the rollback effect of the subduction zone and its movement towards the south, a back-arc basin with an average water depth of 1000 m has been formed to the north of Crete (Angelier et al. 1982; McKenzie 1972; Doutsos & Kokkalas 2001; Reilinger et al. 2006; Seidel et al. 2007; Royden & Papanikolaou 2011). The Hellenic subduction interface dips northwards at 10° to 15° whereas the subducted slab reaches depths of 35 to 45 km beneath Crete and several hundreds of kilometres beneath the central Aegean (e.g., Bohnhoff et al. 2001; van Hinsbergen et al. 2005; Hollenstein et al. 2008). A well-defined Benioff seismic zone reaches a maximum depth of 200 km and ends underneath the volcanic back-arc of the Cyclades including the still active Colombo-complex near Santorini and Milos (Le Pichon & Angelier 1979; Hollenstein et al. 2008).

During Miocene, crustal extension of the overriding Aegean microplate started and lead to a fragmentation of Crete into fault-bounded blocks creating a horst-and-graben structure (Angelier et al. 1982; Peterek & Schwarze 2004; Seidel et al. 2007; Caputo et al. 2010, Mason et al. 2016). The extensional faulting along the Hellenic Trench is accompanied by frequent shallow earthquakes whereas deeper earthquakes are triggered by the descent of the underlying plate subject to subduction (Taymaz et al. 1990; Papazachos & Papazachou 1997).

During history, Crete was hit by several catastrophic seismic events such as the prominent tsunamigenic earthquake that occurred on 21 July AD 365. This earthquake was triggered by a N-E dipping reverse fault located within the overriding plate in the south of Crete (Shaw et al. 2008; Lorito et al. 2008; Flouri et al. 2013) and reached an estimated magnitude of Mw = 8.3 (Stiros 2001; Shaw et al. 2008; Shaw & Jackson 2010). During this earthquake, the western and southwestern parts of Crete experienced coseismic crust uplift of up to 9 m (Fig. 4.1). Today, the pre-AD 365 sea level stand is still visible as well preserved bio-erosive markers and algal rims along the coasts of western Crete (e.g., Spratt 1865; Pirazzoli et al. 1982, 1996; Shaw et al. 2008; Mouslopoulou et al. 2015a). Another strong earthquake (ca.

Mw = 8.0) took place on 8 August AD 1303 and ruptured the eastern part of the Hellenic Arc between Crete and Rhodes (Papadopoulos et al. 2007). Based on several historical documents, an associated tsunami reached Crete's northeastern coast and struck the capital city of Heraklion (Papadopoulos et al. 2007, 2014). During the last century, the strongest tsunamigenic earthquake was generated at a 40 km-long active fault in 1956 offshore Armorgos Island and reached a magnitude of Mw = 7.5 (Nomikou et al. 2018). A detailed overview of all known historical and prehistorical tsunami records in the Mediterranean are listed in earthquake and tsunami catalogues (e.g., Galanopoulos 1960; Papadopoulos & Chalkis 1984; Tinti 1991; Guidoboni et al. 1994; Soloviev et al. 2000; Ambraseys 2009; Hadler et al. 2012; Papadopoulos et al. 2014).


**Fig. 4.1:** Overview of the lower course of the Geropotamos River and the river mouth area into the Cretan Sea (A). Detail maps of the Geropotamos River mouth area (B) and the inactive external bank further inland (C) show locations of vibracoring sites and ERT transects. Isolines in inset map of Crete depict amount of coseismic uplift associated with AD 365 earthquake in meters (after Kelletat 1991; Shaw et al. 2008). Maps based on Google Earth 2017.

### 4.2.2 Geographical setting of the study area

The study area is located at the north coast of Crete in the lower course of the Geropotamos River. The study area is located between the cities of Rethymnon in the west and Heraklion in the east near the villages of Lavris and Panormos (Figs. 4.1, A–C and Fig. 4.2). This region was unaffected by the coseismic uplift of the AD 365 earthquake (Fig. 4.1A; KELLETAT 1991) The Geropotamos River reaches a length of 47 km and its catchment area amounts to 40 km$^2$ (SDAO et al. 2012). In the lower course of the river (Fig. 4.2), the valley meanders are deeply incised into limestones and dolomites of the Tripolitza unit (Jurassic-Eocene limestones overlying the Tyros or Ravdoucha beds comprising Permo-Triassic shales, phyllites and quartzites) as well as into overthrusted Phyllite-Quarzites including the Arna unit (IGMR 1977; PAPANIKOLAOU & VASSILAKIS 2010). Deeply incised river beds in general indicate increased fluvial erosional processes induced by uplifting land masses or low sea levels. The study area is further characterized by major NW-SE/NNW-SSE running faults (IGMR 1977) which seem to be responsible for the overall flow direction of the Geropotamos River. Another fault system trends towards SW-NE.

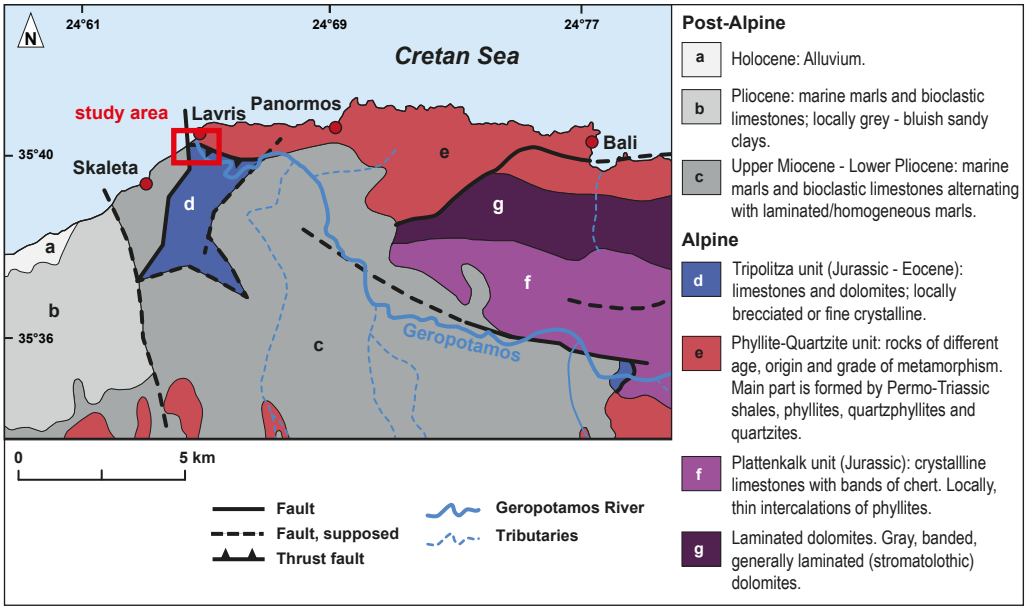


**Fig. 4.2:** Geological map of the Geropotamos River study area, northern Crete, showing geotectonic units. Red box marks location of the study area. Map adapted from IGMR 1977, PAPANIKOLAOU & VASSILAKIS 2010.

Studies in the Geropotamos River valley were conducted in two different areas. First, at the immediate river mouth on top of a pronounced beach ridge and associated washover fans, reaching up to 100 m inland. Second, in an area located ca. 1 km upstream in a former external bank position of the Geropotamos River. This undercut slope is presently inactive and lies today at an elevation of ca. 6 m above sea level (m a.s.l.) and approximately 110 m distant from the present river course. The latter runs at an elevation of ca. 3 m a.s.l. Geomorphological and geophysical investigations were carried out at the slope of the southern

valley flank, exposed to the northwest and out of reach of present fluvial processes. Between the two study sites, the valley floor is only 100 m to 250 m wide.

## 4.3 Material and methods

### 4.3.1 Field work

Geophysical prospection was carried out using electrical resistivity tomography (ERT) in order to pre-examine the bedrock topography and main stratigraphic structures of the near-surface underground. We used a multi-electrode Syscal R1 switch 48 device (type Iris Instruments) with a Wenner-Schlumberger electrode array. Measured data were inverted into depth sections using the RES2DINV software (Geotomo Software). Local stratigraphic data were obtained based on vibracores that were also used to calibrate the results of the ERT measurements. Vibracores were drilled with a closed auger system using a Cobra Pro handheld coring device (type Atlas Copco) and plastic inliners (50 mm in diameter). Vibracore GER 3A was also drilled with an open auger system and was used for microfossil sampling (GER 3). Position and elevation data of ERT electrodes and vibracoring sites were measured with a differential GPS (Topcon Hiper Pro FC-250), reaching a minimum horizontal and vertical precision of 2 cm.

### 4.3.2 Laboratory analyses

In total, ten meters of sediment-filled plastic inliners were cut into halves in the geolaboratory of the Johannes Gutenberg-Universität Mainz, Germany. The core halves were cleaned, photographically documented and analysed. Selected sediment samples (GER 3A: 37 samples; GER 4A: 71 samples) were retrieved from representative stratigraphic units for further sedimentological analyses. Samples for micropalaeontological studies were retrieved from vibracore GER 3, the open drilled version of vibracore GER 3A.

Grain size analyses of sediment samples were conducted using the sieve and pipette method after Köhn (Köhn 1929; DIN/EN ISO 11277 2002). Standard pre-treatment included dry-sieving in order to determine the amount of coarse particles with diameter > 2 mm, followed by twelve hour-peptisation of the fraction <2 mm in sodium pyrophosphate. Percentages of eight grain size classes (clay: < 2 µm, fine silt: 2–6.3 µm, medium silt: 6.3–20 µm, coarse silt: 20–63 µm, finest fine sand: 63–125 µm, fine sand: 125–200 µm, medium sand: 200–630 µm, coarse sand: 630–2000 µm) were determined. Based on a 99-step cosine interpolation function over the grain size classes, (mean) relative frequency distribution curves as well as cumulative frequency curves were calculated for each sample.

The geochemical element composition of sediments (in total 32 elements) was analysed using a portable Niton XL3t 900 S GOLDD XRF handheld analyser (calibration mode SOIL) in vertical steps of 2 cm along the entire cores. The results of the portable XRF (PXRF) technique are semi-quantitative and commonly used to identify trends and changes in geochemical composition between different sediment units (Chagué-Goff 2010; Vött et al. 2011a;

Chagué-Goff et al. 2017; Finkler et al. 2018b; Judd et al. 2017). We used the calcium (Ca)/iron (Fe) ratio in order to differentiate between marine and terrestrial depositional conditions and abrupt environmental changes. Increased iron contents are often associated with terrestrial weathering processes; on the contrary, increased calcium contents are associated with marine input in terms of biogenic marine carbonate, such as marine micro- and macrofauna shells (Vött et al. 2011a, 2015; Chagué-Goff et al. 2014, 2017). However, it is necessary to consider the influence of carbonate bedrock material and anthropogenic effects that may influence these signals (Vött et al. 2015).

A spectrophotometer (Konica Minolta CM-600 d) was used to quantify sediment colour based on the chromaticity values a* and b* of the CIELAB colour space (L*a*b*) with measurements every 2 cm. The variables a* and b* specify the portion of red (+a*) and green (–a*) and yellow (+b*) and blue (–b*) of the overall sediment colour. The sediment colour can be used as an additional tool to discriminate between sedimentary facies, for example to differentiate between sediments accumulated under oxic or anoxic conditions or to highlight differences in the organic content. The magnetic susceptibility of sediments, the content of diamagnetic and magnetic materials of the sediment, was measured in 1 cm steps using a Bartington MS2K surface sensor.

The microfossil content of selected sediment samples (GER 3/3A: 21 samples; GER 4A: 57 samples) was analysed using a semi-quantitative approach in order to reconstruct palaeoenvironmental changes and to differentiate between autochthonous and allochthonous deposits. As preparation for the microfossil analyses, 15 ml of each sample were first sieved in different fractions (> 400 µm, 400–200 µm, 200–125 µm and < 125 µm) and then analysed with the help of a stereomicroscope (Nikon SMZ 745T). Genera and, if possible, species of foraminifera tests were determined after Cimerman & Langer (1991), Murray (2006) and Rönnfeld (2008). In some cases, foraminifera tests were strongly calcified and worn and the species was not determinable. Z-series photos of foraminifera specimens were taken with a light-polarizing microscope (Nikon Eclipse 50i POL with Digital Sight DS-FI2 digital camera).

Six samples underwent $^{14}C$ AMS radiocarbon analysis for geochronological information. We only used plant remains for dating and refrained from choosing marine fossils because of the marine reservoir effects, whose species-specific influence in space and time is still unknown (for further details see discussion Vött et al. 2018a, 2018b). Conventional radiocarbon ages were calibrated using the calibration software Calib Rev 7.10 and the Marine13 and IntCal13 datasets (Reimer et al. 2013).

## 4.4 Results

### 4.4.1 Geropotamos River mouth area

**Pre-coring ERT survey**. We carried out three ERT transects in the river mouth area (Fig. 4.3) for a pre-coring exploration of the near-surface underground. The location and the course of the ERT transects is shown in Fig. 4.1 B. All ERT depth sections were converted to the same scale comprising electrical resistivity values from 1 (dark blue) to > 220 Ωm (purple). Additionally, the ERT depth sections include the position of vibracoring site GER 4A and the related stratigraphy. In general, high resistivity values reflect coarse-grained sand and gravel, partly (very) dry above groundwater level, or bedrock. Low resistivity values indicate fine-grained material, mostly silt and clay and/or water saturated sediments.

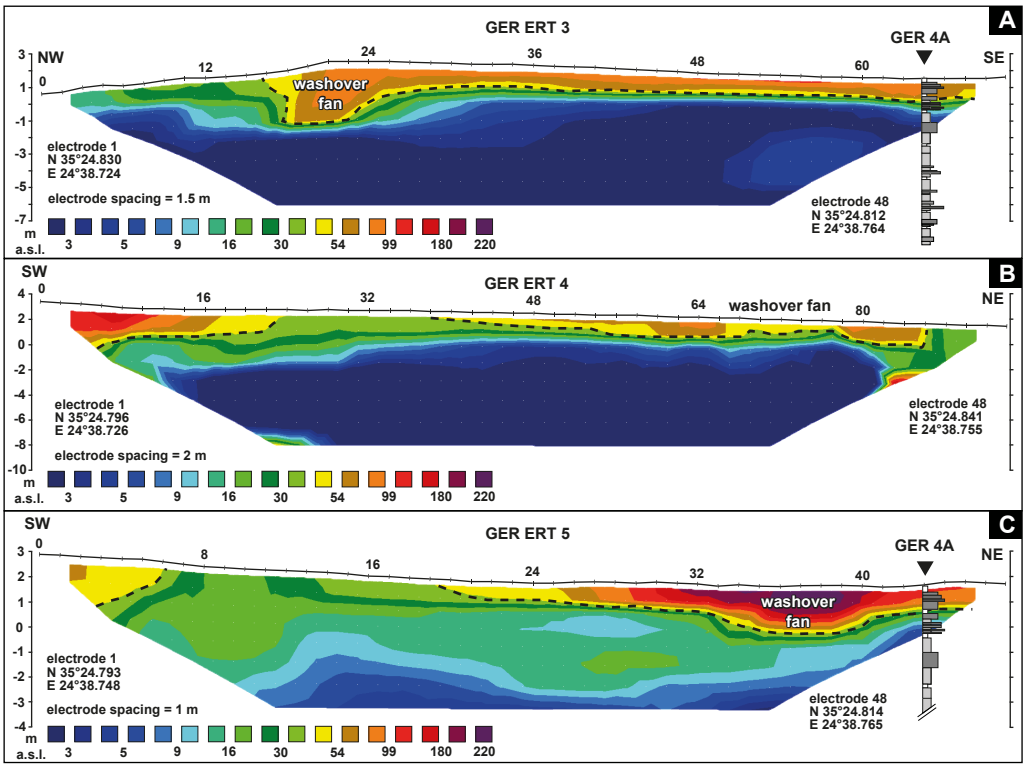


**Fig. 4.3:** ERT depth sections realized within the frame of geophysical prospection in the Geropotamos River mouth area. See text and Fig. 4.1 for further explanation.

ERT transect GER ERT 3 starts at the present shore and runs in a NW-SE direction across the beach ridge to the distal end of a recent washover fan. ERT transects GER ERT 4 and 5 run perpendicular to the flow direction of the Geropotamos River, namely where the beach reaches its highest elevations and in a distal position of the washover fan, respectively. Depth sections GER ERT 3 and 4 show a two-part horizontal composition with (very) low resistivity values (mostly < 5 Ωm) in the lower part reaching up to ca. 0 m a.s.l. and higher

resistivity values at the top (> 42 Ωm). The depth section GER ERT 5 shows a similar composition as transects GER ERT 3 and 4, but with higher electrical resistivity values in the western end of the transect. Furthermore, the depth section of GER ERT 5 shows high to very high values (42 to > 220 Ωm) in the top zone, which appears somewhat incised into the underlying part with lower resistivity values.

**Multi-proxy analysis of vibracore GER 4A**. Vibracore GER 4A was drilled ca. 80 m inland at an elevation of 1.60 m a.s.l. behind the present beach ridge and on top of a washover fan (Figs. 4.1 B and 4.3). The vibracoring site is situated 43 m from the beginning of transect GER ERT 5 and is situated quite in the middle of the entrance of the deeply incised Geropotamos River valley in the east. To the north of the coring site GER 4A, the Geropotamos River discharges into the Cretan Sea. We used a closed auger drill system and reached a maximum coring depth of 10 m below surface (m b.s.). To classify the stratigraphic record of GER 4A, we differentiate between five stratigraphic units inferred from sedimentological criteria namely grain size, sediment colour and macrofossil content (Tab. 4.1).

**Tab. 4.1:** Stratigraphic units found for vibracores GER 4A and GER 3A based on grain size data, sediment colour and macrofossil content.

| | Sediment character | | |
|---|---|---|---|
| **Unit** | **Grain size** | **Colour** | **Macrofossil content** |
| I | clay and silt, partly with higher sand content | dark grey to light grey | |
| II | fine and medium sand | grey to light grey-beige (GER 4A), red-brown (GER 3A) | marine shell fragments |
| III | coarse sand to (fine) gravel | grey to beige (GER 4A), red-brown to multicoloured (GER 3A) | marine shell fragments |
| IV | clay and silt | reddish-beige and gray parts | |
| V | medium and coarse sand | reddish-beige to reddish-dark grey | marine shell fragments |
| VI | silt and fine sand, partly higher sand content | greyish-brown | |
| VII | clay and silt, slate and glimmer fragments | brownish-red | |
| VIII | clay and silt, roots | dark brown | |

The stratigraphic record of vibracore GER 4A (Fig. 4.4 and Tab. 4.1) from 10.00 to 2.10 m b.s. (–8.4 m b.s.l. to 0.50 m a.s.l.; b.s.l. = below sea level) is dominated by clay and silt, greyish and brownish in colour (units I and IV), that partly contain a higher sand content. These fine-grained deposits are intersected by six distinct layers, namely from 9.78 to 9.52 m b.s. (–8.18 to –7.92 m b.s.l.), 8.80 to 8.46 m b.s. (–7.20 to –6.86 m b.s.l.), 7.54 to 7.36 m b.s. (–5.94 to –5.76 m b.s.l.), 6.81 to 6.73 m b.s. (–5.21 to –5.13 m b.s.l.), 5.66 to 5.52 m b.s. (–4.06 to –3.92 m b.s.l.) and 5.34 to 5.25 m b.s. (–3.74 to –3.65 m b.s.l.) by predominantly greyish to light-greyish fine and medium sand (unit II). Each intersecting layer shows a sharp erosional contact to the underlying deposits and visible marine shell fragments.

Two layers of greyish-beige coarse sand and (fine) gravel (unit III) intersect the dominant clay and silt sequence from 7.82 to 7.66 m b.s. (–6.22 to –6.06 m b.s.l.) and from 6.71 to 6.66 m b.s. (–5.11 to –5.06 m b.s.l.). At 3.26 to 2.65 m b.s. (–1.66 to –1.05 m b.s.l.) reddish-

beige coloured medium and coarse sand with marine shell fragments disrupt the clay and silt sequence in the upper part of the vibracore (unit V). Following a loss of sediment, we found an alternating layering of deposits of units III, IV and V from 1.90 to 1.35 m b.s. (–0.30 b.s.l. to 0.25 m a.s.l.). This section is covered by a massive layer out of well-sorted reddish-brown medium and coarse sand (unit V) that reaches up to the present-day's surface. Between 0.60 m b.s. and 0.36 m b.s. (1.00 to 1.24 m a.s.l.), it is intersected by coarse-grained sand and gravel deposits of unit III.

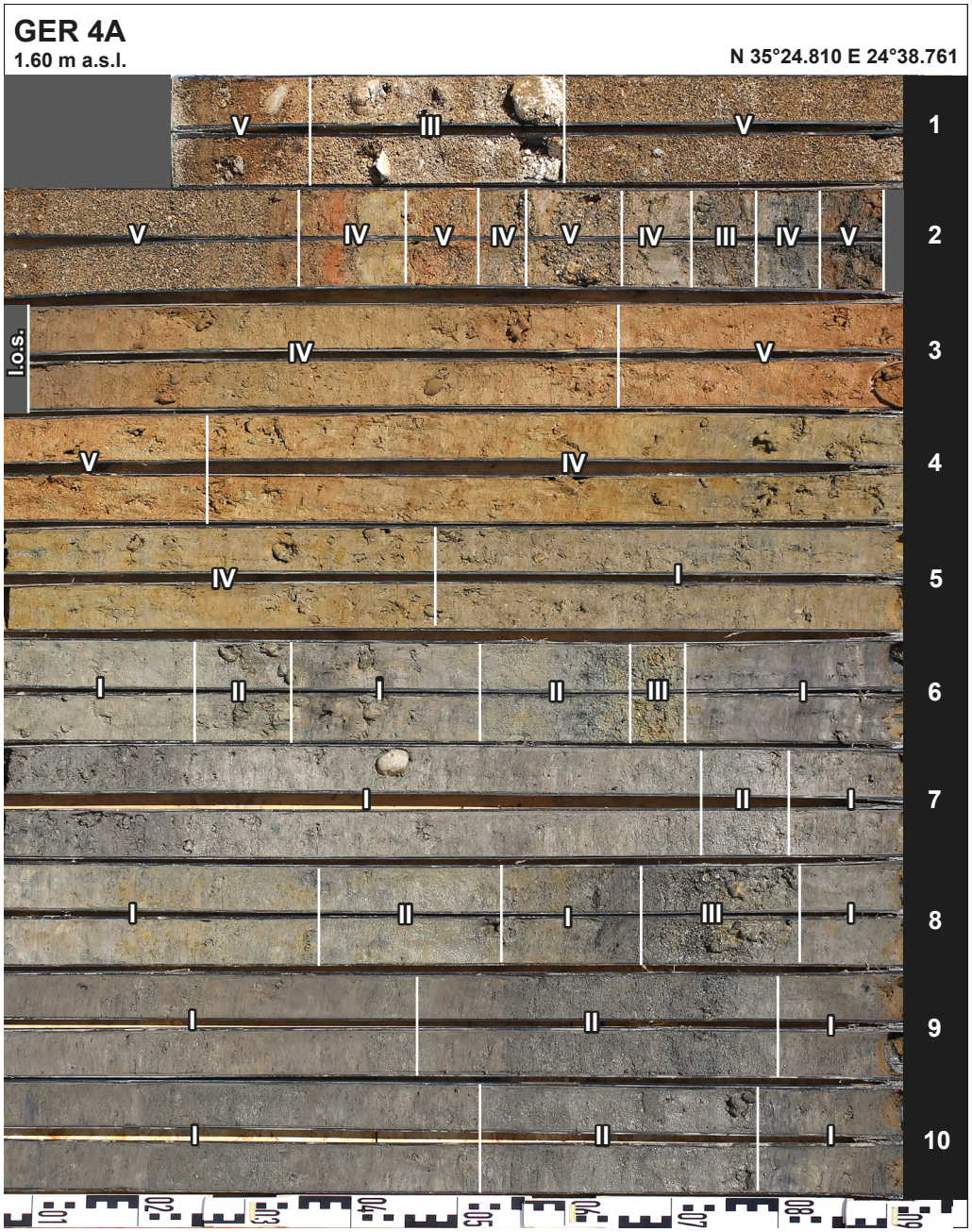


**Fig. 4.4:** Photo of sediment core GER 4A drilled in the Geropotamos River mouth area, ca. 80 m distant from the present-day shoreline. Sedimentary units I to V are based on grain size, colour and macrofossil content. See text and Tab. 4.1 for explanation.

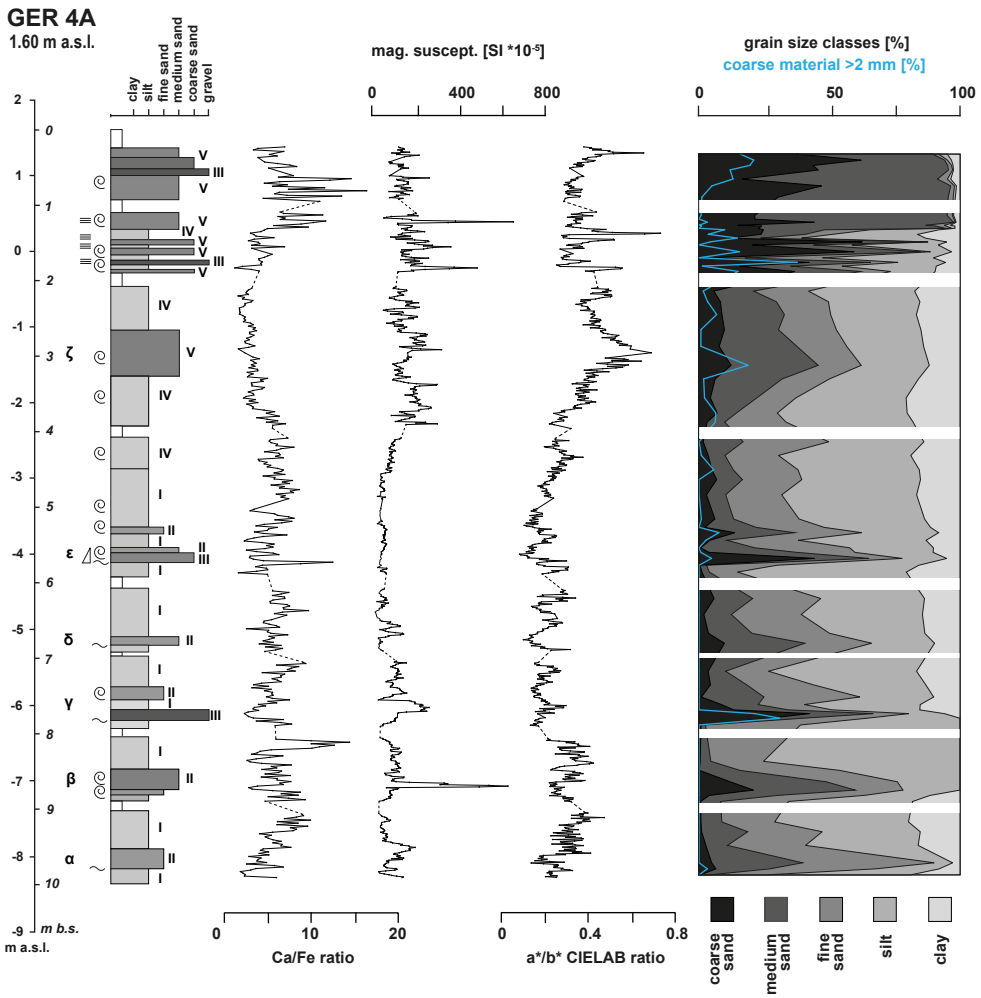


**Fig. 4.5:** Stratigraphic log of vibracore GER 4A compared with selected palaeoenvironmental proxies. Cumulative grain size data refer to fine sediment < 2 mm (sum = 100 %) and coarse sediment >2 mm (blue line; percentage referred to total mass of sample).

The stratigraphic record of vibracore GER 4A is shown in Fig. 4.5 together with selected sedimentary and geochemical parameters. The Ca/Fe log shows maximum values for coarse-grained units (III, IV and V), indicating an increased input of Ca in the upper section of the vibracore. On the contrary, coarse-grained units found in the lower core section show positive as well as negative peaks and a general trend is not discernible. Maximum magnetic susceptibility values and some secondary peaks are associated with coarse-grained layers (units II and III) in the lower core section, but do not show a general trend. With beginning of unit IV up to present-day's surface, the magnetic susceptibility increases and shows higher values on average than in the rest of the core. The a*/b* CIELAB colour ratio traces the transition from greyish to reddish-brown deposits at ca. 3.7 m b.s. (–2.1 m b.s.l.). Three peaks indicate the increase of reddish-brown colours in the upper core section. The results of the grain size analyses neatly reflect the stratigraphic structure of the core. Each coarse-grained unit (II, III and V) shows an increasing percentage of sand (subdivided in coarse sand, medium sand and fine sand). Coarse components with diameters > 2 mm were found

for units II and III of the lower core; from ca. 1.90 m b.s.(–0.3 m b.s.l.) upwards, the percentage of coarse-grained deposits, especially the percentage of coarse and medium sand and components with diameters > 2 mm strongly increases.

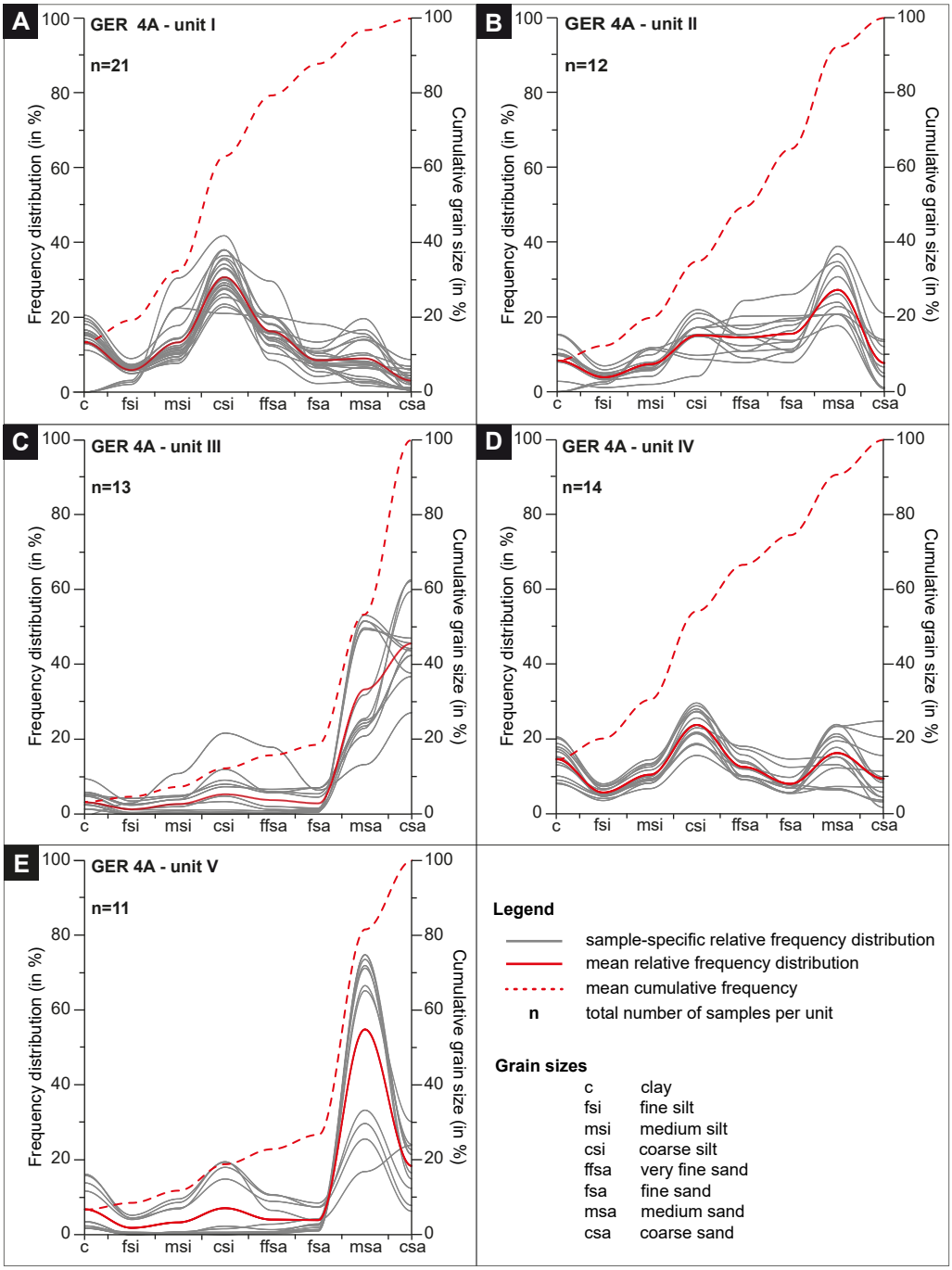


**Fig. 4.6:** Relative frequency distribution curves of grain size data obtained for sediment samples from vibracore GER 4A classified by stratigraphic units I to V. See Tab. 4.1 and text for further explanation.

The mean relative frequency distribution and the mean cumulative frequency of sample-specific grain sizes for each sedimentological unit are depicted in Fig. 4.6. Units I and IV are dominated by coarse silt and clay. In some samples of unit I and most samples of unit IV there is also a maximum for medium sand, resulting in an overall moderate grade of sorting. In contrast, samples from units II, III and V show a clear maximum in the sand fraction and are predominantly characterised by medium sand (units II and V) and medium to coarse sand (unit III). However, the mean relative frequency distribution of units II, III and V shows several secondary maxima, indicating a poor sorting of the deposits.

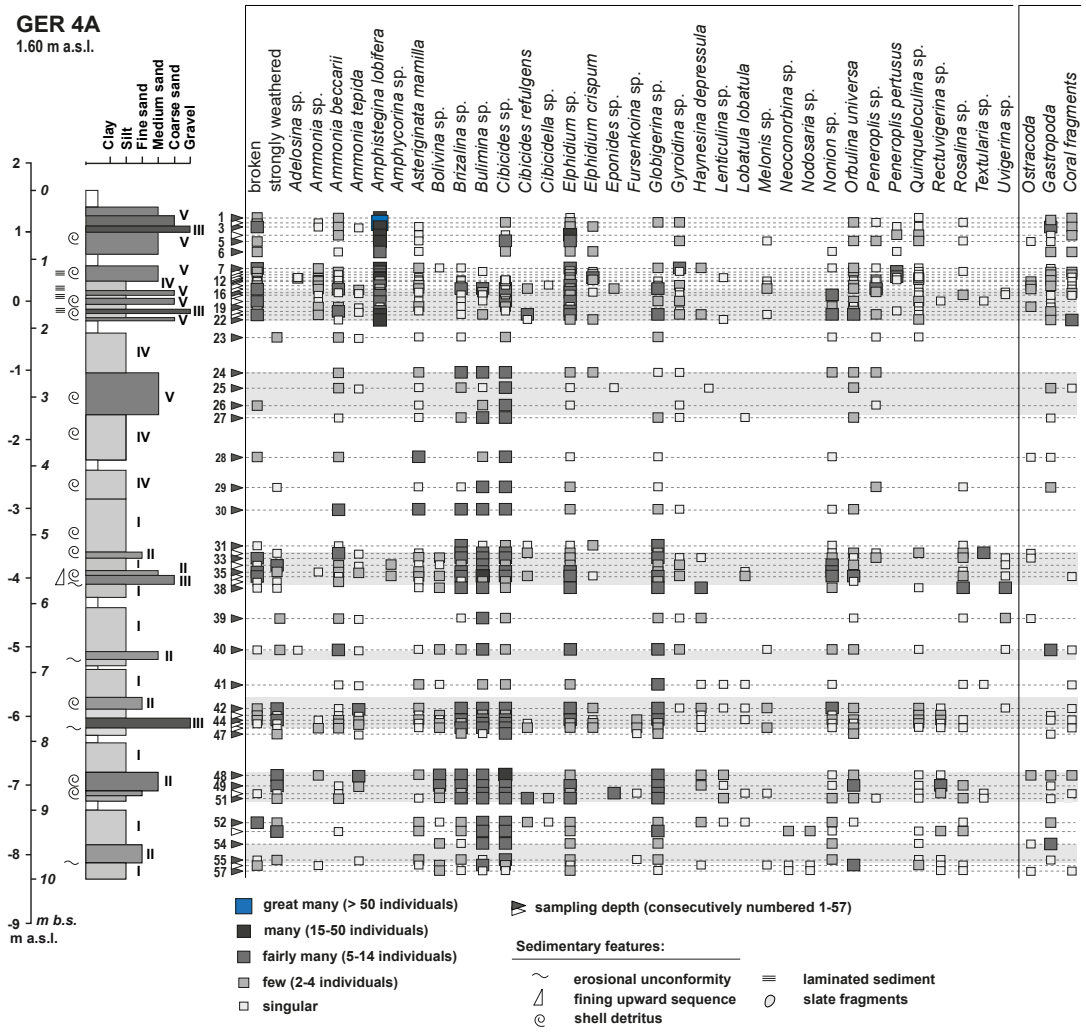


**Fig. 4.7:** Semi-quantitative results of microfossil analysis of sediment samples from vibracore GER 4A. Triangles near scale bar indicate sampling depth of individual samples. Triangles are numbered consecutively from top to base (1 to 57). I to V indicate stratigraphic units. See text, Fig. 4.4 and Tab. 4.1 for further explanation.

The semi-quantitative evaluation of the microfossil content is depicted in Fig. 4.7. Studied samples (black and white triangles to the right of the vibracore log) are consecutively numbered from top to base. A selection of foraminifera species and other microfossils found

typical of vibracore GER 4A is shown in Fig. 4.8. Concerning the abundance and the diversity of foraminifera species, the vibracore shows a three-part division. The lower part of the core generally shows a high abundance and high diversity of found foraminifera species. In the middle part, approximately starting with the appearance of unit IV, abundance and diversity are relatively lowest but increase again towards the top. Maximum abundance and maximum diversity of foraminifera genera is rather associated with coarse-grained sedimentary units (units II, III and V) than with fine-grained deposits (units I and IV). The foraminiferal assemblage of unit I includes species, such as *Ammonia beccarii*, *Ammonia tepida*, *Haynesina depressula* and several ostracods that are associated with brackish habitats, as for example those of lagoons.

The existence of foraminifera that prefer shallow marine habitats, for example *Asteriginata mamilla*, *Nonion* sp. and *Rosalina* sp., indicate constant influence of saltwater. Several shallow marine to fully marine (cold marine) species almost exclusively occur in units II, III and V, namely *Cibicides refulgens*, *Cibicidella* sp., *Elphidium crispum*, *Fursenkonia* sp., *Lobatula lobatula*, *Quinqueloculina* sp. and *Uvigerina* sp. Additionally, coral fragments can be predominantly found in these units. Other foraminifera species such as *Bulimina* sp., *Cibicides* sp. and *Globigerina* sp. occur as a kind of background noise, showing no specific change in abundance. Specimens of *Amphistegina lobifera* were only found in top-core position. They occur for the first time in sample 22 at 1.20 m b.s. (0.40 m a.s.l.).

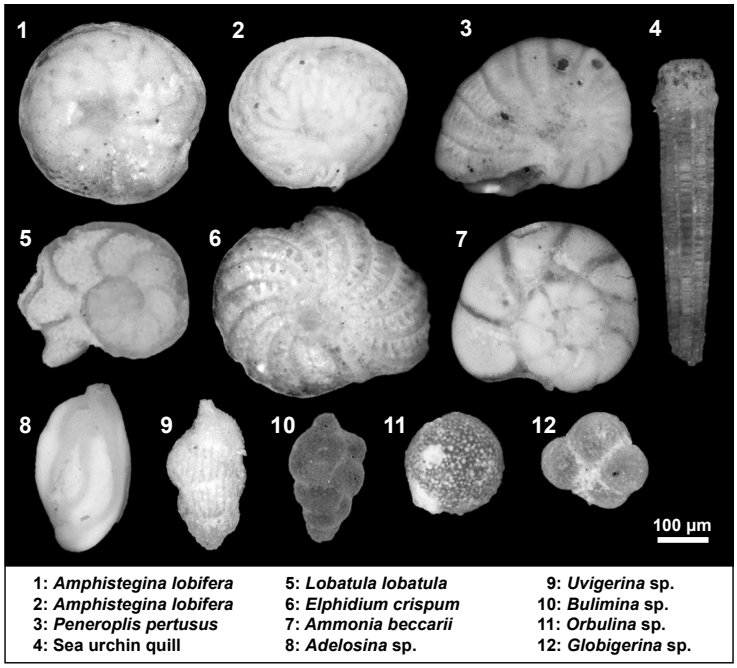


**Fig. 4.8:** Scanning electron microscope photos of selected foraminifera specimens and other microfossils found in samples from vibracore GER 4A.

### 4.4.2 Geropotamos River valley area further inland

**Pre-coring ERT survey.** The depth sections GER ERT 1 and GER ERT 2 of the geophysical exploration realized ca. 1 km further inland from the river mouth are depicted in Fig. 4.9. (A and B) ERT depth sections were converted to the same scale comprising electrical resistivity values from 1 Ωm (dark blue) to > 230 Ωm (purple). Both transects start near the present river bed and run in a NW-SE direction across the inactive undercut slope of the Geropotamos River (see Fig. 4.1 C). They show a more or less two-part horizontal composition with little resistivity values in the lower part (1 to ca. 50 Ωm), speaking for moderate- to fine-grained deposits. In contrast, the upper part is characterised by maximum electrical resistivity values (> 50 Ωm) probably associated with coarse-grained deposits. Moreover, the southeastern part of depth section GER ERT 1 is characterised by another zone of higher resistivity values below the present sea level, most probably representing a distinct zone of coarse-grained sediments.

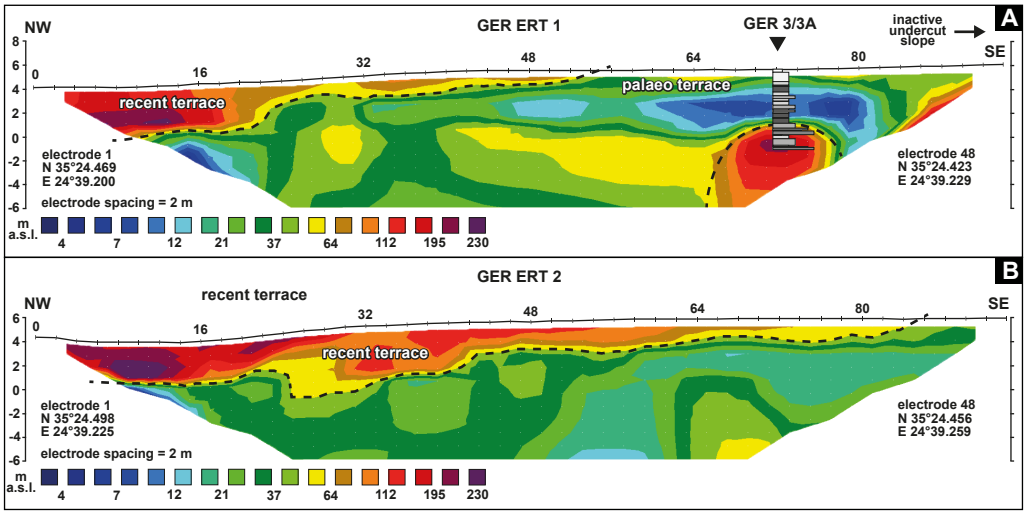


**Fig. 4.9:** ERT depth sections realized within the frame of geophysical prospection in the environs of an inactive external bank of the Geropotamos River further inland. See text and Fig. 4.1 for further explanations.

**Multi-proxy analyses of vibracore GER 3A.** Vibracoring site GER 3A is located ca. 1 km distant from the present-day shoreline, at 72 m of transect GER ERT 1 (Fig. 4.1). Vibracore GER 3A, drilled at 5.66 m a.s.l. on a former external bank of the Geropotamos River, reached a maximum drilling depth of 5 m b.s. (0.66 m a.s.l.). Its stratigraphic record can be divided into five stratigraphic units (Fig. 4.10, Tab. 4.1) inferred from grain size data, sediment colour and visible macrofossil content. The core is predominantly characterised by alternating beige and grey sediment layers consisting of sand and gravel (units II and III) and of clay, silt and fine sand (units VI, VII and VIII). Between 3.36 and 2.72 m b.s. (2.30 to 2.94 m a.s.l.) and between 1.41 and 1.18 m b.s. (4.25 to 4.48 m a.s.l.), clayey and silty deposits include multiple slate and other crystalline bedrock fragments and show a reddish-brown colour (Fig. 4.11).

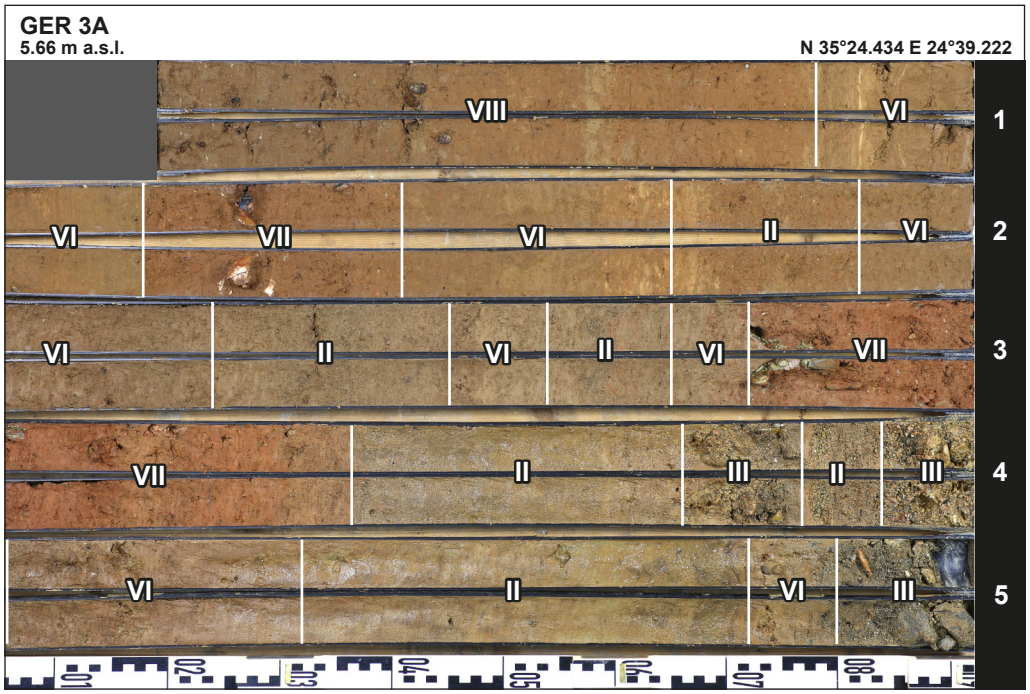


**Fig. 4.10:** Photo of sediment core GER 3A drilled on an inactive external bank of the Geropotamos River valley area ca. 1 km inland. Sedimentary units I to VIII are based on grain size, colour, and macrofossil content. See text and Tab. 4.1 for explanation.

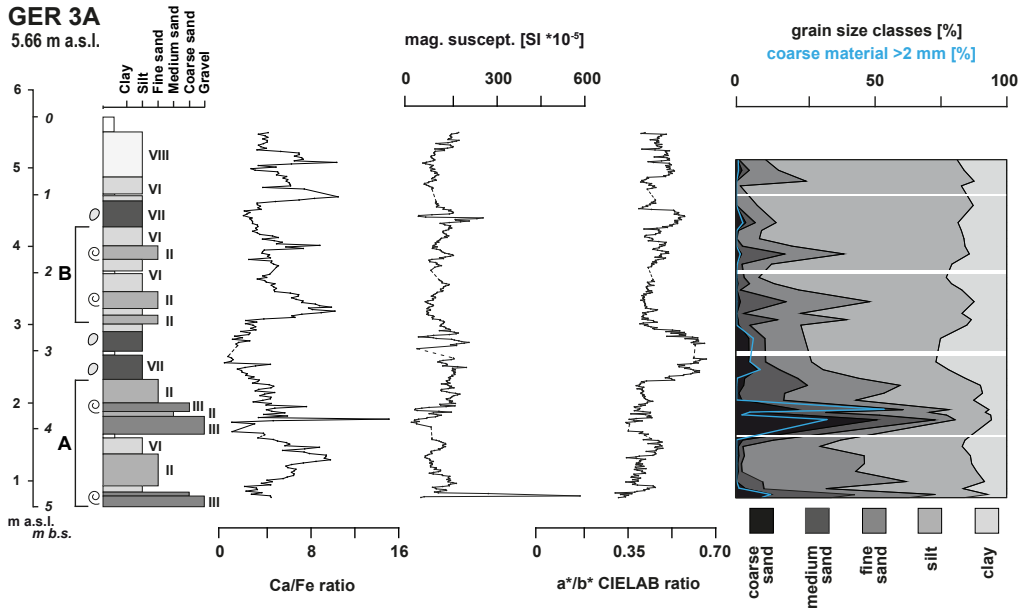


**Fig. 4.11:** Stratigraphic log of vibracore GER 3A compared with selected palaeoenvironmental proxies. Cumulative grain size data refer to fine sediment < 2 mm (sum = 100 %) and coarse sediment > 2 mm (blue line; percentage referred to total mass of sample).

Selected sedimentary and geochemical parameters are summarised in Fig. 4.11. The Ca/Fe ratio shows highest values predominantly associated with coarse-grained units II and III, except for top-core samples. On the contrary, the magnetic susceptibility values do not reveal

a specific trend. Highest values are related to unit III deposits in the lowermost part of the core. Two secondary peaks are associated with unit VII deposits. The colour spectroscopic analysis of GER 3A highlights unit VII sediments with their reddish-brown sediment colour: Between 3.36 and 2.72 m b.s. (2.30 to 2.94 m a.s.l.) and between 1.41 and 1.18 m b.s. (4.25 to 4.48 m a.s.l.), the increasing a*/b* CIELAB ratio shows higher values indicating higher contents of reddish-brown material.

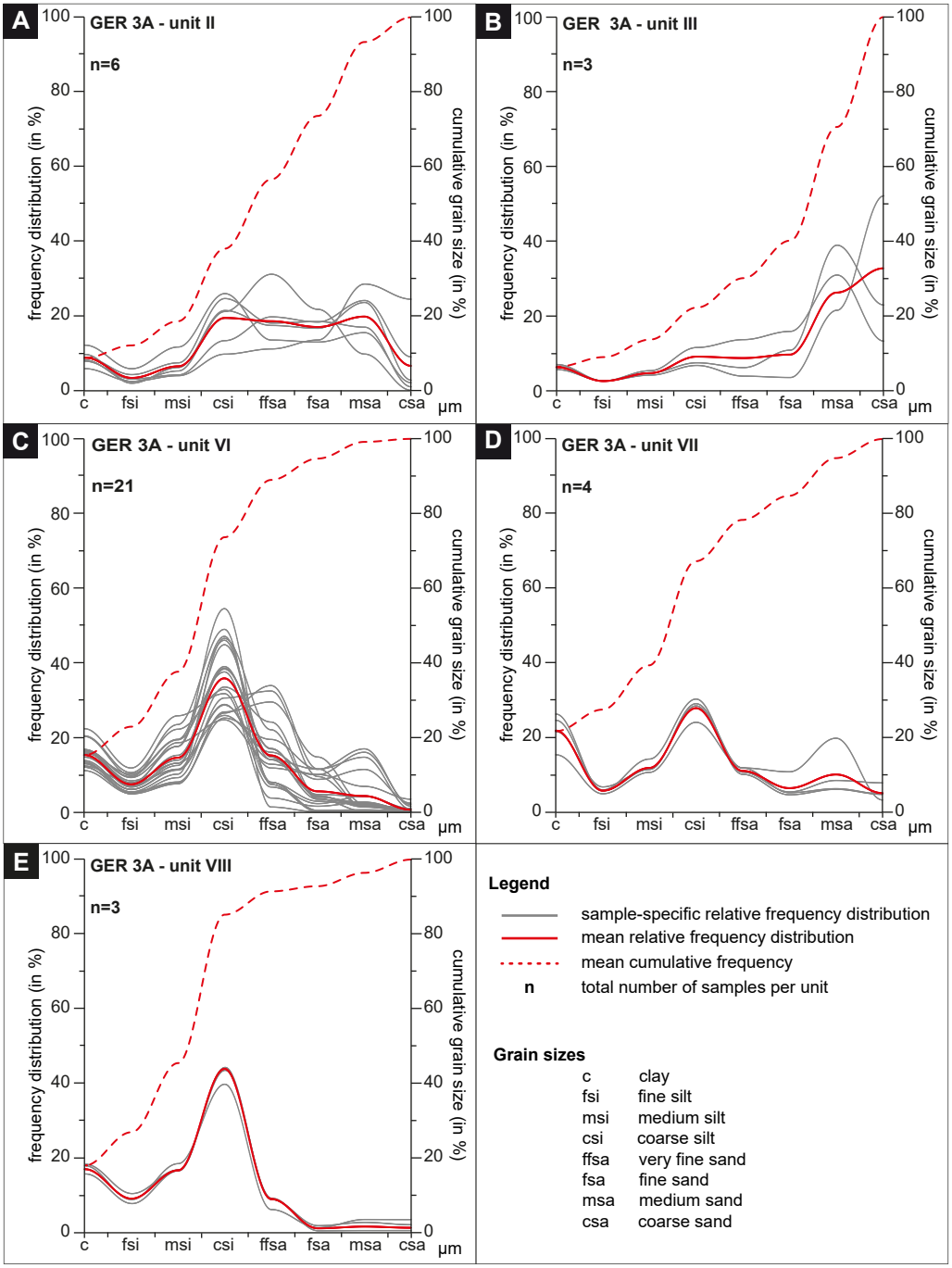


**Fig. 4.12:** Relative frequency distribution curves of grain size data obtained for sediment samples from vibracore GER 3A classified by stratigraphic units II to VIII. See Tab. 4.1 and text for further explanation.

Maximum sand amounts were found for units II and III , in particular coarse sand in units III, in the lower part of the sediment core. Maximum percentages of skeletal components are also associated with unit III deposit. In contrast, from 3.36 m b.s. (2.30 m a.s.l.) towards the present surface, silt and clay represent at least 50–75 % of all clasts. The Fig. 4.12 depicts mean relative frequency grain-size distribution curves for each unit. Sand-dominated unit II shows the poorest sorting of all units with an average of ca. 20 % for all grain sizes between coarse silt and medium sand. Unit III, only with a slightly better sorting, shows a maximum of coarse sand (30 %). Units VI and VIII contain up to 40 % coarse silt and show a secondary maximum for clay (ca. 15 %). Again, unit VII material is poorly sorted but reveals two maxima, namely in the clay and coarse silt fractions.

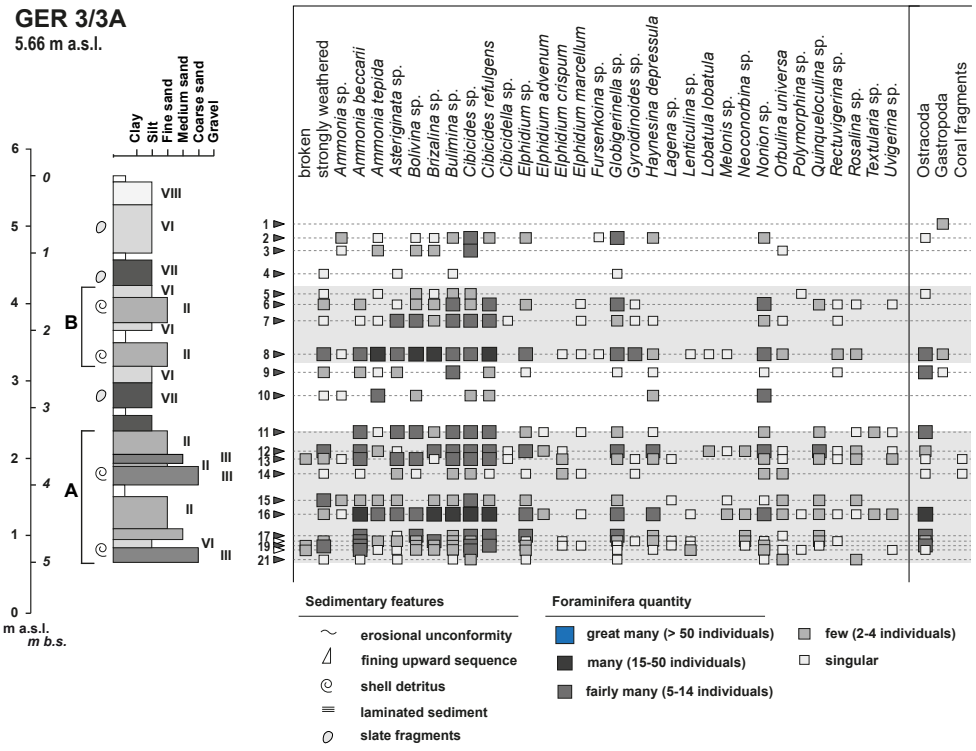


**Fig. 4.13:** Semi-quantitative results of microfossil analysis of sediment samples from vibracore GER 3A. Triangles near scale bar indicate sampling depth of individual samples. Triangles are numbered consecutively from top to base (1 to 21). II to VIII indicate stratigraphic units. See text, Fig. 4.6 and Tab. 4.1 for further explanation.

The semi-quantitative evaluation of the microfossil content is depicted in Fig. 4.13. Studied samples (black and white triangles on the right of the vibracore) are consecutively numbered. Selected foraminifera species and other microfossils typical of vibracore GER 3A are shown in Fig. 4.14. The microfossil content turned out to be unexpectedly high, including a noticeable amount of non-weathered foraminifera tests. Compared to units VI and VII, both the abundance and diversity of foraminifera species are much higher than in units II and III. Fairly many to great many specimens of *Ammonia* sp., *A. beccarii*, *A. tepida*, *Bolivina* sp., *Brizalina* sp., *Bulimina* sp., *Cibicides* sp. and *C. refulgens* were encountered in units VI and VII, while sediments of units II and III only contain a few of these species.

In contrast, specimens of *Elphidium* sp., *E. advenum*, *E. crispum*, *Globigerinella* sp., *Lagena* sp., *Lenticulina* sp., *Lobatula lobatula*, *Melonis* sp., *Neoconorbina* sp., *Rectuvigerina* sp., *Rosalina* sp., *Textularia* sp. and *Uvigerina* sp. are almost exclusively associated with sediments of sandy units II and III. Comparing the results of microfossil analyses in the two vibracores studied, the diversity of foraminifera in vibracore GER 3A is lower than the one found for vibracore GER 4A drilled in the river mouth area (Fig. 4.7). Especially those species (e.g., *Amphistegina lobifera*, *Peneroplis* sp. and *P. pertusus*) that predominantly occur in the upper part of vibracore GER 4A, starting at ca. 1.90 m b.s. (4.09 m a.s.l.) up to present surface, were not found in vibraore GER 3A.

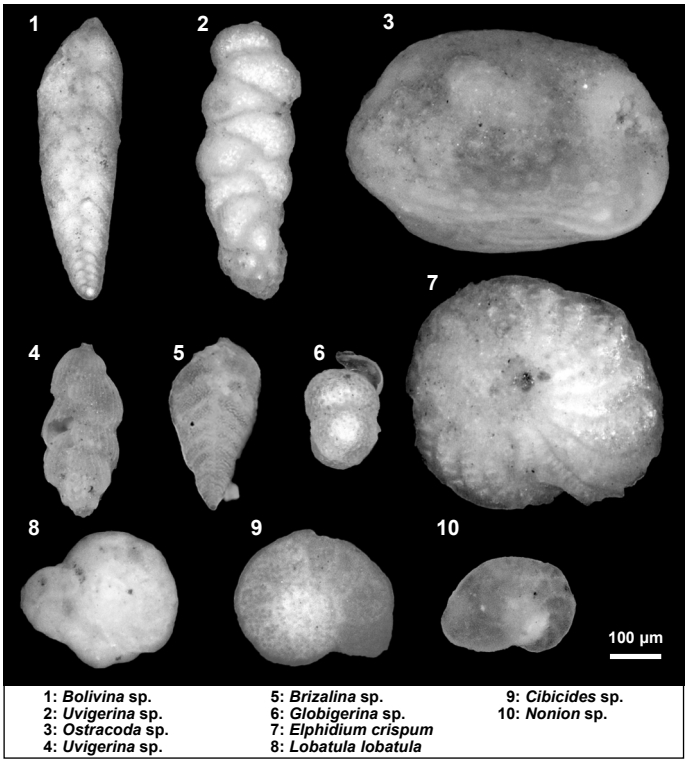


**Fig. 4.14:** Scanning electron microscope photos of selected foraminifera specimens and other microfossils found in samples from vibracore GER 3A.

### 4.4.3 Geochronology

Six samples were retrieved from vibracore GER 4A for 14C AMS radiocarbon dating in order to establish a local event-geochronology for the Geropotamos River study area. Five samples consisted of undetermined plant remains; one sample was made out of wood. Conventional radiocarbon ages were calibrated using the Calib 7.10 software. Radiocarbon dating results are summarised in Tab. 4.2. Sample GER 4A/50 PR 6.65 turned out to be pre-Holocene in age attesting strong reworking processes. Age-depth relations of dated samples from core GER 4A (and an age inferred by the first occurrence of *Amphistegina lobiferea*, an invasive foraminifera species) are depicted in Fig. 4.15 together with results of

similar investigations undertaken by Werner et al. (2018b) to the west of Rethymnon and by Lespez et al. (2003) near Malia.

**Tab. 4.2:** AMS Radiocarbon dating results of samples from vibracore GER 4A.

| Sample | Lab. No. (CEZ) | Depth (m b.s.) | Depth (m a.s.l.) | Sample description | $^{14}$C Age (BP) | $\delta^{13}$C (‰) | 1σ max; min (cal BC/AD) | 2σ max; min (cal BC/AD) |
|---|---|---|---|---|---|---|---|---|
| GER 4A/19 HR 2.23 | 26530 | 2.23 | –0.63 | wood remains | 93 ± 23 | –24.9 | 1696-1917 AD | 1691-1922 AD |
| GER 4A/33 PR 3.88 | 26533 | 3.88 | –2.28 | plant remains | 2660 ± 30 | –32.1 | 831-801 BC | 895-795 BC |
| GER 4A/42 PR 5.43 | 26465 | 5.43 | –3.83 | plant remains | 5199 ± 32 | –27.5 | 4039-3971 BC | 4050-3957 BC |
| GER 4A/50 PR 6.65 | 26466 | 6.65 | –5.05 | plant remains | 42330 ± 730 | –29.5 | 44311-43010 BC | 45123-42372 BC |
| GER 4A/55 PR 7.59 | 26467 | 7.59 | –5.99 | plant remains | 5554 ± 37 | –38.1 | 4446-4354 BC | 4455-4343 BC |
| GER 4A/71 PR 9.81 | 26468 | 9.81 | –8.21 | plant remains | 6633 ± 37 | –33.7 | 5619-5543 BC | 5627-5494 BC |

Note: Lab. No. – laboratory number, CEZ – Curt-Engelhorn-Zentrum für Archäometrie, Mannheim, Germany; b.s. – below ground surface; a.s.l. – above sea level; unit – stratigraphic unit; 1σ max; min (cal BC/AD) – calibrated ages, 1σ range; 2σ max; min (cal BC/AD) – calibrated ages, 2σ range. Calibration based on Calib Rev 7.1 with IntCal 13 dataset (Reimer et al. 2013).

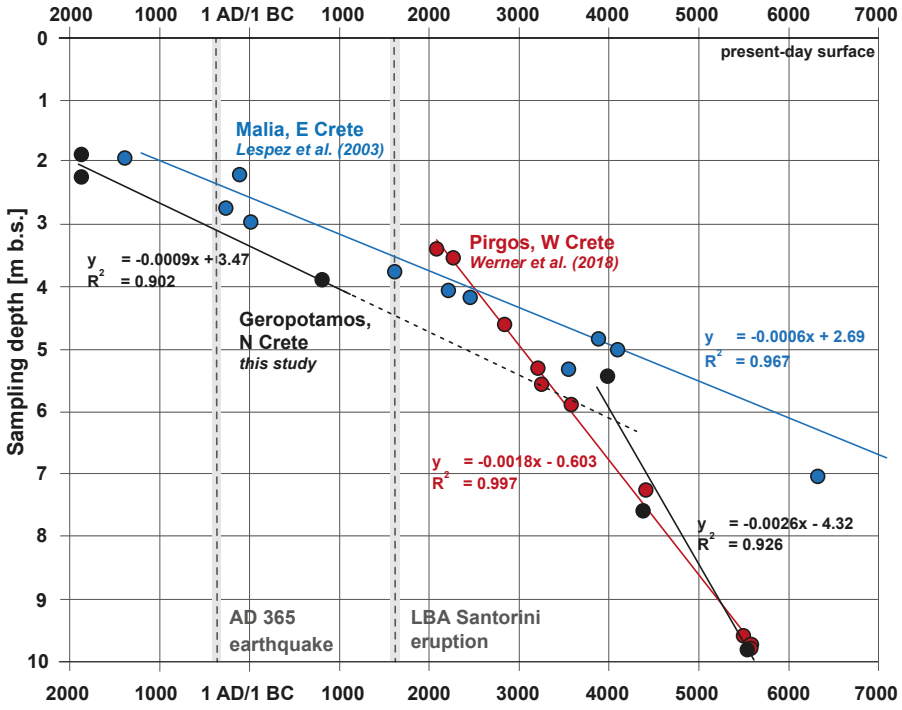


**Fig. 4.15:** Age-depth relations reconstructed for the Geropotamos River study site, northern Crete, (this study) compared to age-depth relations for the Pelekanos site near Pirgos, western Crete (Werner et al. 2018b), and Malia, eastern Crete (Lespez et al. 2003; radiocarbon data recalibrated). The vertical dashed lines depict the timeframe of the LBA Santorini (according to Friedrich et al. 2006: 1621–1605 cal BC, 1σ) and the AD 365 tsunami events. The Geropotamos River trend line shows a strong bend where the large hiatus in core GER 4A was found. See text and Fig. 4.16 for further explanations.

## 4.5 Discussion

### 4.5.1 Sedimentary facies and palaeoenvironmental evolution

Based on multi-proxy analyses results, we are able to discriminate between six sedimentary facies for the Geropotamos River study site (Fig. 4.16). These facies were used to reconstruct palaeoenvironmental changes at the Geropotamos River mouth area and a valley section further inland.

**The Geropotamos River mouth area**. The lower part of sediment core GER 4A is characterised by predominantly low-energy, fine-grained clay and silt (unit I). The mean frequency distribution revealed also a varying minor sand content. In general, the foraminifera abundance and diversity, aside from a high background signal of bedrock-related species (such as *Bolivina* sp., *Brizalina* sp., *Bulimina* sp., *Cibicides* sp. and *Globigerina* sp.; see Drinia et al. 2008) is not very high in unit I deposit. However, in comparison to other units, the foraminiferal assemblage of unit I shows an increased abundance of stress tolerating foraminifera species (e.g., *Ammonia tepida* or *Haynesina depressula*) that are typical inhabitants of brackish/lagoonal environments (Murray 2006; Avnaim-Katav et al. 2013). The foraminifera signature includes several tests of species preferring shallow marine habitats (*Ammonia beccarii*, *Elphidium* sp. and *Lenticulina* sp.), indicating a sporadic saltwater influence.

Considering the foraminiferal assemblage and the sedimentary characteristics, unit I deposits can be associated with a brackish, more or less sheltered, lagoonal depositional environment. Lagoonal conditions were most probably influenced by the Geropotamos River. It must be noted, that lagoonal deposits of unit I do not include many ostracods and embedded plant remains, as it was described for other lagoonal deposits found at the northern coast of Crete (Bottema & Sarpaki 2003; Werner et al. 2018b). This may be explained by the stronger fluvial influence in this study area.

Fine-grained sediments of unit IV show similar sedimentological and microfossil signals as described for unit I. The foraminiferal signature still gives evidence of a brackish environment with sporadic saltwater influence, however with a weaker signal. The reddish-brown sediment colour is most probably related to increased fluvial input of terrestrial material originating from the catchment area. Thus, unit IV can be associated with (fluvio-)lagoonal sediments similar to unit I but with an increased fluvial input.

At the present Geropotamos River mouth position, a long-existing (fluvio-)lagoon-type environment left a homogenous sequence that reaches up to 1.90 m b.s. (–0.30 m b.s.l.). Considering the Holocene sea level development, the position of the former coastline must have been situated further in the north of the study area. However, the (fluvio-)lagoonal sequence is interrupted by six sand-dominated intercalations, testifying to high-energy water inflow into a quiet-reach environment. Intercalated high-energy sand layers are characterised by a mixed foraminiferal assemblage with a strongly increased abundance of shallow marine to fully marine foraminifera species. Concerning their preferred habitats, the latter strongly differ from those species found in lagoonal muds. The input of poorly sorted allochthonous marine sand layers and the input of displaced and transported foraminifera

species indicate a high-energy turbulent water inflow from the sea side within the course of an extreme wave event (EWE). Because of the overall geomorphological setting and the position of the vibracoring site close to the present shore, it is difficult to clearly assign these layers to storm or tsunami influence — a subject that is later discussed in more detail. Nonetheless, EWE influence was of strictly temporary nature and, as shown by foraminiferal and grain size data, the pre-existing lagoonal environment completely recovered anytime soon after an EWE took place. In Fig. 4.16 the identified six EWE layers are labelled with Greek letters α to ζ from older to younger respectively.

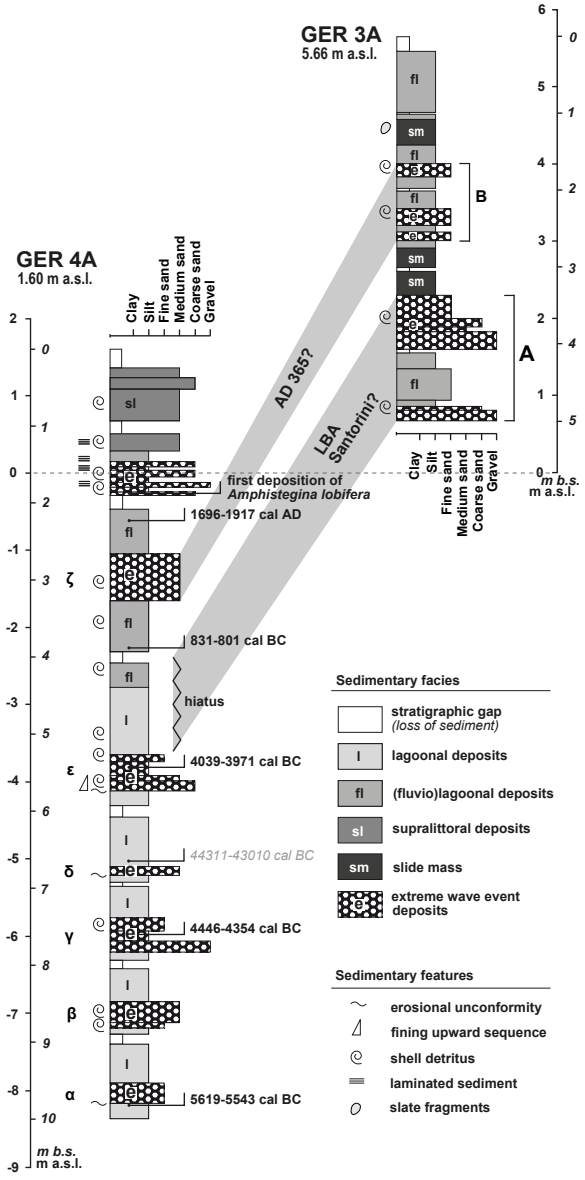


**Fig. 4.16:** Vibracore transect showing stratigraphic logs of sediment cores GER 4A and GER 3A. Extreme wave event (EWE) deposits identified in core GER 4A are labelled with Greek letters α to ζ. The uppermost littoral sequence is strongly affected by storm influence. Based on local age-depth relations (Fig. 4.15), the major hiatus in mid-core position of core GER 4A is suggested to represent the LBA Santorini tsunami event, and event ζ may reflect the AD 365 tsunami event. Candidate layers of the LBA Santorini and the AD 365 tsunamis were also found in core GER 3A drilled on an inactive external bank of the Geropotamos River ca. 1 km inland. For locations of vibracoring sites see Fig. 4.1, for radiocarbon ages see Tab. 4.2. See text and Fig. 4.15 for further explanations.

From 1.90 m b.s. (–0.30 m b.s.l.) to the present surface, a (supra-)littoral sequence follows, consisting almost exclusively of sand and showing an increased Ca/Fe ratio. Although the Ca/Fe ratio was successfully used as a proxy in coastal research in recent studies (for an overview see Chagué-Goff 2010; Chagué-Goff et al. 2017), there is no reliable trend for the river mouth area, except for the uppermost littoral sequence.

The littoral sequence is also characterised by detailed layering associated with all-day littoral dynamics, including sorting and layering of sediments (up to coarse sand) and multiple washover dynamics. Considering the geomorphological setting of vibracore GER 4A, drilled in the landward distal part of a washover fan ca. 50 m south of present-day's beach ridge, it may be speculated that these features are caused by storm influence from the Cretan Sea. The occurrence of *Amphistegina lobifera* at ca. 1.20 m b.s. (0.4 m a.s.l.), an alien species that reached the eastern Mediterranean by opening the Suez channel in AD 1869 (Trianta phyllou et al. 2009), may emphasise reworking processes of the littoral facies during the past 150 or so years.

Based on geochronological data (Fig. 4.16 and Tab. 4.2), we identified a major hiatus between sample GER 4A/33 at 3.88 m b.s. (–2.28 m b.s.l.) and sample GER 4A/42 at 5.43 m b.s. (–3.83 m a.s.l.). The lower part of the sediment core is mid-Holocene in age with high sedimentation rates similar to those found for a lagoonal environment investigated west of Rethymnon (see Werner et al. 2018b); in contrast, the upper part of the core documents the past 2000 or so years. The hiatus is documented in Fig. 4.15 (dashed black line) starting at a sharp bend in the composite age-depth-relation trend line (see section 4.5.5).

**Inactive external bank of Geropotamos River further inland.** In this study, we focus on the identification of the impact of potential EWE and their flow dynamics in interaction with the Geropotamos River valley. At the river mouth area, we detected a (fluvio-)lagoon-type sequence, that was repeatedly affected by marine EWE (α to ζ). In the following, we discuss the question, if one of the EWE has intruded into the Geropotamos River valley and left traces further upstream.

The sedimentary record of core GER 3A is, similar to core GER 4A, characterised by several coarse-grained high-energy layers (units II and III) showing a change in depositional energy in comparison to the over- and underlying fine-grained strata. Poorly sorted unit II and III deposits show a mixture of different grain-sizes varying from coarse silt to coarse sand and gravel. These layers are also related to an increased calcium content that may indicate increased input of biogenic marine carbonate such as marine micro- and macrofauna shells (Vött et al. 2015; Chagué-Goff 2010; Chagué-Goff et al. 2017); this is corroborated by the results of the microfossil analyses. In general, both abundance and diversity are unexpectedly high with regard to the inland position and overall geomorphological setting of the site. Compared to the over-and underlying strata, the high-energy sand layers show increased abundance and biodiversity of foraminifera.

Units II and III show similar marine characteristics as were found for EWE layers in GER 4A in the river mouth area. There are many foraminifera species found both in EWE candidate layers and unit II and III deposits with maximum abundance and diversity at the further landward site GER 3A (Figs. 4.7 and 4.13). However, from those species almost exclusively

restricted to EWE candidate layers at the river mouth, the following species were also exclusively found associated with unit II and III deposits: *Elphidium crispum*, *Quinqueloculina* sp., *Rosalina* sp. This may indicate a genetic correlation between EWE impact at the present river mouth and high-energy flow deposits ca. 1 km inland (Figs. 4.7 and 4.13).

However, because of the overall strong foraminiferal fingerprint in vibracore GER 3A, it is difficult to discriminate between marine foraminifera entrained by EWE and the microfossil signal originated from reworked local foraminifera-bearing bedrock sequences. Drinia et al. (2008) investigated benthic foraminifera assemblages in Pliocene marine deposits in the Ierapetra Basin, southeastern Crete, as a base to reconstruct sedimentary environments. This study yielded species such as *Bolivina* sp., *Cibicides* sp., *Lagena* sp., *Lenticulina* sp., *Textularia* sp. and *Uvigerina* sp. to be representative for Pliocene marine deposits. These species were also encountered in high numbers, often in good preservation conditions, in the high-energy sand layers of GER 3A.

However, we also found foraminifera species that are not described from Pliocene bedrock units (Drinia et al. 2008), such as *Ammonia* sp., *A. tepida*, *Elphidium crispum*, *Haynesina depressula*, *Quinqueloculina* sp. and *Rosalina* sp. All of them were found more or less exclusively, or with an increasing abundance, associated with EWE candidate layers of vibracore GER 4A at the present river mouth. Based on this assessment, we suppose that the foraminifera signatures along the Geropotamos River bear a strong bedrock signal consisting predominantly of Tertiary marine specimens. Nevertheless, it seems as if there are several species, such as *Ammonia beccarii*, *A. tepida* and *Haynesina depressula* that were encountered in the (fluvio-) lagoonal sequence found at the present river mouth and in unit I and II layers of GER 3A ca. 1 km inland in a presently inactive external bank position. So, the identification of marine high-energy sand layers and their foraminiferal assemblage may reveal a genetic correlation between EWE impact at the present river mouth area and ca. 1 km inland and may indicate Holocene marine flooding from the Cretan Sea. We therefore interpret unit II and III deposits of GER 3A as EWE candidate layers. The upper 1.2 m of vibracore GER 4A contain a high quantity of *Amphistegina lobifera*, but this species was not encountered in EWE candidate layers of GER 3A. Consequently, the EWE layers must have been deposited before AD 1869, when the alien species *Amphistegina lobifera* began settling Mediterranean environments due to the opening of the Suez Canal. Additionally, EWE candidate layers do not contain any typical foraminifera species from the littoral zone, such as *Peneroplis* sp. and *Peneroplis pertusus* which are often associated with carbonate-rich sandy beach sediments (Murray 2006; Avnaim-Katav et al. 2013) and were encountered in the upper part of vibracore GER 4A. This also suggests the deposition of EWE candidate layers before the development of the littoral sequence at the present river moth area took place.

Besides the high-energy marine sand layers, the stratigraphic record of GER 3A is dominated by fine-grained fluvial and colluvial deposits (unit VI). The two reddish-brown coloured clay- and silt-dominated unit VII layers are in strong contrast to the under- and overlying strata: The lower unit VII is several decimetres thick whereas the unit VII layer in the upper part of the core shows is slightly thinner; both layers are situated directly on top of an EWE candidate layer. Unit VII deposits are also characterized by high contents of slate and other crystalline bedrock material which make up the valley flanks right seaward of the vibraco-

ring site. Therefore, we interpret unit VII layers as slide mass material from the surrounding valley flanks. The upper unit VIII is subject to present weathering and soil forming processes.

With regard to the geomorphological background, the foraminiferal assemblage, grain size data and the overall setting of this study area, we interpret the stratigraphic record of vibracore GER 3A as holding the signature of two individual EWE layers from the seaside. The lower EWE layer comprises several unit II and III deposits, reflecting at least two wave pulses and ends up with deposits originating from a slide mass (unit VII). The upper EWE candidate also shows several subsections of unit II, supporting multiple pulses and ends up with a sequence of fluvial deposits and another subsequent slide mass.

### 4.5.2 Origin of the EWE layers

Searching for the potential origin of EWE layers in the Geropotamos River area, both extreme storm surges and tsunamis must be taken in account. Tsunamites and tempestites are, on a global scale, very similar in their sedimentological characteristics (e.g., Dominey-Howes et al. 2006; Bahlburg & Weiss 2007; Switzer & Jones 2008; Smedile et al. 2011; Rodríguez-Ramírez et al. 2016; Röbke & Vött 2017) and cannot be differentiated easily based on sedimentary features alone. The overall geographical constellation as well as the dominating wind and wave climate and local to regional tectonics have also to be taken into consideration. Especially in the Mediterranean, tsunamis and palaeotsunamis play an essential role in understanding Holocene coastal sedimentary records and are, in historical times for which numerous accounts on tsunamis exist, much more deadly and costly than storms; in contrast, high-magnitude storms play a subordinate role in the shaping of Mediterranean coastline. So far, the number of regional- and supra-regional-scale tsunamis known and identified by geological evidence is by far larger that the number of storms. The latter have mostly remained on a purely local level. For more details on the role of storms and tsunamis in the Mediterranean, see Vött et al. (2018a, 2018b).

In general, storm surges and tsunamis may be associated with the input of coarse-grained allochthonous sand and gravel in sheltered low-energy sediment environments such as lagoons, back beach swamps or harbour basins (Vött & May 2009; Vött et al. 2018a). In contrast to long-waved tsunamis, storm waves often leave thin-layered deposits and comprise nearshore material, for example beach and nearshore sands. In contrast, tsunami deposits may comprise a wide range of source material ranging from open marine, shelf, littoral and even terrestrial environments (Switzer & Jones 2008; Röbke & Vött 2017).

After the 2004 Indian Ocean tsunami and the 2011 Tōhoku-oki tsunami, numerous studies on tsunami deposits characterisation have been carried out (e.g., Bahlburg & Weiss 2007; Choowong et al. 2008; Goto et al. 2011; Richmond et al. 2012). Several depositional signatures such as a long distance landward transport of sediment often accompanied by a landward thinning were identified as typical of tsunami influence (Bahlburg & Weiss 2007; Richmond et al. 2012). Affected by different flow dynamics of the water masses during different stages of inundation and backflow (Choowong et al. 2008), tsunamites are often characterised by fining upward sequences of grain sizes, a broad spectrum of different grain

sizes, bi- or multi-modal deposits, rip-up clasts, basal erosional unconformities and poor sorting (e.g., Dominey-Howes 2004; Dominey-Howes et al. 2006; Bahlburg & Weiss 2007; Switzer & Jones 2008; Goto et al. 2011; Richmond et al. 2012; Röbke & Vött 2017). As a tool to identify the input of marine sediment, Chagué-Goff et al. 2017) applied geochemical analyses and successfully used calcium and strontium signals to identify tsunami signatures. Also the evaluation of the foraminiferal content has been used as a tool to indicate general palaeoenvironmental changes and to identify tsunami deposits (Dominey-Howes et al. 2006; Pilarczyk et al. 2014). Several studies on Mediterranean palaeotsunamis proved a mixed assemblage of foraminifera from different ecological habitats and preservation states to be characteristic for tsunami deposits (Reinhardt et al. 1994; Goodman et al. 2008; Hadler et al. 2013; Mathes-Schmidt et al. 2013; Fischer et al. 2016a; Finkler et al. 2018a, 2018b; Werner et al. 2018a, 2018b). However, tsunami-influenced foraminiferal assemblages differ from study site to study site and are strongly affected by local geomorphological and bathymetrical conditions. Best results of identifying tsunami influence are given by displaced and transported species, for example, open marine to shallow marine species found in protected lagoonal or marsh settings (Mamo et al. 2009; Pilarczyk et al. 2014).

In the Mediterranean, numerous palaeotsunamites have already been detected in different sedimentary archives, for example along the coasts of the Aegean, Ionian and Adriatic seas and along the northeastern and southwestern coasts of Crete (e.g., Pirazzoli et al. 1992; De Martini et al. 2003; Bruins et al. 2008; Vött et al. 2009a, 2009b, 2011a, 2011b, 2014, 2015; Reicherter et al. 2010; Kortekaas et al. 2011; Mastronuzzi & Sansò 2012; Koster et al. 2015; Willershäuser et al. 2015; Quintela et al. 2016; Werner et al. 2018a, 2018b).

Transferring the described signatures found typical of Mediterranean tsunami to the Geropotamos River mouth area, the following analogies can be found: EWE layers are poorly sorted, contain a broad spectrum of different grain sizes and shell fragments, show a fining upward sequence (layer ε), are bi- to multi-modal, contain a mixed foraminiferal signature and show erosional unconformities towards the underlying strata. However, the Ca/Fe ratio of sediments from the study area do not depict a clear allochthonous signal most probably due to masking effects by local bedrock units.

On the other hand, we also identified EWE layers in the sedimentary record of the landward Geropotamos valley study area. Here, they also appeared poorly sorted, contain a broad spectrum of different grain sizes as well as shell fragments, contain a strong foraminiferal bedrock signal but also fresh displaced marine species. Finally, EWE layer characteristics are in contrast to the over- and underlying strata. Considering the distance of more than 1 km to the present coast – the palaeoshore line was situated even further seaward than today (see above) – storms as origin for these EWE layers can certainly be excluded. Bound to high-frequency waves, Mediterranean storms do not produce water masses large enough to realize inundation distances that long. Present-day geomorphological survey in the neighbouring, funnel shaped Eko creek valley, located some 600 or so meters to the SW of the Geropotamos River mouth, have shown that storm-driven wooden debris and small cobbles were transported maximum 140 m inland during several storm events in 2014. These storm sediments were very thin-layered and patchy. For further discussion of the capacity of storms in the region see Soukissian et al. (2008), Alexandrakis et al. (2011),

Ayat (2013), Tsoukala et al. (2016) and Werner et al. (2018b). We conclude, that the geomorphodynamic potential of the EWE candidate layers found at site GER 3A is far beyond what storms can produce in the Cretan Sea and in the Mediterranean. Consequently, it can be inferred as a reverse conclusion that corresponding EWE layers at the river mouth are of tsunami-related origin as well.

### 4.5.3 Tsunami inundation along river valleys

Rivers usually serve as drainage for surface waters. However, river mouth areas along the coasts are also prone to tsunami penetration as was observed by recent tsunami events of 2004 and 2011 (Adityawan et al. 2012; Tanaka et al. 2012, 2014; Tolkova & Tanaka 2016). During the 2011 Tōhoko-oki tsunami, tsunami waves entered the Kitakami River and propagated up to 17 km inland causing widespread inundation along the riverbank (Tolkova & Tanaka 2016). Tsunami wave propagation along large rivers is characterised by reduced friction and waves maintain their energy far upstream and are able to cause massive landward damage (Tanaka et al. 2012).

The river mouth geometry and geomorphological features such as sand spits or jetties directly influence wave propagation distances (Adityawan et al. 2012; Tanaka et al. 2012). Other important factors are meanders, water depth, bottom friction and the river bed slope (Tanaka et al. 2012; Chanson & Lublin 2013). Based on laboratory experiments and a theoretical approach, Tsuji et al. (1991) suggested that the height of a tsunami in rivers may be amplified by a factor of 1.5. Furthermore, tsunami wave propagation in rivers was found to be associated with strong sediment mixing and massive input of terrestrial sediments (Chanson & Lublin 2013).

In the central part of the Gulf of Cadiz, Morales et al. (2008) identified five different tsunami layers in the sedimentary record of the Huelva Estuary that could be traced upstream over a distance of ten kilometres. Viana-Baptista et al. (2006) calculated tsunami propagation models along the Tagus Estuary of Lisbon, Portugal, that are consistent with geomorphological and sedimentological field evidence and underline the risk of tsunami propagation in rivers and estuaries. In Greece, studies carried out by Ntageretzis et al. (2015b) in a valley to the northwest of Neapoli Vion, Vatika Bay, found tsunami evidence up to at least 400 m inland. The valley, incised into older lithified Pleistocene fans and marine terraces, produced funnelling and acceleration effects that let tsunami water intrude far inland.

### 4.5.4 Reconstruction of Geropotamos valley flow dynamics

Considering tsunami-related flooding of the Geropotamos River valley is only realistic if the valley morphology is taken into account. As shown above, the latter may have a significant influence on the tsunami propagation upstream (Tanaka et al. 2012, 2014). The Geropotamos River mouth area is triangle-type, funnel-shaped, non-blocked and would have been able to catch large water masses of long-wave tsunami waters. The subsequent narrow and incised valley would then have strongly channelled and accelerated intruding water masses towards inland.

We further suppose that channelled water inflow produced strong undercut in outer/external bank positions. The GER 3A sedimentary record shows several sections of unit VII deposits, which are characterized by slate and other crystalline bedrock material which make up the valley flanks right seaward of the vibracoring site. We interpret these units as due to mass wasting triggered by strong undercut processes. It is furthermore striking that unit VII deposits were found directly on top of EWE candidate (units II) so that one might assume that tsunami landfall itself (rather than normal river dynamics) and following inland channelisation of waters is the major cause for these slide masses retrieved in core GER 3A.

### 4.5.5 Age-depth relations

The study area is located to the east of the region of Crete that is known to have experienced coseismic uplift during the AD 365 earthquake. In the frame of their study at Pirgos, located to the west of Rethymnon, Werner et al. (2018b) found sedimentary evidence of coseismic uplift in the range of 1.6 m during the AD 365 event. We compared age-depth trend lines achieved for selected sites along the north coast of Crete, namely the Pirgos site (Werner et al. 2018b), the area around Malia (Lespez et al. 2003) and the Geropotamos River study site (Fig. 4.15).

The older part of the trend line obtained for the Geropotamos River study is almost identical with the general trend line obtained for the Pelekanos site near Pirgos, west of Rethymnon. Starting with a strong bend through the large hiatus in core GER 4A somewhere between ca. 4 m and 5.20 m b.s., however, the trend line subsequently flattens and runs parallel to the line obtained for the Malia study site until more recent times. This general change in slope of the Geropotamos River trend line apparently indicates a change in the subsidence rate of the site (see above), in any case a considerable rise of the relative sea level.

However there are several possibilities to explain and date the hiatus itself. First, it may be speculated that the hiatus was caused by strong coseismic uplift at some point in time between the 5$^{th}$ and the 1$^{st}$ mill. BC by which considerably reduced the accommodation space. Second, erosive processes may have removed large parts of the sedimentary record. As we are in the distal part of the fluvial system, namely at the river mouth, relevant erosion by the river system itself seems rather improbable. However, one may consider erosion by tremendous EWE from the seaside, possibly by the tsunami waves in conjunction with the LBA Santorini eruption that hit the north coast of Crete (Lespez et al. 2003; Bruins et al. 2008; Werner et al. 2018b).

Based on the younger part of the Geropotamos River trend line, we approximated the depth where the sediments of the AD 365 earthquake and tsunami event can be expected as ca. 3 m b.s. (Fig. 4.15). This is exactly the depth where the sedimentary record of core GER 4A shows EWE-related coarse-grained unit V deposits (Figs. 4.5, 4.6, 4.7 and 4.15). We therefore hypothesize that EWE deposit ζ in core GER 4A is a candidate deposit of the AD 365 tsunami. Considering that the youngest tsunamites recorded in the Pirgos archive to west of Rethymnon are the LBA Santorini event and the AD 365 event (Werner et al. 2018b), we further hypothesize that the two major potential tsunamites A and B identified in core GER 3A may represent these two events (Fig. 4.16).

On this speculative base, A would thus be consistent with the LBA Santorini event deposit and B would be consistent with the AD 365 tsunamite. However, to further study this question, precise dating of the EWE deposits recovered from site GER 3A would be required. In this respect, the most promising approach is using OSL dating techniques.

Our evidence supports the suggestion, that the Geropotamos River mouth area is a good archive for mid-Holocene EWE events. For a period of minimum 1700 or so years from the midst of the 6th to the end of the 5th mill. BC, we found sedimentary and microfossil evidence of five EWE. In contrast, the Pirgos sedimentary archive (Werner et al. 2018b) has recorded three EWE for the time period between the midst of the 4th and the end of the 3rd mill. BC.

Finally, as already discussed above, we suggest that both the LBA Santorini and the AD 365 tsunami events are recorded in both study areas. Overall, the event history based on our analyses indicates 10 EWE, some of them clearly defined as tsunamis, during the past ca. 7500 years. This results in a statistical average recurrence interval of ca. 750 years for major EWE in this area. This is consistent with the assessment of Shaw et al. (2008) and Shaw (2012), who stated that tsunami events of the AD 365-type magnitude may occur every 800 years along the Hellenic subduction zone.

## 4.6 Conclusions

The Geropotamos River mouth sedimentary archive revealed specific signatures of repeated EWE influence since the mid-Holocene. The EWE signatures are coarse-grained, sand-dominated layers of few decimetres thickness with a shallow marine to marine foraminiferal background and intersect more or less homogeneous silt-dominated (fluvio-)lagoonal muds making up major parts of the local 10 m-long sedimentary record.

Based on grain size and microfossil evidence at least during some EWE events, inundation reached minimum 1 km inland, leaving EWE signatures in a presently inactive external bank position of the Geropotamos River and triggering mass failures.

Signatures reliably assigned to storm influence are restricted to the uppermost 1.9 m of the sedimentary record in the Geropotamos River mouth area, when the lagoonal environment had already stopped to exist and littoral processes have dominated the vibracoring site. Obviously, storm influence seems to be mostly restricted to the (supra-)littoral zone itself. The appearance of Amphistegina lobifera, an alien species that spread with the opening of the Suez Canal in AD 1869 through the Mediterranean basin, suggests a depositional period of ca. 150 years for the uppermost 1.20 m of the littoral facies.

We hypothesize that the major hiatus found in the Geropotamos River mouth archive may be related to erosional effects of the LBA Santorini tsunami known to have severely hit the north coast of Crete and/or may reflect changes in the subsidence rate and the local accommodation space architecture. The youngest EWE signal — based on specific age-depth relations — appears to have been caused by the AD 365 tsunami event. Candidate deposits

for both tsunami events were identified ca. 1 km further inland documenting channelling and acceleration effects of intruding water masses in the narrow and steeply incised Geropotamos River valley in an upstream direction. However, further geochronological studies based on OSL dating are required to render reliable age control for these deposits.

Together with the Pirgos sedimentary archive (Werner et al. 2018b), the Geropotamos River valley record revealed evidence of ten major EWE that hit the north coast of Crete during the past 7500 or so years leading to a statistical recurrence interval of ca. 750 years for large EWE impacts. This is consistent with statistical recurrence intervals for major tsunamis based on seismological studies (Shaw et al. 2008; Shaw 2012) and underlines the generally high tsunami hazard of the region.

# 5 Synthesis and conclusions

Multi-proxy geoscientific research including micropalaeontological, sedimentological and geophysical methods was carried out at three study sites located at the southwestern (Sougia and Palaiochora – Section 2) and at the northern coast (Pirgos – Section 3; Geropotamos – Section 4) of Crete in order to extend the knowledge of Holocene palaeotsunami history and coastal evolution. Site-specific results will be summarised and compared to each other in the following synoptic compilation focusing on the characterisation of the different geoarchives, characteristics of recorded extreme wave events (Section 5.1), Crete's Holocene tsunami event geochronostratigraphy (Section 5.2) and the Holocene coastal evolution affected by vertical crust movements (Section 5.3). Finally, a perspective for tsunami risk assessment on Crete and a conclusion is given in Sections 5.4 and 5.5.

## 5.1 Fine-sediment archives on Crete and characteristics of recorded extreme wave event deposits

Although Crete's southwestern coast was strongly influenced by the coseismic uplift of the AD 365 earthquake where erosion took away most of the fine sediment, we found excellent archives at Sougia and Palaiochora. The Sougia study site comprised a fine-sedimentary record, at least ten meters thick. In contrast, before the AD 365 uplift took place, the Palaiochora peninsular was submerged and characterised by (sub-)littoral processes. Here, the detected geoarchive revealed a four-meter-long Holocene sedimentary record. Since the AD 365 earthquake and coseismic uplift, both archives were strongly exposed to weathering processes resulting in negative preservation states of foraminifera species.

At the northern coast of Crete, the Pirgos study site revealed a thick Holocene lagoonal sequence comprising at least eleven meters of sediment. Lower uplift rates of the AD 365 earthquake caused weaker post-erosional and weathering processes. To the east of the city of Rethymnon, coseismic uplift associated with the AD 365 earthquake tends toward nil (Pirazzoli et al. 1982; Kelletat 1991; Stiros 2001) and the Geropotamos study site was not affected at all. Here, a thick Holocene near-coast sedimentary record was found at the river mouth, comprising at least ten meters of sediment.

The sedimentary record of the three study sites was analysed using a wide-range of multi-proxy methods in order to detect extreme wave event deposits on Crete. In the Mediterranean, numerous palaeotsunamites were already identified (e.g., Pirazzoli et al. 1992; De Martini et al. 2003; Bruins et al. 2008; Vött et al. 2009, 2011a, 2011b, 2014, 2015, 2018a, 2018b, 2019; Kortekaas et al. 2011; Mastronuzzi & Sansò 2012; Koster et al. 2015; Willershäuser et al. 2015; Quintela et al. 2016). Comparing the described signatures found to be typical of Mediterranean tsunamites with the detected tsunami-related EWE deposits on Crete, the following analogies were found:

- Allochthone marine sand layers with a bi-modal grain-size distribution.
- Erosional contact to the underlying strata.
- Fining upward sequences of grain-sizes and in parts lamination trends.
- Partly cemented as beachrock type.
- A mixed foraminiferal assemblage comprising species and genera from different habitats and preservation states.
- Marine macrofauna and shell debris.
- Major differences in the over- and underlying strata.
- Maximum Ca/Fe ratio, but with strong influence of local carbonate bedrock material.

However, sedimentary, geochemical and microfaunal evidence of tsunami deposits strongly depend on local geomorphological and bathymetric conditions and therefore differ among the study sites. For example, the former near-coast lagoon at Pirgos was most probably protected by a sand spit or a barrier island providing large amounts of sand that were transported and dislocated by tsunami inflow. So, the found EWE layer within the Pirgos sedimentary record is characterised by a high sand content including typical foraminifera species such as *Sorites* sp. and *Peneroplis* sp. which are often associated with carbonate-rich sandy beach sediments (Murray 2006; Avnaim-Katav et al. 2013).

In western and southwestern Crete, the thickness and the preservation state of fine-sedimentary archives are strongly bound to uplift rates and the local pre-AD 365 geomorphological setting as shown for the Sougia and Palaiochora study sites. In the Pirgos study site, located on the northern coast, the coseismic uplift and its effects were less intense resulting in less intense erosion and weathering. The Geropotamos River mouth study site was not affected by the AD 365 uplift and was rather a subject of subsidence.

## 5.2 Establishing a tsunami geochronostratigraphy for Crete in a supraregional context

So far, the AD 365 tsunami event is historically well documented, but reliable geological evidence proving its impact on Crete was missing. Bruins et al. (2008) found a LBA Santorini tsunamite at Palaikastro, eastern Crete, but – before this study was realized – we did not know whether the LBA Santorini tsunami had only affected Crete's eastern part or had also evoked damage on other parts of the island. One of the main objectives of this study, therefore, was to search for and identify LBA Santorini and AD 365 tsunami deposits and additional extreme wave events within the sedimentary records of Crete in order to establish a supraregional palaeotsunami geochronostratigraphy. A compilation of all tsunami-related EWE layers and tsunamite candidates detected on Crete are depicted in Fig. 5.1. The correlated tsunami events are labelled with letters from a to l; the study sites are labelled with numbers from 1 to 9.

Despite the fact that the AD 1303 tsunami impact (a) on Crete is historically well documented for the capital city of Heraklion (6), no reliable tsunamite candidate was found on Crete (for an overview see e.g., Papadopoulos 2014). Event-geochronostratigraphies by Ntageretzis et al. (2015a) revealed multiple tsunami impact at Limnothalassa Moustou (Argolid Gulf) and at the Evratos River delta, were the youngest tsunami impact was dated to the time between the 7th and 15th cent. AD. Both tsunami events most possibly refer to the historically well-known AD 1303 tsunami that affected wide parts of the eastern Mediterranean (Vött & Kelletat 2015). A younger tele-tsunami impact such as the AD 1303 (a) can be taken into account for the uppermost recorded tsunamites in the Gerpotamos area (Section 4). However, without further age control, it remains impossible to reliably correlate EWE deposits.

The sedimentary records of Sougia (1; Section 2) and Palaiochora (2; Section 2) included one EWE layer revealing first reliable geoscientific evidence of the AD 365 tsunami impact (b) on the southwestern coast of Crete. Pirazzoli et al. (1991) and Dominey-Howes et al. (1998) found two tsunamite candidates within Phalasarna's ancient harbour basin (3) at which the lower one yielded calibrated ages between the 1st cent. BC and the 2nd cent. AD so that the authors interpreted this layer as being associated with the earthquake and tsunami event reported for the year AD 66 (c). The upper layer was assumed to be related to the AD 365 tsunami (b), but both Pirazzoli et al. (1991) and Dominey-Howes et al. (1998) did not present reliable geoscientific evidence.

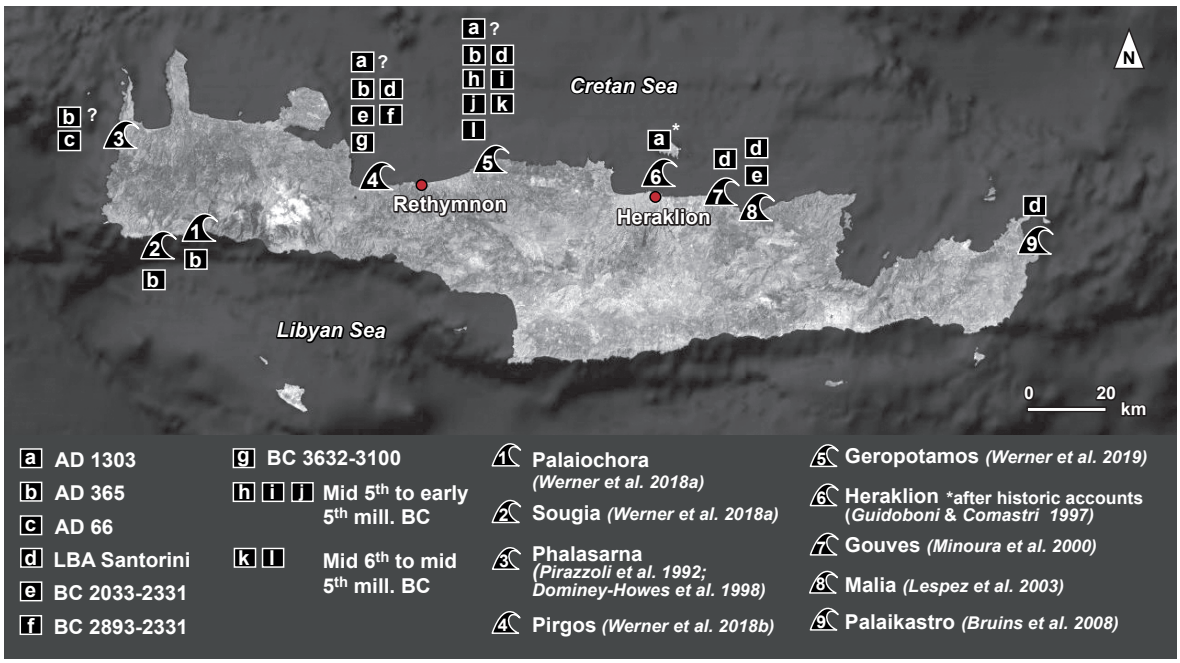


**Fig. 5.1:** Tsunami geochronostratigraphy of Crete. The numbers refer to the different study sites and the corresponding authors (Sougia, Palaiochora, Pirgos and Geropotamos: this study); the letters refer to detected possible tsunami deposits with best-fit age intervals based on radiocarbon dating (modified after Google Earth 2018).

The Pirgos study site sedimentary archive (4; Section 3) recorded five tsunami-related EWE layers that were radiocarbon dated using the sandwich dating approach. Until the uppermost EWE impact with a minimum age of 1250–1080 cal BC (1σ), the Pirgos study site was characterised by continuous lagoonal depositional conditions. After the EWE took place, the Pirgos lagoon stopped existing most probably due to coseismic uplift caused by the AD 365 earthquake. This corresponds well with numerical simulation of the AD 365 tsunami e.g., by Shaw et al. (2008) and Flouri et al. (2013), based on initial parameters inferred from palaeoshorelines on Crete. The tsunami simulation suggested that not only Crete's western and southwestern coasts were affected but also the northern coast. Regarding the age-depth model, the impact of the AD 365 tsunami must have reached eastwards at least to the Geropotamos River study site (5; Section 4) where the uppermost EWE is assumed to be AD 365-related. This study presents first geological evidence of AD 365 tsunami impact (b) at the northern Cretan coast.

Candidate tsunami layers associated with the LBA Santorini eruption (d) and the related tsunami were detected at the Pirgos study site. The EWE layer's age was reconstructed based on linear regression equations calculated from the Pirgos age-depth model to 1675–1516 cal BC which correspond well with the LBA Santorini eruption dated by Friedrich et al. (2006) to 1621–1605 cal BC (1σ). At the Geropotamos River study site, a large hiatus between the 5$^{th}$ and the 1$^{st}$ mill. BC may be associated with erosion by tremendous EWE from the seaside, possibly by the tsunami waves in conjunction with the LBA Santorini eruption. At Crete's northeastern coast, Lespez et al. (2003) found a significant EWE layer at Malia with an age ranging from 1739 to 1513 cal BC (2σ) that is highly consistent with the LBA Santorini layer (d) at Pirgos. At Palaikastro, located at Crete's eastern coast, Bruins et al. (2008) found a chaotic tsunamite which they related to the LBA Santorini eruption based on radiocarbon dating.

The combination of both field evidence and the outcome of numeric simulation of the LBA Santorini tsunami (Fig. 1.3 B and C, bottom) underline the uncertainty of the used initial model parameters. The simulation by Periañez & Abril (2014) correspond well with LBA Santorini tsunamites found at Palaikastro, Geropotamos and Pirgos, where the simulated wave amplitude ranges between ca. 10 to 15 m (light blue to yellow). Highest wave amplitudes were reached at the central northeastern part of Crete. In contrast, the simulation by Novikova et al. (2011) (Fig. 1.3 C) is focused on three different scenarios of pyroclastic flow entries into the sea. None of them fits to all found field evidence of this study. This may be explained by the initial parameters of the model e.g., the volume of the pyroclastic flow or by several tsunami events that were triggered by different pyroclastic flows.

At the Pirgos study site, the sedimentary archive recorded three additional tsunami-related EWE layers for the time period between the midst of the 4$^{th}$ and the end of the 3rd mill. BC. The age of EWE (e), (f) and (g) is defined by best-fit age intervals of 2331–2033 cal BC, 2893–2206 cal BC and 3309–3100 cal BC, respectively. An 'exceptional marine inundation' event found at Malia was dated to ca. 2500–2040 cal BC (Lespez et al. 2003, p. 449) and is in good accordance with EWE (e) at Pirgos (2331–2033 cal BC). This emphasises a supraregional tsunami event that hit the northern coast at least between Pirgos and Malia.

At the central northern coast, the Geropotamos River sedimentary archive revealed from the midst of the 6th to the end of the 5th mill. BC sedimentary and microfossil evidence of five possible tsunami related-EWE (h to l) that affected the northern coast. Summarizing the record of both geoarchives results in ten possible tsunami-related EWE that affected Crete's northern coast in the time period between the mid-6th to late 3rd mill. BC (see Fig. 5.1). Searching for supraregional tsunami events that affected Crete during this time period is difficult because geoarchives covering this long time span are rare. The geoarchives of Delphinos (Bottema & Sarpaki 2003) and Malia (Lespez et al. 2003) comprise an extensive fine-sedimentary record and are well-suited for further detailed multi-proxy palaeotsunami research.

## 5.3 Holocene vertical crust movements of Crete and palaeogeographical coastal changes

Comparing the study sites of Pirgos and Geropotamos located at Crete's northwestern and central northern coast with Malia (eastern Crete; Lespez et al. 2003), all sites revealed steady geomorpho-tectonic settings reflecting subsidence of Crete at least since the 7th mill. BC (Fig. 5.2). This is consistent with the studies on crustal block movements by Pirazzoli et al. (1982) and Tiberti et al. (2014) who found ten small lowering events on Crete between the 4th and the early 1st mill. BC. Located at the southwestern coast, the Sougia study site sedimentary record also revealed stable tectono-geomorphologic conditions providing a thick alluvial plain sequence that was deposited at least since the first half of the 5th mill. BC until the AD 365 coseismic uplift took place. Different subsidence rates suggest that crust downwarp was much stronger in the west (Sougia, Pirgos and Geropotamos) than farther east (Malia), which results in different deposition velocities ($v_{depos\ E} < v_{depos\ W}$) concerning the filling of the locally available accommodation spaces.

On a regional scale, the results correspond well with the tectonic influence of the nearby Hellenic subduction zone between the Aegean and African plates on Crete's geomorphological evolution, where the average uplift trend is characterised by periods of alternating uplift and subsidence (Tiberti et al. 2014). During interseismic periods (Fig. 5.3, top), the crust subsidence rate is much higher in the west than in the east possibly caused by the stronger influence of the subduction processes bound to the Hellenic Subduction Trench (Mouslopoulou et al. 2015b). In a typical subduction zone, the interface is locked after an earthquake and the overriding plate, here the Aegean microplate, is dragged down (Shaw & Jackson 2010).

A hinge separates the subsided areas (areas located above the locked part of the interface) from areas that are uplifted in a flexural bulge (areas located above the free aseismic part of the interface), caused by the overriding plate's downward motion (Shaw & Jackson 2010). Based on this model, the study sites of Sougia, Pirgos and Geropotamos are located much closer to the subduction interface and therefore experience stronger subsidence than Malia (see Fig. 5.3).

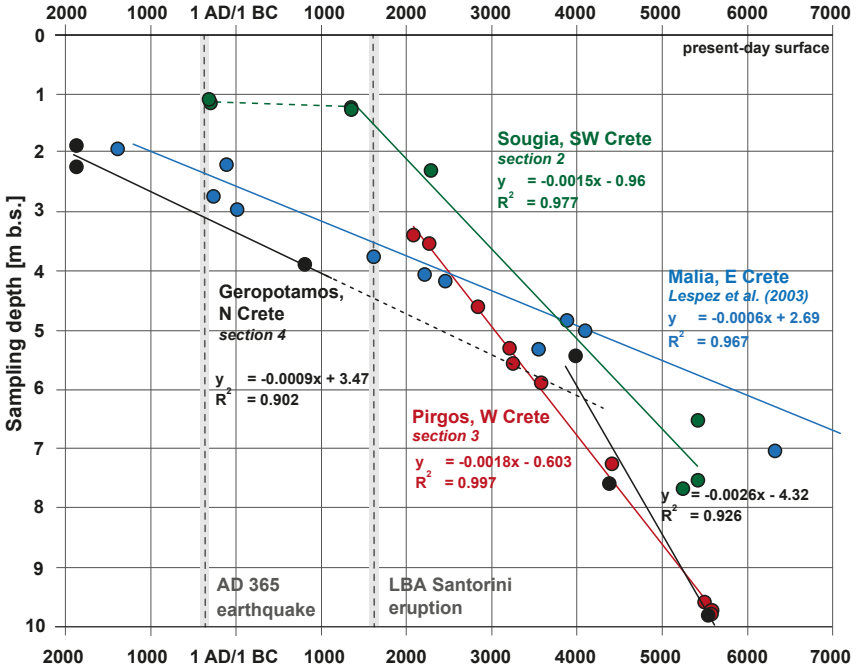


**Fig. 5.2:** Age-depth trend lines of the Sougia, Pirgos and Geropotamos study area and Malia (Lespez et al. 2003).

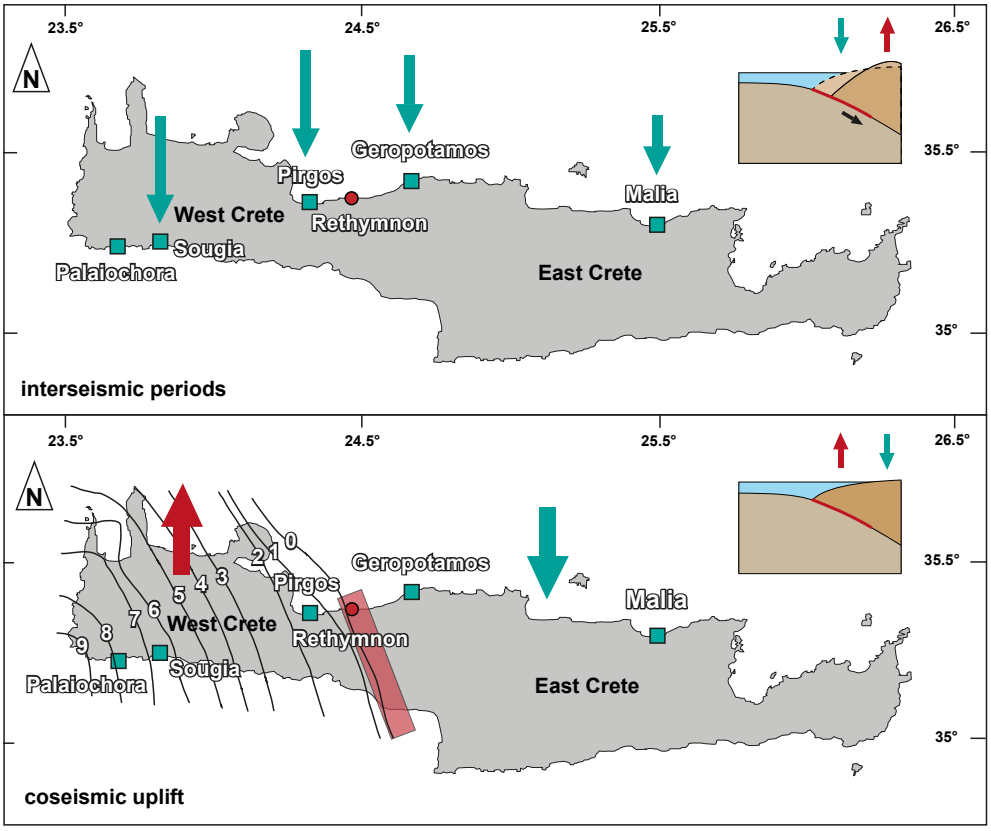


**Fig. 5.3:** Interseismic and seismic periods of Crete. Green arrows: subsidence; red arrows: uplift; red rectangle: the hinge's possible location (adapted from Shaw & Jackson 2010).

During the AD 365 earthquake (Fig. 5.3, bottom), the vertical crust movement was reversed and the areas above the seismogenic part were coseismically uplifted (West Crete). Areas located landward of the hinge (East Crete) are now subject to subsidence. At Sougia and Palaiochora (West Crete), an AD 365 coseismic uplift of 6.83 m and 7.75 m was measured, respectively. At Pirgos, an uplift of 1.64 m was inferred from the age-depth model and oxidised lagoonal deposits. In contrast, no uplift associated with the AD 365 earthquake was registered for the Geropotamos site and comparison of the age-depth trend lines reflects continuous subsidence over the last ca. 3000 years (Fig. 5.2). Regarding the subsidence of the Malia site (Fig. 5.2), the hinge must be located somewhere between Malia in the east and Pirgos in the west, most probably near Rethymnon, where the AD 365-associated uplift is nil (Fig. 5.3).

On a local scale, however, the subsidence at the Pirgos site may be also seen in conjunction with the neotectonic behaviour of the graben structure between Georgioupoli and Petres (Fig. 3.2; Section 3). At the Geropotamos site, a strong bend in the age-depth trend line's older part correlates with a large hiatus in the referred sediment core (Fig. 5.2). This bend apparently indicates a change in the subsidence rate of the site and a considerable relative sea level rise, which may be also associated with the local neotectonic behaviour of surrounding fault patterns (Fig. 4.2; Section 4).

Holocene vertical crust movements on Crete, caused during different periods of the seismic cycle of the Hellenic subduction zone, have strongly affected Crete's coastal evolution. During interseismic periods, the subsidence provides adequate accommodation space for thick sediment sequences. At the southwestern coast, the constant subsidence evokes thick alluvial plain deposits at the Sougia study site. At the northern coast, either a large near-coast lagoonal system or several smaller lagoons were located in today's Almiros Bay between the study sites of Delphinos (Bottema & Sarpaki 2003) and of Pirgos (Section 3). The Pirgos lagoon existed between the first half of the 6$^{th}$ mill. BC and (at least) until the end of the 2$^{nd}$ mill. BC and was most likely separated from the open sea by beach barriers that evolved where Neogene marl reached the surface or came close to it, generating an obstacle that initiated littoral sediment accumulation. At the Geropotamos study site (Section 4), located at the central northern coast, lagoonal depositional conditions lasted minimum from the mid-6$^{th}$ to the late 5$^{th}$ mill. BC, followed by a large hiatus and fluvio-lagoonal deposits between at least the early 1$^{st}$ mill. BC and the late 20$^{th}$ cent. AD. The hiatus can be explained by strong coseismic uplift at some point in time between the 5$^{th}$ and the 1$^{st}$ mill. BC and its associated reduction of the accommodation space. The hiatus can also be explained by strong erosive processes, which may have removed large parts of the sedimentary sequence.

The crust movement was reversed during the AD 365 earthquake, producing changes in coastal evolution with the strongest effects along the western and southwestern coasts of Crete. The coastal plain of Sougia (Section 2) was uplifted by 6.8 m and a small cliff that is assumed to have existed at the seaward front of the plain, became inactive and is still visible today. Moreover, the coseismic uplift would have had negative effects, comparable to the harbour of Phalasarna (Pirazzoli et al. 1992), on a possible harbour basin which is supposed to be located somewhere at the Sougia coastal plain. The Palaiochora study site

(Section 2) experienced the strongest uplift of all study sites with 7.7 m. Here, the central Palaiochora coastal plain was situated ca. 4.3 m below the pre-AD 365 earthquake sea level and only the southern part was laying above the sea. Since then, two new beaches have developed along the emerged Palaiochora coastal plain by reworking AD 365 tsunami deposits and sorting their uppermost parts in the present littoral zone.

At the northern coast, the lagoonal systems at Pirgos and most probably also at Delphinos (Section 3, Bottema & Sarpaki 2003) were uplifted by 1.6 m during the AD 365 earthquake. Possibly, both lagoonal systems were destroyed by the uplift in combination with the sediment input caused by the associated tsunami. Since then, a wide beach system has developed at the Almiros Bay. In contrast, the Geropotamos study site was not affected by the AD 365 crust uplift.

In summary, Holocene vertical crust movements on Crete, caused during different periods of the seismic cycle of the Hellenic subduction zone, had a strong impact on Crete's coastal evolution. During the interseismic phase that lasted at least since the 7$^{th}$ mill. BC, subsidence of the study areas predominates. During the seismic phase of the AD 365 earthquake, the crust movement was reversed and west Crete was coseismically uplifted.

## 5.4 Re-evaluation of the tsunami risk for Crete

Considering the classification by Papadopolous & Papageorgious (2014) and Papazachos & Dimitriu (1991), Crete's southern coasts are prone to high tsunami risk and intensity caused by the exposition to the Hellenic subduction zone. After Shaw et al. (2008), the recurrence interval of earthquakes similar to the AD 365 earthquake would be 800 years, if the same tectonic processes were assumed for the entire Hellenic subduction zone.

On the contrary, the tsunami risk at Crete's northern coasts has, so far, been underestimated. Summarising the tsunami layers detected at both Pirgos and Geropotamos sites over the last ca. 7500 years results in a recurrence interval of ca. 750 years. The AD 365 tsunami not only affected Crete's western and southwestern coast. First geological evidence found at the Pirgos and Geropotamos sites reveal that the AD 365 tsunami also affected vast areas along Crete's northern coast. Although numerous historic reports on the impact of the AD 1303 tsunami exist, investigated fine-sediment geoarchives did not reveal a reliable AD 1303 tsunamite candidate within this study.

The interaction of tsunami waves with the exposed river mouth area of the Geropotamos River study site pointed out that such areas are prone to tsunami penetration. This could be observed during the tsunami events of 2004 and 2011 (Adityawan et al. 2012; Tanaka et al. 2012, 2014; Tolkova & Tanaka 2016). Because of its funnel shape, the Geropotamos River mouth would catch large water masses produced by a long-wave tsunami and the subsequent narrow and incised valley would evoke strong channelling and acceleration effects. The comparison between the sedimentary records of the Geropotamos River mouth area with an area farther inland showed that several tsunami-related waves entered the Geropotamos River and propagated up to 1 km inland.

To conclude, seismically triggered tsunamis, such as the AD 365 tsunami, had much more widespread effects than assumed before. They did not only affect the areas directly exposed to the Hellenic Arc, but also reached the northern coasts of Crete. Depending on the tsunami wave propagation, the local bathymetry and the local geomorphological setting, tsunami waves may also enter exposed river mouths and extend the tsunami risk far inland by causing widespread inundation along the river banks. Crete's three major cities are located directly at the coast, comprise nearly half of the Cretan population (Hellenic Statistical Authority 2011) and are economy and tourism hotspots. The public awareness about tsunami risk and evacuation plans is little (Mitsoudis et al. 2012), so even minor events may have a significant impact. Therefore, regarding possible future tsunami events, it is important to combine geo-scientific studies on palaeotsunami impact on Crete with tsunami simulations in order to improve local risk assessment and evacuation plans.

## 5.5 Conclusions and perspectives

The southwestern and northern coasts of Crete offered a variety of adequate Holocene near-coast geoarchives covering information on coastal evolution over the last ~ 7000 years. The age-depth-model comparison highlighted that Holocene vertical crust movements, caused by different stages of the seismic cycle in the Hellenic subduction zone, have strongly influenced Crete's coastal evolution. During the interseismic phase, subsidence at the study areas predominated, resulting in positive effects for the local accommodation space architecture. During the seismic phases of the AD 365 earthquake, the crust movement was reversed and west Crete was coseismically uplifted resulting in strong erosion and loss of accommodation space.

Hence, searching for further Holocene near-coast sediment archives on western and northern Crete must be seen firstly in the context of the AD 365 uplift intensity. Secondly, further fine-sediment archives, especially along the southwestern and western coast, where the AD 365 coseismic uplift reached its maximum, should be searched in context of extraordinary pre-AD 365 local geomorphological and topographical settings as it was observed at Sougia. Visualisation of the pre-AD 365 topographical setting e.g., by a high-resolution uplift contour line map and a digital elevation model combined with evaluation of historically known harbour sites could help to detect new study areas in order to reconstruct the impact of the AD 365 tsunami on Crete.

The fine-sedimentary geoarchives detected at Sougia, Palaiochora, Pirgos and Geropotamos recorded altogether ten EWE some of which were found associated with known palaeotsunami events that hit Crete. With the focus on the AD 365 and the LBA Santorini tsunami, AD 365 tsunami layers were found in geoarchives at Sougia, Palaiochora and Pirgos. At the more landward located Geropotamos site, the sedimentary record contained two noticeable tsunamite candidates implicating that water masses entered the river mouth and propagated at least 1 km upstream triggering mass failures at a presently inactive external bank position of the Geropotamos River. The youngest EWE signal appears to have been caused by the AD 365 tsunami event. The older EWE is probably associated with a tsunami

that entered the Geropotamos valley and evoked strong erosion creating a hiatus within the sedimentary record that fits to the timeframe of the LBA Santorini eruption.

However, at the Geropotamos site, younger tsunami events must be taken into account as well, such as the historically well-documented AD 1303 tsunami. Hence, to create a detailed age-depth model of these deposits, more research in terms of further geochronological studies based on OSL dating and radiocarbon dating is required. Additionally to the Geropotamos study site, LBA Santorini tsunamite candidates were also identified within the Pirgos sedimentary record. In summary, this is the first study presenting reliable geological evidence of the LBA Santorini and AD 365 tsunami on Crete at Pirgos and Sougia/Palaiochora, respectively.

Combining the Pirgos sedimentary archive with the Geropotamos River valley record revealed evidence of ten major EWE that hit Crete's northern coast during the past ~7500 years. This leads to a statistical recurrence interval of ca. 750 years for large EWE impacts which is consistent with statistical recurrence intervals (800 years) for major tsunamis based on seismological studies (Shaw et al. 2008; Shaw 2012). Together with the simulation results of the AD 365 tsunami by Shaw et al. (2008) and Flouri et al. (2013), the results of this study showed that the AD 365 tsunami not only affected the western and southwestern coast but may have also affected wide areas along the northern coast.

The AD 1303 earthquake was triggered in the eastern segment of the Hellenic Arc. However, details on the earthquake's mechanisms are not yet fully understood. Based on historical accounts, the capital city of Heraklion was damaged by the AD 1303 earthquake and the associated tsunami but so far, no reliable geological evidence was found. More research is necessary to reconstruct the impact of the AD 1303 tsunami on Crete's coast and to re-evaluate the tsunami risk originating from the eastern segment of the Hellenic arc. A dense network of palaeotsunami field evidence on Crete combined with tsunami simulations might help to better assess possible future tsunami events and to increase public awareness of Crete's high tsunami hazard.

# References


## A

Ad-hoc-AG Boden (2005): Bodenkundliche Kartieranleitung, 5th ed. Hannover.

Adityawan, M. B., Roh, M., Tanaka, H., Mano, A., & Udo, K. (2012): Investigation of tsunami propagation characteristics in river and on land induced by The Great East Japan Earthquake 2011. Journal of Earthquake and Tsunami 6/03, 1–22.

Aitken, M.J. (1998): An Introduction to Optical Dating - The Dating of Quaternary Sediments by the Use of Photon-stimulated Luminescence. Clarendon Press, Oxford. 280 pp.

Alexandrakis, G., Poulos, S., Petrakis, S. & Collins, M. (2011): The development of a Beach Vulnerability Index (BVI) for the assessment of erosion in the case of the North Cretan Coast (Aegean Sea). Hellenic Journal of Geosciences 45, 11.

Ambraseys, N. (2009): Earthquakes in the Mediterranean and Middle East. A multidisciplinary study of seismicity up to 1900. Cambridge University Press, Cambridge. 968 pp.

Andrianakis, M. (1982): Ο νομός Χανίων κατά την Παλαιοχριστιανική Περίοδο (Κατάλογος Μνημείων). Annual Publication of the Municipality of Chania ('in Greek').

Angelier, J., Lybéris, N., Le Pichon, X., Barrier, E. & Huchon, P. (1982): The Tectonic Development of the Hellenic Arc and the Sea of Crete: A Synthesis. Tectonophysics, 86. 159-169.

Athanassoulis, G.A. & Skarsoulis, E.K. (1992): Wind and Wave Atlas of North-east Mediterranean Sea. Laboratory of Nautical and Marine Hydrodynamics, Athens.

Avnaim-Katav, S., Almogi-Labin, A., Sandler, A. & Sivan, D. (2013): Benthic foraminifera as palaeoenvironmental indicators during the last million years in the eastern Mediterranean inner shelf. Paleogeography, Palaeoclimatology, Palaeoecology 386, 512–530.

Ayat, B. (2013): Wave power atlas of Eastern Mediterranean and Aegean seas. Energy 54, 251–262.

## B

Bahlburg, H. & Weiss, R. (2007): Sedimentology of the December 26, 2004, Sumatra tsunami deposits in eastern India (Tamil Nadu) and Kenya. International Journal of Earth Sciences 96/6, 1195–1209.

Blackman, D.J. (1976) Lisos or Lissos (Greece). In: Stillwell, R., MacDonald, W., McAlister L. & Holland, M. (Eds). The Princeton Encyclopedia of classical sites. Princeton University Press, Princeton.

Bohnhoff, M., Makris, J., Papanikolaou, D. & Stavrakakis, G. (2001): Crustal investigation of the Hellenic subduction zone using wide aperture seismic data. Tectonophysics 343, 239–262.

Bony, G., Marriner, N., Morhange, C., Kaniewski, D., & Perinçek, D. (2012): A high-energy deposit in the Byzantine harbour of Yenikapı, Istanbul (Turkey). Quaternary International 266, 117–130.

Bottema, S. & Sarpaki, A. (2003): Environmental changes in Crete: a 9000-year record of Holocene vegetation history and the effect of the Santorini eruption. The Holocene 13/5, 733-749.

Bøtter-Jensen, L., McKeever, S. W. S. & Wintle, A. G. (2003): Optically Stimulated Luminescence Dosimetry. Elsevier, Amsterdam.

Boulton, S.J. & Whitworth, M.R.Z. (2017): Block and boulder accumulation on the southern coast of Crete (Greece): evidence for the 365 CE tsunami in the Eastern Mediterranean. Geological Society, London, Special Publications 456.

Branigan, K. (1976): Palaiokhora (Kalamyde) Selinos, Crete. In: Stillwell, R., MacDonald, W., McAlister L. & Holland, M. (Eds). The Princeton Encyclopedia of classical sites. Princeton University Press, Princeton.

Bruins, H. J., MacGillivray, J. A., Synolakis, C. E., Benjamini, C., Keller, J., Kisch, H. J., Klügel, A. & van der Plicht, J. (2008): Geoarchaeological tsunami deposits at Palaikastro (Crete) and the Late Minoan IA eruption of Santorini. Journal of Archaeological Science 35/1, 191–212.

## C

Caputo, R., Catalano, S., Monaco, C., Romagnoli, G., Tortorici, G. & Tortorici, L. (2010): Active faulting on the island of Crete (Greece). Geophysical Journal International 183, 111–126.

Cavaleri, L., Bertotti, L. & Lionello, P. (1991): Wind wave cast in the Mediterranean Sea. Journal of Geophysical Research: Oceans 96 (C6), 10739–10764.

Cavicchia, L., von Storch, H. & Gualdi, S. (2014): Mediterranean tropical-like cyclones in present and future climate. Journal of Climate 27/19, 7493–7501.

Chagué-Goff, C. (2010): Chemical signatures of palaeotsunamis: A forgotten proxy? Marine Geology 271/1–2, 67–71.

Chagué-Goff, C., Schneider, J.-L., Goff, J. R., Dominey-Howes, D. & Strotz, L. (2011): Expanding the proxy toolkit to help identify past events – Lessons from the 2004 Indian Ocean Tsunami and the 2009 South Pacific Tsunami. Earth-Science Reviews 107, 107–122.

Chagué-Goff, C., Goff, J., Wong, H.K.Y. & Cisternas, M. (2015): Insights from geochemistry and diatoms to characterise a tsunami‘s deposits and maximum inundation limit. Marine Geology 359, 22–34.

Chagué-Goff, C., Szczuciński, W. & Shinozaki, T. (2017): Applications of geochemistry in tsunami research: A revive. Earth-Science Reviews 165, 203–244.

Chanson, H. & Lubin, P. (2013): Mixing and Sediment Processes induced by Tsunamis propagating Upriver. Tsunamis: Economic Impact, Disaster Management and Future Challenges. Nova Science Publishers, Hauppauge NY, USA, pp. 65–102.

Choi, B.H., Pelinovsky, E., Kim, K.O. & Lee, J.S. (2003): Simulation of the trans-oceanic tsunami propagation due to the 1883 Krakatau volcanic eruption. Natural Hazards and Earth System Sciences 3, 321–332.

Choowong, M., Murakoshi, N., Hisada, K., Charoentitirat, T., Charusiri, P., Phantuwongraj, S., Wongkok, P., Choowong, A., Subsayjun, R., Chutakositkanon, V., Jankaew, K. & Kanjanapayont, P. (2008): Flow conditions of the 2004 Indian Ocean tsunami in Thailand, inferred from capping bedforms and sedimentary structures. Terra Nova 20, 141–149.

Christodoulakos, G. & Markoulaki, S. (2006): Συία - αρχαίο υδραγωγείο, Αρχαίοι Τόποι και Μνημεία. Municipality of Chania 2006 (‘in Greek’).

Cimerman, F. & Langer, M.R. (1991): Mediterranean Foraminifera. Slovenska Akademija

Znanosti, Ljubljana. 118 pp.

Cioni, R., Gurioli, L., Sbrana, A. & Vougioukalakis, G. (2000): Precursors to the Plinian eruptions of Thera (Late Bronze Age) and Vesuvius (AD 79): Data from archaeological areas. Physics and Chemistry of the Earth, Part A: Solid Earth and Geodesy 25/9–11, 719–724.

Cuven, S., Paris, R., Falvard, S., Miot-Noirault, E., Benbakkar, M., Schneider, J.-L. & Billy, I. (2013): High-resolution analysis of a tsunami deposit: case-study from the 1755 Lisbon tsunami in southwestern Spain. Marine Geology, 337, 98–111.

**D**

De Martini, P.M., Burrato, P., Pantosti, D., Maramai, A., Graziani, L. & Abramson, H. (2003): Identification of tsunami deposits and liquefaction features in the Gargano area (Italy): paleoseismological implication. Annals of Geophysics 46/5, 883–902.

De Martini, P. M., Barbano, M. S., Smedile, A., Gerardi, F., Pantosti, D., Del Carlo, P. & Pirrotta, C. (2010): A unique 4000 year long geological record of multiple tsunami inundations in the Augusta Bay (eastern Sicily, Italy). Marine Geology 276/1-4, 42–57.

De Rijk, S., Troelstra, S. R. & Rohling, E. J. (1999): Benthic foraminiferal distribution in the Mediterranean Sea. Journal of Foraminiferal Research 29/2, 93–103.

DIN/EN ISO 11277 (2002): Bodenbeschaffenheit - Bestimmung der Partikelgrößenverteilung in Mineralböden - Verfahren mittels Siebung und Sedimentation. ISO 11277: 1998 and ISO 11277, Corrigendum 1. Beuth Verlag GmbH, Berlin.

Dominey-Howes, D. (2004): A re-analysis of the Late Bronze Age eruption and tsunami of Santorini, Greece, and the implications for the volcano-tsunami hazard. Journal of Volcanology and Geothermal Research 130, 107–132.

Dominey-Howes, D., Dawson, A. & Smith, D. (1998): Late Holocene coastal tectonics at Falasarna, western Crete: a sedimentary study. In: Stewart, I.S. & Vita-Finzi, C. (Eds.), Coastal Tectonics. Geological Society Special Publication 146, 343–352.

Dominey-Howes, D. T., Humphreys, G. S. & Hesse, P. P. (2006): Tsunami and palaeotsunami depositional signatures and their potential value in understanding the late-Holocene tsunami record. The Holocene, 16/8, 1095–1107.

Doutsos, T. & Kokkalas, S. (2001): Stress and deformation patterns in the Aegean region. Journal of Structural Geology 23, 455–472.

Driessen, J. & Macdonald, C. F. (1997): The Troubled Island. Minoan Crete Before and After the Santorini Eruption. Aegaeum 17, Liège and Austin, 284 pp.

Drinia, H., Antonarakou, A. & Kontakiotis, G. (2008): On the occurrence of early Pliocene marine deposits in the Ierapetra Basin, eastern Crete, Greece. Bulletin of Geosciences 83/1, 63–78.

Druitt, T.H. & Francaviglia, V. (1992): Caldera formation on Santorini and the physiography of the islands in the late Bronze Age. Bulletin of Volcanology 54, 484–493.

Druitt, T. H., Edwards, L., Mellors, R. M., Pyle, D. M., Sparks, R. S. J., Lanphere, M., Davies, M. & Barreirio, B. (1999): Santorini volcano. Geological Society Memoir 19.

Doumas, C. (1980): The stratigraphy of Akrotiri. In: Doumas, C. (Ed.), Thera and the Aegean world, 1, London (1980), pp. 777–782.

Durazzo-Morosini, Z., von Gaertringen, F. F. H., Reck, H. & Dobe, F. (1936): Santorin, die fantastische Insel. Gebrüder Mann.

## E

Evans, A. J. (1928): The Palace of Minos: A Comparative Account of the Successive Stages of the Early Cretan Civilization as Illustrated by the Discoveries at Knossos, Part I: Fresh Lights on Origins and External Relations: The Restoration in Town and Palace after Seismic Catastrophe towards Close of M. M. III, and the Beginnings of the New Era, Vol. 2, Macmillan and Co., London, 390 pp.

## F

Fassoulas, C., Kilias, A. & Mountrakis, D. (1994): Postnappe stacking extension and exhumation of high-pressure/low-temperature rocks in the island of Crete, Greece. Tectonics 13, 127–138.

Finkler, C., Fischer, P., Baika, K., Rigakou, D., Metallinou, G., Hadler, H. & Vött, A. (2018a): Tracing the Alkinoos Harbor of ancient Kerkyra, Greece, and reconstructing its paleotsunami history. Geoarchaeology 33/1, 24-42.

Finkler, C., Baika, K., Rigakou, D., Metallinou, G., Fischer, P., Hadler, H., Emde, K. & Vött, A. (2018b): Geoarchaeological investigations of a prominent quay wall in ancient Corcyra–Implications for harbour development, palaeoenvironmental changes and tectonic geomorphology of Corfu Island (Ionian Islands, Greece). Quaternary International 473, 91–111.

Finkler, C., Baika, K., Rigakou, D., Metallinou, G., Fischer, P, Hadler, H. & Vött, A. (2019): The sedimentary record of the Alkinoos Harbour of ancient Corcyra (Corfu Island, Greece) – geoarchaeological evidence for rapid coastal changes induced by co-seismic uplift, tsunami inundation and human interventions. Zeitschrift für Geomorphologie (in press), https://doi.org/10.1127/zfg_suppl/2018/0514.

Fischer, P. Finkler, C., Röbke, B.R, Baika, K., Hadler, H., Willershäuser, T., Rigakou, D., Metallinou, G. & Vött, A. (2016a): Impact of Holocene tsunamis detected in lagoonal environments on Corfu (Ionian Islands, Greece) – geomorphological, sedimentary and microfaunal evidence. Quaternary International 401, 4–16.

Fischer, P., Wunderlich, T., Rabbel, W., Vött, A., Willershäuser, T., Baika, K., Rigakou, D. & Metallinou, G. (2016b): Combined Electrical Resistivity Tomography (ERT), Direct-Push Electrical Conductivity (DP-EC) Logging and Coring–A New Methodological Approach in Geoarchaeological Research. Archaeological Prospection 23/3, 213–228.

Flemming, N. C. (1978): Holocene eustatic changes and coastal tectonics in the northeast Mediterranean: implications for models of crustal consumption. Phil. Trans. R. Soc. Lond. A, 289 (1362), 405–458.

Flouri, E. T., Kalligeris, N., Alexandrakis, G., Kampanis, N. A. & Synolakis, C. E. (2013): Application of a finite difference computational model to the simulation of earthquake generated tsunamis. Applied Numerical Mathematics 67, 111–125.

Font, E., Nascimento, C., Omira, R., Baptista, M. A. & Silva, P. F. (2010): Identification of tsunami-induced deposits using numerical modeling and rock magnetism techniques: A study case of the 1755 Lisbon tsunami in Algarve, Portugal. Physics of the Earth and Planetary Interiors 182. 187-198.

Franz, L., Okrusch, M., Seidel, E., & Kreuzer, H. (2005): Polymetamorphic evolution of pre-Alpidic basement relics in the external Hellenides, Greece. Neues Jahrbuch für Mineralogie-Abhandlungen: Journal of Mineralogy and Geochemistry 181/2, 147–172.

Friedrich, W. L. (2013): The Minoan Eruption of Santorini around 1613 B.C. and its consequences. Tagungen des Landesmuseums für Vorgeschichte, Halle, 9, 37–48.

Friedrich, W. L. & Heinemeier J. (2009): The Minoan eruption of Santorini radiocarbon dated to 1613 ±13 BC, in Warburton D.A. (Ed.) Time‘s up! Dating the Minoan eruption of Santorini: Acts of the Minoan Eruption Chronology Workshop, Sandbjerg, November 2007. Monographs of the Danish institute at Athens, 10, Athens, 56–63.

Friedrich, W. L., Kromer, B., Friedrich, M., Heinemeier, J., Pfeiffer, T. & Talamo, S. (2006): Santorini Eruption Radiocarbon Dated to 1627–1600 B.C. Science 312, 548.

Frost, F., J. & Hadjidaki, E. (1990): Excavations at the Harbor of Phalasarna in Crete: The 1988 Season. The Journal of the American School of Classical Studies at Athens 59 /3, 513–527.

**G**

Galanopoulos, A. G. (1960): Tsunamis observed on the coasts of Greece from antiquity to present time. Annals of Geophysics 13/3–4, 369–386.

Galbraith, P. & Roberts, P. G. (2012): Statistical aspect of equivalent dose and error calculation and display in OSL dating: An overview and some recommendations. Quaternary Geochronology 11, 1–27.

Galbraith, R. F., Roberts, R. G., Laslett, G. M., Yoshida, H. & Olley, J. M. (1999): Optical dating of single and multiple grains of quartz from Jinmium rock shelter, northern Australia: part I, experimental design and statistical models. Archaeometry 41/2, 339–364.

Georgalas, G. C. (1953): L’éruption du volcan de Santorin en 1950: Bulletin Volcanologique 13, 39–55.

Georgalas, G. C. (1962): Catalogue of the active volcanoes and solfatara fields of Greece: Rome, International Association of Volcanology 12, 14–29.

Gianfreda, F., Mastronuzzi, G. & Sanso, P. (2001): Impact of historical tsunamis on a sandy coastal barrier: an example from the northern Gargano coast, southern Italy. Natural Hazards and Earth System Sciences 1, 213–219.

Goiran, J. P., Tronchère, H., Salomon, F., Carbonel, P., Djerbi, H. & Ognard, C. (2010): Palaeoenvironmental reconstruction of the ancient harbors of Rome: Claudius and Trajan‘s marine harbors on the Tiber delta. Quaternary International 216/1, 3–13.

Gondicas, D. (1988): Recherches sur la Crète occidentale. De l‘époque géométrique à l‘époque romaine. Inventaires des sources archéologiques et textuelles, position du problème. A.M. Hakkert, Amsterdam.

Goodman, B., Reinhardt, E., Dey, Hendrik, Boyce, J., Schwarcz, H., Sahoglu, V., Erkanal, H. & Artzy, M. (2008): Evidence for Holocene marine transgression and shoreline progradation due to barrier development in Iskele, Bay of Izmir, Turkey. Journal of Coastal Research 24/5, 1269–1280.

Goodman-Tchernov, B.N., Dey, H.W., Reinhardt, E.G., McCoy, F. & Mart, Y. (2009): Tsunami waves generated by the Santorini eruption reached Eastern Mediterranean shores. Geology 37, 943–946.

Goto, K., Chagué-Goff, C., Fujino, S., Goff, J., Jaffe, B., Nishimura, Y., Richmond, B., Sugawara, D., Szczuciński, W., Tappin, D.R., Witter, R.C. & Yulianto, E. (2011): New insights of tsunami hazard from the 2011 Tohoku-oki event. Marine Geology 290, 46–50.

Goto, K., Hashimoto, K., Sugawara, D., Yanagisawa, H. & Abe, T. (2014): Spatial thickness variability of the 2011 Tohoku-oki tsunami deposits along the coastline of Sendai Bay.

Marine Geology 358, 38–48.

Guidoboni, E. & Comastri, A. (1997): The large earthquake of 8 August 1303 in Crete: seismic scenario and tsunami in the Mediterranean area. Journal of Seismology 1/1, 55–72.

Guidoboni, E. & Comastri, A. (2005): Catalogue of Earthquakes and Tsunamis in the Mediterranean Area from the 11th to the 15th Century. INGV-SGA, Rome–Bologna, Italy p. 1037.

Guidoboni, E., Comastri, A. & Traina, G. (1994): Catalogue of Ancient Earthquakes in the Mediterranean up to the 10th Century. Istituto Nazionale di Geofisica, SGA, Roma. 504 pp.

**H**

Hadjidaki, E. (1988): Preliminary Report of Excavations at the Harbor of Phalasarna in West Crete. American Journal of Archaeology 92/4, 463–479.

Hadjidaki E. (1996): The Hellenistic Harbor of Phalasarna in Western Crete: A comparison with the Hellenistic Inner Harbor of Straton's Tower. In: Raban A. & Holum K. G. (Eds.), Caesarea Maritima. A Retrospective after two Millenia. Brill, 53–64.

Hadler, H., Willershäuser, T., Ntageretzis, K., Henning, P. & Vött, A. (2012): Catalogue entries and non-entries of earthquake and tsunami events in the Ionian Sea and the Gulf of Corinth (eastern Mediterranean, Greece) and their interpretation with regard to palaeotsunami research. In: Vött, A. & Venzke, J.F. (Eds.), Beiträge der 29. Jahrestagung des Arbeitskreises "Geographie der Meere und Küsten", 28. bis 30. April 2011 in Bremen, Bremer Beiträge zur Geographie und Raumplanung 44, 1–15.

Hadler, H., Vött, A., Koster, B., Mathes-Schmidt, M., Mattern, T., Ntageretzis, K., Reicherter, K. & Willershäuser, T. (2013): Multiple late-Holocene tsunami landfall in the eastern Gulf of Corinth recorded in the palaeotsunami geo-archive at Lechaion, harbour of ancient Corinth (Peloponnese, Greece). Zeitschrift für Geomorphologie N.F., Supplementary Issue 57/4, 139–180.

Hadler, H., Vött, A., Fischer, P., Ludwig, S., Heinzelmann, M. & Rohn, C. (2015): Temple-complex tsunami deposits found in the ancient harbour basin of Ostia (Rome, Italy). Journal of Archaeological Science 61, 78–89.

Hadler, H., Fischer, P., Obrocki, L., Heinzelmann, M. & Vött, A. (2019): River channel evolution and tsunami impacts recorded in local sedimentary archives – The 'Fiume Morto' at Ostia Antica (Tiber River, Italy). Sedimnetology (accepted), doi.org/10.1111/sed.12599.

Hamilton, E., Cairns, H., & Cooper, L. (1961): The collected dialogues of Plato. Princeton University Press. 1776 p.

Hammer, C. U., Clausen, H. B., Friedrich, W. L. & Tauber, H. (1987): The Minoan eruption of Santorini in Greece dated to 1645 BC? Nature 328/6130, 517–519.

Hébert, H., Schindele, F., Altinok, Y., Alpar, B. & Gazioglu, C. (2005): Tsunami hazard in the Marmara Sea (Turkey): a numerical approach to discuss active faulting and impact on the Istanbul coastal areas. Marine Geology 215/1–2, 23–43.

Hellenic Statistical Authority (2011): 2011 Population-Housing Census. URL: www.statistics.gr/en/2011-census-pop-hous (27.12.18).

Hindson, R. A., Andrade, C. & Dawson, A. G. (1996): Sedimentary processes associated with the tsunami generated by the 1755 Lisbon earthquake on the Algarve coast,

Portugal. Physics and Chemistry of the Earth 21, 57-63.

Hobbes, T. (1845): The english works of Thomas Hobbes of Malmesbury Vol. 10, London, 536 pp.

Hollenstein, C., Müller, M. D., Geiger, A. & Kahle, H.-G. (2008): Crustal motion and deformation in Greece from a decade of GPS measurements, 1993-2003. Tectonophysics 449, 17–40.

Hori, K., Kuzumoto, R., Hirouchi, D., Umitsu, M., Janjirawuttikul, N. & Patanakanog, B. (2007): Horizontal and vertical variation of 2004 Indian tsunami deposits: an example of two transects along the western coast of Thailand. Marine Geology 239/3, 163–172.

**I**

Institute of Geology and Mineral Exploration (IGME) (2002): Palaeochora Sheet, 1:50.000. Greece.

Institute of Geological and Mining Research (IGMR) (1977): General geological map of Greece. Crete Island. Scale 1:200.000.

**J**

Jolivet, L., Goffé, B., Monié, P., Truffert-Luxey, C., Patriat, M. & Bonneau, M. (1996): Miocene detachment in Crete and exhumation P-T-t paths of high-pressure metamorphic rocks. Tectonics 15/6, 1129–1153.

Judd, K., Chagué-Goff, C., Goff, J., Gadd, P., Zawadzki, A. & Fierro, D. (2017): Multi-proxy evidence for small historical tsunamis leaving little or no sedimentary record. Marine Geology 385, 204–215.

**K**

Karathanasi, F., Soukissian, T. & Sifnioti, D. (2015): Offshore wave potential of the Mediterranean Sea. Renewable Energy and Power Quality Journal 13, 461–465.

Kelletat, D. (1991): The 1550 BP tectonic event in the Eastern Mediterranean as a basis for assuring the intensity of shore processes. Zeitschrift für Geomorphologie 81, 181–194.

Kelletat, D. & Zimmermann, L. (1991): Verbreitung und Formtypen rezenter und subrezenter organischer Gesteinsbildungen an den Küsten Kretas. Geographische Arbeiten 23, 168.

Kelly, G. (2004): Ammianus and the great tsunami. Journal of Roman studies 94, 141–167.

Köhn, M. (1929): Korngrößenbestimmung vermittels Pipettanalyse. Tonindustrie-Zeitung 55, 729–731.

Kontopoulos, N. & Avramidis, P. (2003): A late Holocene record of environmental changes from the Aliki lagoon, Egion, North Peloponnesus, Greece. Quaternary International 111/1, 75–90.

Kortekaas, S., Papadopoulos, G.A., Ganas, A., Cundy, A.B. & Diakantoni, A. (2011): Geological identification of historical tsunamis in the Gulf of Corinth, Central Greece. Natural Hazards and Earth System Sciences 11/7, 2029–2041.

Koster, B. & Reicherter, K. (2014): Sedimentological and geophysical properties of a ca. 4000 year old tsunami deposit in southern Spain. Sedimentary Geology 314, 1–16.

Koster, B., Hadler, H., Vött, A. & Reicherter, K. (2013): Application of GPR for visualising spatial distribution and internal structures of tsunami deposits – Case studies from Spain and Greece. Zeitschrift für Geomorphologie N.F., Supplementary Issue 57/4, 29–45.

Koster, B., Vött, A., Mathes-Schmidt, M. & Reicherter, K. (2015): Geoscientific investigations in search of tsunami deposits in the environs of the Agoulinitsa peatland, Kaiafas Lagoon and Kakovatos (Gulf of Kyparissia, western Peloponnese, Greece). Zeitschrift für Geomorphologie N.F., Supplementary Issues 59/4, 125–156.

**L**

Lang, A. (1996): Die Infrarot-Stimulierte-Lumineszenz als Datierungsmethode für holozäne Lössderivate. Ein Beitrag zur Chronometrie kolluvialer, alluvialer und limnischer Sedimente in Südwestdeutschland., Ph.D. thesis, Ruprecht-Karls-Universität Heidelberg.

Le Pichon, X. & Angelier, J. (1979): The Hellenic arc and trench system: a key to the neotectonic evolution of the eastern Mediterranean area. Tectonophysics 60/1, 1–42.

Lespez, L., Dalongeville, R., Pastre, J. F., Darmon, F., Mathieu, R. & Poursoulis, G. (2003): Late-Middle-Holocene palaeo-environmental evolution and coastline changes of Malia (Crete). In: The Mediterranean World Environment and History. Elsevier, Amsterdam, 439–452.

Loeblich, E.R. & Tappan, H.N. (1988): Foraminiferal Genera and Their Classification. Van Nostrand Reinhold Company, New York. 730 pp.

Lorito, S., Tiberti, M.M., Basili, R., Piatanesi, A. & Valensise, G. (2008): Earthquake-generated tsunamis in the Mediterranean Sea: Scenarios of potential threats to southern Italy. Journal of Geophysical Research: Solid Earth 113/B1, 1–14.

Luque, L., Lario, J., Silva, P.G., Zazo, G., Goy, J.L. & Dabrio, C.J. (2002): Sedimentary record of a tsunami during Roman times, Bay of Cadiz, Spain. Journal of Quaternary Sciences 17/5–6, 623–631.

**M**

Maas, G. & Macklin, M. (2002): The impact of recent climate change on flooding and sediment supply within a Mediterranean mountain catchment, southwestern Crete, Greece. Earth Surface Processes and Landforms 27/10, 1087–1105.

Mamo, B., Strotz, L. & Dominey-Howes, D. (2009): Tsunami sediments and their foraminiferal assemblages. Earth Science Reviews 96, 263–278.

Marinatos, S. (1939): The volcanic destruction of Minoan Crete. Antiquity 13, 425–439.

Markoulaki, S. (1982): Σούγια στην αρχαιότητα και σήμερα, Χανιά. Chania - Annual Publication of the Municipality of Chania, 77–82 ('in Greek').

Marriner, N. & Morhange, C. (2007): Geoscience of ancient Mediterranean harbours. Earth-Science Reviews 80/3, 137–194.

Mason, J., Schneiderwind S., Pallikarakis, A., Wiatr T., Mechernich, S., Papanikolaou, I. & Reicherter, K. (2016): Fault structure and deformation rates at the Lastros-Sfaka Graben, Crete. Tectonophysics 683, 216–232.

Mastronuzzi, P. & Sansò, P. (2012): The role of strong earthquakes and tsunami in the Late Holocene evolution of the Fortore River coastal plain (Apulia, Italy): A synthesis. Geomorphology 138/1, 89–99.

Mathes-Schmidt, M., Schwarzbauer, J., Papanikolaou, I., Syberberg, F., Thiele, A., Witt-

KOPP, F. & REICHERTER, K. (2013): Geochemical and micropalaeontological investigations of tsunamigenic layers along the Thracian Coast (Northern Aegean Sea, Greece). Zeitschrift für Geomorphologie N. F., Supplementary Issue, 57/4, 5–27.

MATSUMOTO, D., SHIMAMOTO, T., HIROSE, T., GUNATILAKE, J., WICKRAMASOORIYA, A., DELILE, J., YOUNG, S., RATHNAYAKE, C., RANASOORIYA, J. & MURAYAMA, M. (2010): Thickness and grain-size distribution of the 2004 Indian Ocean tsunami deposits in Periya Kalapuwa Lagoon, eastern Sri Lanka. Sedimentary Geology 230, 95–104

MAY, S. M., VÖTT, A., BRÜCKNER, H., GRAPMAYER, R., HANDL, M. & WENNRICH, V. (2012): The Lefkada barrier and beachrock system (NW Greece) - controls on coastal evolution and the significance of extreme wave events. Geomorphology 139, 330–347.

MCCLUSKY, S., BALASSANIAN, S., BARKA, A., DEMIR, C., ERGINTAV, S., GEORGIEV, I., GURKAN, O., HAMBURGER, M., HURST, K., KAHLE, H., KASTENS, K., KEKELIDZE, G., KING, R., KOTZEV, V., LENK, O., MAHMOUD, S., MISHIN, A., NADARIYA, M., OUZOUNIS, A., PARADISSIS, D., PETER, Y., PRILEPIN, M., REILINGER, R., SANLI, I., SEEGER, H., TEALEB, A., TOKSÖZ, M.N. & VEIS, G. (2000): Global positioning system constraints on plate kinematics and dynamics in the eastern Mediterranean and Caucasus. Journal of Geophysical Research: Solid Earth 105, 5695–5719.

MCCOY, F. W. & DUNN, S. (2002): Modelling the climatic effects of the LBA eruption of Thera: new calculations of tephra volumes may suggest a significantly larger eruption than previously reported. In: Proceedings of the Chapman Conference on Volcanism and the Earth's Atmosphere.

MCCOY, F.W. & HEIKEN, G. (2000): Tsunami generated by the Late Bronze Age eruption of Thera (Santorini), Greece. Pure and Applied Geophysics 157, 1227–1256.

MCKENZIE, D. (1972): Plate Tectonics of the Mediterranean Region. Nature 226, 239–243.

MCKENZIE, D. (1978): Active tectonics of the Alpine Himalayan Belt, the Aegean Sea and surrounding regions. Geophysical Journal International 55/81, 217–254.

MELTZNER, A.J., SIEH, K., ABRAMS, M., AGNEW, D.C., HUDNUT, K.W., AVOUAC, J.-P. & NATAWIDJAJ D.H. (2006): Uplift and subsidence associated with the great Aceh-Andaman earthquake 2004. Journal of Geophysical Research 111, B2.

MENENDEZ, M., GARCÍA-DÍEZ, M., FITA, L., FERNÁNDEZ, J., MÉNDEZ, F. J. & GUTIÉRREZ, J. M. (2014): High-resolution sea wind hindcasts over the Mediterranean area. Climate Dynamics 42/7-8, 1857–1872.

MEULENKAMP, J. E. (1969): Stratigraphy of Neogene deposits in the Rethymnon province, Crete, with special reference to the phylogeny of uniserial Uvigerina from the Mediterranean region (Doctoral dissertation), Utrecht University.

MEULENKAMP, J. E., VAN DER ZWAAN, G. J. & VAN WAMEL, W. A. (1994): On late Miocene to recent vertical motions in the Cretan segment of the Hellenic arc. Tectonophysics 234, 53–72.

MINOURA, K., IMAMURA, F., KURAN, U., NAKAMURA, T., PAPADOPOULOS, G., TAKAHASHI, T. & YALCINER, A. (2000): Discovery of Minoan tsunami deposits. Geology 28, 59–62.

MITSOUDIS, D. A., FLOURI, E. T., CHRYSOULAKIS, N., KAMARIANAKIS, Y., OKAL, E. A. & SYNOLAKIS, C. E. (2012): Tsunami hazard in the southeast Aegean Sea. Coastal Engineering 60, 136–148.

MORALES, J. A., BORREGO, J., SAN MIGUEL, E. G., LÓPEZ-GONZÁLEZ, N. & CARRO, B. (2008): Sedimentary record of recent tsunamis in the Huelva Estuary (southwestern Spain). Quaternary Science Reviews 27/7-8, 734-746.

Mourtzas, N., Kolaiti, E. & Anzidei, M. (2015): Vertical land movements and sea level changes along the coast of Crete (Greece) since Late Holocene. Quaternary International 401, 43–70.

Mouslopoulou, V., Begg, J., Nicol, A., Oncken, O. & Prior, C. (2015a): Formation of Late Quaternary paleoshorelines in Crete, Eastern Mediterranean. Earth and Planetary Science Letter 431, 294–307.

Mouslopoulou, V., Nicol,A., Begg, J., Oncken, O. & Moreno, M. (2015b): Clusters of megaearthquakes on upper plate faults control the Eastern Mediterranean hazard, AGU Geophysical Research Letters 42, 1–7.

Murray, J.W. (2006): Ecology and Application of Benthic Foraminifera. Cambridge University Press, Cambridge. 426 pp.

Murray, A.S. & Wintle, A.G. (2000): Luminescence dating of quartz using an improved single-aliquot regenerative-dose protocol. Radiation Measurements 32, 57–73.

Murray, A.S. & Wintle, A.G. (2003): The single aliquot regenerative dose protocol: potential for improvements in reliability. Radiation Measurements 37, 377–381.

**N**

Newhall, C. G. & Self, S. (1982): The volcanic explosivity index (VEI) an estimate of explosive magnitude for historical volcanism. Journal of Geophysical Research: Oceans 87/C2, 1231–1238.

Nomikou, P., Druitt, T. H., Hübscher, C., Mather, T. A., Paulatto, M., Kalnins, L. M., Kelfoun, K., Papanikolaou, D., Bejelou, K., Lampridou, D. Pyle, D.M., Carey, S., Watts, A.B., Weiss, B. & Parks, M.M. (2016): Post-eruptive flooding of Santorini caldera and implications for tsunami generation. Nature communications 7, 1–10.

Nomikou, P., Hübscher, Papanikolaou, D., Farangitakis, G.P., Ruhnaub, M. & Lampridou, D. (2018): Expanding extension, subsidence and lateral segmentation within the Santorini - Amorgos basins during Quaternary: Implications for the 1956 Amorgos events, central - south Aegean Sea, Greece. Tectonophysics 722, 138–153.

Novikova, T., Papadopoulos, G.A. & McCoy, F.W. (2011): Modelling of tsunami generated by the giant Late Bronze Age eruption of Thera, South Aegean Sea, Greece. Geophysical Journal International 186, 665–680.

Ntageretzis, K., Vött, A., Fischer, P., Hadler, H., Emde, K., Röbke, B. R. & Willershäuser, T. (2015a): Traces of repeated tsunami landfall in the vicinity of Limnothalassa Moustou. Zeitschrift für Geomorphologie 59, Supplementary Issues 4, 301–317.

Ntageretzis, K., Vött, A., Fischer, P., Hadler, H., Emde, K., Röbke, B. R. & Willershäuser, T. (2015b): Palaeotsunami history of the Elos Plain (Evrotas River delta, Peloponnese, Greece). Zeitschrift für Geomorphologie 59, Supplementary Issues 4, 253–273.

Ntageretzis, K., Vött, A., Emde, K., Fischer, P., Hadler, H., Röbke, B. R. & Willershäuser, T. (2015c): Palaeotsunami record in near-coast sedimentary archives in southeastern Lakonia (Peloponnese, Greece). Zeitschrift für Geomorphologie 59, Supplementary Issues 4, 275–299.

**O**

Olley, J. M., Caitcheon, G. G. & Roberts, R. G. (1999): The origin of dose distributions in fluvial sediments, and the prospect of dating single grains from fluvial deposits using optically stimulated luminescence. Radiation Measurements 30/2, 207–217.

Ozel, N. M., Ocal, N., Cevdet, Y. A., Kalafat, D. & Erdik, M. (2011): Tsunami hazard in the Eastern Mediterranean and its connected seas: Toward a Tsunami warning center in Turkey. Soil Dynamics and Earthquake Engineering 31/4, 598–610.

**P**

Papadopoulos, G.A. (2011): A Seismic History of Crete: Earthquakes and Tsunamis, 2000 B.C. - A.D. 2011. Ocelotons, Athens. 365 pp.

Papadopoulos, G.A. & Chalkis, B.J. (1984): Tsunami observed in Greece and the surrounding area from antiquity up to present times. Marine Geology 56, 309–317.

Papadopoulos, G.A., Daskalaki, E., Fokaefs, A. & Giraleas, N. (2007): Tsunami hazards in the eastern Mediterranean: strong earthquakes and tsunamis in the east Hellenic Arc and Trench system. Natural Hazards and Earth System Sciences 7, 57–64.

Papadopoulos, G., Minoura, K., Imamura, F., Kuran, U., Yalçiner, A., Fokaefs, A. & Takahashi, T. (2012): Geological evidence of tsunamis and earthquakes at the Eastern Hellenic Arc: correlation with historical seismicity in the eastern Mediterranean Sea. Research in Geophysics 2/12, 92–99.

Papadopoulos, G. A., Gràcia, E., Urgeles, R., Sallares, V., De Martini, P. M., Pantosti, D., González, M., Yalciner, A.C., Mascle, J., Sakellariou, D., Salamon, A., Tinti, S., Karastathis, V., Fokaefs, A., Camerlenghi, A. Novikova, T. & Papageorgiou, A. (2014): Historical and pre-historical tsunamis in the Mediterranean and its connected seas: Geological signatures, generation mechanisms and coastal impacts. Marine Geology 354, 81–109.

Papanikolaou, D. & Vassilakis, E. (2010): Thrust faults and extensional detachment faults in Cretan tectonostratigraphy: implications for Middle Miocene extension. Tectonophysics 488, 233–247.

Papazachos, B. S. (1996): Large seismic faults in the Hellenic arc. Annali Geofisica 34/5, 891–903.

Papazachos, B. C. & Dimitriu, P. P. (1991): Tsunamis in and near Greece and their relation to the earthquake focal mechanisms. Natural Hazards 4(2-3), 161–170.

Papazachos, B.C. & Papazachou, C. (1997): The Earthquakes of Greece. Editions Ziti. Thessaloniki. 304 pp.

Pareschi, M., Favalli, M. & Boshi, E. (2006): Impact of the Minoan tsunami of Santorini: simulated scenarios in the eastern Mediterranean. Geophysical Research Letters 33, 1–6.

Pashley, R. (1837): Travels in Crete, Vol. 2. Murray, Cambridge. 326 pp.

Perianez, R. & Abril, J.M. (2014): Modelling tsunamis in the Eastern Mediterranean Sea. Application to the Minoan Santorini tsunami sequence as a potential scenario for the biblical Exodus. Journal of Marine Systems 139, 91–102.

Perlman, P. (2004a): Elyros (n. 959). In: Hansen M.H. & Nielsen T. H. (Eds), An Inventory of Archaic and Classical Poleis. Oxford University Press, Oxford, 1161.

Perlman, P. (2004b): Lisos (n. 973). In: Hansen M.H. & Nielsen T. H. (Eds), An Inventory of Archaic and Classical Poleis. Oxford University Press, Oxford, 1174–1175.

Peterek, A. & Schwarze, J. (2004): Architecture and Late Pliocene to recent evolution of outer-arc basins of Hellenic subduction zone (south-central Crete, Greece). Journal of Geodynamics 38, 19–55.

Pilarczyk, J. E., Dura, T., Horton, B. P., Engelhart, S. E., Kemp, A. C. & Sawai, Y. (2014): Microfossils from coastal environments as indicators of paleo-earthquakes, tsunamis and storms. Palaeogeography, Palaeoclimatology, Palaeoecology 413, 144-157.

Pirazzoli, P. A., Laborel, J. & Stiros, S.C. (1996): Earthquake clustering in the Eastern Mediterranean during historical times. Journal of Geophysical Research 101, 6083–6097.

Pirazzoli, P. A., Thommeret, J., Thommeret, Y., Laborel, J. & Montaggioni, L.F. (1982): Crustal block-movements from Holocene shorelines: Crete and Antikythira (Greece). Tectonophysics 86, 27–43.

Pirazzoli, P. A., Ausseil-Badie, J., Giresse, P., Hadjidaki, E. & Arnold, M. (1992): Historical environmental Changes at Phalasarna harbor, west Crete. Geoarchaeology 7, 371–392

Polonia, A., Bonatti, E., Camerlenghi, A., Lucchi, R. G., Panieri, G. & Gasperini, L. (2013): Mediterranean megaturbidite triggered by the AD 365 Crete earthquake and tsunami. Scientific reports 3.

Preusser, F., Degering, D., Fuchs, M., Hilgers, A., Kadereit, A., Klasen, N., Krebetschek, M., Richter, D. & Spencer, J.Q.G. (2008): Luminescence dating: basics, methods and applications. Eiszeitalter und Gegenwart 57/1-2, 95–149.

Preusser, F., Chithambo, M., L., Götte, T., Martini, M., Ramseyer, K., Sendezera, E. J., Susino, G.J. & Wintle, A. (2009): Quartz as a natural luminescence dosimeter. Earth Science Reviews 97/1-4, 184–214.

**Q**

Quintela, M., Costa, P. J., Fatela, F., Drago, T., Hoska, N., Andrade, C. & Freitas, M. C. (2016): The AD 1755 tsunami deposits onshore and offshore of Algarve (south Portugal): Sediment transport interpretations based on the study of Foraminifera assemblages. Quaternary International 408, 123–138.

**R**

Reicherter, K., Papanikolaou, I., Roger, J., Mathes-Schmidt, M., Papanikolaou, D., Rössler, S., Grützner, C. & Stamatis, G. (2010): Holocene tsunamigenic sediments and tsunami modeling in the Thermaikos Gulf area (northern Greece). Zeitschrift für Geomorphologie 54,Supplementary Issue 3, 99-126.

Reilinger, R., McClusky, S., Vernant, P., Lawrence, S., Ergintav, S., Cakmak, R., Ozener, H., Kadirov, F. Guliev, I., Stepanyan, R., Nadariya, M., Hahubia, G., Mahmoud, S., Sakr, K., Ar- Rajehi, A., Paradissis, D., Al-Aydrus, A., Prilepin, M., Guseva, T., Evren, E., Dmitrotsa, A., Filikov; S.V., Gomez, F., Al-Ghazzi, R. & Karam, G. (2006): GPS constraints on continental deformation in the Africa–Arabia–Eurasia continental collisional zone and implications for the dynamics of plate interactions. Journal of Geophysical Research: Solid Earth 111, 2–26.

Reimer, P. J., Bard, E., Bayliss, A., Beck, J. W., Blackwell, P. G., Ramsey, C. B., Buck, C. E., Cheng, H., Edwards, R. L., Friedrich, M., Grootes, P. M., Guilderson, T. P., Haflidason, H., Hajdas, I., Hatté, C., Heaton, T. J., Hoffmann, D. L., Hogg, A. G., Hughen, K. A., Kaiser, K. F., Kromer, B., Manning, S. W., Niu, M., Reimer, R. W., Richards, D. A., Scott, E. M., Southon, J. R., Staff, R. A., Turney, C. S. M. & von der Pflicht, J. (2013): Intcal13 and Marine13 radiocarbon age calibration curves 0-50,000 years cal BP. Radiocarbon 55/4, 1869–1887.

Reinhardt, E.G., Patterson, R.T. & Schröder-Adams, C.J. (1994) Geoarchaeology of the ancient harbor site of Caesarea Maritima, Israel: evidence from sedimentology and palaeoecology of benthic foraminifera. Journal of Foraminiferal Research 24/1, 37–48.

Richmond, B., Szczuciński, W., Chagué-Goff, C., Goto, K., Sugawara, D., Witter, R., Tappin, D.R., Jaffe, B., Fujino, S., Nishimura, Y. & Goff, J. (2012): Erosion, deposition and landscape change on the Sendai coastal plain, Japan, resulting from the March 11, 2011 Tohoku-oki tsunami. Sedimentary Geology 282, 27–39.

Rieser, U. (1991): Low-Level Gamma-Spektrometrie zum Zwecke der Dosisleistungbestimmung bei Lumineszenz-Datierung. Ph.D. thesis, Universität Heidelberg.

Rodríguez-Ramírez, A., Villarías-Robles, J.J.R. Pérez-Asensio, J.N., Santos, A., Morales, J.A., Celestino-Pérez, S., León, A. & Santos-Arévalo, F.J. (2016): Geomorphological record of extreme wave events during Roman times in the Guadalquivir estuary (Gulf of Cadiz, SW Spain): An archaeological and paleogeographical approach. Geomorphology 261, 103–118.

Röbke, B.R. & Vött, A. (2017): The Tsunami phenomenon. Progress in Oceanography 159, 296–322.

Röbke, B. R., Schüttrumpf, H., & Vött, A. (2016). Effects of different boundary conditions and palaeotopographies on the onshore response of tsunamis in a numerical model–A case study from western Greece. Continental Shelf Research 124, 182–199.

Röbke, B. R., Schüttrumpf, H., Fler, T. W., Fischer, P., Hadler, H., Ntageretzis, K., Willershäuser, T. & Vött, A. (2013): Tsunami inundation scenarios for the Gulf of Kyparissia (western Peloponnese, Greece) derived from numerical simulations and geoscientific field evidence. Zeitschrift für Geomorphologie, Supplementary Issues 57(4), 69–104.

Rönnfeld, W. (2008): Foraminiferen - Ein Katalog typischer Foraminiferen. Institut für Geowissenschaften der Universität Tübingen. Tübingen. 146 pp.

Roller, D., W. (2014): Geography of Strabo: An English Translation, with Introduction and Notes. Cambridge University Press, Cambridge. 907 pp.

Royden, L.H. & Papanikolaou, D.J. (2011): Slab segmentation and late Cenozoic disruption of the Hellenic arc. Geochemistry, Geophysics, Geosystems 12/3, 1–24.

## S

Sakellariou, D., Rousakis, G., Nomikou, P., Groff Bell, K., Carey, S. & Sirgurdsson, H. (2012): Tsunami Triggering Mechanisms Associated with the 17th cent. BC Minoan Eruption of Thera Volcano, Greece. Proceedings of the Twenty-second International Offshore and Polar Engineering Conference, Rhodes, Greece, June 17–22, 2012.

Sanders, I.F. (1982): Roman Crete: An Archaeological Survey and Gazetteer of Late Hellenistic. Roman, and Early Byzantine Crete. Warminster, 57–63.

Scheffers, A. & Kelletat, D. (2004): Bimodal tsunami deposits – a neglected feature in palaeo-tsunami research. Coastline Reports 1, 67–75.

Scheffers, A. & Scheffers, S. (2007): Tsunami deposits on the coastline of west Crete (Greece). Earth and Planetary Science Letters 259/3, 613–624.

Scheffers, A., Kelletat, D., Vött, A., May, S. M. & Scheffers, S. (2008): Late Holocene tsunami traces on the western and southern coastlines of the Peloponnesus (Greece). Earth and Planetary ScienceLetters 269, 271– 279.

Scheuer, L.E.A. & Vortisch, W. (2011): Sedimentological and geomorphological effects of the Sumatra–Andaman Tsunami in the area of Khao Lak, southern Thailand. Environ-

mental Earth Sciences 63/4, 785–796.

Schrott, L. (2015): Gelände-Arbeitsmethoden in der Geomorphologie. In: Ahnert, F. (Eds.), Einführung in die Geomorphologie, 5th ed., UTB, Stuttgart, 396–413.

Scicchitano, G., Monaco, C. & Tortorici, L. (2007): Large boulder deposits by tsunami waves along the Ionian coast of south-eastern Sicily (Italy). Marine Geology 238, 75–91.

Sdao, F., Parisi, S., Kalisperi, D., Pascale, S., Soupios, P., Lydakis-Simantiris, N. & Kouli, M. (2012): Geochemistry and quality of the groundwater from the karstic and coastal aquifer of Geropotamos River Basin at north-central Crete, Greece. Environmental Earth Sciences 67/4, 1145–1153.

Seidel, M., Seidel, E. &, Stöckhert, B. (2007): Tectono-sedimentary evolution of lower to middle Miocene half-graben basins related to an extensional detachment fault (western Crete, Greece). Terra Nova 19, 39–47.

Shaw, B. (2012): The AD 365 earthquake: Large tsunamigenic earthquakes in the Hellenic Trench. In: Shaw, B., Active tectonics of the Hellenic subduction zone. Springer Theses, pp. 7-28. Springer, Berlin, Heidelberg.

Shaw, B. & Jackson, J. (2010): Earthquake mechanisms and active tectonics of the Hellenic subduction zone. Geophysical Journal International 181, 966–984.

Shaw, B., Ambraseys, N.N., England, P.C., Floyd, M.A., Gorman, G.J., Higham, T.F.G., Jackson, J.A., Nocquet, J.-M., Pain, C.C. & Piggott, M.D. (2008): Eastern Mediterranean tectonics and tsunami hazard inferred from the AD 365 earthquake. Nature Geoscience 1, 268–276.

Shipley, G. (2012): Pseudo-Skylax's Periplous: Circumnavigation of the Inhabited World. Liverpool University Press. Liverpool.

Sigurdsson, H., Carey, S., Alexandri, M., Vougioukalakis, G., Croff, K., Roman, C., Sakellariou, D., Anagnostou, C., Rousakis, G., Ioakim, C. Goguo, A., Ballas, D., Misaridis, T. & Nomikou, P. (2006): Marine investigations of Greece's Santorini volcanic field. EOS, Transactions American Geophysical Union 87/34, 337–342.

Smedile, A., De Martini, P.M., Pantosti, D., Bellucci, L., Del Carlo, P., Gasperini, L., Pirrotta, C., Polonia, A. & Boschi, E. (2011): Possible tsunami signatures from an integrated study in the Augusta Bay offshore (Eastern Sicily–Italy). Marine Geology 281, 1–13.

Soloviev, S.L., Solovieva, O.N., Go, C.N., Kim, K.S. & Shchetnikov, N.A. (2000): Tsunamis in the Mediterranean Sea 2000 B.C. – 2000 A.D. Springer Netherlands, Dordrecht. 237 pp.

Soukissian T., Hatzinaki M., Korres G., Papadopoulos A., Kallos G. & Anadranistakis, E. (2007): Wind and wave atlas of the Hellenic seas. Hellenic Centre for Marine Research Publications, HCMR.

Soukissian, T., Prospathopoulos, A., Hatzinaki, M. & Kabouridou, M. (2008): Assessment of the wind and wave climate of the Hellenic Seas using 10-year hindcast results. Open Ocean Engineering Journal 1, 1–12.

Spratt, T. A. B. (1865): Travels and Researches in Crete. Harvard University Press, London. 484 pp.

Stefanakis, M.I. (2010): Western Crete: From Captain Spratt to modern archaeoseismology. In: Sintubin, M., Stewart I.S, Niemi, T.M. & Altunel, E. (Eds.). Ancient earthquakes. Geological Society of America Special Paper 471, Boulder, Colorado, 67–79.

Stiros, S. C. (2001): The AD 365 Crete earthquake and possible seismic clustering during the fourth to sixth centuries AD in the Eastern Mediterranean: a review of historical and archaeological data. Journal of Structural Geology 23, 545–562.

Stiros, S. C. (2010): The 8.5+ magnitude, AD 365 earthquake in Crete: Coastal uplift, topography changes, archaeological and historical signature. Quaternary International 216, 54–63.

Subarya, C., Chlieh, M., Prawirodirdjo, L., Avouac, J. P., Bock, Y., Sieh,. K., Meltzner, A.J., Natawidjaja, D.H. & McCaffrey, R. (2006): Plate-boundary deformation associated with the great Sumatra–Andaman earthquake. Nature 440, 46–51.

Switzer, A. D. & Jones, B. G. (2008): Large-scale washover sedimentation in a freshwater lagoon from the southeast Australian coast: sea-level change, tsunami or exceptionally large storm? The Holocene 18/5, 787–803.

**T**

Tanaka, H., Tinh, N. X., Umeda, M., Hirao, R., Pradjoko, E., Mano, A. & Udo, K. (2012): Coastal and estuarine morphology changes induced by the 2011 Great East Japan Earthquake Tsunami. Coastal Engineering Journal 54/1, 1–25.

Tanaka, H., Kayane, K., Adityawan, M. B., Roh, M. & Farid, M. (2014): Study on the relation of river morphology and tsunami propagation in rivers. Ocean Dynamics 64/9, 1319–1332.

Taymaz, T., Jackson, J. & Westaway, R. (1990): Earthquake mechanisms in the Hellenic trench near Crete. Geophysical Journal International 102, 695–731.

Thommeret, Y., Thommeret, J., Laborel, J., Montaggioni, L. & Pirazzoli, P. (1981): Late Holocene shoreline changes and seismotectonic displacements in western Crete (Greece). Zeitschrift für Geomorphologie N.F. 40, 127–149.

Tiberti, M. M., Basili, R. & Vannoli, P. (2014): Ups and downs in western Crete (Hellenic subduction zone). Scientific reports 4, 1–7.

Tinti, S. (1991): Assessment of tsunami hazard in the Italian seas. Natural Hazards 4, 267–283.

Tinti, S. & Maramai, A. (1996): Catalogue of tsunamis generated in Italy and in Cote d'Azur, France: a step towards a unified catalogue of tsunamis in Europe. Annali di Geofisica 39, 1253–1299.

Tolkova, E. & Tanaka, H. (2016): Tsunami Bores in Kitakami River. Pure and Applied Geophysics 173, 4039.

Triantaphyllou, M.V., Koukousioura, O. & Dimiza, M.D. (2009): The presence of the Indo-Pacific symbiont-bearing foraminifer Amphistegina lobifera in Greek coastal ecosystems (Aegean Sea, Eastern Mediterranean). Mediterranean Marine Science 10/2, 73–85.

Tsoukala, V. K., Chondros, M., Kapelonis, Z. G., Martzikos, N., Lykou, A., Belibassakis, K. & Makropoulos, C. (2016): An integrated wave modelling framework for extreme and rare events for climate change in coastal areas – the case of Rethymno, Crete. Oceanologia 58/2, 71–89.

Tsuji Y, Yanuma T, Murata I. & Fujiwara C. (1991): Tsunami ascending in rivers as an undular bore. Natural Hazards 4, 257–266.

Tyuleneva, N., Braun, Y., Katz, T., Suchkov, I. & Goodman-Tchernov, B. (2018): A new chalcolithic-era tsunami event identified in the offshore sedimentary record of Jisr

al-Zarka (Israel). Marine Geology 396, 67–78.

## V

Valle, B. L., Kalligeris, N., Findikakis, A. N., Okal, E. A., Melilla, L. & Synolakis, C. E. (2014): Plausible megathrust tsunamis in the eastern Mediterranean Sea. Proceedings of the Institution of Civil Engineers-Engineering and Computational Mechanics 167/3, 99–105.

van Hinsbergen, D. J. & Meulenkamp, J. E. (2006): Neogene supradetachment basin development on Crete (Greece) during exhumation of the South Aegean core complex. Basin Research 18/1, 103–124.

van Hinsbergen, D. J., Hafkenscheid, E., Spakman, W., Meulenkamp, J. E. & Wortel, R. (2005): Nappe stacking resulting from subduction of oceanic and continental lithosphere below Greece. Geology 33/4, 325–328.

Viana-Baptista, M.A., Soares, P.M., Miranda, J.M. & Luis, J.F. (2006): Tsunami propagation along Tagus estuary (Lisbon, Portugal) preliminary results. Science of Tsunami Hazards 24/5, 329–338.

Vött, A. & Kelletat, D. (2015): Holocene palaeotsunami landfalls and neotectonic dynamics in the western and southern Peloponnese (Greece). Zeitschrift für Geomorphologie, Supplementary Issues 59.4, 1-5.

Vött, A. & May, S.M. (2009): Auf den Spuren von Tsunamis im östlichen Mittelmeer. Geographisches Rundschau 12, 42–48.

Vött, A., May, M., Brückner, H. & Brockmüller, S. (2006): Sedimentary evidence of Late Holocene Tsunami events near Lefkada Island (NW Greece). Zeitschrift für Geomorphologie N.F., Supplementary Issue 146, 139–172.

Vött, A., Brückner, H., Brockmüller, S., Handl, M., May, S.M., Gaki-Papanastassiou, K., Herd, R., Lang, F., Maroukian, H., Nelle, O. & Papanastassiou, D. (2009a): Traces of Holocene tsunamis across the Sound of Lefkada, NW Greece. Global and Planetary Change 66, 112–128.

Vött, A., Brückner, H., May, S.M., Sakellariou, D., Nelle, O., Lang, F., Kapsimalis, V., Jahns, S., Herd, R., Handl, M. & Fountoulis, I. (2009b): The Lake Voulkaria (Akarnania, NW Greece) palaeoenvironmental archive – a sediment trap for multiple tsunami impact since the mid-Holocene. Zeitschrift für Geomorphologie N.F., Supplementary Issue 53/1, 1–37.

Vött, A., Bareth, G., Brückner, H., Curdt, C., Fountoulis, I., Grapmayer, R., Hadler, H., Hoffmeister, D., Klasen, L., Lang, F., Masberg, P., May, P., Ntageretzis, K., Sakellariou, D. & Willershäuser, T. (2010): Beachrock-type calcarenitic tsunamites along the shores of the eastern Ionian Sea (western Greece) – case studies from Akarnania, the Ionian Islands and the western Peloponnese. Zeitschrift für Geomorphologie, Supplementary Issues 54/3, 1–50.

Vött, A., Lang, F., Brückner, H., Gaki-Papanastassiou, K., Maroukian, H., Papanastassiou, D., Giannikos, A., Hadler, H., Handl, M., Ntageretzis, K., Willershäuuser, T. & Zander, A. (2011a): Sedimentological and geoarchaeological evidence of multiple tsunamigenic imprint on the Bay of Palairos-Pogonia (Akarnania, NW Greece). Quaternary International 242, 213–239.

Vött, A., Bareth, G., Brückner, H., Lang, F., Sakellariou, D., Hadler, H., Ntageretzis, K. & Willershäuser, T. (2011b): Olympia's harbour site Pheia (Elis, western Peloponnese, Greece) destroyed by tsunami impact. Die Erde 142/3, 259–288.

Vött, A., Hadler, H., Willershäuser, T., Ntageretzis, K., Brückner, H., Warnecke, H., Grootes, P.M., Lang, F., Nelle, O. & Sakellariou, D. (2014): Ancient harbours used as tsunami sediment traps - the case study of Krane (Cefalonia Island, Greece). In: Ladstätter, S., Pirson, F. & Schmidts, T. (Eds) Häfen und Hafenstädte im östlichen Mittelmeerraum von der Antike bis in byzantinische Zeit. Neue Entdeckungen und aktuelle Forschungsansätze, pp. 743–771. Harbors and Harbor Cities in the Eastern Mediterranean from Antiquity to the Byzantine Period: Recent Discoveries and Current Approaches. Byzas 19, Veröffentlichungen des Deutschen Archäologischen Instituts Istanbul, Österreichisches Archäologisches Institut Sonderschriften 52 (II), Istanbul.

Vött, A., Fischer, P., Röbke, B.R., Werner, V., Emde, K., Finkler, C., Hadler, H., Handl, M., Ntageretzis, K. & Willershäuser, T. (2015): Holocene fan alluviation and terrace formation by repeated tsunami passage at Epitalio near Olympia (Alpheios River valley, Greece). Zeitschrift für Geomorphologie, Supplementary Issue 59/4, 81–123.

Vött, A., Hadler, H., Koster, B., Mathes-Schmidt, M., Röbke, B. R., Willershäuser, T. & Reicherter, K. (2018a): Returning to the facts: Response to the refusal of tsunami traces in the ancient harbour of Lechaion (Gulf of Corinth, Greece) by 'non-catastrophists' – Reaffirmed evidence of harbour destruction by historical earthquakes and tsunamis in AD 69–79 and the 6$^{th}$ cent. AD and a preceding pre-historical event in the early 8$^{th}$ cent. BC. Zeitschrift für Geomorphologie.

Vött, A., Bruins, H.J., Gawehn, M., Goodman-Tchernov, B.N., De Martini, P.M., Kelletat, D., Mastronuzzi, G., Reicherter, K., Röbke, B.R., Scheffers, A., Willershäuser, T., Avramidis, P., Bellanova, P., Costa, P.J.M., Finkler, C., Hadler, H., Koster, B., Lario, J., Reinhardt, E., Mathes-Schmidt, M., Ntageretzis, K., Pantosti, D., Papanikolaou, I., Sansò, P., Scicchitano, G., Smedile, A. & Szczuciński, W. (2018b): Publicity waves based on manipulated geoscientific data suggesting climatic trigger for majority of tsunami findings in the Mediterranean – Response to 'Tsunamis in the geological record: Making waves with a cautionary tale from the Mediterranean' by Marriner et al. (2018a). Zeitschrift für Geomorphologie N.F. Supplementary Issue.

Vött, A., Willershäuser, T., Röbke, B., Obrocki, L., Fischer, P., Hadler, H., Emde, K., Eder, B., Gehrke, H.-J. & Lang, F. (2018c): Major flood events recorded in the Holocene sedimentary sequence of the uplifted Ladiko and Makrisia basins near ancient Olympia (western Peloponnese, Greece). Zeitschrift für Geomorphologie, Supplementary Issues. 10.1127/zfg_suppl/2018/0499.

## W

Werner, V., Baika, K., Fischer, P., Hadler, H., Obrocki, L., Willershäuser, T., Tzigounaki, A., Tsigkou, A., Reicherter, K., Papanikolaou, I., Emde, E. & Vött, A. (2018a): The sedimentary and geomorphological imprint of the AD 365 tsunami on the coasts of southwestern Crete (Greece) – Examples from Sougia and Palaiochora. Quaternary International 473, 66–90.

Werner, V., Baika, K., Tzigounaki, A., Reicherter, K., Papanikolaou, I., Emde, K., Fischer, P. & Vött, A. (2018b): Mid-Holocene tectonic geomorphology of northern Crete deduced from a coastal sedimentary archive near Rethymnon and a Late Bronze Age Santorini tsunamite candidate. Geomorphology 326, 167–189.

Werner, V., Baika, K., Tzigounaki, A., Reicherter, K., Papanikolaou, I., Emde, K., Fischer, P., Vött, A. (2018c): Extreme wave events recorded in sedimentary archives of the Geropotamos River (north-central Crete, Greece). Zeitschrift für Geomorphologie N.F. Supplementary Issue (in press).

Willershäuser, T., Vött, A., Brückner, H., Bareth, G., Nelle, O., Nadeau, M.-J., Hadler, H. & Ntageretzis, K. (2013): Holocene tsunami landfall along the shores of the inner Gulf of Argostoli (Cefalonia Island, Greece). Zeitschrift für Geomorphologie, N. F., Suppl. Issue 57/4, 105–138.

Willershäuser, T., Vött, A., Hadler, H., Fischer, P., Röbke, B., Ntageretzis, K., Emde, K. & Brückner, H. (2015): Geo-scientific evidence of tsunami impact in the Gulf of Kyparissia (western Peloponnese, Greece). Zeitschrift für Geomorphologie N.F., Supplementary Issue 59/4, 43–80.

Wintle, A.G. & Murray, A. S. (2006): A review of quartz optically stimulated luminescence characteristics and their relevance in single-aliquot regeneration dating protocols. Radiation Measurements 41, 369–391.